Enhancing Accuracy in Large-Signal Millimetre-Wave Measurement Systems

Alexander Baddeley

A thesis submitted for the degree of

Doctor of Philosophy

Cardiff University

December 2025

Abstract

Power amplifiers are essential components in the transmit chain of RF communication systems. Most commercial applications fall within the sub-6 GHz bands, with mobile communication networks being a notable example. Since the inception of these networks, considerable efforts have been made, and continue to be made, in both industry and research to design linear and power-efficient architectures. Techniques employed to improve peak efficiency exploit harmonic terminations, whilst load modulation techniques remain a mainstay for applications requiring signals with a high peak-to-average power ratio (PAPR).

There is a growing demand for higher data rates, with new spectrum allocation opening up in the mm-wave bands, enabling advancements in mobile networks and satellite applications. However, this presents numerous challenges, as it is not simply a matter of replicating developments from sub-6 GHz frequencies to mm-wave bands.

Numerous challenges exist in device development, including wafer growth and fabrication. System-level engineers must contend with higher path loss and greater signal complexity, while power amplifier designers face the challenge of designing with transistors with lower gain and higher parasitics. This thesis focuses on mm-wave characterisation systems, emphasising the improvement of measurement reliability and accuracy. This focus is motivated by the desire to improve the quality of data used to generate device models, which, in turn, can increase the success rate of device tape-outs.

This work presents a state-of-the-art mm-wave harmonic load-pull system with waveform measurement capability operating up to 100 GHz. The calibration pro-

cedure and configuration of the system to perform waveform measurements are detailed, with a strong focus on achieving accurate and reliable measurements. Mechanical fixtures were designed to support measurement fixtures and avoid any degradation in the phase alignment at the phase meter measurement plane to achieve reliable waveform measurements. For the first time, multi-harmonic load-pull and waveform measurements are demonstrated on a 27.5 GHz GaAs pHEMT, which showed an improvement of power-added efficiency over fundamental tuning of greater than 3%.

The primary focus was to ensure reliability and accuracy in practical active and passive mm-wave load-pull systems. It was determined that achieving highly accurate measurements for high-power load-pull requires a dynamic range of 70 dB during the vector calibration stage. However, this is not trivial due to the attenuation needed on the VNA receivers to prevent saturation.

Unavoidable calibration errors also arise when configuring a mm-wave system for device measurements. It was shown that mechanical alterations to the system introduce changes to the equivalent network parameters, resulting in load-dependent errors. These effects become more pronounced at higher frequencies.

To address this, a second-step method was developed to extend the traditional large-signal calibration procedure. This approach effectively 'recalibrates' the system in its final measurement configuration. The technique involves performing a load-pull measurement on a thru calibration standard and applying a least-squares fit to the measured waves to determine a new S-parameter matrix, which is then used to recalculate the TRL error box. This technique was demonstrated on the measurement of a GaAs pHEMT at 82.5 GHz, improving the accuracy of the PAE by 8%.

List of Publications

[1] A. Baddeley et al. "Gate Bias Voltage Dependence of Cardiff Admittance Model in Ka-Band GaAs pHEMTs". In: *IEEE Top. Conf. on RF/Microw. Power Amplifiers for Radio and Wireless Appl. (PAWR)*. 2022, pp. 8–10.

[2] A. Baddeley et al. "Millimeter-Wave On-Wafer Large Signal Characterization System for Harmonic Source/Load Pull and Waveform Measurements". In: *IEEE MTT-S Int. Microw. Symp. (IMS)*. 2023, pp. 1101–1104.

[3] S.E. Ghozati, A. Baddeley, and R. Quaglia. "Large-Signal Characterization and Behavioral Modeling of mm-wave GaN HEMT Switches Tailored for Advanced Power Amplifier Architectures". In: *IEEE Top. Conf. on RF/Microw. Power Amplifiers for Radio and Wireless Appl. (PAWR)*. 2024, pp. 21–23.

[4] A. Baddeley, R. Quaglia, and P. Tasker. "Evaluation and Improvement of mm-wave Load Pull Measurement accuracy". In: *ARMMS RF & Microw. Society Conf.* Apr. 2024.

[5] A. Baddeley, R. Quaglia, and P. J. Tasker. "Calibration Error Reduction in Millimeter-Wave Load–Pull Systems Measuring Highly Reflective Loads". In: *IEEE Trans. Microw. Theory Techn.* (2024), pp. 1–13. DOI: 10.1109/TMTT.2024.3495544.

Acknowledgements

In memory of Mum, who I miss more than words can express.

I owe a huge thanks and deep appreciation to my supervisor, Dr. Roberto Quaglia, for his invaluable guidance and support throughout my Bachelor's, Master's, and PhD projects. His almost endless knowledge on any topic was inspiring. He works tirelessly to support all of his students; I will never know where he finds the time for it. I am grateful for all the extra opportunities and projects he provided, through which I had the chance to meet many wonderful people in both industry and academia.

A big thanks to Dr. Kauser Chaudhry and Dr. Ehsan Azad for making me feel so welcome when I joined the research group; I enjoyed all of our lunchtime chats and have learnt so much from both of you, personally and professionally. I'll always be left with the caffeine addiction you encouraged during our breaks.

There are so many great people to thank along this journey: my fellow Ph.D. students Timmy, Seyed (Urman), Wesley, Arthur, JB, Indy, Derek, and Aquila, to name just a few. They have made this experience full of memorable moments and laughter.

Thanks to the wider CHFE research group for making this experience so enjoyable, especially Prof. Adrian Porch, who organised all of the CHFE walks and breakfasts. It's been a wonderful opportunity to explore some of the beautiful spots across South Wales.

I would like to thank Qorvo Inc., EPSRC, and the CDT in Compound Semiconductor Manufacturing for their financial support of this PhD project. The devices

and calibration structures provided by Qorvo Inc. were invaluable, forming the foundation for most of the calibration activities throughout my research.

I would also like to express my appreciation to Dr. Chris Sanabria for his ongoing support and to Mr. Bo Zhao for our enjoyable monthly meetings and for sharing his expertise on mm-wave power amplifiers.

Acronyms

2DEG	Two Dimensional Electron Gas
1G	First Generation Mobile Communication System
2G	Second Generation Mobile Communication System
3G	Third Generation Mobile Communication System
4G	Fourth Generation Mobile Communication System
5G	Fifth Generation Mobile Communication System
ADS	Advanced Design System
ANN	Artificial Neural Networks
CW	Continuous Wave
DCIV	Direct Current Current and Voltage
DCRF	Direct Current to Radio Frequency efficiency
DUT	Device Under Test
FoM	Figure of Merit
FR1	Frequency Range 1
FR2	Frequency Range 2

eLRRM	Enhanced Line-Reflect-Reflect-Match
GaAs	Gallium Arsenide
GaN	Gallium Nitride
GSG	Ground-Signal-Ground
HEMT	High Electron Mobility Transistor
HPR	Harmonic Phase Reference
IC	Integrated Circuit
IF	Intermediate Frequency
ISS	Impedance Standard Substrate
LEO	Low Earth Orbit
LP	Load-pull
LRRM	Line-Reflect-Reflect-Match
LUT	Look-up Table
MAG	Maximum Available Gain
MSG	Maximum Stable Gain
MMIC	Monolithic Microwave Integrated Circuit
mTRL	multi-line Thru-Reflect-Line
NVNA	Nonlinear Vector Network Analyser
NMSE	Normalised Means Square Error
NCO	Numerically Controlled Oscillator

PA	Power Amplifier
PAE	Power Added Efficiency
PCB	Printed Circuit Board
PDF	Probability Distribution Function
pHEMT	Pseudomorphic HEMT
RF	Radio Frequency
SOL	Short-Open-Load
SOLT	Short-Open-Load-Thru
SP	Source-pull
SMA	SubMiniature version A
TEM	Transverse Electric and Magnetic
TWTA	Travelling Wave Tube Amplifier
TRL	Thru-Reflect-Line
TRM	Thru-Reflect-Match
UOSM	Unknown Thru-Short-Open-Match
VNA	Vector Network Analyser

Contents

List of Figures

List of Tables

Chapter 1

Introduction

1.1 Motivation

Since the inception of the first mobile communication systems (1G) in 1982, the demand and requirement for greater data rate and connectivity have expanded rapidly with the development of subsequent mobile networks (2G, 3G, 4G, and 5G). The systems have become ever more complex to facilitate this growth, with modulation schemes to encourage spectral efficiency and higher carrier frequencies to accommodate growing modulation bandwidths. This growth is matched by an ever-increasing

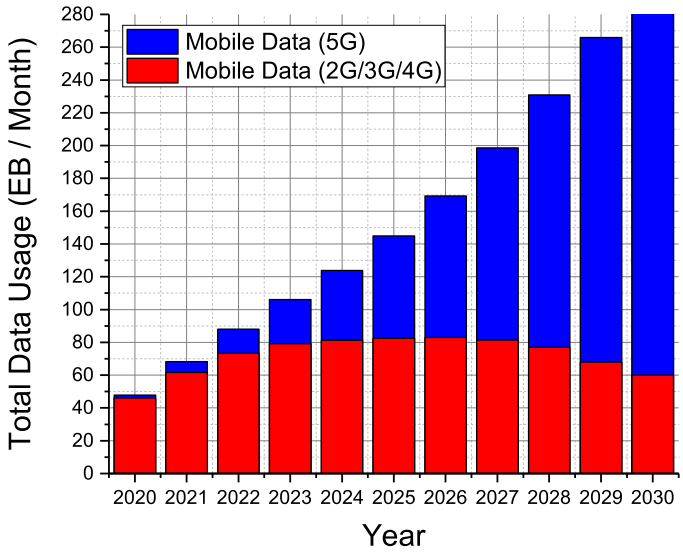

Figure 1.1: The reported and forecasted global total mobile network data traffic per month by system, published in [1] in 2024.

customer demand, as shown in the following figures.

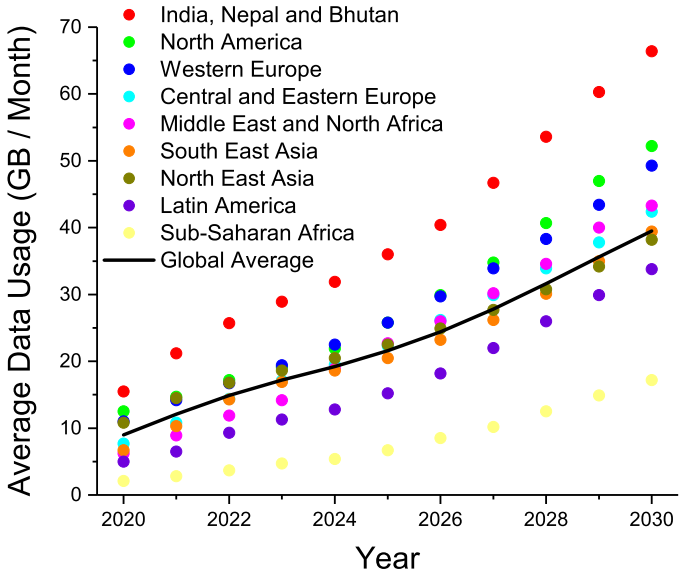

Figure 1.2: The reported and forecasted average mobile data per smartphone per month by region, published in [1] in 2024.

Figure 1.1 shows that over time, not only is the demand for mobile data increasing year on year, but the market share for 5G is becoming a significant proportion of that demand, with its higher capacity and data rate against the other systems [1].

This trend can be split by region, shown in Figure 1.2; globally, the forecasted average amount of data a user demands is increasing yearly in all parts of the world [1]. These trends require the technology employed by the network operators to match these market-driven demands.

The latest generation (5G) is the first mobile network that has looked to expand beyond the sub-6-GHz frequency range. However, the bulk of the network relies on the FR1 bands [2] (694-790 MHz and 3.4-3.8 GHz), the FR2 bands (24-27.5 GHz and 26.5-29.5 GHz) has been allocated to mm-wave bands to accommodate short-range high bandwidth links.

With the advances in solid-state device technology over the legacy TWTA's, satellite networks are also becoming promising solutions that offer low latency and high-speed internet connectivity, with the LEO satellite market expected to grow from $33.37 billion in 2023 to $102.9 billion by 2032 [3]. To deliver these outputs, the use of mm-wave frequencies is becoming commonplace, with spectrum available [4]

at X-band (7.25-7.75 GHz and 7.9-8.4 GHz), Ku-band (10-13 GHz and 14-18 GHz), Ka-band (17.7-21.2 GHz and 27.5-31 GHz), Q-band (37.5-51.4 GHz) and E-band (71-76 GHz and 81-86 GHz).

For the rollout of mm-wave technology to be successful, several technological challenges must be overcome across several disciplines.

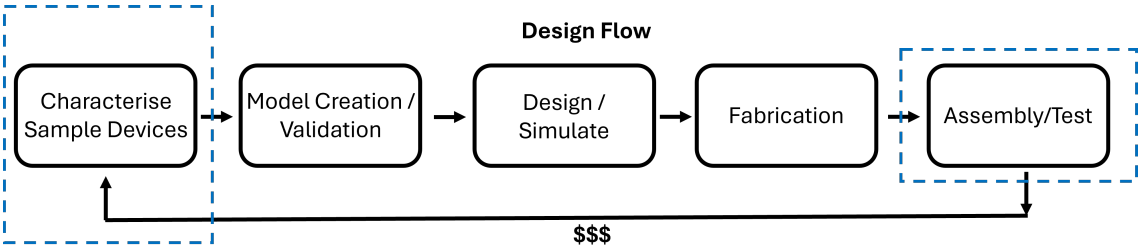

Figure 1.3: Flow Chart describing a typical power amplifier design flow chart

Figure 1.3 outlines a typical power amplifier design flow. The first step involves characterising transistor unit cells. Semiconductor foundries typically supply these as bare dies, which must be mounted onto a carrier plate by the designer before they can be probed on a probe station. Tests include DC-IV and S-parameter measurements from low frequency up to at least the highest frequency of interest. In practice, measurements are usually taken to the upper limit of the available equipment to enable comprehensive comparison with the simulation models. Load-pull measurements may also be performed at this stage to provide a more complete dataset, enabling comparison of DC, small-signal, and large-signal performance.

When designing with a foundry process, the foundry usually supplies a device model. This is an encrypted simulation model compatible with the designer's software (e.g., MWO or ADS). The model is intended to replicate the behaviour of the physical device and to be fully scalable across frequency, periphery (gate fingers and gate width), input power, temperature, and bias conditions. Achieving a fully scalable and accurate model requires a modelling technique capable of encapsulating all of these parameters and scaling them correctly. Additionally, developing such a model would require the foundry to undertake an extensive measurement campaign and subsequently validate the extracted model. This level of characterisation

is rarely performed due to the substantial resources required for each technology. Instead, the foundry typically selects a limited set of parameters from each characteristic and extracts a model that only loosely represents the physical device. Consequently, characterising sample devices is essential in order to understand the magnitude and nature of the model error.

After validating the model, the designer can proceed with simulation and layout generation. The layout is then submitted to the foundry for fabrication. Foundries commonly offer shared wafer runs, allowing multiple customers to share the cost rather than purchasing an entire wafer.

Once fabrication is complete, the wafer is diced, and the foundry performs basic continuity tests before singulating and shipping the dies to the customer.

The designer then performs RF testing, including S-parameters and large-signal measurements, and compares the measured performance with the simulated results. Ideally, the two would be similar, allowing the design to progress to production and packaging. At mm-wave frequencies, however, this is rarely the case due to process variability and limitations in model accuracy. If the design does not meet the required specification, an additional design iteration is necessary. Each iteration incurs significant cost and delay, which can determine the commercial viability of the product. For example, a 6-inch wafer of 0.15 μm GaN-on-SiC devices can cost between \$50,000 and \$100,000.

This design flow highlights the importance of understanding the accuracy and limitations of both the models and the unit cells. Such understanding can only be achieved with a measurement system that is capable of performing the required characterisation over the full frequency and power ranges of interest, together with measurements of adequate accuracy to provide a reliable representation of the device. The primary aim of this thesis is therefore to develop characterisation methodologies that enhance both the capability and the accuracy of on-wafer measurements, enabling the reliable optimisation of transistors for mm-wave power amplifier applications.

1.2 Research Objectives

To advance the field of mm-wave characterisation, the aim of this thesis is to offer characterisation methodologies to accurately measure and optimise on-wafer transistors for use as mm-wave power amplifiers; several objectives have been defined to set out criteria for success. These are as follows:

The first objective is to present a first-of-its-kind mm-wave source/load-pull measurement system by demonstrating the calibration and measurement of on-wafer GaN and GaAs devices across the frequencies of interest for next-generation communication systems, in particular Ka-band and E-band. This involves fundamental and multi-harmonic load-pull measurements.

The second objective is to evaluate mm-wave load-pull measurement systems, including Cardiff University's passive and active systems, to understand the best-case accuracy that can be achieved and the mechanisms for error.

The third objective is to develop a correction methodology that can easily be implemented into any practical measurement system, using the information learned from the second objective, to ensure optimal accuracy of mm-wave load-pull systems.

1.3 Chapter Summary

The objectives above are achieved across the thesis with three literature review chapters that provide a technical background and build upon the motivation for the research chapters that present the state-of-the-art mm-wave measurement systems at Cardiff University and the activities to produce accurate and reliable measurements. The details of each chapter are discussed:

Chapter 2 - RF Measurement Techniques provides technical background on RF measurements, with a detailed discussion on the hardware required to perform on-wafer mm-wave measurements, such as the vector network analyser, coaxial connectors and on-wafer probing techniques. The chapter discusses S-parameters and large-signal techniques, with load-pull measurements being the primary focus.

Chapter 3 - Error Correction Methods builds on the measurement literature review chapter and describes the error correction techniques essential for evaluating device performance at the terminals of a device. This provides the technical background for research chapters 5, 6 and 7.

Chapter 4 - Device Modelling is a literature review chapter that covers the background of device modelling, describing the different methods used to model devices. This section aims to provide context and the motivation for performing and optimising the accuracy of mm-wave measurements.

Chapter 5- Millimetre-wave Harmonic Source/Load-pull Measurement System is the first research chapter and discusses a first-of-its-kind measurement system at Cardiff University that is capable of performing passive multi-harmonic source/load-pull up to 110 GHz on a single sweep. The system can capture current and voltage waveforms up to a maximum frequency of 100 GHz which allows for the future optimisation of mm-wave devices. The chapter details the error correction process flow, and special attention is paid to the techniques employed to achieve accurate and reliable measurements.

Chapter 6 - Error Correction Uncertainty Evaluation for mm-wave Load-pull Systems. This chapter builds upon the conclusions from the mm-wave measurement system chapter and analyses the mechanisms contributing to uncertainty when measuring on-wafer devices at mm-wave.

Chapter 7 - Error correction Enhancement Technique for Accurate Millimetre-wave Load-pull Measurements chapter describes a technique that compliments a standard large-signal calibration process and is used to reduce calibration error analysed in Chapter 6.

Chapter 8 summarises the thesis, draws conclusions from the set of works, and provides suggestions for future work that builds upon the findings of this thesis.

References

[1] Ericsson. *Mobile data traffic outlook*. Tech. rep. Ericsson, Nov. 2024.

[2] OFCOM. *United Kingdom Frequency Allocation Table*. Tech. rep. OFCOM, Jan. 2017.

[3] Polaris Market Research. *LEO Satellite Market Research Report*. Tech. rep. Polaris Market Research, June 2024.

[4] Qorvo Inc. *How Modern LEO Satellite Technologies are Changing the Space Race*. Qorvo Inc. URL: https://www.qorvo.com/design-hub/blog/how-modern-leo-satellite-technologies-are-changing-the-space-race.

Chapter 2

RF Measurement Techniques

2.1 Introduction

This chapter provides the background on the techniques required to perform accurate RF measurements, which is central to the work of this thesis. This includes the general principles of the hardware, connectors, and probing techniques, which require detailed knowledge to achieve high-accuracy, repeatable measurements. The chapter describes the underlying small and large signal RF measurement techniques for characterising RF devices.

2.2 Hardware and Instrumentation

2.2.1 Power Meter

The power meter is an essential piece of equipment in any RF laboratory, measuring RF power in a system or circuit. These devices remain fundamental to measurement systems, especially in cost-sensitive setups, and are used in scalar systems to collect information on a DUT's amplitude-related parameters. Even in more complex measurement systems that use vector network analysers, power meters are still used to provide an absolute power reference for the measurements.

Power meters are implemented in various ways, but fundamentally, they consist

of a sensor that collects and converts RF energy into a DC voltage. A factory calibration correlates this voltage to the RF power using a known reference source [1].

Most sensors use thermal conversion techniques, where the RF power is absorbed into a load, and the temperature is measured using a thermopile thermocouple or a thermistor [1]. These techniques, especially the thermistor-based sensor, offer a high-accuracy average power measurement; In the frequency bands of interest for this work, a new factory-calibrated *high-accuracy* power meter can provide an uncertainty of absolute power measurement of ±0.12 dB between 26-40 GHz and ±0.28 dB between 95-110 GHz [2]. However, their dynamic range is limited by the sensitivity; the R&S thermal power meter [3] can measure a minimum power of approximately -35 dBm.

Figure 2.1: Rohde & Schwarz NRP110T power meter [4].

The other approach involves the diode detection of RF power, which converts the RF to a rectified DC signal. These can be used for peak and average power measurements but have lower accuracy. In the frequency bands of interest for this work, a new factory-calibrated *high-accuracy* power meter can provide an uncertainty of absolute power measurement of ±0.21 dB between 30-40 GHz and ±0.38 dB between 67-90 GHz [2]. These power meters have a higher dynamic range than thermistor-based meters [5] and can be extended even further by using multiple path diode detectors, with a minimum power of around -70 dBm for commercial power meters [3].

2.2.2 Vector Network Analyser

The Vector Network Analyser (VNA) is a frequency-domain measurement tool for characterising microwave network parameters. It measures both the amplitude and relative phase of a device under test (DUT), offering a more comprehensive data set than legacy scalar measurement equipment (Power meters) that only measures amplitude quantities.

(a) ZVA67 [6] (b) PNA-X [7]

Figure 2.2: Commerical VNAs showing (a) ZVA67 by Rohde & Schwarz and (b) PNA-X by Keysight Technologies.

VNAs were introduced in the 1960s and have become essential equipment in most laboratories. One of the earliest and most well-established VNAs in labs in the 1980s was the HP 8510[8]. Since then, the functionality of VNAs has significantly expanded to cover a broader range of use cases. Figure 2.2 illustrates two commercially available VNAs: the ZVA67 from Rohde & Schwarz and the PNA-X from Keysight Technologies.

Operation

A simplified block diagram of a VNA is shown in Figure 2.3. A switched source injects a signal at a given frequency into port 1 or 2. A dual directional coupler samples the incident and reflected signals as $a_{1,m}$, $b_{1,m}$, $a_{2,m}$ and $b_{2,m}$. The sampled waves are then down-converted to an intermediate frequency (IF), as $a_{1,IF}$, $b_{1,IF}$, $a_{2,IF}$ and $b_{2,IF}$ and digitised. After signal processing, the scattering parameters are displayed. This process repeats for the entire frequency sweep.

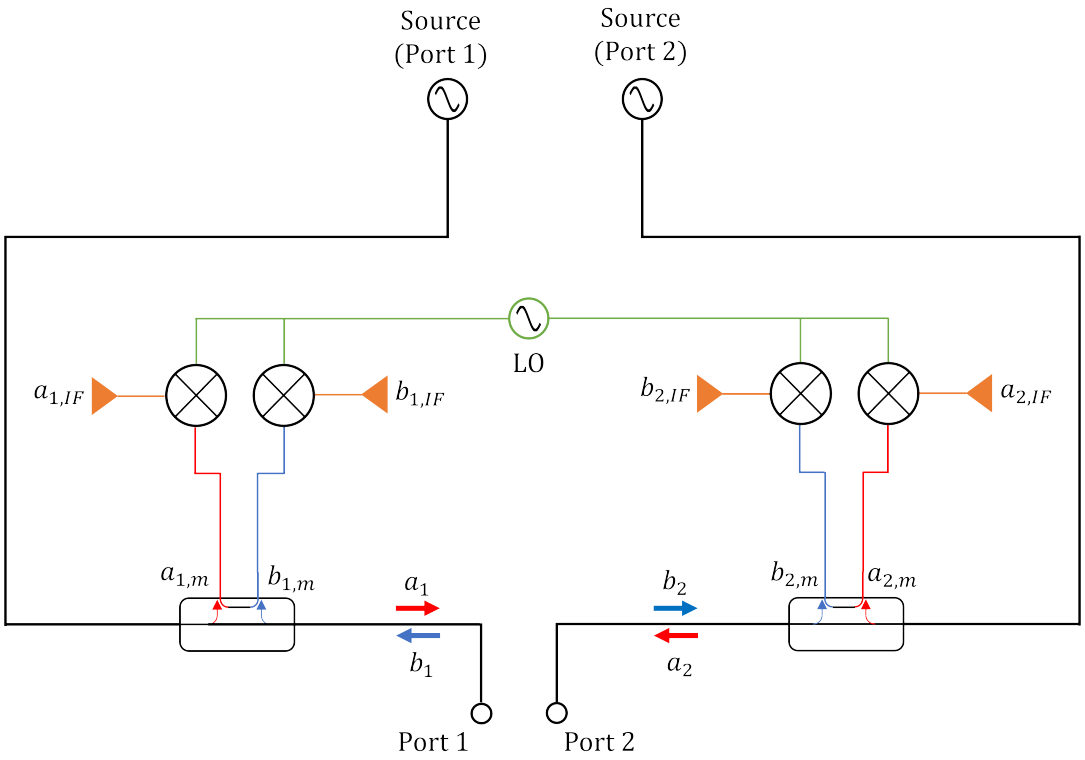

Figure 2.3: Simplified block diagram of a Vector Network Analyser.

Modern VNAs employ significantly more complex architectures than shown in Figure 2.3, with an expanded range of features. It is common to find VNAs with direct receiver access, which enables the operator to bypass the port reflectometer and directly interface with the measurement receivers. This capability allows for reconfigurability and is essential for applications like load-pull measurements, where versatility is crucial.

Another advancement in high-end VNAs is the integration of digitally controlled sources that use an NCO. These sources provide precise phase control, essential for modulated and nonlinear measurements.

Commercially available instruments can now perform single-sweep measurements up to 220 GHz [9]. Higher frequency measurements are achievable in waveguide-banded solutions, which use up/down conversion techniques to measure devices up to terahertz frequencies [10].

Parameters

The VNA has several settings to configure measurements, such as frequency,

power, and tools to visualise data in different formats. However, this section will focus on the parameters that directly impact a measurement's quality.

The IF bandwidth is an important parameter for VNA measurements; it defines the bandwidth of the IF filter after down-conversion from RF. A reduction in the IF bandwidth increases the measurement time but also lowers the noise floor of the receiver due to a decrease in the thermal noise power, shown in the standard equation below:

$$P_{\mathrm{N}} = kT\Delta f_{\mathrm{c}} \tag{2.1}$$

where k is the Boltzmann constant, T is the temperature and Δf_{c} is the IF filter bandwidth.

The ideal thermal noise in a matched environment at room temperature is -174 dBm/Hz, which is degraded by the noise figure of the instrument and the hardware connected to the VNA. The receiver noise floor can be adjusted by changing the IF bandwidth or applying averaging. Since thermal noise is Gaussian by nature, increasing the averaging by a factor of 10 reduces the noise floor by 10 dB. Similarly, reducing the IF bandwidth by the same factor achieves the same result.

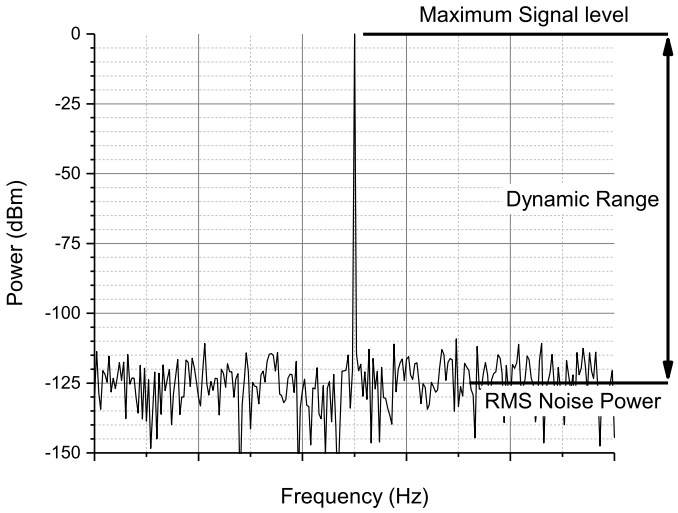

Figure 2.4: VNA dynamic range.

The maximum dynamic range of a VNA receiver is defined by its noise floor (the minimum detectable signal level) and compression point (the maximum signal level

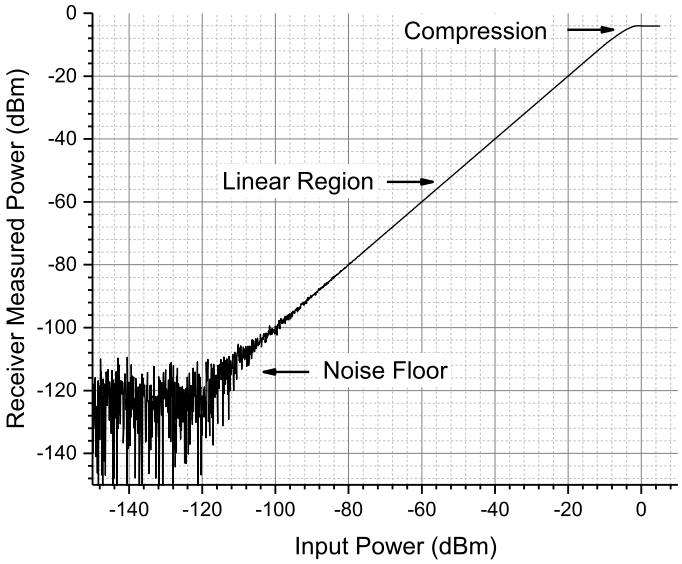

Figure 2.5: An example of a VNA receiver measured power versus swept input power showing the linear and nonlinear regions of a receiver.

it can accurately measure).

Figures 2.4 and 2.5 illustrate this concept from two perspectives. Figure 2.4 presents a spectrum plot showing a peak at a single frequency, while Figure 2.5 shows a power sweep of the receiver.

In the power sweep, three regions are highlighted. The first is the noise floor, below which the signal power is too low and is indistinguishable from the thermal noise power. The second is the linear region, where the receiver exhibits a linear measured response to the input signal. For highly accurate VNA measurements, the receivers must operate in this region. Finally, as the measured receiver power increases beyond the linear region, compression is reached; this is where the receiver begins to exhibit a nonlinear measured response. This region must be avoided due to the reduced measurement accuracy, which cannot be fixed by error correction techniques, which will be discussed later.

In modern VNAs with direct receiver access, the receiver compression point typically occurs around -5 dBm [1].

The VNA integrates all the coaxial and on-wafer error correction algorithms, allowing the user to directly measure a DUT's response at any given reference plane; these techniques will be described in a later chapter.

2.2.3 Coaxial Fixtures and Connectors

Coaxial connectors and cables are essential for connecting hardware in microwave systems, and their construction plays a vital role in minimising transition loss. Table 2.1 shows the standard list of commercial coaxial connectors.

Table 2.1: Microwave and mm-wave coaxial connectors [1].

Connector Type	**Maximum Frequency**	**Compatible with**
SMA	18 GHz	3.5 mm and 2.92 mm
3.5 mm	26.5 GHz	SMA and 2.92 mm
2.92 mm	40 GHz	SMA and 3.5 mm
2.4 mm	50 GHz	1.8 mm
1.85 mm	67 GHz	2.4 mm
1 mm	110 GHz	/
0.8 mm	145 GHz	/

The SMA connector is most commonly used for microwave fixtures due to its low cost, compact footprint and frequency performance. However, as the system frequency increases beyond 18 GHz unwanted modes propagate in the connector caused by the dielectric constant of the centre pin support structure [1]. For the SMA connector, it is a solid dielectric made from PTFE.

(a) SMA [11] (b) 3.5 mm [12]

Figure 2.6: Microwave coaxial connectors.

The key difference between the SMA and 3.5 mm connectors lies in the dielectric support structure. Figure 2.6 illustrates male SMA and 3.5 mm connectors. In the

SMA connector, the dielectric fully supports the centre pin. In contrast, the 3.5 mm connector features a more complex support structure that is not directly visible when looking into the connector. The support structure is modelled in Solidworks in Figure 2.7.

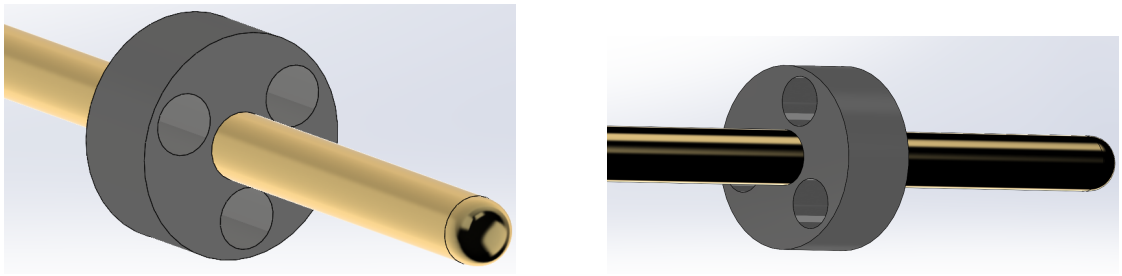

(a) Front (b) Rear

Figure 2.7: 3D model showing the dielectric bead holding the centre pin.

Figure 2.7 presents a 3D model of the centre pin and the dielectric support structure of the 3.5 mm connector. At the base, a thin layer of dielectric material encases the pin. To maximise mechanical support while minimising dielectric loading, the material is blind drilled in a pattern of three holes from both directions, offset in a regular pattern.

A similar support structure is used to support mode-free propagation beyond 26.5 GHz, but the dimensions are reduced for each subsequent connector in Table 2.1.

2.2.4 Microwave Probing

It is common practice for microwave circuits to build connectorised test fixtures, which allow for measurement using coaxial connectors and cables. For device-level characterisation, this practice introduces errors in repeatability and relies upon accurate de-embedding of the test fixture.

Microwave probes, shown in Figure 2.8, can be used for enhanced accuracy. A Ground-Signal-Ground (GSG) probe consists of a coaxial connector to probe tip transition, with the probe tip made up of three contact fingers with the signal probe at the centre; they are designed to minimise crosstalk and come in different probe pitches (probe to probe spacing) for mm-wave, this ranges from 50-200 µm [13].

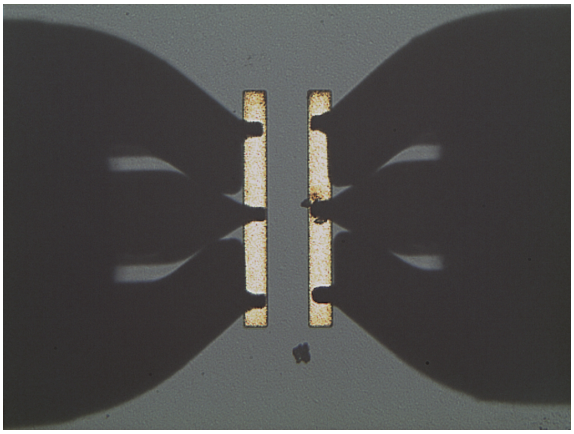

Figure 2.8: On-wafer 200 µm T-Plus GSG probes.

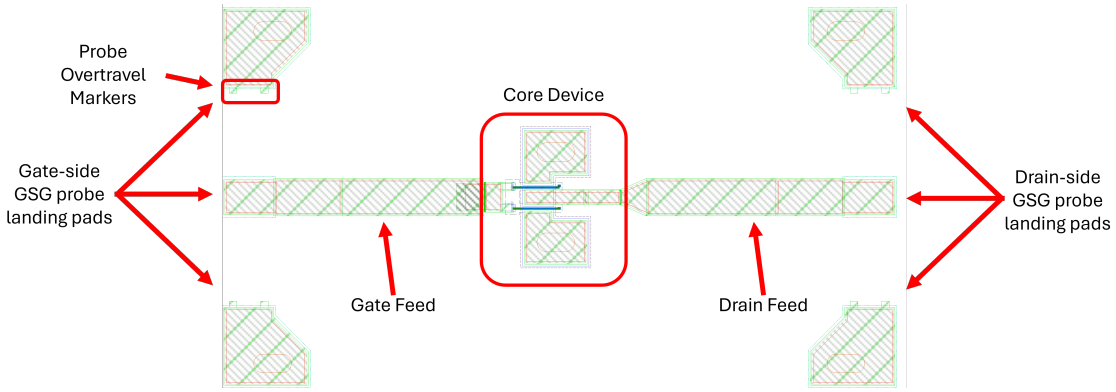

Figure 2.9: On-wafer multi-finger microstrip transistor layout with feeds and CPW landing areas.

Test and calibration structures must be fabricated to fit the desired probe configuration. Figure 2.9 illustrates an example of device-level characterisation. At the centre is the core device; either side consists of a feed line and a CPW landing area for the GSG probes, which must be specifically designed to achieve accurate measurements; a reference guide is shown in [14]. The CPW pads consist of markers that show the operator where to land the probe and the overtravel required to obtain consistent and repeatable measurements.

2.3 Measurement Techniques

2.3.1 Scattering Parameters

At microwave frequencies, the dimensions of the transmission lines become comparable to the wavelength. As a result, the voltage/current amplitudes cannot be considered constant along a line, unlike in low-frequency analysis, where transmission lines are modelled by lumped elements. To apply network analysis techniques to microwave circuits, the concept of power flow and the scattering parameters are introduced [15][1].

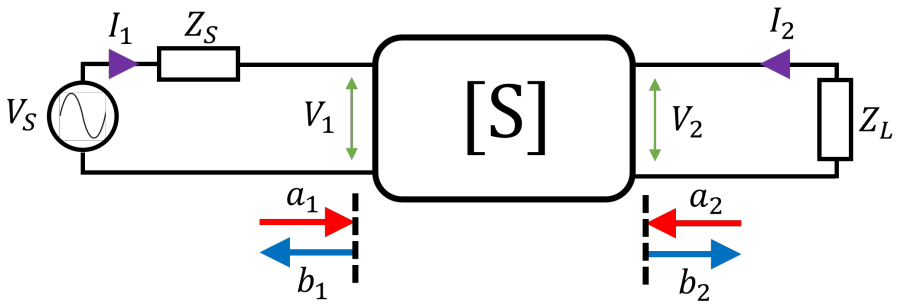

Figure 2.10: Two-port network.

The analysis begins with defining a test circuit, as shown in Figure 2.10. In this circuit, a network is driven by a source generator, represented by a sinusoidal time-varying voltage source, V_S, and a source impedance, Z_S. The network is terminated with a load impedance, Z_L.

$$V_S(t) = |V_S|\ cos(\omega t + \theta) = |V_S|\ e^{j(\omega t+\theta)} \tag{2.2}$$

Expressing time-domain quantities as travelling waves in the forward and reverse direction, where the port is denoted, n:

$$V_n = V_n^+ + V_n^- \tag{2.3}$$

making the assumption that $Z_S = Z_L = Z_0$ (port impedance) :

$$V_n^+ = \frac{1}{2}(V_n + Z_0 I_n) \tag{2.4}$$

$$V_n^- = \frac{1}{2}(V_n - Z_0 I_n) \tag{2.5}$$

Equations (2.4) and (2.5) represent the generalised travelling waves at port n.

$$a_n = \frac{V_n + Z_0 I_n}{2\sqrt{|Re(Z_0)|}} \tag{2.6}$$

$$b_n = \frac{V_n - Z_0^* I_n}{2\sqrt{|Re(Z_0)|}} \tag{2.7}$$

The generalised travelling waves can be converted into normalised power waves, where a and b are defined as the forward and reverse power waves, respectively. Their definitions are shown in equations (2.6) and (2.7).

Based on these definitions, a set of wave ratios can be defined to characterise any two-port network.

$$\begin{aligned} S_{11} &= \left.\frac{b_1}{a_1}\right|_{a_2=0} & S_{12} &= \left.\frac{b_1}{a_2}\right|_{a_1=0} \\ S_{21} &= \left.\frac{b_2}{a_1}\right|_{a_2=0} & S_{22} &= \left.\frac{b_2}{a_2}\right|_{a_1=0} \end{aligned} \tag{2.8}$$

The scattering parameter matrix is an $n \times n$ set of travelling wave ratios and can be used to characterise any linear n-port network. Although the focus is placed on microwave frequencies, the definition of S-parameters holds for lumped circuits. Equation 2.8 shows the S-parameters for a two-port network.

Scattering parameters (S-parameters) are a linear measurement technique used to characterise a device's small-signal response. Unlike impedance or admittance parameters, S-parameters require the load impedance to match the system impedance, which is typically $50\,\Omega$ in microwave systems, which results in the condition of $a_1 = 0$ or $a_2 = 0$.

The key advantage of S-parameters versus impedance or admittance parameters is their practicality in measurement. They avoid the need to terminate the circuit with an open or short circuit, which is challenging to implement in microwave structures such as waveguides or microstrip environments.

The parameters consist of a reflection coefficient, S_{11} and S_{22} that quantifies the mismatch between the system and the network input/output impedance. The transmission parameters, S_{21} and S_{12}, describe the transfer properties from input to output and vice versa. As shown in equation 2.9, the system of scattering parameters can be generalised into a set of matrix equations that describe the response, b, of a device to some impulse, a, and the scattering parameters.

$$\begin{bmatrix} b_1 \\ \vdots \\ b_n \end{bmatrix} = \begin{bmatrix} S_{11} & \dots & S_{1n} \\ \vdots & \ddots & \vdots \\ S_{n1} & \dots & S_{nn} \end{bmatrix} \cdot \begin{bmatrix} a_1 \\ \vdots \\ a_n \end{bmatrix} [1] \tag{2.9}$$

The foundry model S-parameters from an NP-12 $4 \times 50\,\mu$m Win Semiconductor common-source transistor are presented, biased at maximum gm of $V_{\mathrm{D}} = 28\,\mathrm{V}$ and $V_{\mathrm{G}} = -1.2\,\mathrm{V}$.

The standard 2-port S-parameters are presented in Figure 2.11, with the input and output reflection parameters S_{11} and S_{22}, shown, respectively.

The S-parameters can be used to calculate performance metrics such as the

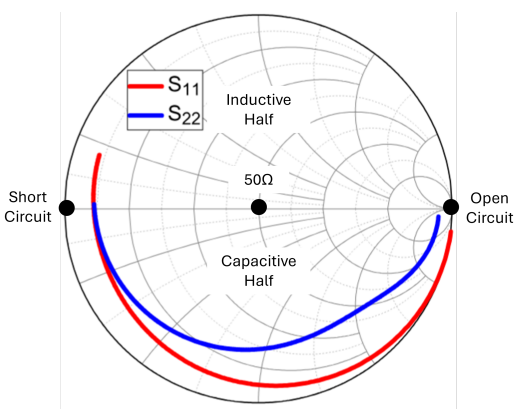

(a) Reflection Parameters

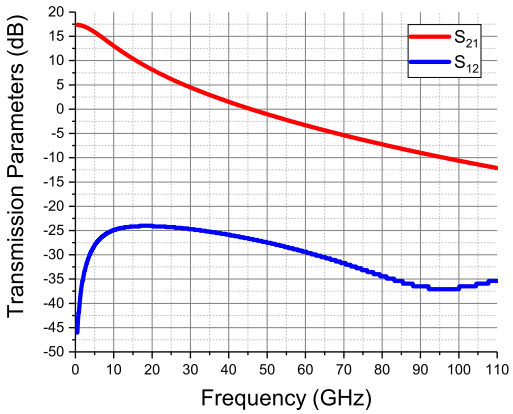

(b) Transmission Parameters

Figure 2.11: Reflection and transmission scattering parameters of a foundry modelled $4 \times 50\mu$m transistor up to 110 GHz.

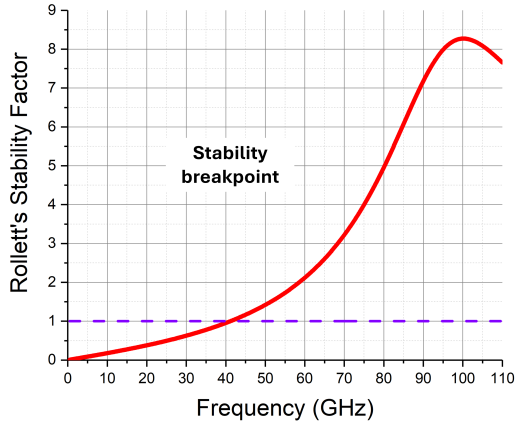

(a) K-Factor

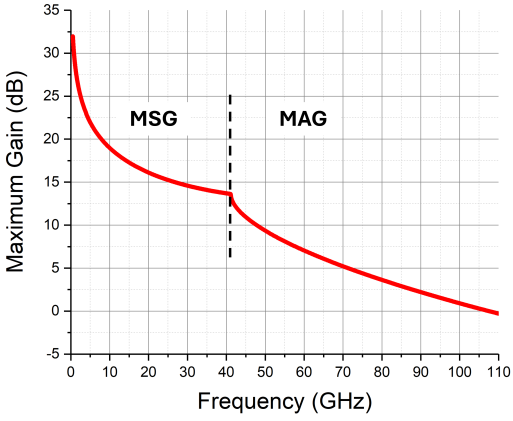

(b) MAG and MSG

Figure 2.12: Transistor parameters of a foundry modelled $4 \times 50\mu$m transistor up to 110 GHz.

device's stability and maximum available gain, shown in Figure 2.12.

Due to the combination of high gain and feedback between the output and input, devices can exhibit conditional stability for specific input and output impedance terminations. The Rollett stability factor, K-factor, is a method that was developed to indicate whether a device's stability depends on the passive source or load impedance presented to the device. It is an important stability metric that serves as a guide to designers to ensure that transistors do not operate as oscillators [16].

$$K = \frac{1 - |S_{11}|^2 - |S_{22}|^2 + {\Delta_S}^2}{2|S_{21}S_{12}|} \tag{2.10}$$

where $\Delta_S = S_{11}S_{22} - S_{21}S_{12}$.

The definition of the K-factor is not mathematically sufficient to determine stability; it is tied to another condition:

$$|\Delta_S| < 1 \tag{2.11}$$

If the source or load stability circle lies within the Smith chart (Γ_L or $\Gamma_\mathrm{S} < 1$), the device is conditionally stable corresponding to $K < 1$. Conversely, if the device's stability is independent of the passive source or load impedance, it is considered unconditionally stable, with $K \geq 1$ and $|\Delta| < 1$. The device is unconditionally stable in Figure 2.12(a) when $f > 42\,\mathrm{GHz}$.

This technique is the most popular stability metric, but it is only valid for analysing stability at a device's input and output terminals; other methods for determining stability within the network involve pole and zero analysis but are not discussed any further in detail in this thesis.

The other metric in Figure 2.12(b) is the Maximum available Gain (MAG). The transmission parameter S_{21} represents the transmission when the device is terminated in $50\,\Omega$, whereas MAG assumes the device is conjugately matched at both the input and output. The figure shows a breakpoint at 42 GHz because MAG is defined only when the device is unconditionally stable ($K \geq 1$).

$$MAG = (K - \sqrt{K^2 - 1})\frac{|S_{21}|}{|S_{12}|} \text{ for } K > 1 \tag{2.12}$$

The Maximum Stable Gain (MSG) is used for frequencies where K < 1.

$$MSG = \frac{|S_{21}|}{|S_{12}|} \text{ for } K < 1 \tag{2.13}$$

The reflection parameters from Figure 2.11 can be used to achieve a conjugate match at the source and load of the DUT, resulting in a reflectionless match.

2.3.2 Large-signal Measurements

To maximise the output power in real transistors, alternative techniques must be used as opposed to S-parameters; this is because real devices are voltage or current-limited, this is a point of discussion by Cripps in [17]. The current generator is limited by the gate Schottky diode conduction and channel saturation, whilst the voltage is limited by device breakdown and resistive effects [18].

In ideal cases where a device has no parasitic effects, is biased in class A and operates in the linear region, a graphical technique called the load-line method can be used to select the load impedance required to deliver maximum output power to the load. With reference to Figure 2.13, the load line technique involves plotting the DCIV characteristics and tracing out a diagonal line from the maximum current to the maximum voltage; the gradient of this line represents the load impedance required to obtain the maximum voltage and current swing and, hence, maximum output power. The optimal load, R_{opt}, is given by:

$$R_{opt} = \frac{V_{max}}{I_{max}} \tag{2.14}$$

The plot from [18] was recreated to show a comparison between a conjugate match and a load-line match using DCIV data from the foundry model of the NP-12 $4 \times 50\mu$m Win Semiconductor common-source transistor.

Figure 2.13 shows the load trajectory of two matching strategies. The conjugate

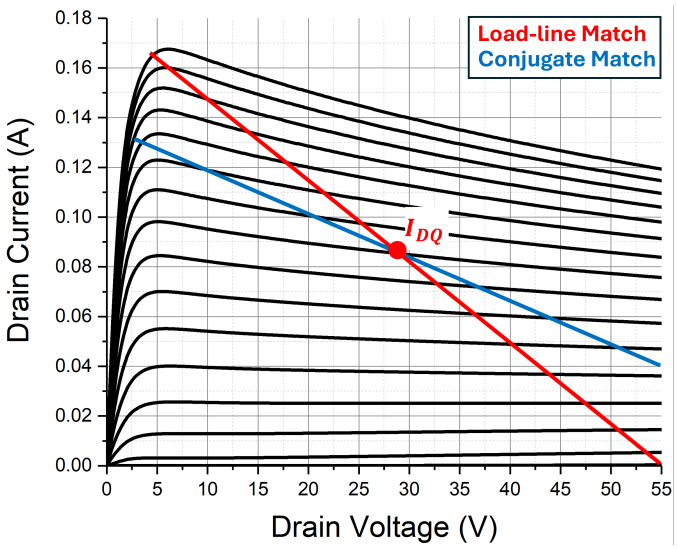

Figure 2.13: DCIV plot showing the load trajectory for a conjugate match (blue) and a load-line match (red).

match achieves a full voltage swing but results in a current swing that is not maximised, whilst the load-line match equalises both the voltage and current swing to achieve maximum output power.

When accounting for the complexities of real devices, such as parasitics, which introduce frequency dependence and compression, which produces non-linear frequency components, the load-line technique becomes impractical, requiring alternative methods.

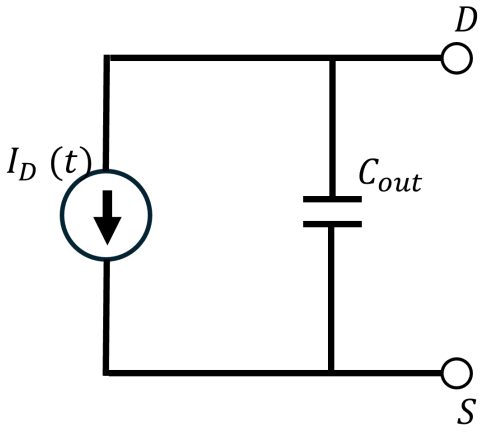

Figure 2.14: Simplified equivalent circuit of the output of a transistor.

A simplified equivalent circuit of the output of a microwave transistor is shown in Figure 2.14. It shows the intrinsic current generator I_{D}, and equivalent parasitic

output capacitance, C_{out}. This section will demonstrate the load-pull technique that is used to determine the optimum loading conditions to maximise power transfer and other performance metrics.

In large-signal measurements, the same definition for power waves is used from (2.6) and (2.7) but now re-expressed to include a harmonic frequency index.

$$a_{n,h} = \frac{V_{n,h} + Z_0 I_{n,h}}{2\sqrt{|Re(Z_0)|}} \tag{2.15}$$

$$b_{n,h} = \frac{V_{n,h} - Z_0^* I_{n,h}}{2\sqrt{|Re(Z_0)|}} \tag{2.16}$$

Fundamental quantities to the characterisation and design of microwave power amplifiers are related to the power, gain, efficiency and reflection coefficients.

The power related terms are the available power, P_{av}, delivered input power, P_{in} and output power, P_{out} which can be calculated from the power waves using:

$$P_{\text{av}}(W) = |a_1|^2 \tag{2.17}$$

$$P_{\text{in}}(W) = |a_1|^2 - |b_1|^2 \tag{2.18}$$

$$P_{\text{out}}(W) = |b_2|^2 - |a_2|^2 \tag{2.19}$$

The gain-related terms are the transducer gain, G_{T}, and the power gain, G_{P} which can be calculated from the power waves using:

$$G_{\text{T}} = \frac{P_{\text{out}}}{P_{\text{av}}} = \frac{|b_2|^2 - |a_2|^2}{|a_1|^2} \tag{2.20}$$

$$G_{\text{P}} = \frac{P_{\text{out}}}{P_{\text{in}}} = \frac{|b_2|^2 - |a_2|^2}{|a_1|^2 - |b_1|^2} \tag{2.21}$$

The reflection coefficient related terms are the input and load reflection coeffi-

cient, Γ_{in} and Γ_{L}, which can be calculated from the power waves using:

$$\Gamma_{\text{L,n}} = \frac{a_{2,n}}{b_{2,n}} \tag{2.22}$$

$$\Gamma_{\text{in,n}} = \frac{b_{1,n}}{a_{1,n}} \tag{2.23}$$

$$Z = Z_0(\frac{1+\Gamma}{1-\Gamma}) \tag{2.24}$$

$$\Gamma = \frac{Z - Z_0}{Z + Z_0} \tag{2.25}$$

(2.22) and (2.23) can be converted between the reflection coefficient and impedance using (2.24) and (2.25).

The efficiency-related terms are DC-RF and power-added efficiency (PAE), which can be calculated using:

$$DCRF\,(\%) = \frac{P_{\text{out}}}{P_{\text{DC}}} * 100 \tag{2.26}$$

$$PAE\,(\%) = \frac{P_{\text{out}} - P_{\text{av}}}{P_{\text{DC}}} * 100 \tag{2.27}$$

This definition can be interchangeable; for measuring amplifiers, the input mismatch is considered, and the available power, P_{av} term is used, whereas for load-pull measurements, the input mismatch is neglected, and the delivered input power, P_{in}, is used.

It is difficult to determine the equivalent circuit of a transistor analytically so the performance and optimal loading conditions are determined in measurement. For power amplifiers, the load termination is the most crucial for optimising peak output power so load-pull measurements are performed. The load-pull technique is performed on a DUT/transistor. The transistor can either be in packaged form mounted onto a PCB or can be on a semiconductor die probed by RF probes. A

VNA is used to generate the RF input signal and is typically buffered by later stages of amplification to sufficiently drive the transistor into non-linear operating conditions. With an RF signal injected into the device, the load impedance presented to the device is controlled, changing it across the Smith chart, this is achieved either passively, using a physical tuneable impedance or actively, by injecting a signal to replicate a load impedance. By collecting the measured waves from VNA, and using the equations above, contours of output power, efficiency or linearity can be plotted. As power amplifiers are typically operated in a non-linear state to exploit high efficiency operating conditions, the load-pull method is performed across a swept input power level from linear to non-linear. This data can be collected to be used directly in design or it can be used to generate a device model that can be used to represent the device in simulator. The technique is always performed for the fundamental frequency but also can be performed for harmonic frequencies to exploit high efficient operating conditions (for high-efficiency modes [19]).

An example of a typical fundamental load-pull measurement is shown.

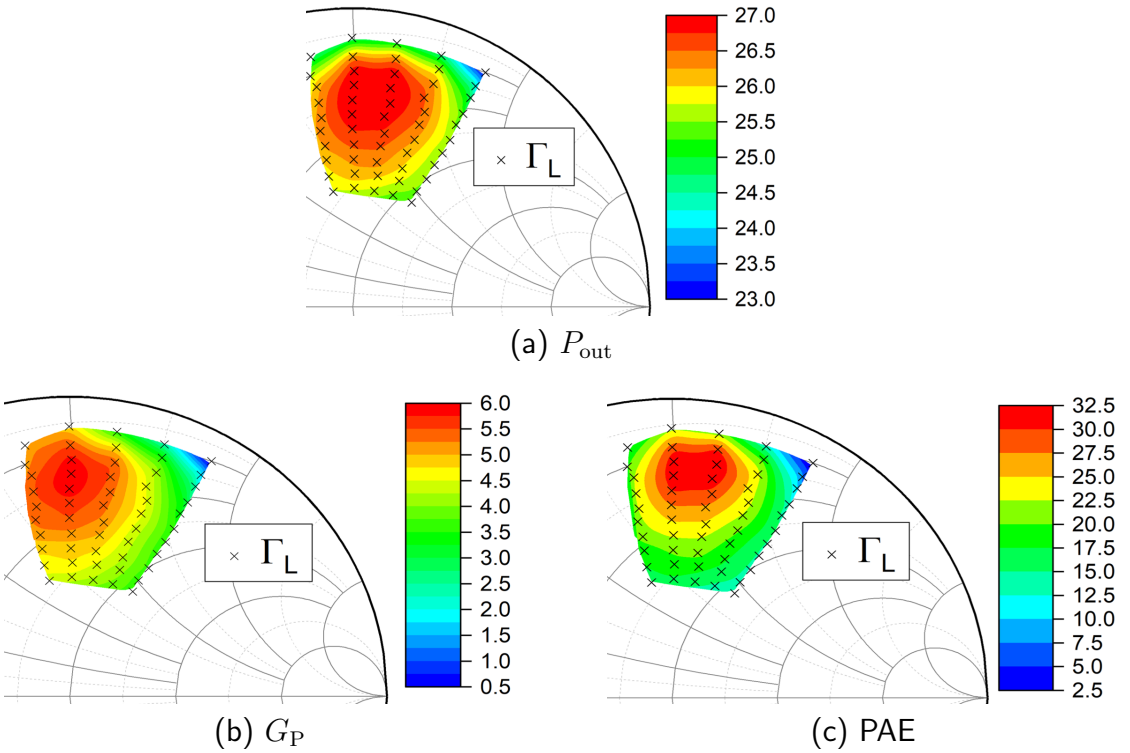

Figure 2.15: Load-pull contours of a GaN HEMT measured at 30 GHz showing (a) P_{out} in dBm, (b) Power Gain in dB and (c) PAE in %.

Figure 2.15 illustrates the measured load-pull reflection coefficient and contours. These plots are fundamental to PA designs, allowing designers to balance performance metrics to achieve specific design goals.

A load impedance can be synthesised either passively, using standard passive networks, or actively, by injecting a signal into the output of the DUT to adjust the a_2 parameter in (2.22). Both techniques are described in the following section.

The load-pull systems discussed in this thesis are real-time systems that utilise a vector network analyser to measure waves and provide real-time feedback on the measured quantities. While these methods are costly due to the expense of the VNA, they offer high accuracy and reliability through standard error correction techniques.

Alternatively, scalar methods offer a cost-effective solution using power meters to measure absolute quantities. However, these systems have disadvantages, including the limited dynamic range of the system's power meters. They typically have lower accuracy than vector methods due to the reliance on fixture characterisation, de-embedding and the requirement to re-calibrate the tuner, each of which can introduce errors.

Passive Load-Pull

A passive tuner is an electromechanical instrument that controls the load impedance. It typically consists of a transmission line structure with a tuneable metallic slug. The slug is retracted from the transmission line to perturb the surrounding electric field, changing the susceptance and, therefore, altering the magnitude of the reflection coefficient. The reflection coefficient phase is controlled by sliding the slug along the length of the transmission line.

Figure 2.16 (a) presents a 3D model representation of a passive tuner. The tuner comprises a central conductor with an RF port, and the impedance is adjusted by changing the position of the metallic tuning slug. This is demonstrated in Figure 2.16 (b), where the tuning slug is moved towards the central conductor, which results in a change in $|\Gamma_L|$ along a line of constant susceptance, and a change in the tuning

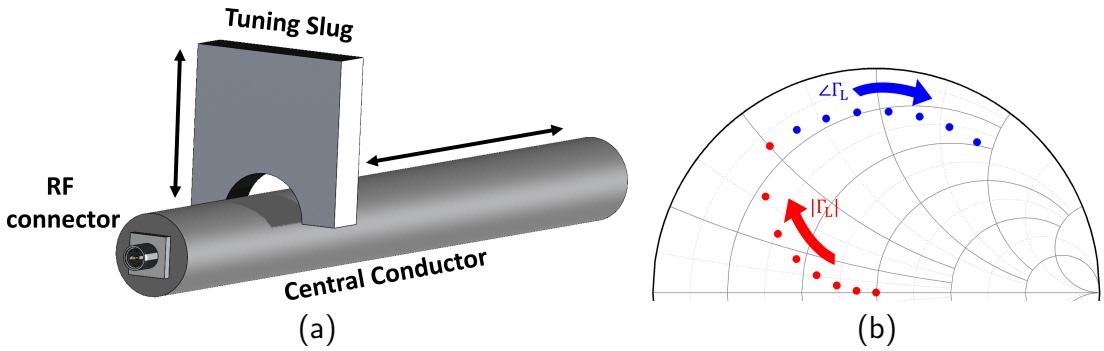

Figure 2.16: (a) shows a single slug passive tuner 3D model, and (b) shows the change of imposed reflection coefficient when the tuning slug is moved vertically to the central conductor (red) and laterally along the central conductor (blue).

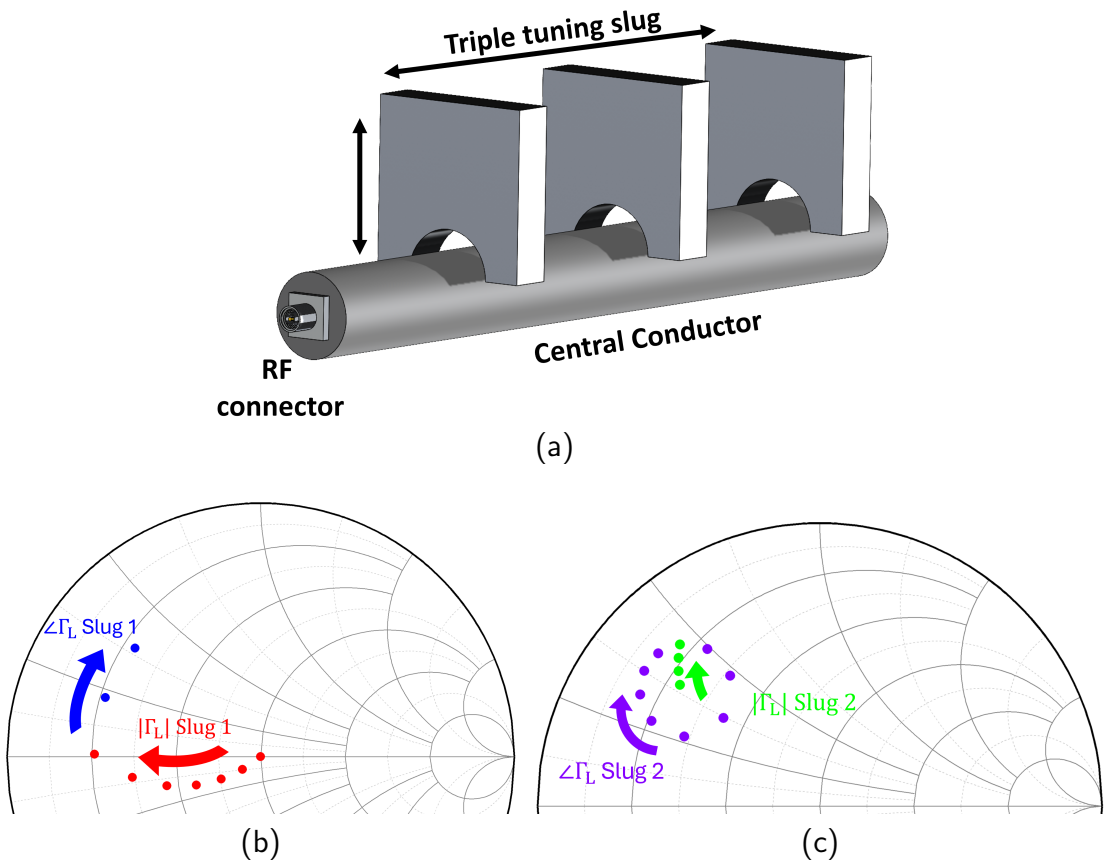

Figure 2.17: (a) shows a three-slug passive tuner 3D model and (b) shows the change of imposed reflection coefficient when the first tuning slug is moved in isolation vertically to the central conductor (red) and laterally along the central conductor (blue). With the first slug fixed in position, (c) shows the change in the imposed reflection coefficient when the second slug is moved vertically to the central conductor (green) and laterally along the central conductor (purple).

slug position along the line results in a change in $\angle\Gamma_L$

This concept can be extended further by adding additional tuning slugs. This serves two purposes; firstly, this vastly increases the possible combinations of tuner slug positions, and it also allows for an increased reflection coefficient and simultaneous tuning of harmonics at the cost of additional tuner calibration time. This tuner is presented in 3D model form in Figure 2.17, which shows a triple-slug tuner designed for multi-harmonic load-pull.

The tuning slug/s can be manually or digitally controlled using a stepper motor operated through software. The primary advantages of passively controlling the load impedance are simplicity and relative cost-effectiveness.

The disadvantage of a passive tuner is the loss between the DUT and the tuning elements, which limits the maximum achievable reflection coefficient. This issue becomes more pronounced in mm-wave measurements, especially with on-wafer devices, where increased losses further reduce performance. These challenges can be partly mitigated by integrating directional couplers into the tuners and positioning the tuners close to the DUT. This adds additional complexity to the system design, as the tuner must be mounted directly onto the probes.

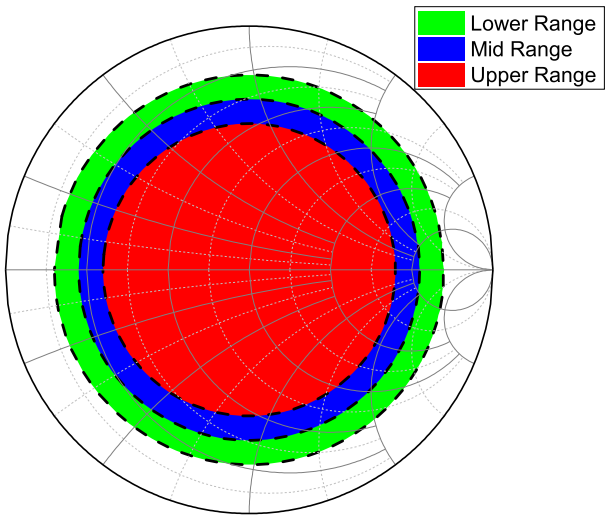

Figure 2.18: Smith chart coverage of a broadband tuner covering frequencies up to 110 GHz. The green, blue and red areas are the Smith chart coverage for the tuner's lower, mid and upper-frequency range, respectively.

Figure 2.18 illustrates a typical tuning range for a broadband mm-wave tuner covering frequencies from 20 to 110 GHz. At the lower frequency range, the maximum $|\Gamma_L| = 0.8$, which decreases with frequency, reaching approximately $|\Gamma_L| = 0.6$ at the upper end. These values can vary depending on the frequency range, power handling and the number of harmonic frequencies the tuner covers.

These tuners provide system flexibility due to their broad frequency range and sufficient tuning range for most applications. However, they become limited at very high frequencies (>67 GHz) or when measuring mm-wave GaN transistors, which typically have an optimum reflection coefficient of $|\Gamma_L| = 0.8$ for maximum output power. Additionally, these tuners have limited utility for harmonic tuning, as the optimum termination requires a full reflect condition, $|\Gamma_L| = 1$.

Companies such as Focus Microwaves and Maury Microwave specialise in providing passive LP hardware and software solutions. Off-the-shelf passive tuners offer a broad frequency range and are controlled by supplier software; typical prices for single slug tuners are around £30k up to 18 GHz and £65k for 110 GHz models. These figures increase to £60k and £95k for triple slug tuners, respectively.

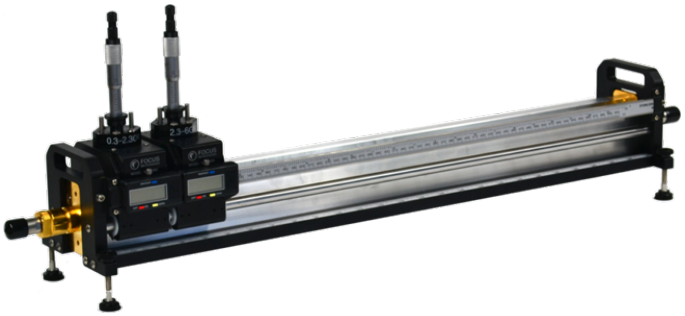

Figure 2.19: The Focus Microwaves MMT series manual passive tuner, operating up to 18 GHz, features a double-slug design for extended frequency performance. [20].

Two examples of passive load-pull tuners are shown in Figure 2.19 and 2.20. The first shows a manually-controlled tuner, while the second shows a high-frequency triple slug tuner designed for mm-wave applications.

Active load-pull is an alternative method for performing load-pull measurements that overcomes some of the disadvantages of passive measurement systems; these are discussed in the following section.

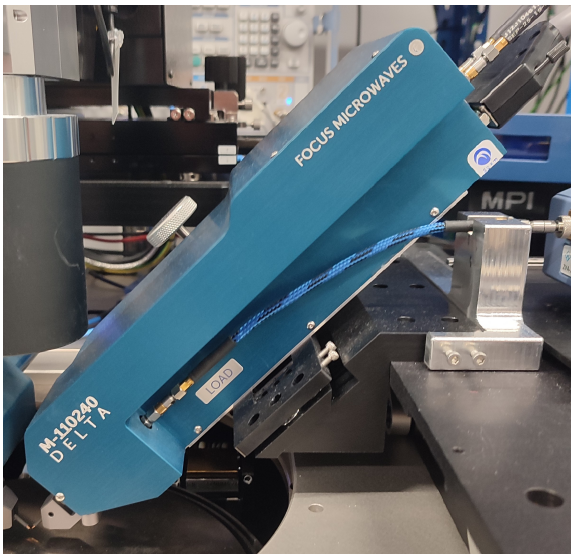

Figure 2.20: The Focus Microwaves M110-240 Delta passive tuner, covering 24–110 GHz, incorporates a triple slug for multi-harmonic measurements.

Active Load-Pull

In the 1970s and 1980s, active load-pull methodologies began to emerge, including open-loop [21] and closed-loop [22] LP systems. These methods aimed to overcome the reflection coefficient limitations of passive systems. By actively controlling the injected signal at the output, a_2, these systems theoretically allow for the synthesis of any desired load impedance.

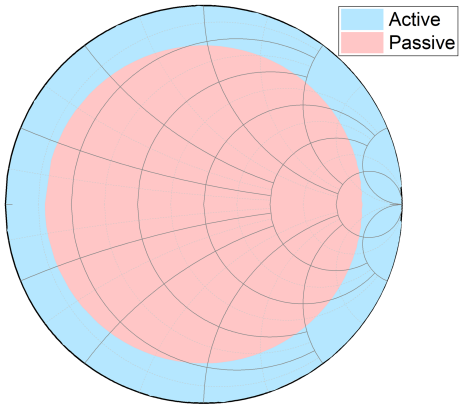

Figure 2.21: Comparison of Smith chart coverage for passive and active load-pull methods.

Figure 2.21 compares a typical maximum obtainable reflection coefficient for load-pull measurements using passive and active methods. At mm-wave frequencies, passive systems are typically limited to a reflection coefficient of 0.8, whereas

active systems can theoretically achieve any reflection coefficient. Open-loop and closed-loop techniques are described in the following section.

Open-Loop Load-Pull

The first active load-pull implementation, the open-loop method, was reported by Takayama [21].

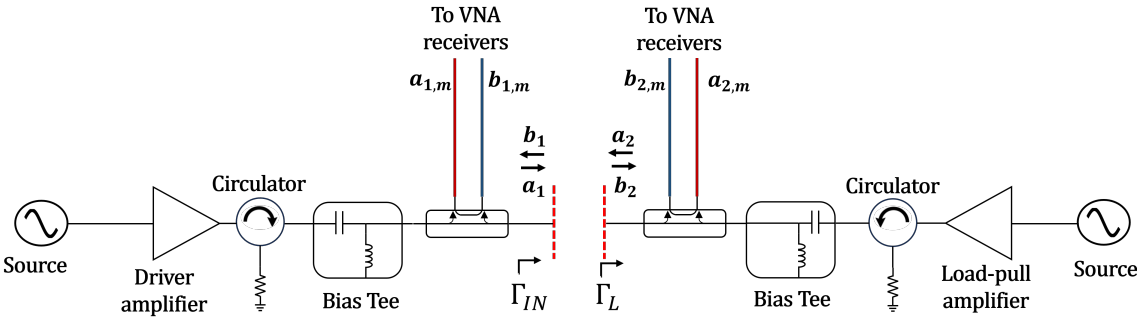

Figure 2.22: Active open-loop load-pull diagram.

Figure 2.22 illustrates a generalised active open-loop LP system. In this configuration, a circulator, a load-pull amplifier, and a microwave source replace the passive tuner. The load impedance of the device is actively controlled by injecting a signal from the microwave source, which is amplified. The circulator isolates the DUT from the LP amplifier, minimising the risk of damage caused by large standing wave conditions.

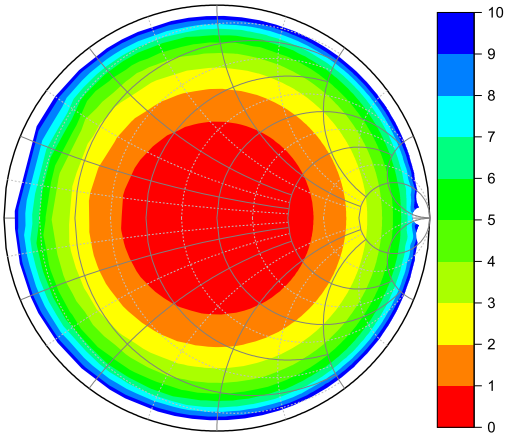

Figure 2.23: Mismatch loss, in decibels, between the load-pull amplifier and imposed reflection coefficient.

This implementation can theoretically achieve any reflection coefficient at the

DUT. However, practical limitations arise due to the power requirements of the LP amplifier. Figure 2.23 illustrates the mismatch loss in dB between the LP amplifier and the imposed load reflection coefficient, assuming the LP amplifier is matched to the amplifier 50 Ω. The LP amplifier must generate sufficient power to compensate for this mismatch and the imposed reflection coefficient.

To generate a desired load reflection coefficient, the control software must set the source power to produce the correct a_2 at the DUT reference plane. This is not a trivial task.

For purely passive devices, the relationship between a_2 at the DUT and the VNA load generator power, a_L, can be calculated directly. The correction accounts for the complex gain between the VNA load generator and the DUT and the mismatch. However, when measuring active nonlinear devices, this relationship becomes more complex. A common solution to this challenge is an iterative nonlinear convergence algorithm, such as the Newton-Raphson method. This algorithm adjusts the VNA source power until the desired reflection coefficient is achieved. The operator can control the tolerance between the set and the measured load impedance to trade-off accuracy against measurement time. The algorithm must be carefully designed to ensure that the load impedance does not present an impedance outside of the Smith chart or an unstable region to prevent damage to the device under test.

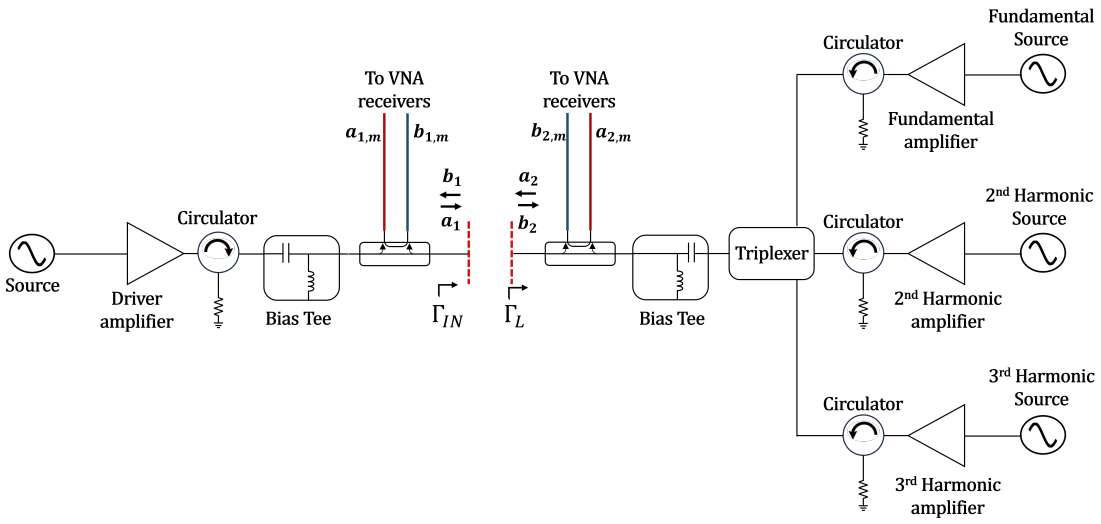

Figure 2.24: Active open-loop diagram for multi-harmonic LP.

To extend the open-loop active LP concept for measuring harmonic impedances, as shown in Figure 2.24, a multiplexer can be used on the output to combine harmonic load generator networks, which are all driven by the VNA and controlled by the load-pull algorithm.

The open-loop architecture is the most commonly used active technique and is the method used in this thesis. Its advantage is its reliability and simple hardware configuration. The alternative active load-pull technique, closed-loop, is discussed in the following section.

Closed-Loop Load-Pull

The closed-loop architecture was first reported by Bava et al. in [22].

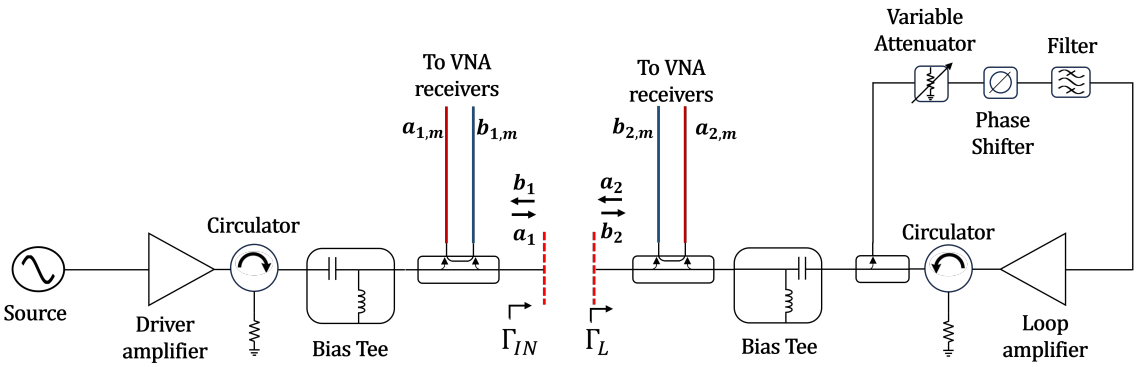

Figure 2.25: Active closed-loop load-pull diagram.

The closed-loop architecture, shown in Figure 2.25, builds upon the open-loop design by introducing a feedback loop, thereby eliminating the need for a second source. A directional coupler samples the device response, b_2, while a phase shifter, attenuator, and loop amplifier adjust its magnitude and phase to generate an a_2 to achieve the desired reflection coefficient.

The hardware implementation of the closed-loop system is significantly more complex than that of the open-loop system, primarily due to practical limitations in the feedback loop. The loop requires a highly selective filter to suppress oscillations to ensure stability. Additionally, a phase shifter with adequate phase control is required.

Like the open-loop system, control software is required to achieve the desired

reflection coefficient. However, instead of controlling the load generator, the software adjusts the phase shifter, attenuator, and gain of the loop amplifier. This process employs a nonlinear convergence algorithm, which is even more complex than the open-loop architecture. The added complexity arises because the algorithm must control a phase shifter, typically varactor-based, introducing an additional layer of nonlinearity compared to the digitally controlled sources in the open-loop system.

The practicality of the closed-loop architecture is significantly more limited than the open-loop technique. In both systems, performing measurements in different frequency bands requires replacing the amplifier and circulator. However, the closed-loop system also necessitates a new filter and phase shifter for each frequency band, making it more expensive and less practical for real-world applications.

Baseband Load-Pull

The previously described techniques are used primarily for the optimisation of a device operating with a single-tone excitation. In real communication systems, devices are driven by multi-tone signals in order to maximise the data throughput. It is, therefore, important to be able to characterise devices when driven by these types of signals and to measure important linearity-related metrics such as Adjacent Channel Power Ratio (ACPR) and Error Vector Magnitude (EVM). To facilitate these measurements, the device is driven by vector signal generators (VSG) to produce the modulated input signal and a vector single analyser (VSA) is used to capture the magnitude and phase relationships of the modulated waves at the input and output of the device through directional couplers before downconversion and digitising to view the modulated signal and related parameters.

Several studies [23][24][25] have discussed the link between baseband impedance and linearity performance metrics; the linearity is degraded by indirect mixing of the second-order intermodulation products (IM2) at baseband, e.g. $(f_2 - f_1)$. Hence, baseband load-pull techniques have been developed to actively tune the baseband impedance termination; these systems [26],[27], use active injection through the bias-tee and they sample the measured waves using a directional coupler which allows

the load-pull software to determine the baseband impedance.

References

[1] J. P. Dunsmore. *Handbook of Microwave Component Measurements with Advanced VNA Techniques*. New Jersey, USA: Wiley, 2020.

[2] Rohde and Schwarz. *NRP Power Meter Family Specifications*. 2023. URL: https://www.rohde-schwarz.com/fi/products/test-and-measurement/rf-and-Microw.-power-sensors/rs-nrpxxt-tn-twg-twgn-thermal-power-sensors_63493-197529.html.

[3] Rohde & Schwarz. *RF & Microwave power meters*. URL: https://www.rohde-schwarz.com/fi/products/test-and-measurement/rf-and-Microw.-power-meters_63672.html.

[4] Rohde & Schwarz. *R&S®NRPxxT/TN/TWG/TWGN Thermal power sensors*. URL: https://www.rohde-schwarz.com/fi/products/test-and-measurement/rf-and-Microw.-power-sensors/rs-nrpxxt-tn-twg-twgn-thermal-power-sensors_63493-197529.html.

[5] Keysight Technologies. *Educational Overview of RF Power Measurement and Applications*. Tech. rep. Keysight Technologies, Dec. 2017.

[6] Rohde and Schwarz. *ZVA Vector Network Analyzer Product Brochure*. URL: www.rohde-schwarz.com/brochure-datasheet/zva.

[7] Keysight Technologies. *PNA Network Analyzer Family*. URL: www.keysight.com/gb/en/products/network-analyzers/pna-network-analyzers.html.

[8] Keysight Technologies. *The Evolution of RF/Microw. Network Analyzers*. URL: about.keysight.com/en/newsroom/backgrounders/na.

[9] Anritsu. *VectorStar Broadband VNA ME7838/AX/EX/D/G*. URL: https://www.anritsu.com/en-gb/test-measurement/products/me7838.

[10] Virginia Diodes. *Vector Network Analyzer Extenders*. URL: www.vadiodes.com/en/products/vector-network-analyzer-extension-modules.

[11] Pasternack. *SMA Male to 3.5mm Female Adapter*. URL: https://www.pasternack.com/sma-male-3.5mm-female-straight-adapter-pe9723-p.aspx.

[12] Pasternack. *SMA Female to 3.5mm Male Adapter*. URL: https://www.pasternack.com/sma-female-3.5mm-male-straight-adapter-pe9724-p.aspx.

[13] M. Sayed V. Teppati A. Ferrero. *Modern RF and Microwave Measurement Techniques*. Cambridge, U.K: Cambridge, 2014.

[14] X. Shang and N. Ridler and J. Ding and M. Geen. *Introductory Guide to Making Planar S-parameter Measurements at Millimetre-wave Frequencies*. Tech. rep. NPL, Jan. 2021.

[15] D. M. Pozar. *Microwave Engineering*. New York, USA: Wiley, 2005.

[16] J. Rollett. “Stability and Power-Gain Invariants of Linear Twoports”. In: *IRE Trans. on Circuit Theory* 9.1 (1962), pp. 29–32. DOI: 10.1109/TCT.1962.1086854.

[17] S. C. Cripps. *RF Power Amplifiers for Wireless Communications*. Massachusetts, USA: Artech House, 1999.

[18] E. Limiti P. Colantonio F. Giannini. *High Efficiency RF and Microwave Solid State Power Amplifiers*. Chichester, UK: Wiley, 2009.

[19] D. Barataud et al. “Measurement and Control of Current/Voltage Waveforms of Microwave Transistors Using a Harmonic Load-Pull System for the Optimum Design of High Efficiency Power Amplifiers”. In: *IEEE Trans. Instrum. Meas.* 48.4 (1999), pp. 835–842. DOI: 10.1109/19.779185.

[20] Focus Microw.s. *Manual Tuners*. URL: https://focus-Microwaves.com/products/manual-tuners.

[21] Y. Takayama. “A New Load-Pull Characterization Method for Microwave Power Transistors”. In: *IEEE MTT-S Int. Microw. Symp. (IMS)*. 1976, pp. 218–220.

[22] G. P. Bava, U. Pisani, and V. Pozzolo. “Active Load Technique for Load-Pull Characterisation at Microwave Frequencies”. In: *Electronics Letters* 18 (1982), pp. 178–180.

[23] Xiaofan Chen et al. “Enhanced Analysis and Design Method of Concurrent Dual-Band Power Amplifiers With Intermodulation Impedance Tuning”. In: *IEEE Trans. Microw. Theory Techn.* 61.12 (2013), pp. 4544–4558. DOI: 10.1109/TMTT.2013.2282283.

[24] Eigo Kuwata et al. “Effects of Load Impedances at Third Order Intermodulation Tones”. In: *IEEE Eur. Microw. Integr. Circuits Conf. (EuMIC)*. 2021, pp. 201–204.

[25] M. Akmal et al. “The Effect of Baseband Impedance Termination on the Linearity of GaN HEMTs”. In: *IEEE Eur. Microw. Conf.* 2010, pp. 1046–1049. DOI: 10.23919/EUMC.2010.5616369.

[26] Muhammad Akmal Chaudhary et al. “Modulated Waveform Measurement and Engineering System”. In: *IEEE Int. Conf. on Electron., Circuits, and Syst. (ICECS)*. 2015, pp. 252–255. DOI: 10.1109/ICECS.2015.7440296.

[27] F.L. Ogboi et al. “A LSNA Configured to Perform Baseband Engineering for Device Linearity Investigations Under Modulated Excitations”. In: *IEEE Eur. Microw. Conf.* 2013, pp. 684–687. DOI: 10.23919/EuMC.2013.6686748.

Chapter 3

Error Correction Methods

Obtaining an accurate measurement of a DUT involves more than simply connecting it to the two ports of a VNA and measuring a set of S-parameters. The VNA and measurement setup all have frequency-dependent physical properties, such as loss, mismatch, and leakage, that degrade accuracy. Error correction is performed to eliminate hardware-related errors and shift the measurement reference plane from the VNA receivers to the DUT.

3.1 Small-Signal

3.1.1 Error Models

Error correction involves modelling the errors associated with the physical hardware and constructing an S-parameter matrix to represent them. This matrix can be mathematically removed from the DUT S-parameter measurement, presenting results as if they were obtained directly at the DUT terminals. This process assumes the measurement system is linear and independent of power level.

The error sources in a linear S-parameter measurement system can be categorised into the following quantities [1]. For simplicity, the descriptions focus on errors in the forward measurement direction, although they apply equally to the reverse direction.

- Mismatch: The source and load match terms characterise mismatch errors.

The source match refers to the mismatch between the VNA source and the DUT. When the VNA source does not present an ideal $50\,\Omega$ impedance, the DUT response, b_1, is reflected back towards the DUT, reducing the accuracy of both transmission and reflection measurements. Similarly, the load match represents the mismatch between the VNA receiver and the DUT's load impedance. When the receiver does not present an ideal $50\,\Omega$ impedance, the DUT response, b_2, is reflected back towards the DUT, degrading measurement accuracy.

- Frequency Response: The frequency response errors are the transmission and reflection tracking. The transmission tracking accounts for the difference in the frequency response between the receivers capturing the incident signal, a_1, and the response signal, b_2. The reflection tracking captures the difference between the frequency response of the measurement and reference receivers capturing signals a_1 and b_1, respectively.

- Leakage: The leakage error terms include directivity and crosstalk. The directivity of the reflectometer is captured. Ideally, an incident signal, a_1, passing through the reflectometer into a perfect $50\,\Omega$ would see a portion of the signal, $a_{1,m}$, at the reference receiver but no signal, $b_{1,m}$ at the measurement receiver, but in reality, the directivity is limited. Hence, a portion of the signal appears at the measurement receiver.

  The leakage error terms include directivity and crosstalk. Directivity describes the ability of the reflectometer to separate incident and reflected signals. Ideally, when an incident signal, a_1, passes through the reflectometer into a perfect $50\,\Omega$ termination, a portion of the signal appears at the reference receiver, while no signal appears at the measurement receiver. However, due to the limited directivity of the reflectometer, a portion of the signal appears at the measurement receiver. The crosstalk term captures the leakage between the source and the output measurement receiver. This is negligible in modern

VNAs, so it is typically ignored in 8-term and 12-term calibration algorithms.

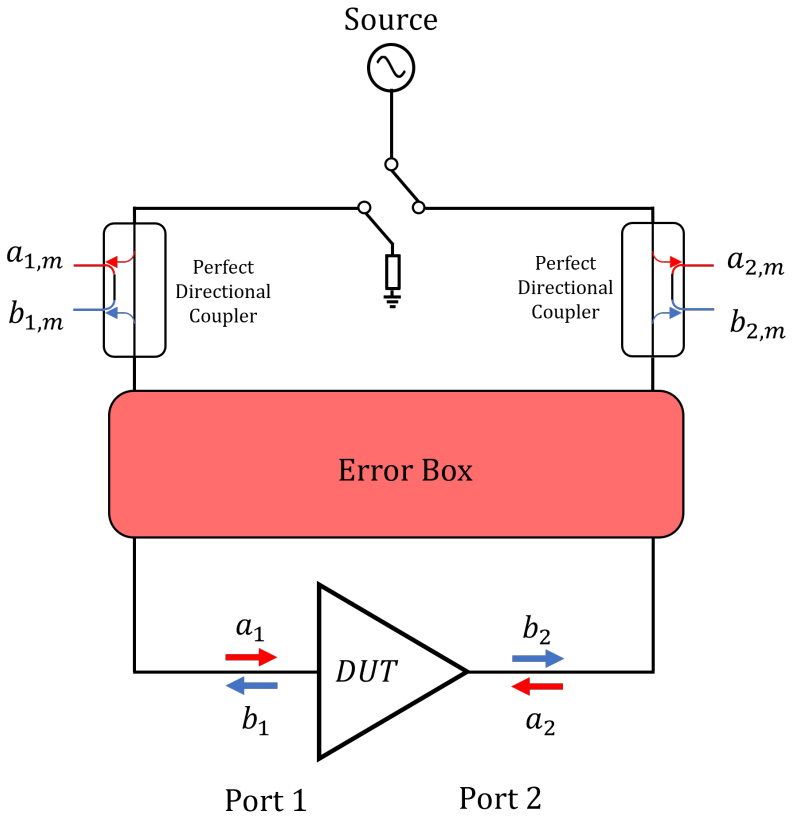

Figure 3.1: Simplified block diagram of a Vector Network Analyser with error box

Using Figure 3.1, an imperfect measurement system can be modelled by assigning all errors to an error adaptor/box. This error box is represented by an S-parameter matrix composed of error correction coefficients, which account for all the error mechanisms discussed above. This error box can be used to mathematically remove the measurement system error from a set of raw measured S-parameters, yielding corrected results.

12-term Error Model

We can describe the system using a 12-term error flow graph, which requires measuring waves at three receivers in both forward and reverse directions. These flow graphs can be expanded to a 16-term case to include additional leakage terms. However, these extra terms are negligible and not considered for most calibration techniques, including those discussed in this thesis.

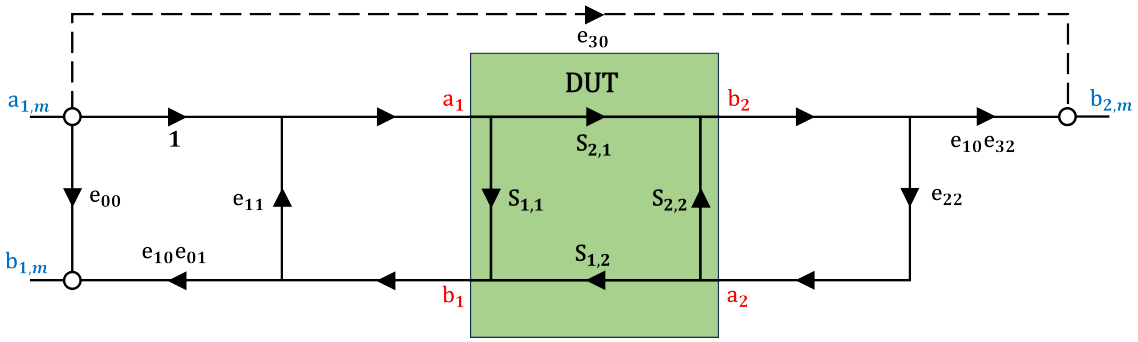

Figure 3.2: 12-term forward error model [2].

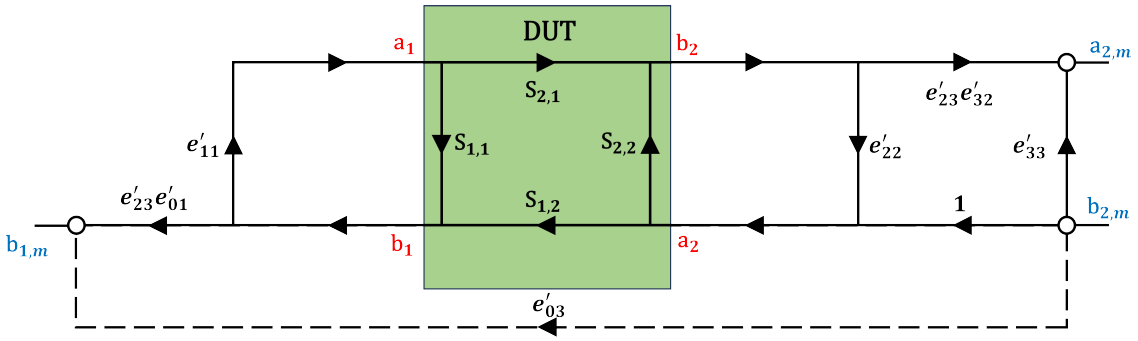

Figure 3.3: 12-term reverse error model [2].

Figures 3.2 and 3.3 show the 12-term forward and reverse error models for a network analyser. These models are the foundation for calibration methods that correct the S-parameters and measured waves. The commonly used terminology for the error terms in the flow graphs is provided in Table 3.1, along with the two most common notations in the literature.

Table 3.1: VNA Error Terms using two commonly used notations [3][2].

Error	Forward	Reverse
Source Match	e_{11} (ESF)	e'_{22} (ESR)
Load Match	e_{22} (ELF)	e'_{11} (ELR)
Transmission Tracking	$e_{10}e_{32}$ (ETF)	$e'_{23}e'_{01}$ (ETR)
Reflection Tracking	$e_{10}e_{01}$ (ERF)	$e'_{23}e'_{32}$ (ERR)
Directivity	e_{00} (EDF)	e'_{33} (EDR)
Crosstalk	e_{30} (EXF)	e_{03} (EXR)

Using the six error terms in the forward and reverse directions, we can translate the measured waves to S-parameters at the DUT plane with knowledge of the error

terms and measured waves using (3.1) - (3.5) [2].

We can translate the raw measured waves to corrected S-parameters at the DUT plane using the six error terms in the forward and reverse directions. This translation is achieved with knowledge of the error terms and measured waves, as described in (3.1) - (3.5) [2].

$$S_{11} = \frac{\left(\frac{S_{11,m}-e_{00}}{e_{10}e_{01}}\right)\left[1+\left(\frac{S_{22,m}-e'_{33}}{e'_{23}e'_{32}}\right)e'_{22}\right] - e_{22}\left(\frac{S_{21,m}-e_{30}}{e_{10}e_{32}}\right)\left(\frac{S_{12,m}-e'_{03}}{e'_{23}e'_{01}}\right)}{D} \tag{3.1}$$

$$S_{21} = \frac{\left(\frac{S_{21,m}-e_{30}}{e_{10}e_{32}}\right)\left[1+\left(\frac{S_{22,m}-e'_{33}}{e'_{23}e'_{32}}\right)(e'_{22}-e_{22})\right]}{D} \tag{3.2}$$

$$S_{12} = \frac{\left(\frac{S_{12,m}-e'_{03}}{e'_{23}e_{01}}\right)\left[1+\left(\frac{S_{11,m}-e_{00}}{e_{10}e_{01}}\right)(e_{11}-e'_{11})\right]}{D} \tag{3.3}$$

$$S_{22} = \frac{\left(\frac{S_{22,m}-e'_{33}}{e'_{23}e'_{32}}\right)\left[1+\left(\frac{S_{11,m}-e_{00}}{e_{10}e_{01}}\right)e_{11}\right] - e'_{11}\left(\frac{S_{21,m}-e_{30}}{e_{10}e_{32}}\right)\left(\frac{S_{12,m}-e'_{03}}{e'_{23}e'_{01}}\right)}{D} \tag{3.4}$$

$$D = \left[1+\left(\frac{S_{11,m}-e_{00}}{e_{10}e_{01}}\right)e_{11}\right]\left[1+\left(\frac{S_{22,m}-e'_{33}}{e'_{23}e'_{32}}\right)e'_{22}\right] - \left(\frac{S_{21,m}-e_{30}}{e_{10}e_{32}}\right)\left(\frac{S_{12,m}-e'_{03}}{e'_{23}e'_{01}}\right)e_{22}e'_{11} \tag{3.5}$$

8-term Error Model

The 8-term model is another commonly used method of representing a network analyser. It uses all four receivers on modern VNAs but omits the eight leakage terms found in the 16-term model.

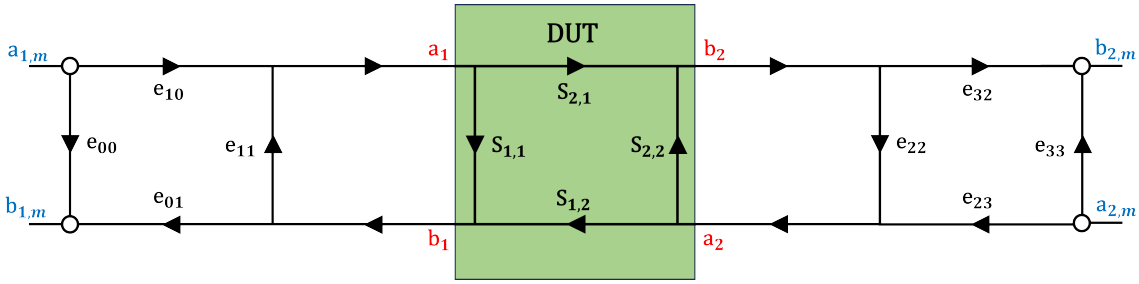

Figure 3.4: 8-term error model [2].

The 8-term model is shown in Figure 3.4. A single model can represent both forward and reverse measurements using all four measurement receivers. However,

a switch correction measurement must be performed during the calibration procedure. In the standard S-parameter definition, the loaded port is assumed to be perfectly matched, meaning that in a forward measurement, $a_2 = 0$. In a real microwave measurement system, this is never the case and some signal is measured at the measurement receiver as $a_{2,m}$. Therefore, the switch correction translates the measured waves as if they were measured in a perfectly matched system. The switch terms are typically captured during the measurement of the thru standard. These are the reflection coefficient, Γ_3, seen by the receivers at port 2 when measuring in the forward direction and by port 1 in the reverse direction, Γ_0.

The equations for applying the switch corrections to raw measured S-parameters are shown below [2], [4].

$$\Gamma_0 = \frac{a'_{1,m}}{b'_{1,m}} \tag{3.6}$$

$$\Gamma_3 = \frac{a_{2,m}}{b_{2,m}} \tag{3.7}$$

Where $'$ represents the reverse measurement direction.

$$\begin{aligned} S_{11,m} &= \frac{\frac{b_{1,m}}{a_{1,m}} - \frac{b'_{1,m}}{a'_{2,m}}\frac{b_{2,m}}{a_{1,m}}\Gamma_3}{d} \qquad S_{12,m} = \frac{\frac{b'_{1,m}}{a'_{2,m}} - \frac{b_{1,m}}{a_{1,m}}\frac{b'_{1,m}}{a'_{2,m}}\Gamma_0}{d} \\ S_{21,m} &= \frac{\frac{b_{2,m}}{a_{1,m}} - \frac{b'_{2,m}}{a'_{2,m}}\frac{b_{2,m}}{a_{1,m}}\Gamma_3}{d} \qquad S_{22,m} = \frac{\frac{b'_{2,m}}{a'_{2,m}} - \frac{b_{2,m}}{a_{1,m}}\frac{b'_{1,m}}{a'_{2,m}}\Gamma_0}{d} \end{aligned} \tag{3.8}$$

Where:

$$d = 1 - \frac{b_{2,m}}{a_{1,m}}\frac{b'_{1,m}}{a'_{2,m}}\Gamma_0\Gamma_3 \tag{3.9}$$

3.1.2 Coaxial Calibrations

This subsection will cover the main coaxial calibration techniques, but it will be addressed in less detail since this thesis focuses on on-wafer device characterisation.

Short-Open-Load-Thru (SOLT)

The SOLT technique is the most commonly used two-port calibration method for coaxial systems. Each SOL standard in the kit is connected and measured at each port, followed by a direct connection of both ports (Thru).

Each standard must have a known response for the calibration technique to be accurate. This becomes more challenging at microwave frequencies, as each standard exhibits a frequency-dependent reactance associated with an equivalent inductance for the short standard or capacitance for the open standard.

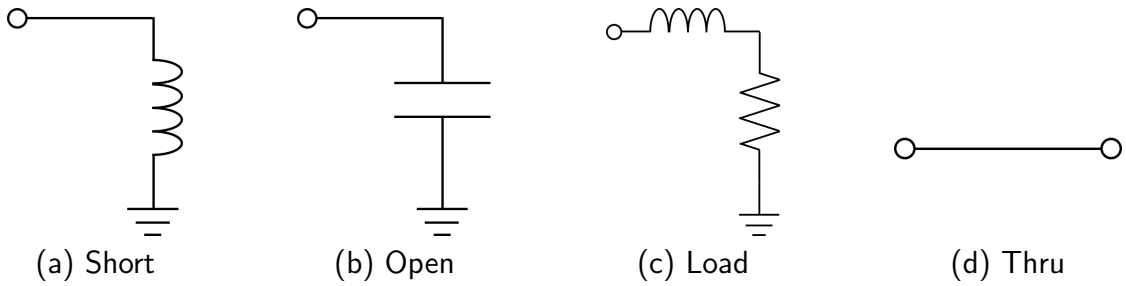

Figure 3.5: Calibration standards with parasitic reactance.

Figure 3.6: 1 mm coaxial calibration standards, match, open and short (from left to right) from Rohde & Schwarz ZV-Z210 calibration kit [5].

As shown in Figure 3.5, the short, open and load have a parasitic reactance that becomes more dominant as frequency increases. The short and load standards are

associated with a series parasitic inductance, while the open standard exhibits fringing capacitance. These are the dominant effects in these standards; other parasitic elements are not included in the equivalent circuit diagrams for clarity.

The standards for microwave frequency calibration kits are typically defined by a behavioural polynomial equation up to the third order, which captures the effects of the fringing capacitance or series inductance.

$$C = C_0 + C_1 f + C_2 f^2 + C_3 f^3 \tag{3.10}$$

$$L = L_0 + L_1 f + L_2 f^2 + L_3 f^3 \tag{3.11}$$

Where L_n and C_n are the polynomial coefficients and f is the measurement frequency.

The thru standard is typically modelled as a transmission line with an equivalent delay. This is accounted for in calibration software by assigning this delay to obtain the correct calibration reference plane.

As the equivalent circuit model becomes even more complex at mm-wave frequencies, it is no longer feasible to model the standard using a polynomial equation. Instead, the calibration kit is supplied with S-parameter measurements for all standards, individually characterised using a highly accurate reference system.

For simplicity, the one-port SOL calibration algorithm is described using the basic equation shown below:

$$\Gamma_M = e_{00} + \Gamma_R \Gamma_M e_{11} - \Gamma_R \Delta e \tag{3.12}$$

Three separate measurements are required to solve this equation for the three unknowns. To cover the maximum measurement space, the two extremes, short and open, along with the centre of the Smith chart, $50\,\Omega$, are used. Expanding and rearranging into matrix form to include the three measurements gives the basic equation needed to solve for the error terms, e, using the measured reflection

coefficients, $\Gamma_{M,n}$, and standard definition of the reflection coefficient, $\Gamma_{R,n}$.

$$\begin{bmatrix} e_{00} \\ e_{11} \\ \Delta e \end{bmatrix} = \begin{bmatrix} 1 & \Gamma_{R,1}\Gamma_{M,1} & -\Gamma_{R,1} \\ 1 & \Gamma_{R,2}\Gamma_{M,2} & -\Gamma_{R,2} \\ 1 & \Gamma_{R,3}\Gamma_{M,3} & -\Gamma_{R,3} \end{bmatrix}^{-1} \begin{bmatrix} \Gamma_{M,1} \\ \Gamma_{M,2} \\ \Gamma_{M,3} \end{bmatrix} \tag{3.13}$$

where Δe is the determinant of the error box.

3.1.3 On-wafer Calibrations

For device-level characterisation, measurement systems are set up for on-wafer measurements, where the bare die is contacted using on-wafer RF probes. This requires a different approach to calibration techniques to ensure accurate measurements at the device plane.

In the coaxial environment, the standard calibration technique is SOLT, as described in the previous section. However, on-wafer, this technique is not accurate. The key characteristic of SOLT calibration is the use of accurately defined standards. On-wafer, it is not possible to fabricate a perfect open, short, or load standard due to parasitic effects from metalisation and the substrate material. Additionally, providing a set of reference measurements for each standard becomes challenging due to the manufacturing variability and mechanical errors, such as probe placement and repeatability.

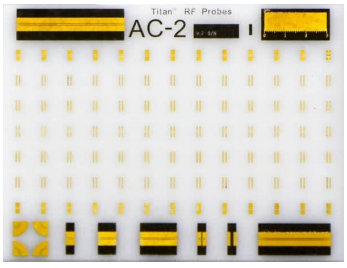

Figure 3.7: AC-2 Impedance standard substrate from MPI corporation [6].

The tile used for calibration typically comes in two forms. One common form is the Impedance Standard Substrate (ISS), as shown in Figure 3.7, an alumina tile containing a set of standards for calibrating to the probe tips.

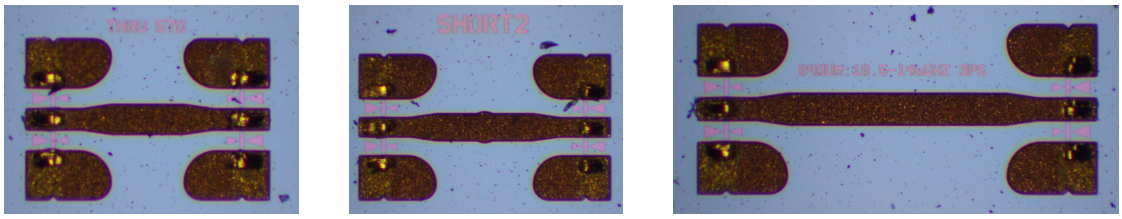

(a) Thru (b) Short (c) Line

Figure 3.8: On-wafer TRL calibration standards on GaAs substrate manufactured by Qorvo.

An alternative to probe-tip calibration on an ISS tile is to design a calibration kit directly on the same wafer as the target device. Figure 3.8 shows an example of a TRL calibration kit designed for a GaN substrate. This introduces additional complexity in designing the calibration kit, but various good practice guides describe calibration kit design to optimise accuracy [7]. This method offers significant benefits. First, it ensures that the probe-to-substrate contact produces the same field pattern as the target device, which improves calibration accuracy compared to calibrating on alumina and then transitioning to the target substrate. Second, the kit can be designed to directly calibrate out the feed lines of the structure, eliminating the need for separate de-embedding steps [8, 9].

The following subsections describe standard calibration techniques devised to overcome the challenges of the SOLT calibration technique.

Thru-Reflect-Match (TRM)

The TRM method [10, 11, 12] is widely used for on-wafer measurements. It relies on three standards: a thru, which provides a zero-length direct connection between the ports; a reflect, which requires only the assumption that it is a short or an open; and a match, which establishes the reference impedance for the calibration. This is a broadband technique that performs well at microwave frequencies.

However, a key drawback is a need for a known or precise match standard, which becomes increasingly challenging at millimetre-wave frequencies. Since the match standard is typically a resistive layer on the tile, the precision can be improved by

laser trimming to achieve a closer approximation to 50 Ω, thereby improving calibration accuracy. This technique improves upon the accuracy of the SOLT technique [13] although it has limited application beyond 20 GHz unless the match standard can be precisely modelled. The difficulty of accurately defining the calibration standards was overcome by the Line-Reflect-Reflect-Match (LRRM) calibration technique.

Line-Reflect-Reflect-Match (LRRM)

The LRRM technique, [14] and [15], is a widely adopted industry-standard calibration algorithm for mm-wave frequencies. It uses both reflect standards and a match standard to achieve accurate broadband calibration. An extension of this technique, the enhanced LRRM (eLRRM) by Cascade Microtech [15], further improves performance by automatically calculating the equivalent load inductance of the match standard. This feature mitigates the limitations of algorithms such as TRM that require a precise definition of the match standard. The method is relatively insensitive to probe placement errors, making it more robust in practical applications. This technique has been demonstrated to perform effectively at frequencies up to 100 GHz [16], [13].

Thru-Reflect-Line (TRL)

The TRL [17] calibration algorithm is widely recognised as the most accurate on-wafer calibration technique [16], [13]. The thru standard, as shown in Figure 3.9 consists of a reciprocal feed structure connected together; it is made up of CPW landing pads and a feed line. In the TRL calibration algorithm, the reference plane of the calibration is defined at its centre. The thru standard must be carefully designed to optimise accuracy. As suggested in [7], the feed line should be long enough to fully launch the microstrip modes from the CPW probes but shorter than $\lambda/4$ to avoid resonances. This structure forms the base of the calibration kit; all standards are fed by half of this standard.

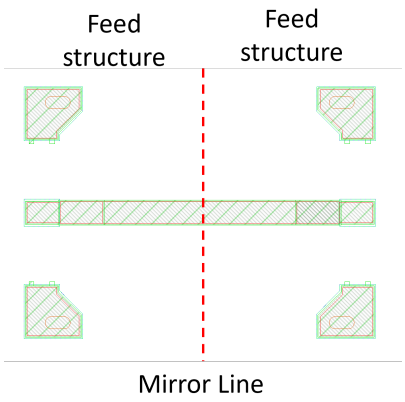

Figure 3.9: Thru standard.

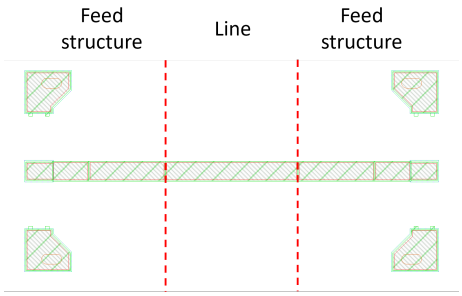

Figure 3.10: Line standard.

The line standard, as shown in Figure 3.10 replaces the match standard used in the TRM method and defines the reference impedance for the calibration. It consists of a length of line whose impedance is Z_0, and its electrical length must equal $90 \pm \angle 70\,^\circ$ across all frequencies within the calibration bandwidth. This requirement is a limitation of the TRL technique, particularly for wideband measurements. The multi-line TRL (mTRL) technique provides a broadband alternative.

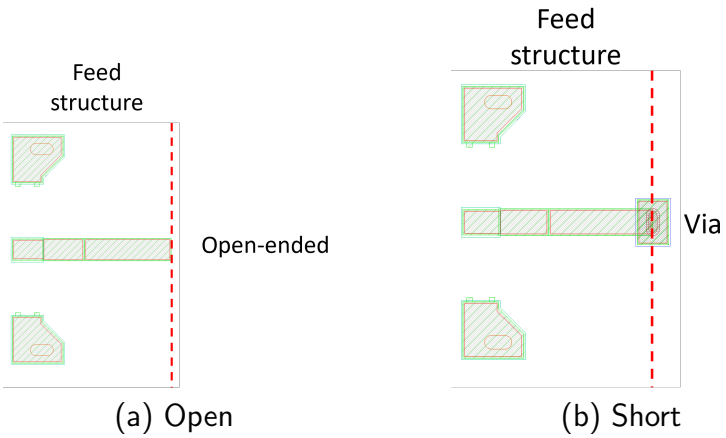

Figure 3.11: Reflect standards.

The reflect standard, as shown as a short or open structure in Figure 3.11 requires no prior knowledge other than that it is either an on-wafer short or open. As suggested in [7], the reflect standard should be placed at the end of the feed structure.

This section details the TRL calibration technique's algorithm and derivation, as it is central to the context of this thesis.

Wave-cascading matrices are used instead of S-parameters to facilitate chain matrix calculations. This conversion is performed as follows:

$$\begin{bmatrix} b_1 \\ a_1 \end{bmatrix} = \begin{bmatrix} R \end{bmatrix} \begin{bmatrix} a_2 \\ b_2 \end{bmatrix} = \frac{1}{S_{21}} \begin{bmatrix} -\Delta_S & S_{11} \\ -S_{22} & 1 \end{bmatrix} \begin{bmatrix} a_2 \\ b_2 \end{bmatrix} \tag{3.14}$$

Where Δ_S is the determinant of the S-parameter matrix.

We can express the thru and line standards in the wave-cascading matrix form as:

$$\begin{bmatrix} R_D^{Thru} \end{bmatrix} = \begin{bmatrix} 1 & 0 \\ 0 & 1 \end{bmatrix} \tag{3.15}$$

and

$$\begin{bmatrix} R_D^{Line} \end{bmatrix} = \begin{bmatrix} e^{-yl} = & 0 \\ 0 & e^{yl} \end{bmatrix} \tag{3.16}$$

Where y and l represent the propagation constant and the length of the line, respectively.

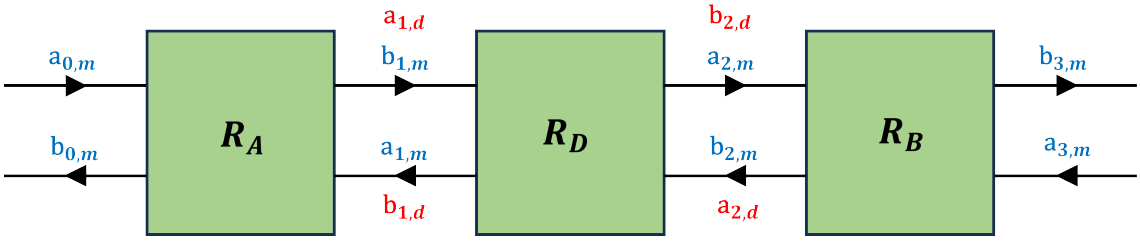

Figure 3.12: TRL error box.

Examining the system in its wave-cascading matrix form, as shown in Figure 3.12, there are the error boxes R_A and R_B, as well as the measurement of the standard, R_D. This diagram can be deconstructed into a set of matrix equations that relate

the measured waves, $a_{0,m}, b_{0,m}, b_{3,m}$ and $a_{3,m}$ to the waves at the DUT, $a_{1,d}, b_{1,d}, b_{2,d}$ and $a_{2,d}$.

$$\begin{bmatrix} b_{0,m} \\ a_{0,m} \end{bmatrix} = \begin{bmatrix} R_{\mathrm{M}} \end{bmatrix} \begin{bmatrix} a_{3,m} \\ b_{3,m} \end{bmatrix} \tag{3.17}$$

where:

$$\begin{bmatrix} R_{\mathrm{M}} \end{bmatrix} = \begin{bmatrix} R_{\mathrm{A}} \end{bmatrix} \begin{bmatrix} R_{\mathrm{D}} \end{bmatrix} \begin{bmatrix} R_{\mathrm{B}} \end{bmatrix} \tag{3.18}$$

The deconstructed matrix equation that relates the measured to actual waves by the error box.

$$\begin{bmatrix} b_{0,m} \\ a_{0,m} \end{bmatrix} = \begin{bmatrix} R_{\mathrm{A}} \end{bmatrix} \begin{bmatrix} b_{1,d} \\ a_{1,d} \end{bmatrix} \tag{3.19}$$

$$\begin{bmatrix} a_{2,d} \\ b_{2,d} \end{bmatrix} = \begin{bmatrix} R_{\mathrm{B}} \end{bmatrix} \begin{bmatrix} a_{3,m} \\ b_{3,m} \end{bmatrix} \tag{3.20}$$

The error box consists of a 2×2 set of error terms.

$$\begin{bmatrix} R_{\mathrm{A}} \end{bmatrix} = R_{22}^{A} \begin{bmatrix} \frac{R_{11}^{A}}{R_{22}^{A}} & \frac{R_{12}^{A}}{R_{22}^{A}} \\ \frac{R_{21}^{A}}{R_{22}^{A}} & 1 \end{bmatrix} = R_{22}^{A} \begin{bmatrix} a & b \\ c & 1 \end{bmatrix} \tag{3.21}$$

$$\begin{bmatrix} R_{\mathrm{B}} \end{bmatrix} = R_{22}^{B} \begin{bmatrix} \frac{R_{11}^{B}}{R_{22}^{B}} & \frac{R_{12}^{B}}{R_{22}^{B}} \\ \frac{R_{21}^{B}}{R_{22}^{B}} & 1 \end{bmatrix} = R_{22}^{B} \begin{bmatrix} \alpha & \beta \\ \gamma & 1 \end{bmatrix} \tag{3.22}$$

Using the definitions of the error boxes provided above, we can now calculate the error terms' values based on the standards' measurements.

The equation for the thru standard is straightforward, as it represents the cascaded error boxes.

$$\begin{bmatrix} R_{\mathrm{M}}^{Thru} \end{bmatrix} = \begin{bmatrix} R_{\mathrm{A}} \end{bmatrix} \begin{bmatrix} R_{\mathrm{B}} \end{bmatrix} \tag{3.23}$$

and for the line:

$$\left[R_{\mathrm{M}}^{Line}\right] = \left[R_{\mathrm{A}}\right]\left[R_{\mathrm{D}}^{Line}\right]\left[R_{\mathrm{B}}\right] \tag{3.24}$$

Defining the term X as:

$$\left[X\right] = \left[R_{\mathrm{M}}^{Line}\right]\left[R_{\mathrm{M}}^{Thru}\right]^{-1} \tag{3.25}$$

Multiplying X by R_A gives:

$$\left[X\right]\left[R_{\mathrm{A}}\right] = \left[R_{\mathrm{A}}\right]\left[R_{\mathrm{D}}^{Line}\right] \tag{3.26}$$

Solving for R_A and expanding results in the below set of equations:

$$X_{11}R_{11}^{A} + X_{12}R_{21}^{A} = R_{11}^{A}e^{-yl} \tag{3.27}$$

$$X_{21}R_{11}^{A} + X_{22}R_{21}^{A} = R_{21}^{A}e^{-yl} \tag{3.28}$$

$$X_{11}R_{12}^{A} + X_{12}R_{22}^{A} = R_{12}^{A}e^{yl} \tag{3.29}$$

$$X_{21}R_{12}^{A} + X_{22}R_{22}^{A} = R_{22}^{A}e^{yl} \tag{3.30}$$

Solving (3.27) and (3.28) for $\frac{a}{c}$ gives the quadratic equation:

$$X_{21}(\frac{a}{c})^2 + (X_{22} - X_{11})(\frac{a}{c}) - X_{12} = 0 \tag{3.31}$$

Solving (3.29) and (3.30) for b gives the quadratic equation:

$$X_{21}b^2 + (X_{22} - X_{11})b - X_{12} = 0 \tag{3.32}$$

We observe that the same base quadratic equation appears in both cases. The solutions to this quadratic equation are:

$$Root_{1,2} = \frac{-(X_{22} - X_{11}) \pm \sqrt{(X_{22} - X_{11})^2 + 4X_{21}X_{12}}}{2X_{21}} \tag{3.33}$$

Next, we need to select which root corresponds to which error term. We can determine the appropriate root selection using (3.19).

$$a_{0,m} = R^A_{22}(\frac{R^A_{11}}{R^A_{22}}a_{1,d} + \frac{R^A_{12}}{R^A_{22}}b_{1,d}) \tag{3.34}$$

and

$$b_{0,m} = R^A_{22}(\frac{R^A_{21}}{R^A_{22}}a_{1,d} + b_{1,d}) \tag{3.35}$$

It is reasonable to assume that in a stable measurement system $|R^A_{11}| \gg |R^A_{12}|$. Assuming this condition holds, we can proceed with the following: $|\frac{R^A_{11}}{R^A_{12}}| \gg 1$ and $|\frac{R^A_{21}}{R^A_{22}}| \ll 1$. This leads too:

$$|\frac{R^A_{21}}{R^A_{22}}| \ll |\frac{R^A_{11}}{R^A_{12}}| \tag{3.36}$$

Which can be rearranged too:

$$|\frac{R^A_{12}}{R^A_{22}}| \ll |\frac{R^A_{11}}{R^A_{21}}| \tag{3.37}$$

Converting this to the coefficient notation of (3.21) leads to this condition:

$$|b| \ll |\frac{a}{c}| \tag{3.38}$$

We assign the solutions of the quadratic equation in (3.33) to satisfy (3.38).

$$b = \begin{cases} Root_1 & \text{if } Root_1 < Root_2, \\ Root_2 & \text{otherwise} \end{cases} \tag{3.39}$$

$$\frac{c}{a} = \begin{cases} \dfrac{1}{Root_2} & \text{if } Root_1 < Root_2, \\ \dfrac{1}{Root_1} & \text{otherwise} \end{cases} \tag{3.40}$$

We now proceed to solve the remaining error terms.

$$\left[R_B\right] = \left[R_{\mathrm{A}}\right]^{-1}\left[R^{thru}_{\mathrm{M}}\right] \tag{3.41}$$

Expanding these matrices gives two more error terms, $\frac{\beta}{\alpha}$ and γ.

$$\frac{\beta}{\alpha} = \frac{R_{12}^{thru} - (b)R_{22}^{thru}}{R_{11}^{thru} - (b)R_{21}^{thru}} \tag{3.42}$$

$$\gamma = \frac{(\frac{c}{a})R_{11}^{thru} - R_{21}^{thru}}{(\frac{c}{a})R_{12}^{thru} - R_{22}^{thru}} \tag{3.43}$$

We can determine $\frac{a}{\alpha}$ using the reflect measurement. The following equations outline the steps to calculate this, and it will be demonstrated that no knowledge of the reflect standard is required. The measured and actual reflection coefficient for a measurement at port 1 can be linked using:

$$\Gamma_1 = \frac{b + a\Gamma_R}{1 + c\Gamma_R} \tag{3.44}$$

where Γ_1 is the reflect standard's measured reflection coefficient from port 1 and Γ_R is the actual reflection coefficient.

Rearranging for $a\Gamma_R$.

$$a\Gamma_R = \frac{\Gamma_1 - b}{1 - \frac{c}{a}\Gamma_1} \tag{3.45}$$

We can do the same for the measured reflection coefficient at port 2, Γ_2.

$$\alpha\Gamma_R = \frac{\Gamma_2 + \gamma}{1 + \frac{\beta}{\alpha}\Gamma_2} \tag{3.46}$$

By forming a ratio of these terms, we eliminate the need for knowledge of Γ_R.

$$\frac{a}{\alpha} = (\frac{\Gamma_1 - b}{1 - \frac{c}{a}\Gamma_1})(\frac{1 + \frac{\beta}{\alpha}\Gamma_2}{\Gamma_2 + \gamma}) \tag{3.47}$$

Expanding (3.23) for the thru standard and solving for $a\alpha$.

$$a\alpha = \frac{\frac{R_{11}^{thru}}{R_{22}^{thru}} - b\frac{R_{21}^{thru}}{R_{22}^{thru}}}{1 - \frac{R_{12}^{thru}}{R_{22}^{thru}}(\frac{c}{a})} \tag{3.48}$$

Using both solutions from (3.47) and 3.48), we can solve for a.

$$a = \pm\sqrt{(a\alpha)(\frac{a}{\alpha})} \tag{3.49}$$

The sign of a can be determined using the reflect standard type (open/short) and the measurement of that standard. Either solution for a can be used in the equation below.

$$\Gamma_R = \frac{(\Gamma_1 - b)}{(1 - (\frac{c}{a})\Gamma_1)}(\frac{1}{a}) \tag{3.50}$$

An if statement can be applied to determine the sign of a.

$$a = \begin{cases} -a & \text{if } \mathrm{Re}\left(\dfrac{\Gamma_R}{\Gamma_R^{\mathrm{std}}}\right) \ll 0, \\ a & \text{otherwise} \end{cases} \tag{3.51}$$

Here Γ_R^{std} is the ideal definition of the standard. Open $= 1\angle\,0\,^\circ$ and Short $= -1\angle\,0\,^\circ$.

All remaining terms can now be solved to obtain a complete set of error terms. The equation for the normalised R_{22}^B is shown below:

$$R_{22}^B = \frac{R_{22}^{thru}}{(1 + c\beta)R_{22}^A} \tag{3.52}$$

A transform from the wave-cascading form, R_A and R_B in (3.21) and (3.22) to S-parameters gives the standard error box, E.

$$E_A = \begin{bmatrix} e_{00} & e_{01}e_{10} \\ 1 & e_{11} \end{bmatrix} \tag{3.53}$$

$$E_B = \begin{bmatrix} e_{22} & \frac{e_{23}}{e_{10}} \\ e_{32}e_{10} & e_{33} \end{bmatrix} \tag{3.54}$$

The calibration technique requires knowledge of seven of the eight error terms. The output contains a set of ratioed error terms, $e_{01}e_{10}$, $\frac{e23}{e10}$ and $e_{32}e_{10}$. In this case, the unknown term that allows for uncoupling all the terms is the power scaling term, e_{10}, which is explained in a later section on power measurements.

3.1.4 Application

This subsection presents the matrix calculations required to apply error correction to S-parameter measurements.

The process begins with the S-parameter error boxes described in (3.53) and (3.54), obtained from the calibration algorithm. These error boxes are converted into wave-cascading matrix form using (3.16). The term e_{10} is omitted, as it is normalised to 1 for S-parameter calibration.

The resulting error boxes take the following form:

$$\left[R_{\mathrm{A}}\right] = R_{22}^{A} \begin{bmatrix} \frac{R_{11}^{A}}{R_{22}^{A}} & \frac{R_{12}^{A}}{R_{22}^{A}} \\ \frac{R_{21}^{A}}{R_{22}^{A}} & 1 \end{bmatrix} = \begin{bmatrix} -\Delta E_A & e_{00} \\ -e_{11} & 1 \end{bmatrix} \tag{3.55}$$

$$\left[R_{\mathrm{B}}\right] = R_{22}^{B} \begin{bmatrix} \frac{R_{11}^{B}}{R_{22}^{B}} & \frac{R_{12}^{B}}{R_{22}^{B}} \\ \frac{R_{21}^{B}}{R_{22}^{B}} & 1 \end{bmatrix} = \frac{1}{e_{32}} \begin{bmatrix} -\Delta E_B & e_{22} \\ -e_{33} & 1 \end{bmatrix} \tag{3.56}$$

The raw S-parameters are first converted into wave-cascading matrix form, as described by (3.18), to use chain matrix mathematics to apply the error correction.

$$\left[R_{\mathrm{D}}\right] = \left[R_{\mathrm{A}}\right]^{-1} \left[R_{\mathrm{M}}\right] \left[R_{\mathrm{B}}\right]^{-1} \tag{3.57}$$

The calibrated S-parameters are obtained through a simple matrix inversion (3.57) and conversion from wave-cascading matrix to S-parameters.

3.2 Large-signal

3.2.1 Procedure

This section outlines the calibration procedure specifically tailored to large-signal measurements. The large-signal calibration and measurement procedure follows the steps outlined below:

1. Vector calibration
2. Absolute calibration
3. Application of calibration
4. Configure system for DUT measurement

Vector Calibration

The basic principle of vector calibration for large-signal measurements remains the same as for small-signal measurements. However, there are a few additional steps for passive load-pull systems.

In a passive load-pull system, the tuner must be characterised and calibrated to ensure the control software knows the impedance presented to the DUT at each tuner position. This calibration step also establishes the density and coverage of the load reflection coefficient.

The tuner characterisation process begins by initialising the tuners to a defined reference state. From this state, the source and load tuner can be isolated from the

rest of the measurement system. A detailed method for performing this characterisation is presented.

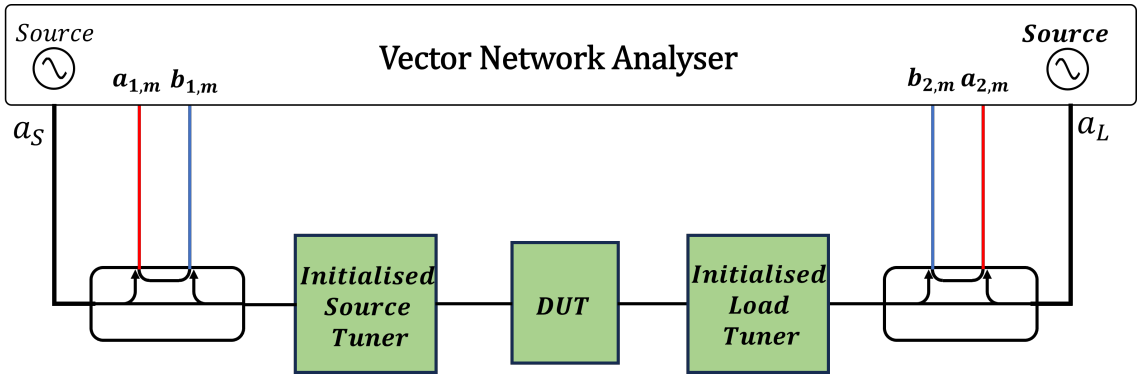

Figure 3.13: A passive source/load-pull setup with tuners in-situ.

The measurement system is set up as illustrated in Figure 3.13. A two-stage characterisation process follows, allowing for the generation of two S-parameter matrices representing the initialised source and load-tuner.

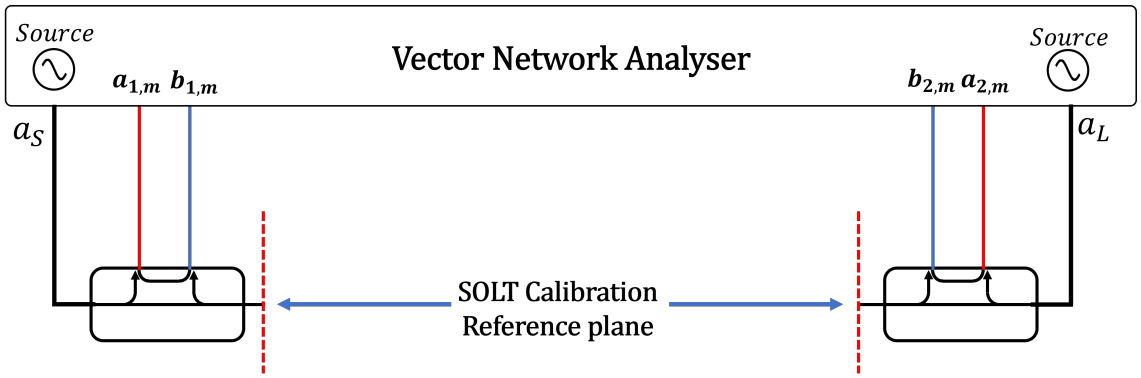

Figure 3.14: A SOLT calibration is carried out between the two external directional couplers to bring the reference plane to the ports of the tuners.

The first stage involves using a coaxial kit to perform a SOLT or UOSM calibration. This step shifts the reference plane from the VNA to the external directional couplers, as illustrated in Figure 3.14.

In the second stage, the tuners are connected to the directional couplers. In this example, a TRL calibration is performed on-wafer, resulting in two error boxes representing the source and load tuners.

With the source and load tuners fully characterised in their initialised positions, they can be calibrated at each slug position. The tuner slug positions are swept in-

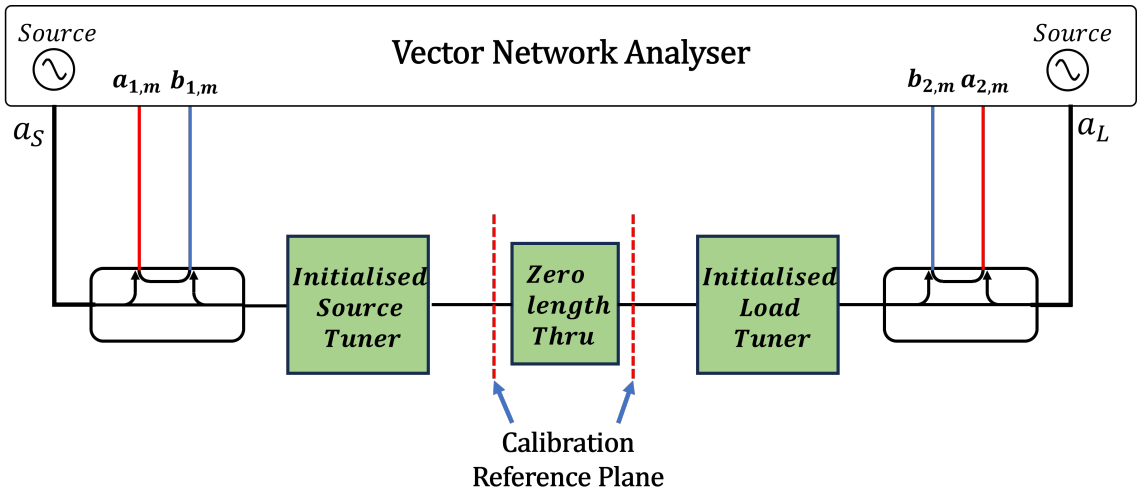

Figure 3.15: TRL calibration brings the reference plane from the directional coupler to the centre of a zero-length thru.

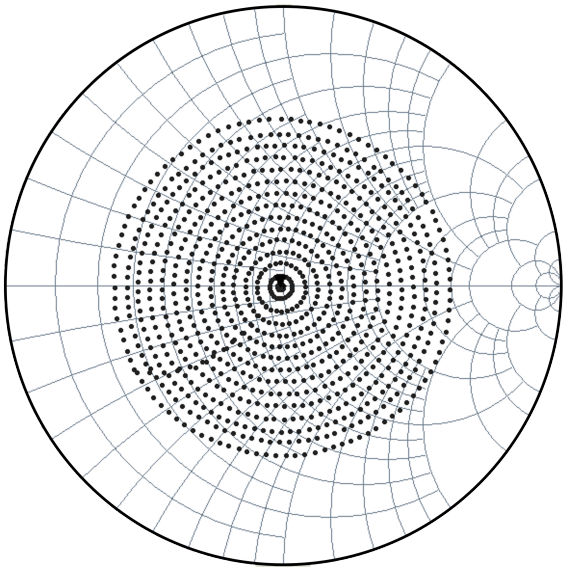

Figure 3.16: Tuner calibrated points for a single tuning slug using the Focus Microwaves Delta tuners at 27.5 GHz.

dependently, and the measured S-parameters at each step are recorded. An example of calibrated tuner positions for a dense grid of impedances is shown in Figure 3.16.

In passive load-pull systems, the control software must know the relationship between tuner slug positions and reflection coefficient to optimise measurement speed. The control software correlates the desired load reflection coefficient with the tuner's mechanical position and adjusts the stepper motor until the target position is achieved.

Modern high-frequency load-pull systems utilising vector-receiver architectures adopt this method in a hybrid manner. In these systems, the tuner calibration is used to determine the load impedance, while the measured waves are sampled by a directional coupler integrated into the tuner. This approach provides several advantages, including faster measurement times, accurate calibration, and a maximisation of the tuning range.

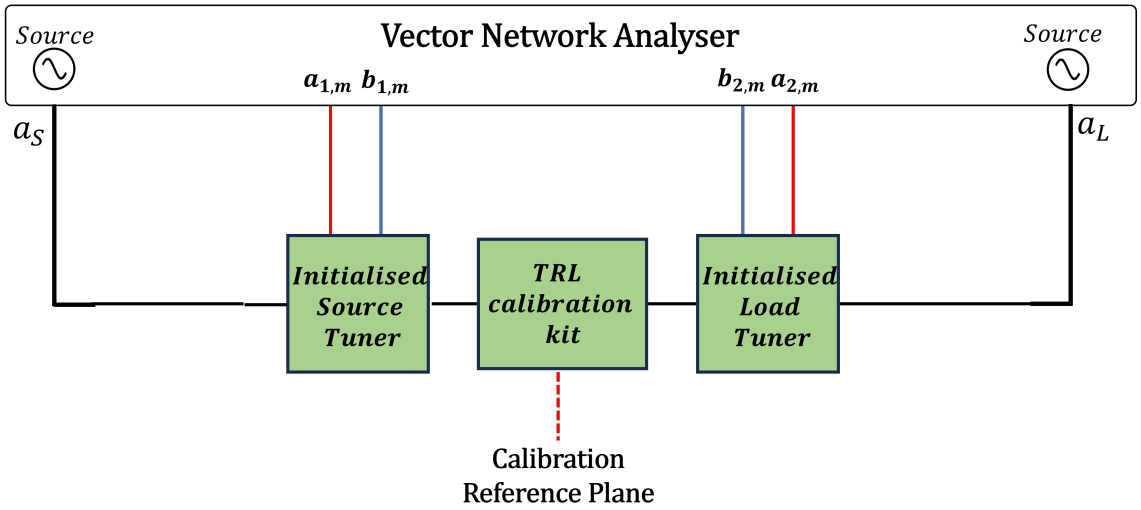

Figure 3.17: Vector calibration set-up for moving the measurement reference plane to the centre of the thru line from the TRL calibration kit.

After tuner calibration, the external directional couplers can be removed from the system, shown in Figure 3.17. A standard vector calibration is then performed, bringing the reference plane to the DUT plane.

Absolute Calibration

After the vector calibration, an absolute calibration is performed, consisting of two parts: power and phase calibration. In S-parameter calibration, only seven of the eight error terms are needed for ratio measurements. However, all eight error terms are required in large-signal measurements, where power and phase-related quantities are measured at both fundamental and harmonically related frequencies. To decouple the ratio error terms the solution to e_{10} is required, this is found by performing an absolute calibration.

The power calibration uses a power meter at the DUT plane as a reference to scale the magnitude of e_{10}. On-wafer power meters do not exist, so the power reference is obtained using a coaxial power meter at an extended port plane.

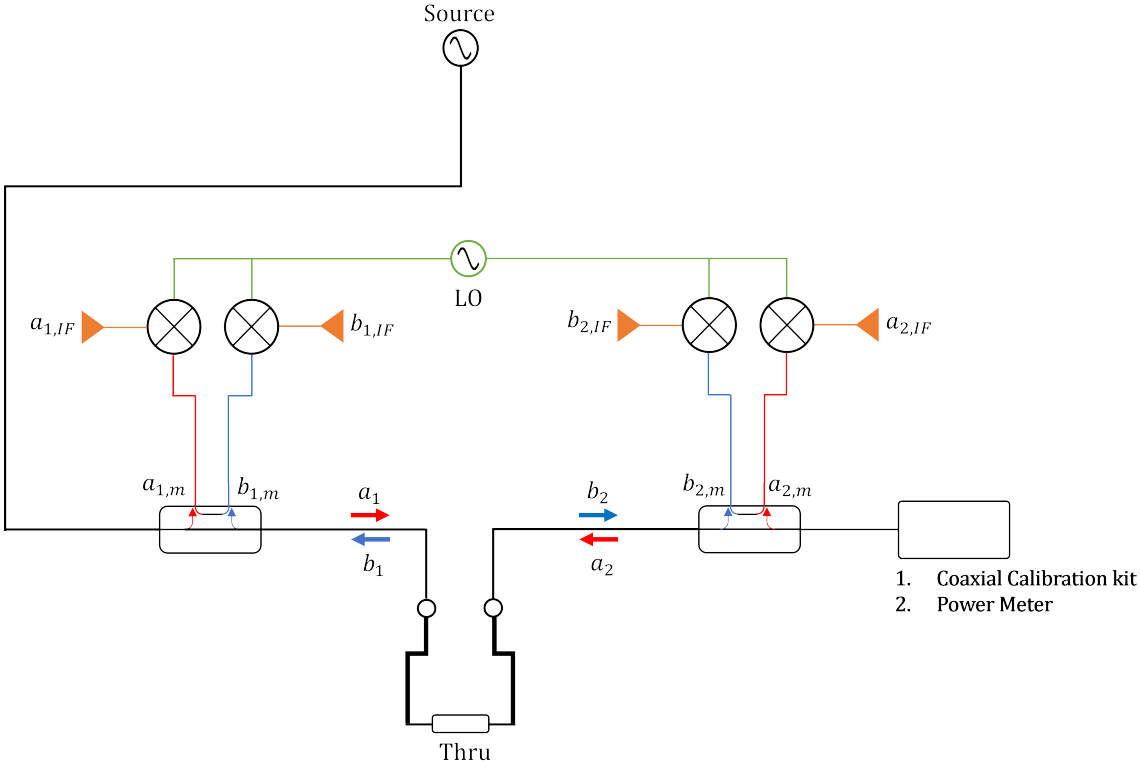

Figure 3.18: Power calibration configuration diagram.

The system is configured for power calibration, as shown in Figure 3.18.

An extended port calibration is performed close to the DUT plane at the output port of the load reflectometer. This is a one-port coaxial calibration, as described in Equation (3.13).

The power calibration is performed by measuring the power at the extended port plane. The measured reflection coefficient at the centre of the thru standard, using the vector calibration coefficients, and the reflection coefficient looking towards the power meter, using the extended calibration coefficients, are known and used to move the power reference plane to the centre of the thru standard. This is achieved by normalising the measured power by the difference in the reflection coefficient.

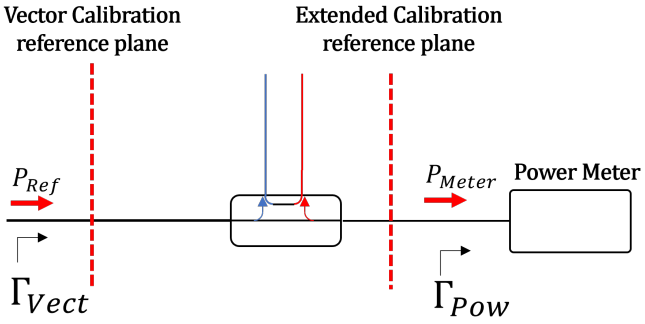

Figure 3.19: Different reference planes for each calibration stage.

Figure 3.19 shows the different calibration reference planes for the power calibration. Γ_{Vect} is the reflection coefficient at the centre of the vector calibration reference plane, whilst P_{Ref} is unknown and is the delivered power at the vector calibration reference plane. The reflection coefficient, Γ_{Pow} is the calibrated reflection coefficient at the extended port plane, whilst P_{Meter} is the measured power result from the power meter. P_{Ref} is calculated using these parameters.

$$\Gamma_{\text{Norm}} = \frac{\Gamma_{\text{Vect}}}{\Gamma_{\text{Pow}}} \tag{3.58}$$

$$P_{Ref} = P_{Meas}\Gamma_{\text{Norm}} \tag{3.59}$$

The magnitude of the power scaling term is:

$$e_{10} = \sqrt{\frac{P_{Ref}}{P_{Cal}}} \tag{3.60}$$

Phase alignment between the fundamental and harmonic frequencies is necessary to construct a time-domain signal from a set of frequency-domain measurements.

This phase alignment is achieved through either a phase calibration or the direct capture of the phase relationship, which requires a phase-calibrated source or measurement device.

The method shown in Figure 3.20 uses an oscilloscope as a phase meter to directly capture the phase information from the waves at the oscilloscope port. The time base between the VNA and oscilloscope is synchronised by using the VNA port 3 source as a trigger input to the oscilloscope. This provides a straightforward solution for reconstructing a time-domain measurement from the device under test. This method is the direct capture of measured waves and does not theoretically require a calibration, however, to obtain accurate phase relationship a calibration procedure to de-embed the RF path between the instrument and the DUT plane is required. It is not a typical solution due to the cost and limited availability of oscilloscopes with sufficient bandwidth, especially at mm-wave frequencies, but it must be used in cases where there is a lack of phase reference.

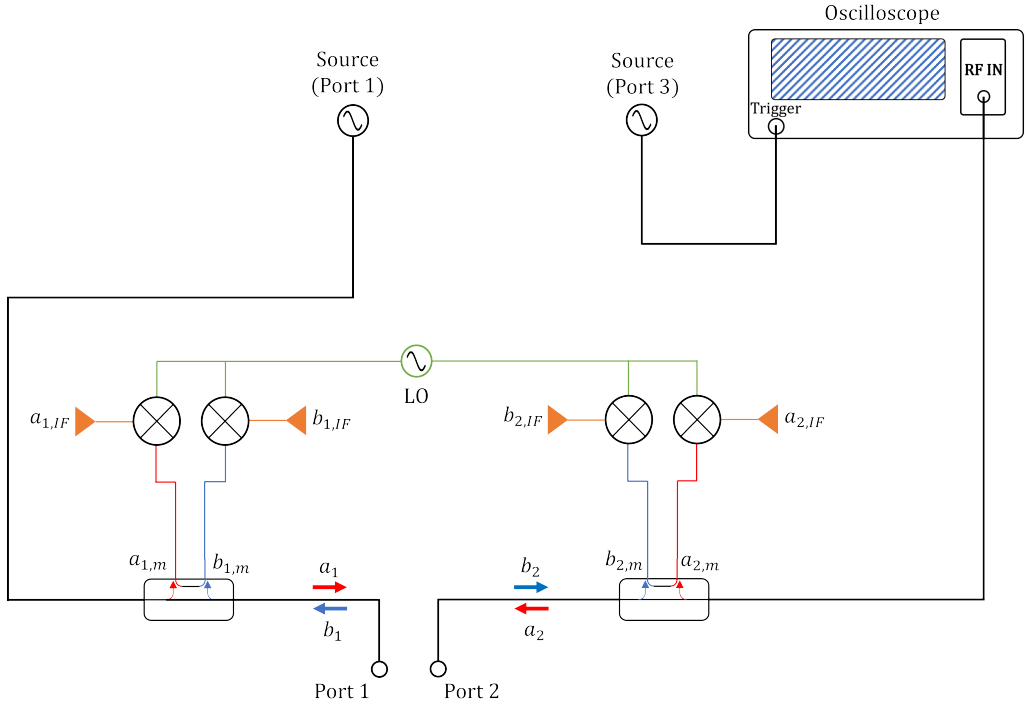

Figure 3.20: Phase coherence using an oscilloscope as a phase meter.

A harmonic phase reference (HPR) module is a more cost-effective solution for achieving phase alignment in a measurement system but requires a calibration pro-

cedure to ensure correct alignment of the harmonic frequencies. Typically based on a comb generator, the HPR generates tones with a fixed, known phase relationship; this data is stored in a lookup table. To perform phase calibration using the HPR, an additional receiver and source channel on the VNA are required.

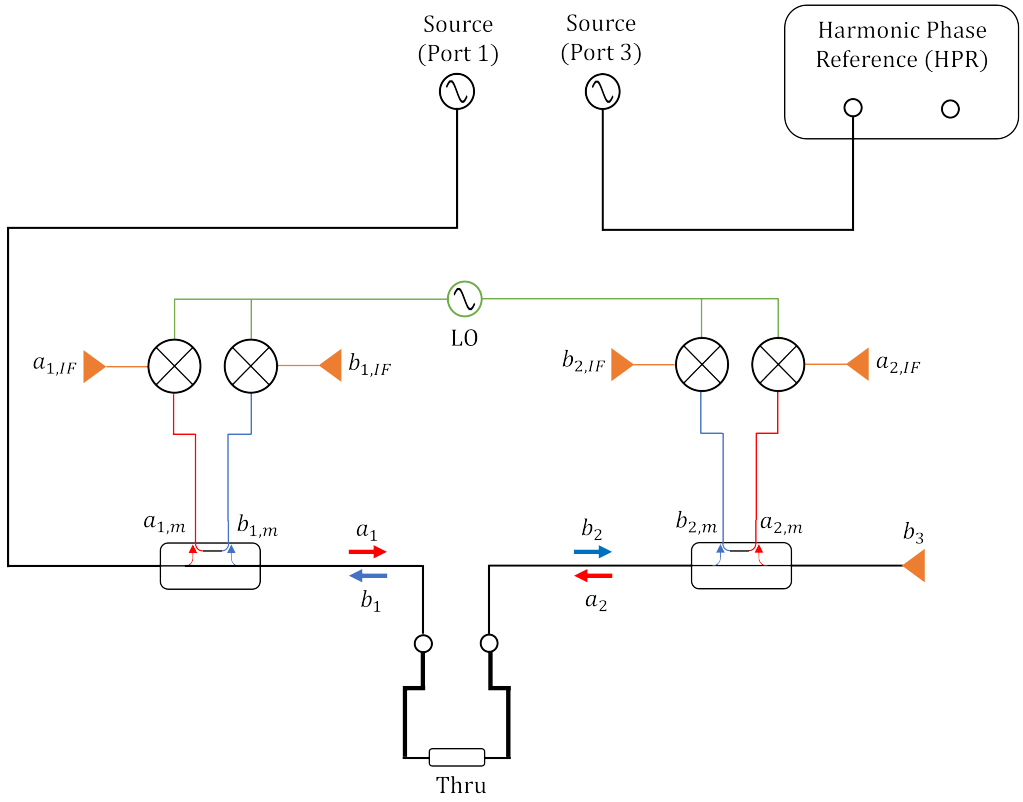

Figure 3.21: Phase coherence using a harmonic phase reference module.

The measurement system is first configured as shown in Figure 3.21, with the harmonic phase reference (HPR) connected to the VNA source port 3, which is phase-locked to the source of port 1. The VNA's measurement receiver for phase calibration (b_3) is connected directly to the extended port plane. The VNA then sweeps frequencies from the fundamental to the n^{th} harmonic, recording the phase at frequency.

Secondly, as shown in Figure 3.22, a power meter is connected to the source of port three to provide a power reference for the HPR. A lookup table is used to apply a correction phase for the phase component of e_{10} across the harmonics.

Figure 3.23 shows the configuration for multi-harmonic large-signal measurements. The measurement receiver of port three is used to measure the output

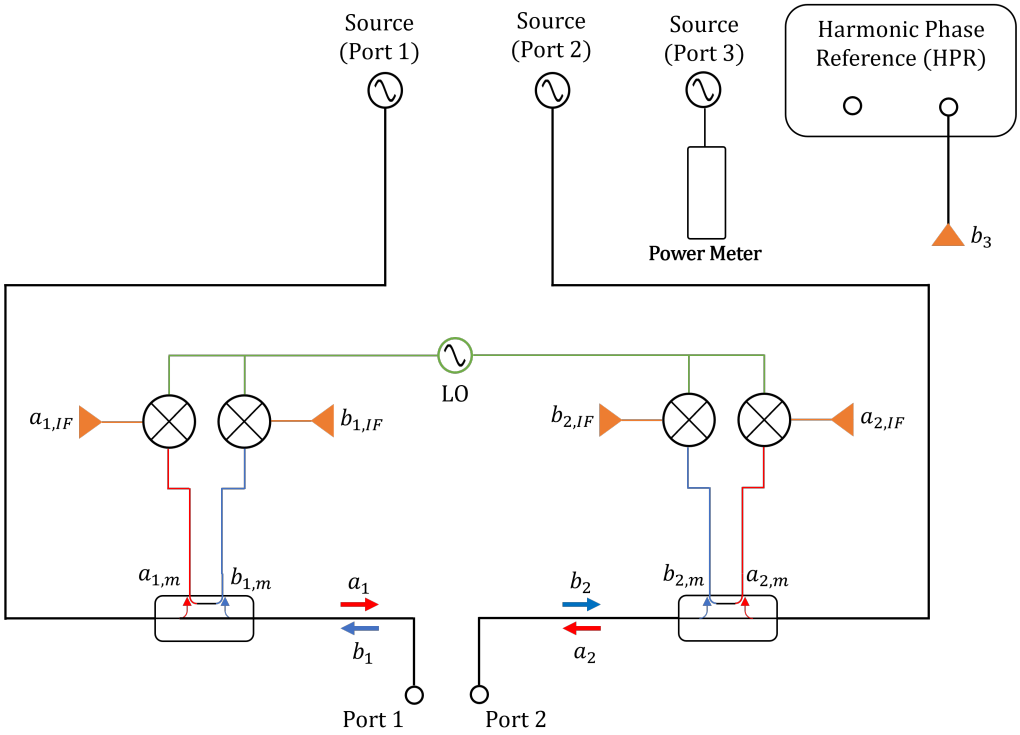

Figure 3.22: Phase calibration, measuring the VNA source power.

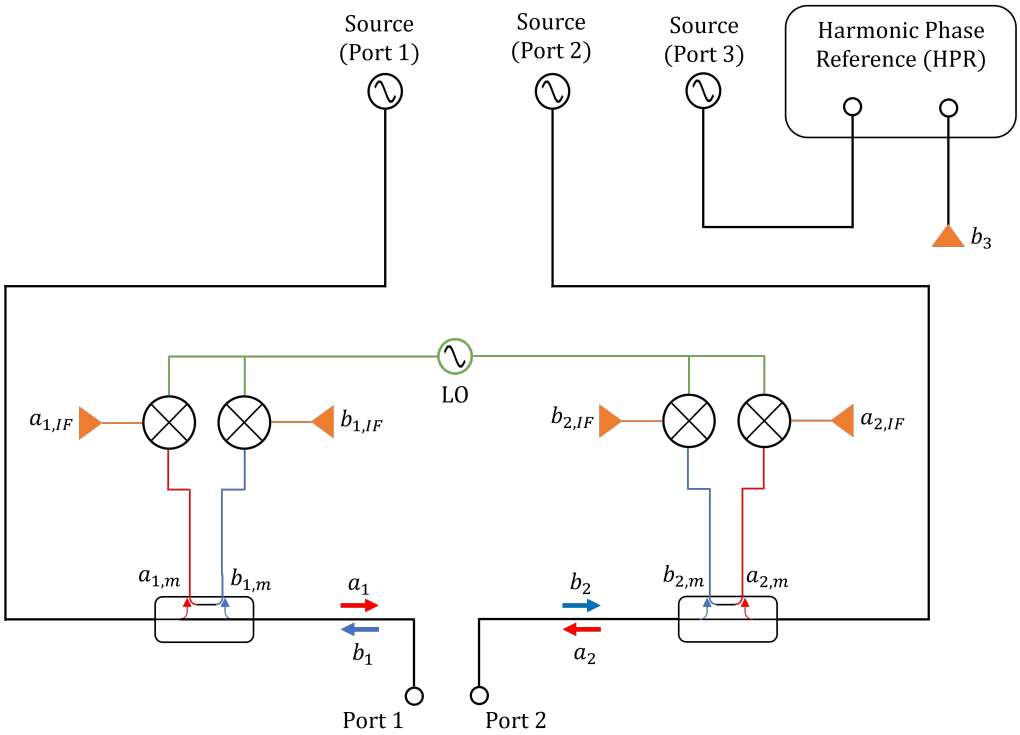

Figure 3.23: Phase calibration, measuring the output of the harmonic phase reference.

of the harmonic phase reference.

Application

This subsection presents the matrix calculations required to apply a calibration to a set of raw wave measurements.

First, the S-parameter error boxes from the calibration algorithm, as defined in (3.53) and (3.54), are converted into wave-cascading matrix form using (3.16).

This transformation results in the error boxes represented in the form:

$$\left[R_{\mathrm{A}}\right] = R_{22}^{A} \begin{bmatrix} \frac{R_{11}^{A}}{R_{22}^{A}} & \frac{R_{12}^{A}}{R_{22}^{A}} \\ \frac{R_{21}^{A}}{R_{22}^{A}} & 1 \end{bmatrix} = \begin{bmatrix} -\Delta E_A & e_{00} \\ -e_{11} & 1 \end{bmatrix} \tag{3.61}$$

$$\left[R_{\mathrm{B}}\right] = R_{22}^{B} \begin{bmatrix} \frac{R_{11}^{B}}{R_{22}^{B}} & \frac{R_{12}^{B}}{R_{22}^{B}} \\ \frac{R_{21}^{B}}{R_{22}^{B}} & 1 \end{bmatrix} = \frac{1}{e_{32}e_{10}} \begin{bmatrix} -\Delta E_B & e_{22} \\ -e_{33} & 1 \end{bmatrix} \tag{3.62}$$

To apply error correction to a set of raw measured waves, (3.19) and (3.20) are used. Corrected measurements are obtained by inverting R_A from (3.61). Using R_A^{-1} and R_B, the calibration correction equation is assembled in matrix form to transform measured waves into corrected waves. Here, the absolute calibration stage determines e_{10}. The resulting equation is shown below:

$$\begin{bmatrix} b_{1,d} \\ a_{1,d} \\ b_{2,d} \\ a_{2,d} \end{bmatrix} = \frac{1}{e_{10}} \begin{bmatrix} \frac{1}{e_{01}} & -\frac{e_{00}}{e_{01}} & 0 & 0 \\ \frac{e_{11}}{e_{01}} & -\frac{\Delta E_A}{e_{01}} & 0 & 0 \\ 0 & 0 & \frac{1}{e_{32}} & -\frac{e_{33}}{e_{32}} \\ 0 & 0 & \frac{e_{22}}{e_{32}} & \frac{-\Delta E_B}{e_{32}} \end{bmatrix} \begin{bmatrix} b_{1,m} \\ a_{1,m} \\ b_{2,m} \\ a_{2,m} \end{bmatrix} \tag{3.63}$$

This section discusses the fundamental calibration techniques that form the basis of the technical chapters in this thesis. It covers various calibration algorithms, from

coaxial techniques such as the SOLT, which becomes inaccurate for on-wafer mm-wave calibrations due to the difficulty of defining the standards. To overcome these issues, the LRRM, TRL and mTRL techniques are used, as they do not require precise standard definitions to achieve accurate calibration. the TRL and mTRL techniques are used throughout this thesis.

References

[1] Copper Mountain Technologies. *Systematic Errors*. URL: https://coppermountaintech.com/help-s2/systematic-errors.html.

[2] D. Rytting. *Network Analyzer Error Models and Calibration Methods*. Presentation Slides. Agilent Technologies.

[3] J. P. Dunsmore. *Handbook of Microwave Component Measurements with Advanced VNA Techniques*. New Jersey, USA: Wiley, 2020.

[4] R. B. Marks. "Formulations of the Basic Vector Network Analyzer Error Model iIncluding Switch-Terms". In: *ARFTG Microw. Meas. Conf.* Vol. 32. 1997, pp. 115–126.

[5] Rohde & Schwarz. *R&S®ZN-Z2xx network analyzer calibration kits*. URL: https://www.rohde-schwarz.com/uk/products/test-and-measurement/manual-calibration-and-verification-kits/rs-zn-z2xx-network-analyzer-calibration-kits_63493-592909.html.

[6] MPI Corporation. *MPI RF Calibration Substrates*. URL: https://www.mpi-corporation.com/ast/mpi-rf-probes-accessories/mpi-rf-calibration-substrates.

[7] X. Shang and N. Ridler and J. Ding and M. Geen. *Introductory Guide to Making Planar S-parameter Measurements at Millimetre-wave Frequencies*. Tech. rep. NPL, Jan. 2021.

[8] A. Rumiantsev et al. "Application of On-Wafer Calibration Technology for Advanced High-Speed BiCMOS Technology". In: *IEEE Bipolar/BiCMOS Circuits and Technol. Meet. (BCTM)*. 2010, pp. 98–101.

[9] K. Yau et al. "Device and IC Characterization Above 100 GHz". In: *IEEE Microw. Magazine* 13.1 (2012), pp. 30–54.

[10] H.-J. Eul and B. Schiek. "Thru-Match-Reflect: One Result of a Rigorous Theory for De-Embedding and Network Analyzer Calibration". In: *IEEE Eur. Microw. Conf.* 1988, pp. 909–914.

[11] H. J. Eul and B. Schiek. "A Generalized Theory and New Calibration Procedures for Network Analyzer Self-Calibration". In: *IEEE Trans. Microw. Theory Techn.* (1991).

[12] M. A. Pulido-Gaytán et al. "Generalized Theory of the Thru-Reflect-Match Calibration Technique". In: *IEEE Trans. Microw. Theory Techn.* 63.5 (2015), pp. 1693–1699.

[13] D. F. Williams, R. B. Marks, and A. Davidson. “Comparison of On-Wafer Calibrations”. In: *ARFTG Microw. Meas. Conf.* Vol. 20. 1991, pp. 68–81. DOI: 10.1109/ARFTG.1991.324040.

[14] A. Davidson, K. Jones, and E. Strid. “LRM and LRRM Calibrations with Automatic Determination of Load Inductance”. In: *ARFTG Microw. Meas. Conf.* Vol. 18. 1990, pp. 57–63.

[15] L. Hayden. “An Enhanced Line-Reflect-Reflect-Match Calibration”. In: *ARFTG Microw. Meas. Conf.* 2006, pp. 143–149.

[16] S. Shin et al. “Comparison of On-Wafer Calibrations for Measurements of Active and Passive Devices at Millimeter-wave Frequencies”. In: Nov. 2023.

[17] G.F. Engen and C.A. Hoer. “Thru-Reflect-Line: An Improved Technique for Calibrating the Dual Six-Port Automatic Network Analyzer”. In: *IEEE Trans. Microw. Theory Techn.* 27.12 (1979), pp. 987–993.

Chapter 4

Device Modelling

This chapter provides a brief theoretical background on device modelling, illustrating and motivating this thesis's central aim: to achieve accurate measurements at mm-wave frequencies. These measurements are essential for generating datasets for extracting and validating device models, which improves reliability and enhances tapeout success rates. By presenting this background, the chapter establishes the reasoning for this work's objectives.

Transistor modelling involves creating a mathematical representation that accurately predicts a transistor's measured characteristics. This approach enables computer-aided design of power amplifiers within a simulation environment, significantly reducing the need for multiple fabrication and testing stages.

Figure 4.1 illustrates the power amplifier design process, comparing approaches with and without a device model. In the left flowchart, the absence of a device model leads to design iterations only after device fabrication. In contrast, the right flowchart uses a device model, enabling design and test iterations within simulation software before fabrication. This approach eliminates several fabrication stages, significantly reducing design costs.

These flowcharts assume that the model accurately represents the physical transistor under identical operating conditions, a major ongoing focus in device modelling research.

Various device modelling strategies are employed in industry and academia to

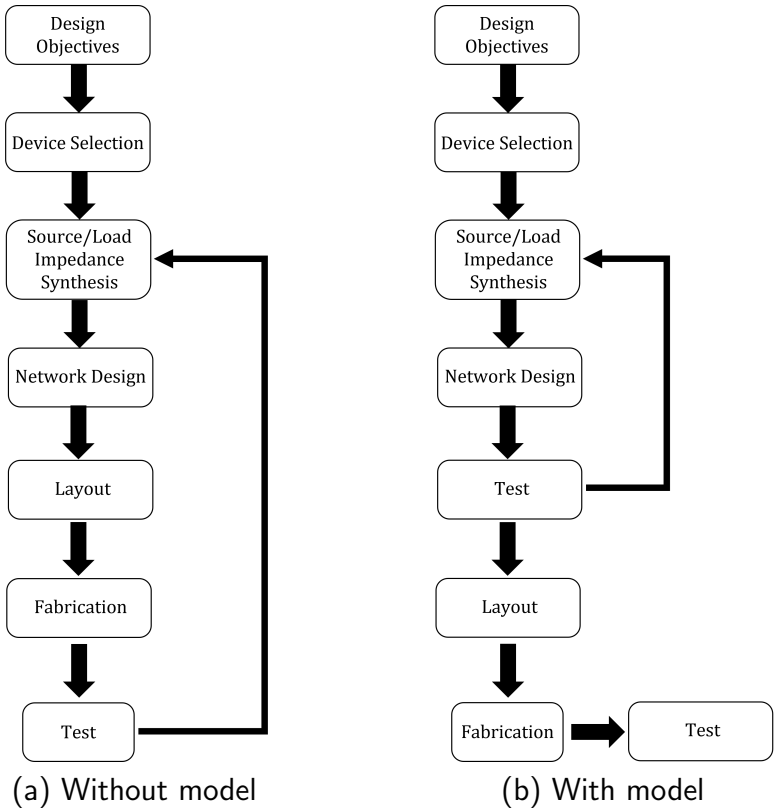

Figure 4.1: Power amplifier design flowchart without (a) and with (b) a device model.

develop accurate device models. The following section explores these approaches, highlighting their respective advantages and disadvantages.

4.1 Look-up Table Modelling

The look-up table method for device modelling is the least computationally intensive but the most labour-intensive method. It consists of measuring a device at various operational conditions, which are stored in a look-up table for use in a simulator.

Figure 4.2 illustrates the look-up table method, showing an example data structure for measuring a power amplifier. The data is organised across three conditions: load reflection coefficient magnitude and phase and available source power, resulting in a dataset size of $i \times j \times k$.

The primary limitation of this method is that the device can only be simulated under the exact conditions of measurement. The accuracy of the model outside of these measured points rely upon the interpolation and extrapolation technique

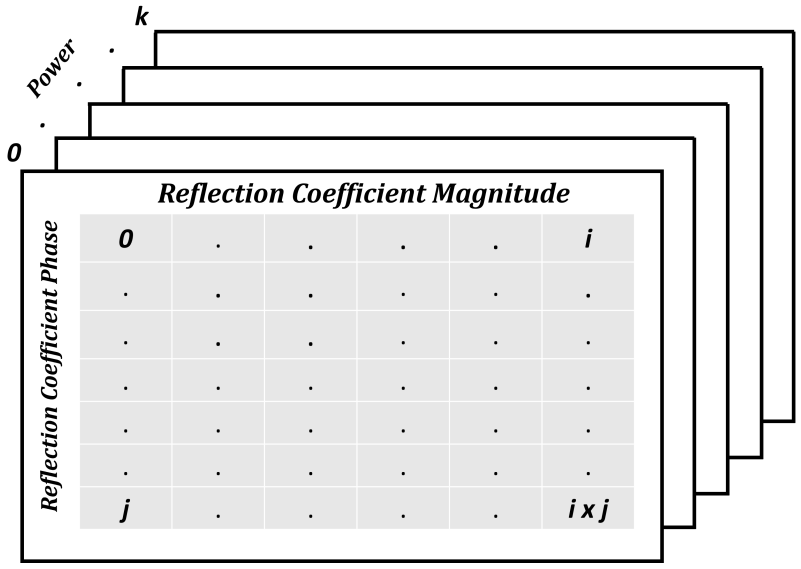

Figure 4.2: Look-up table modelling method.

employed by the simulator that the model is implemented within, this could lead to unpredictable and erroneous results. Behavioural modelling expands the look-up table concept to allow for valid interpolated results. As shown in Figure 4.2, the measurement-intensive nature of this modelling strategy becomes evident when a model requires multiple variables, such as the load reflection coefficient (Γ_{L}), available input power (P_{av}), frequency, bias, or temperature. These datasets become multidimensional, leading to significant file sizes. For a dataset with x variables per condition and n conditions, the total number of required data points, y, is given by:

$$y = x^n \tag{4.1}$$

(4.1) demonstrates that the practicality of this modelling strategy is restricted to applications requiring a finite dataset.

This strategy is the most sensitive to measurement accuracy, as the data is directly used in the simulator; the data will include any calibration errors alongside measurement uncertainty, including random noise.

4.2 State Function Modelling

This section presents the state function modelling approach, outlining its benefits and drawbacks. It includes an example breakdown of a high-frequency transistor, demonstrating how the model structure links to device operation, and examples of widely implemented state function models.

State function modelling takes a physics-based approach to device modelling, offering insights into the physical structure and operation of the device. While this approach is extensive and complex, it is typically the most accurate across various operational characteristics. Although the methodologies and topologies are rooted in device physics, the mathematical equations that describe device operation are often behavioural.

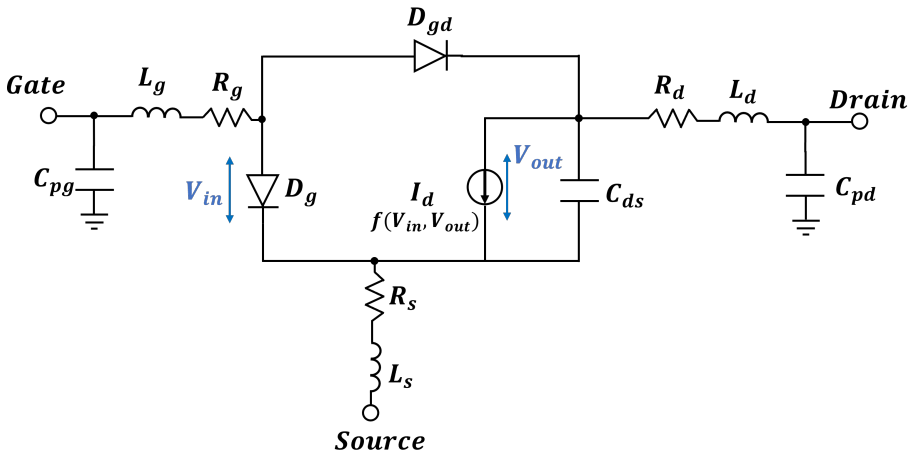

Figure 4.3: A simplified large signal model.

Figure 4.3 shows a simplified large signal model. An equivalent circuit element is assigned to model the characteristics of the construction to describe the likely behaviour of materials and material interfaces.

The equivalent circuit components are divided into two categories: extrinsic effects, which are operationally independent, and intrinsic effects, which are operationally dependent.

Extrinsic effects relate to the physical structure and metalisation. The metalisation of the transistor can be approximated by three circuit elements: resistance,

inductance, and capacitance. The metalised contacts have an associated inductance, represented by L_{g}, L_{d}, and L_{s}. The resistivity of the metal and ohmic contact is represented as R_{g}, R_{d}, and R_{s}. The charge separation between contacts can be approximated by capacitors, represented by C_{pg}, C_{pd}.

The intrinsic parameters are operationally dependent; in large signal models, these are typically modelled by the gate and feedback diodes, with the current generator, I_D, dependent upon the V_{in} and V_{out}. The output reactance of the transistor is modelled by the shunt capacitor, C_{ds}.

A typical extraction method for a model of this type involves measuring the device under various operational conditions to determine the equivalent circuit parameters as functions of frequency and bias. This section describes two prominent state function models.

4.2.1 Example Models

Two prominent and effective large-signal models used in commercial HEMT device modelling are the Angelov model [1][2], widely reported in the literature, and the Keysight EEHEMT1 model [3] [4], which builds upon the work in [5] and [6], and is used in the commercial modelling software IC-CAP. The Angelov model uses generalised equations based on the hyperbolic tangent to describe the current profile, while the EEHEMT1 model employs a piecewise function to model different operational modes. This piecewise approach allows the transconductance profile to be modelled asymmetrically, in contrast to the symmetric nature of the Angelov model. Recent developments in these models have included optimised functions to better model temperature and trapping effects [7], [8], and [9].

The Angelov and EEHEMT model's equivalent circuits are shown in Figure 4.4. The extraction process is significant and requires multiple measurement systems, from small and large signal RF systems to I/V and C/V systems. The extraction processes of both models are well detailed in [10] and [4].

The EEHEMT model extraction process involves pulsed DCIV and S-parameter

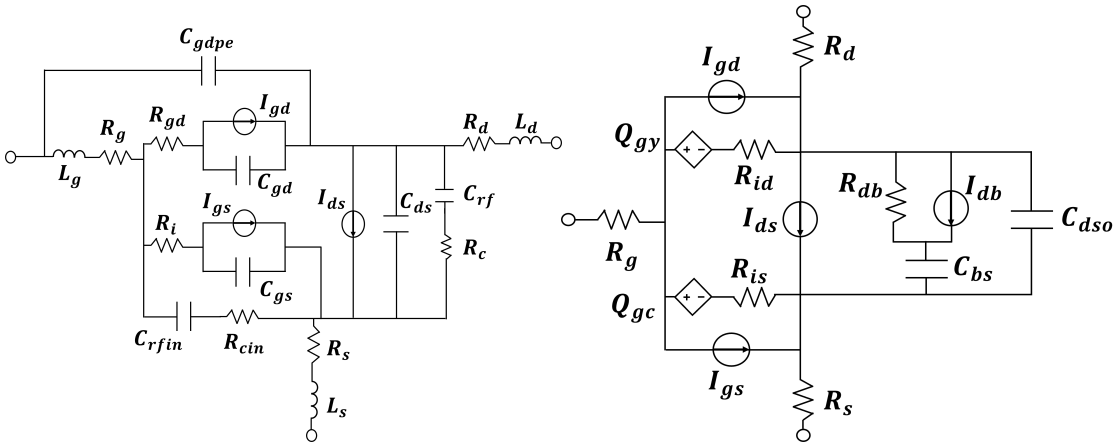

(a) Angelov [10] (b) EEHEMT1 [3]

Figure 4.4: Equivalent circuit models for the Angelov (a) and EEHEMT1 (b) device models.

measurements; pulsing is used to avoid self-heating of the device. The model can be extracted in two different ways; the first is to use standard extraction procedures for small signal models followed by extensive numerical optimisation; the extrinsic parameters are kept constant across bias whilst the intrinsic parameters are allowed to vary, allowing for a separate model for each bias condition. To extend this to a large signal model, the large signal equivalent components are extracted using the model non-linear equations and the extracted intrinsic capacitance and DCIV measurements. The second method is to directly optimise straight from the large signal non-linear model equations to fit the measurement data. The first procedure allows for a starting point for optimisation, possibly leading to more realistic circuit values. Still, it requires significant optimisation, whilst direct optimisation requires less time to extract multiple models. It may lead to a better measurement to model fit but have non-physical component values.

The Angelov model performs the multi-bias S-parameter measurements as per the EEHEMT extraction procedure but also conducts an additional C/V measurement process. This process uses cold FET S-parameters to extract the extrinsic parasitics, whilst the current generator component values are extracted using I/V measurements, and the C/V measurements extract the capacitance values. These measurements are then used with the model equations to extract the equivalent

circuit values to produce a single stand-alone, multi-bias, non-linear model.

To validate these models for use as large signal device models, load-pull measurements are performed on the devices and the contours can be compared with the modelled results. This leads to further tuning and optimisation [11] of the model parameters to match the measured contours. Both models' extraction and validation procedure highlights the importance of measurement accuracy. Each extraction procedure involves optimising a set of component values to match the measured parameter, with the Angelov method using up to four different measurement techniques. Uncertainty or calibration error can easily propagate to the large signal model and lead to an inaccurate model.

4.3 Behavioural Modelling

The state function models described in the previous section are purely based on the physics of device operation but typically use behavioural equations to characterise device behaviour. In this section, purely behavioural models are discussed.

These models treat the device as a black box, using curve-fitting equations to describe its response to a set of incident signals, as shown in Figure 4.5 of a two-port DUT.

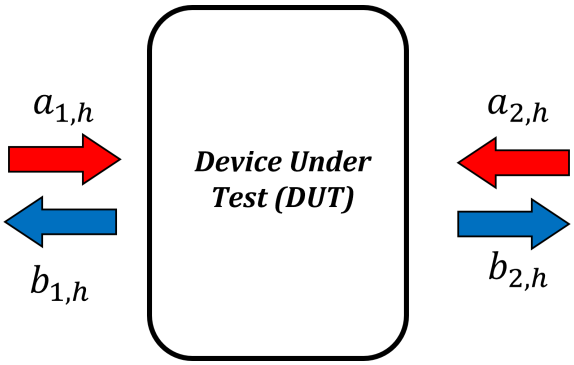

Figure 4.5: Simplified diagram of a behavioural model.

Behavioural models are highly accurate but have limited scope, as they require a set of measurements for each variable, including frequency, power, bias, temperature, and others. This limitation defines their use cases: they are ideal for small-scale

designs where a device model doesn't exist or in situations requiring high accuracy when existing models have not been tuned for a specific use case. This is especially common at mm-wave frequencies, where parasitic effects add complexity and the costs of owning and operating an mm-wave measurement system are significant.

Behavioural models are heavily dependent on the accuracy of the measurement data. Any errors introduced during device measurement will propagate through to the model.

4.3.1 Example Models

Examples of well-established behavioural models include Keysight's X-parameters [12] and the Cardiff model [13]. Both are frequency-domain models based on poly-harmonic distortion theory, and are used to predict the response to an incident signals using a set of coefficients.

X-Parameters

$$B_{p,k} = X^{(FB)}_{p,k} P^k + \sum_{\mathrm{l=1}}^{\mathrm{q=N,l=K}} X^{(S)}_{\mathrm{p,k;q,l}} A_{q,l} P^{k-l} + \sum_{\mathrm{q=1,l=1}}^{\mathrm{q=N,l=K}} X^{(T)}_{\mathrm{p,k;q,l}} A^*_{q,l} P^{k+l} \quad [12] \qquad (4.2)$$

where B is the response, A is the incident signal, q and p are the input and output ports, respectively and l and k are the input and output harmonics, respectively.

The X-parameter model equation, shown in (4.2), is a mathematical extension of S-parameters designed to capture the non-linear response of a device. As the input power is reduced and the harmonic content becomes negligible, the coefficients converge to the linear condition of S-parameters.

The model is linearised around a large-signal drive tone, $A_{1,1}$, and the equation and extraction procedure can be broken down into three measurements.

First, the coefficient X^{FB} is determined by injecting a large signal tone and measuring the fundamental and harmonic response.

The other two coefficients, X^S and X^T, are obtained by injecting a small signal extraction tone at A_2, using separate measurements that are orthogonal in phase.

These can be extracted using either an on-frequency or off-frequency method. In the on-frequency method, the frequency is the same as the large signal extraction tone; in the off-frequency method, the frequency is offset. Since the models rely on small-signal offsets in A_2, the model requires significant extrapolation capability across all reflection coefficients, which can introduce inaccuracies. This process can be repeated across a grid of load impedances, increasing the dataset of coefficients required to accurately model a device [14]. To validate this model, a load-pull measurement can be taken using data points at different impedances to the impedances used for extraction and the modelled and measurement data compared.

The formulation can also be extended to minimise measurement intensity when adding additional dimensions for modelling characteristics such as capturing memory effects [15], scaling transistor periphery [16] and frequency scaling [17].

The Cardiff Model

The original Cardiff model equation was published in [13]. Since then, subsequent works have further developed its standard form. The version most commonly cited in recent years is shown in (4.3).

$$B_{p,h} = \angle A_{1,1}^{h} \sum_{\mathrm{r=0}}^{1} \sum_{\mathrm{n=n_{min}}}^{\mathrm{n_{max}}} K_{\mathrm{p,h,m,n}} \left|A_{2,1}\right|^{\mathrm{m}} \left(\frac{\angle A_{2,1}}{\angle A_{1,1}}\right)^{n} \qquad \text{[18]} \tag{4.3}$$

where B is the response and A is the incident signal, K is the Cardiff model coefficients indexed by p, the port number, h, the harmonic frequency index, r the magnitude indexing term, m and n, the magnitude and phase exponents, respectively.

The Cardiff model attempts to relate the response wave to the incident wave using a set of coefficients. The coefficients are indexed by magnitude and phase terms, which can be described by thinking about the concept in the frequency domain. There are two incident signals at the input, A_1 and at the output, A_2. This produces a frequency mixing effect on the magnitude and phase components. The coefficients produced are indexed as mixing terms of different orders, the higher the

order of the model the greater the number of mixing terms. In a linear system, the incident can be mapped to the response using 1st order coefficients. But in Power amplifiers, driving the device into compression generates non-linear effects which require higher mixing terms to relate signals. In essence, the higher the model order, the greater the ability of the model to accurately relate to response to the incident signal. This order selection is discussed in later paragraphs.

The big difference between the Cardiff model and X-parameters is the coefficient extraction method. X-parameter extraction relies upon specific load conditions to be met to extract coefficients, as described above. In the Cardiff model the extraction procedure is load independent. The typical extraction process involves performing a load-pull measurement around the optimum condition for output power. Each measured load condition generates a dataset of power waves, A and B. By performing a least squares fit, coefficients, K, can be generated that correlate the response wave to the injected wave.

Extensions of this basic formulation have been published incorporating parameters such as input power level [19] and DC bias [18]. Recent publications in this area have used artificial neural networks (ANN) techniques to extract the Cardiff model coefficients [20], [21] and [22].

A common challenge in all of these variations of the Cardiff model is the ability to extract a model that accurately represents the measured data. In this model, the operator can select the model mixing order which is related to how many coefficients are required to model a response. To evaluate the model order requirement, the order can be truncated and the model performance can be viewed. Typically, the model performance is validated by comparing the modelled and measured B-wave for a data point not used to generate the model. The Normalised Means Square Error (NMSE) between these values is evaluated. For the Cardiff model, the targetted NMSE is -30 dB. This is a trade-off between model accuracy and avoiding modelling measurement noise. A systematic review of model complexity was explored in [23] and shows that to obtain -30 dB a model order of 5-7 is required.

The Cardiff and the X-parameter models correlate incident and response measurement data through their coefficients and require no information or knowledge of device physics. Although the models are more insensitive to noise-related measurement errors due to extracting coefficients from large data sets using least squares fitting, the model's accuracy is still very sensitive to uncertainties or calibration errors. These errors will be directly propagated to the modelled coefficients. Therefore, to obtain an accurate model of a device, it is essential to have some knowledge of the measurement uncertainty and calibration error present in the measurement system. Currently, no literature discusses the propagation of measurement uncertainty and calibration error into the behavioural model.

In this section, some different device modelling techniques are highlighted, from black box techniques that use only the incident and reflected waves to represent the response of a device. The simplest was the look-up table modelling, which directly uses measurement data. Behavioural modelling attempts to model the measurement data using behavioural equations to add the ability for interpolation, which lowers measurement intensity. The physics-based approach is the state function models, which represent characteristics by equivalent circuits; these are the most encompassing models but are very intensive extraction procedures. This section showed that although there are many different techniques for extracting a device model, ultimately, the model can only be as accurate as the underlying data provided to it. This provides significant motivation to enhance the scope of measurement systems, to produce more data for extracting and validating models, and to enhance measurement accuracy so that the extracted models become inherently more accurate and reliable.

References

[1] I. Angelov, H. Zirath, and N. Rosman. "A New Empirical Nonlinear Model for HEMT and MESFET Devices". In: *IEEE Trans. Microw. Theory Techn.* 40.12 (1992), pp. 2258–2266.

[2] I. Angelov, L. Bengtsson, and M. Garcia. “Extensions of the Chalmers Nonlinear HEMT and MESFET Model”. In: *IEEE Trans. Microw. Theory Techn.* 44.10 (1996), pp. 1664–1674.

[3] Keysight Technologies. *EE HEMT1*. URL: qthelp://ads.2024update1/doc/ccnld/EE_HEMT1.html#EEHEMT1-reference2.

[4] S. Chalermwisutkul. “Large Signal Modeling of GaN HEMTs for UMTS Base Station Power Amplifier Design Taking into Account Memory Effects”. PhD thesis. RWTH Aachen University, 2007.

[5] W.R. Curtice. “A MESFET Model for Use in the Design of GaAs Integrated Circuits”. In: *IEEE Trans. Microw. Theory Techn.* 28.5 (1980), pp. 448–456.

[6] P.C. Canfield, S.C.F. Lam, and D.J. Allstot. “Modeling of Frequency and Temperature Effects in GaAs MESFETs”. In: *IEEE Journal of Solid-State Circuits* 25.1 (1990), pp. 299–306.

[7] I. Angelov, L. Bengtsson, and M. Garcia. “Temperature and Dispersion Effect Extentions of Chalmers Nonlinear HEMT and MESFET Model”. In: *IEEE MTT-S Int. Microw. Symp. (IMS)*. 1995, 1515–1518 vol.3.

[8] C. Lautensack, S. Chalermwisutkul, and R. H. Jansen. “Modification of EEHEMT1 Model for Accurate Description of GaN HEMT Output Characteristics”. In: *Asia-Pacific Microw. Conf.* 2007, pp. 1–4.

[9] P. Luo, O. Bengtsson, and M. Rudolph. “Novel Approach to Trapping Effect Modeling Based on Chalmers Model and Pulsed S-parameter Measurements”. In: *IEEE Eur. Microw. Integr. Circuits Conf. (EuMIC)*. 2016, pp. 157–160.

[10] Wenyuan Zhang et al. “An Angelov Large-Signal FET Model Up To 67 GHz”. In: *IEEE Trans. on Electron Devices* 66.6 (2019), pp. 2577–2582. DOI: 10.1109/TED.2019.2913395.

[11] Iltcho Angelov et al. “On the Large Signal Evaluation and Modeling of GaN FET”. In: *IEICE Trans. Electron.* 93-C.8 (2010), pp. 1225–1233. DOI: 10.1587/TRANSELE.E93.C.1225.

[12] D.E. Root et al. “X-parameters: The New Paradigm for Measurement, Modeling, and Design of Nonlinear RF and Microwave components”. In: *Microw. Eng. Eur.* 12 (2008), p. 16.

[13] H. Qi, J. Benedikt, and P. J. Tasker. “Nonlinear Data Utilization: From Direct Data Lookup to Behavioral Modeling”. In: *IEEE Trans. Microw. Theory Techn.* 57.6 (2009), pp. 1425–1432.

[14] J. J. Bell. “Input Harmonic and Mixing Behavioural Model Analysis”. PhD thesis. Cardiff University, 2014.

[15] J. Verspecht et al. “Extension of X-Parameters to Include Long-Term Dynamic Memory Effects”. In: *IEEE MTT-S Int. Microw. Symp. (IMS)*. 2009, pp. 741–744.

[16] D. E. Root et al. “Scaling of X-parameters For Device Modeling”. In: *IEEE MTT-S Int. Microw. Symp. (IMS)*. 2012, pp. 1–3.

[17] D. E. Root et al. “Frequency-Scalable Nonlinear Behavioral Transistor Model From Single Frequency X-Parameters Based on Time-Reversal Transformation Properties”. In: *ARFTG Microw. Meas. Conf.* 2015, pp. 1–7.

[18] E. M. Azad et al. “New Formulation of Cardiff Behavioral Model Including DC Bias Voltage Dependence”. In: *IEEE Microw. and Wireless Compon. Lett.* 32.6 (2022), pp. 607–610.

[19] M. R. Moure et al. “Direct Extraction of an Admittance Domain Behavioral Model From Large-Signal Load-Pull Measurements”. In: *IEEE MTT-S Int. Microw. Symp. (IMS)*. 2017, pp. 1057–1060.

[20] M. Tian et al. “A Novel Cardiff Model Coefficients Extraction Process Based on Artificial Neural Network”. In: *IEEE Top. Conf. on RF/Microw. Power Amplifiers for Radio and Wireless Appl. (PAWR)*. 2023, pp. 1–3.

[21] M. Tian et al. “Artificial Neural Network Nonlinear Transistor Behavioral Models: Structure and Parameter Determination Process Based on the Cardiff Model”. In: *IEEE Trans. Microw. Theory Techn.* (2024), pp. 1–15.

[22] W. Yuan, M. Tian, and J.J. Bell. “Implementation Efficiency Comparison Between ANN and the Cardiff Model in ADS”. In: *Int. Workshop on Integr. Nonlinear Microw. and Millimetre-Wave Circuits (INMMIC)*. 2023, pp. 1–4.

[23] M. Rocio Moure et al. “A Systematic Investigation of Admittance Domain Behavioral Model Complexity Requirements”. In: *IEEE MTT-S Latin Am. Microw. Conf. (LAMC)*. 2018, pp. 1–4. DOI: 10.1109/LAMC.2018.8699054.

Chapter 5

Millimetre-wave Harmonic Source/Load-pull Measurement System

5.1 Introduction

The proliferation of mm-wave power amplifiers has been primarily driven by the demand for satellite communication systems offering higher data rates, extensive coverage areas, and the ability to support high user loads. Examples include Low Earth Orbit (LEO) systems operating in the Ka-band (26–40 GHz) and the rising demand for high-throughput satellite (HTS) communication systems in the W-band (75–110 GHz). These advancements have been enabled by progress in compound semiconductor technologies, which facilitate the combination of high-power and high-frequency operation.

Traditionally, GaAs technology has dominated the satellite communication market due to its high electron mobility and technological maturity. However, in recent years, GaN technology has gained prominence. Its high electron mobility, wide bandgap, and high breakdown voltage allow GaN devices to achieve significantly higher output power for a given device size than GaAs.

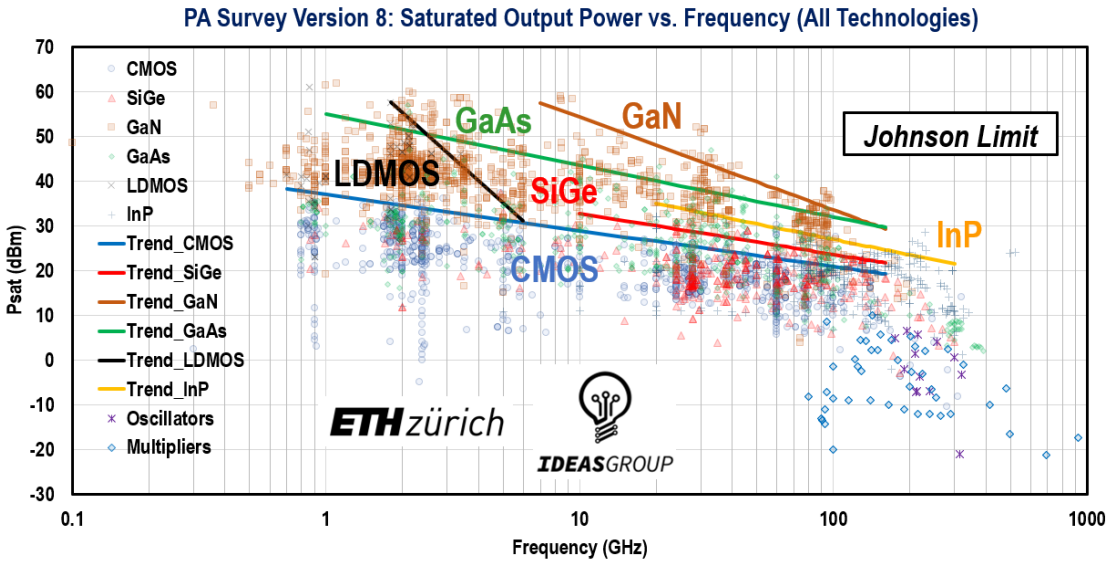

Figure 5.1: Power amplifier survey by ETH Zurich from November 2024 [1]. This shows saturated output power versus frequency for different semiconductor technologies .

The significant proliferation of this technology has led to a surge in mm-wave power amplifier designs, achieving performance levels that rival those of microwave frequency amplifiers; these trends are detailed in the power amplifier survey from ETH Zurich in Figure 5.1. The figure plots data points of published power amplifier designs in different technologies, each benchmarked by their material, output power and frequency of operation. LDMOS technology has had significant use in base station power amplifiers due to its power density and cost; however, it cannot compete with technologies at mm-wave. SiGe and CMOS technologies have shown performance well into the hundreds of GHz, but the trend shows that the devices typically have low saturated output power. GaAs and GaN technologies offer huge performance benefits in terms of output power with PA's demonstrating 35 dBm output power at 100 GHz. InP is an expensive technology, but its benefits are the very high maximum operational frequency, up to 500 GHz.

The density of data points in the mm-wave range, particularly from 20 to 100 GHz, highlights the demand for mm-wave PAs. This, in turn, presents numerous challenges, one of which is the availability of measurement systems capable of accurately characterising these devices.

In the S-parameter measurement space, external test sets utilising frequency conversion techniques allow for single sweep measurements up to 220 GHz [2].

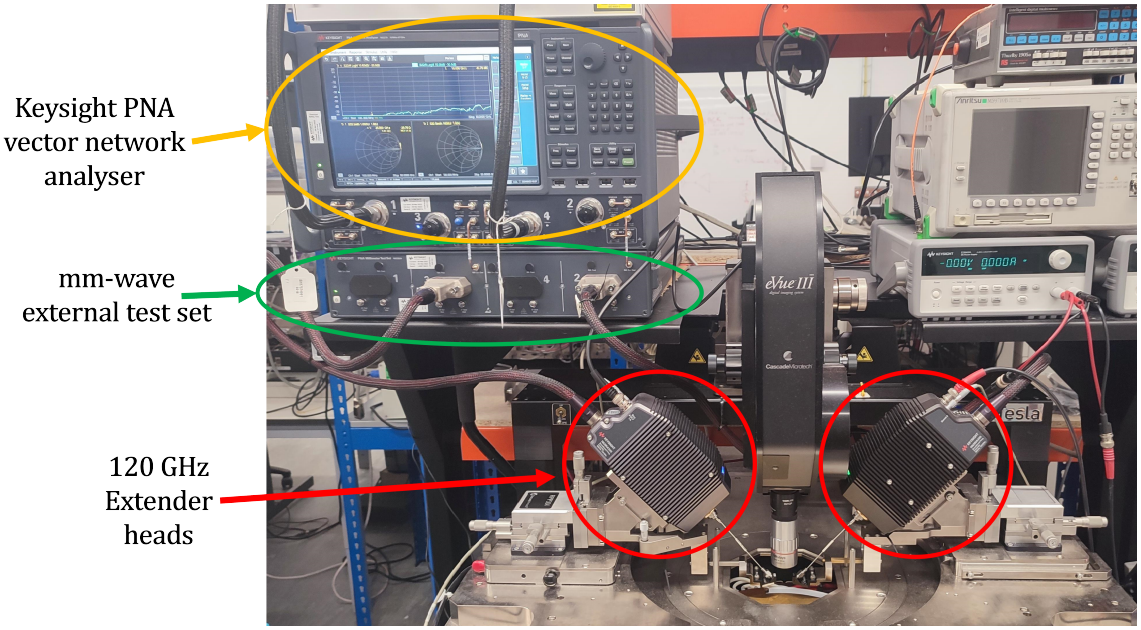

Figure 5.2: on-wafer S-parameter measurement system using the Keysight extender modules for frequencies up to 120 GHz.

A commercial example of an S-parameter measurement system that utilises frequency conversion techniques to achieve measurement up to 120 GHz is the Keysight N5293AX03 extender modules [3], which are connectorised units that are configured as external test set and linked to the base VNA. This setup is shown in Figure 5.2, with the modules integrated into an on-wafer measurement system.

Other solutions exist to extend frequency performance beyond 220 GHz, typically employing banded waveguide modules from suppliers such as VDI [4] and Eravant [5]. While these waveguide-based systems achieve maximum frequencies extending into the terahertz range, their limited bandwidth, dictated by the high-pass nature of waveguides, restricts their versatility.

However, these systems are not well-suited for performing large-signal load-pull measurements. The primary limitation lies in their lack of reconfigurability. In large-signal measurement systems, reconfigurability is critical and is achieved by integrating external directional couplers near the measurement reference plane. This allows changes to the source and load fixtures without affecting the system calibra-

tion. Such flexibility is essential for performing absolute calibration or incorporating additional fixtures—such as bias tees, circulators, and external amplifiers—necessary for measuring devices operating deep into compression.

Various systems capable of performing load-pull measurements in the mm-wave spectrum have been reported in the literature, employing a range of methodologies. Early systems employed scalar techniques to perform active load-pull up to 40 GHz [6]. Even in recent years, scalar systems have been used to demonstrate W-band measurements [7].

Other systems adopt vector-receiver methods. For instance, researchers at the University of California Santa Barbara (UCSB) have reported both passive and active load-pull systems utilizing frequency conversion techniques for fundamental load-pull at W-band [8], [9]. Similarly, the millimetre-wave group at ETH Zurich has implemented a closed-loop active load-pull system for W-band measurements using frequency conversion techniques [10]. Additionally, the authors of [11] explored and implemented methods to extend commercial VNAs using frequency extenders for load-pull measurements.

Situated at Cardiff University is a state-of-the-art load-pull system developed from a collaboration between Focus Microwaves and Rohde & Schwarz and it is a first of its kind capable of operating up to 110 GHz. This system is based on frequency conversion techniques, can perform harmonic source/load-pull measurements across a single sweep, and offers waveform measurement functionality.

This chapter describes the authors contributions to this prior developed system. It expands upon the work in [12] and describes in detail the configuration and demonstrates the calibration and verification procedures necessary to achieve highly accurate and reliable measurements at Ka-band upto the third harmonic as well as fundamental frequency measurements to 110 GHz.

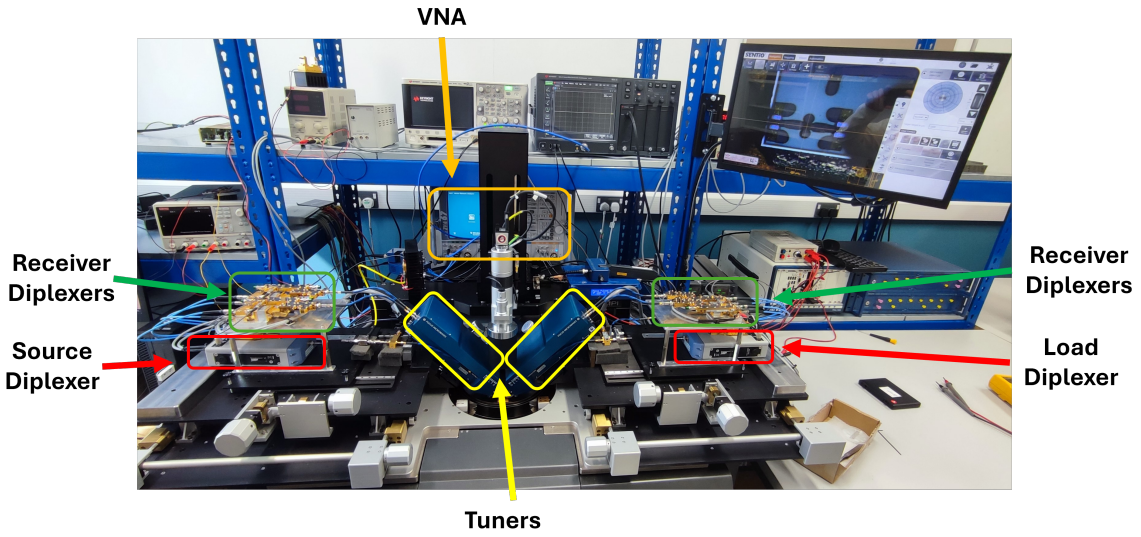

Figure 5.3: The 110 GHz passive source/load-pull measurement system.

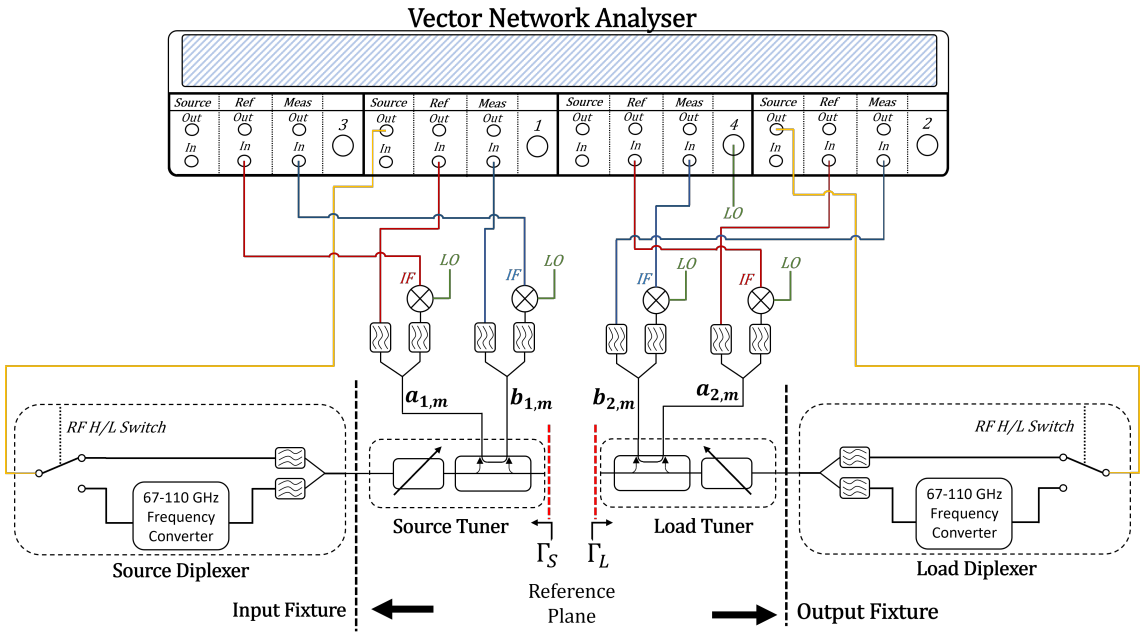

Figure 5.4: mm-wave on-wafer large signal characterisation system. The equipment shown are the Focus Microwave M-110240 passive tuners, the Rohde&Schwarz waveguide diplexer, the ZVA 67 vector network analyser, the ZD-110 source/load diplexer, and the ZRX110L receiver. The on-wafer probes are MPI T110A GSG100.

5.2 System Description

Figures 5.3 and 5.4 present an image and a generalized diagram of the system, respectively. The system is based on the ZVA67 vector network analyser with four measurement channels, passive tuners and frequency conversion modules.

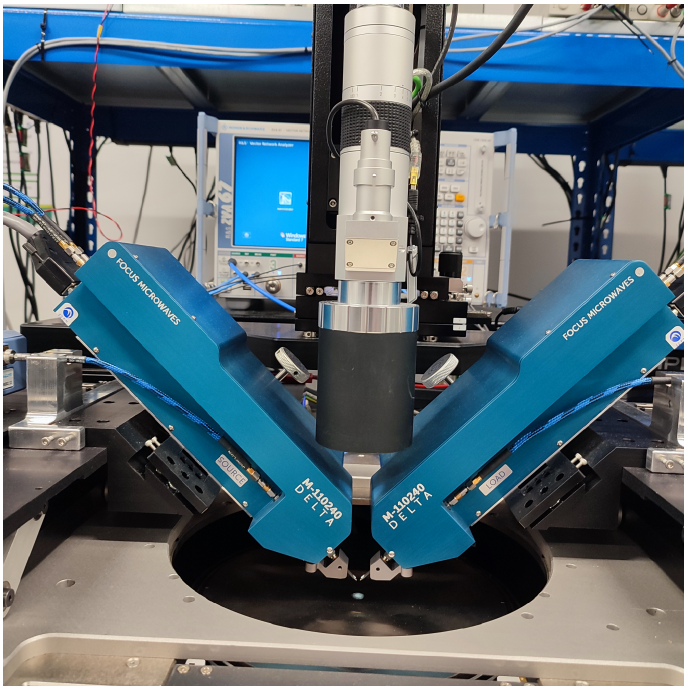

Figure 5.5: The tuner and probes on the measurement system. Focus Microwaves (M-110240) Delta tuners and 110 GHz MPI GSG probes.

Figure 5.5 shows the 24–110 GHz Focus Microwaves (M-110240) Delta tuners, which are coaxial triple-slug harmonic tuners integrated with a directional coupler to maximize the tuning range. Attached to the tuners are MPI 110 GHz on-wafer GSG probes. A computer-controlled microscope is also included to facilitate precise probing of the measurement sample.

As illustrated in Figure 5.4 and the image in Figure 5.6, the system's source and receiver paths are configured for generating and detecting RF waves.

For the source, the VNA is connected to the Rohde & Schwarz (ZD-210) switched diplexer module via a 1.85 mm coaxial cable and a control cable. Within this module is a RF switch, for frequencies below 67 GHz, the VNA triggers the diplexer module to switch to a through state where the RF signal passes through the unit to the

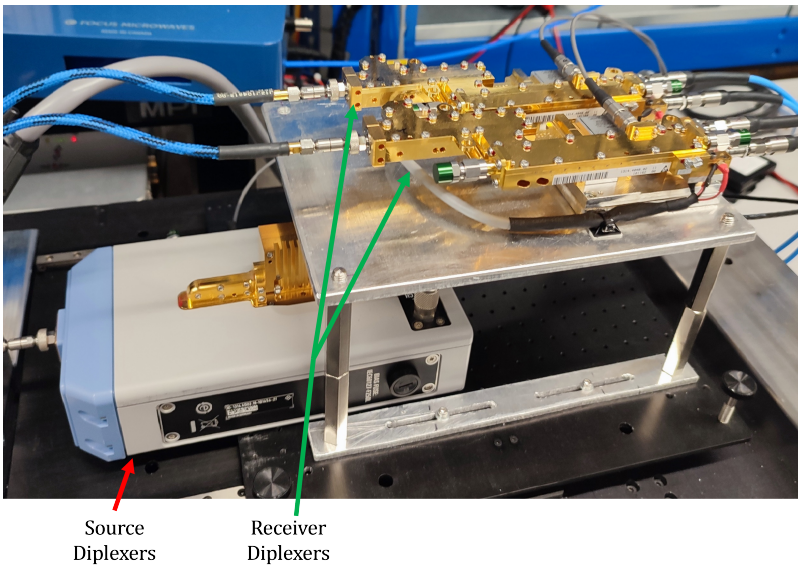

Figure 5.6: The source and receiver diplexers on the load-side of the measurement system.

DUT, with loss increasing proportional to signal frequency. For frequencies above 67 GHz, the VNA triggers the switch for the RF signal to be diverted, up-converted and amplified to the desired frequency. The difference in source power across the full frequency span of the system can be levelled during the source levelling procedure described in the following sections.

To capture the measured waves, the directional couplers in the tuners sample the forward and reverse travelling waves. These signals are routed through a coaxial-to-waveguide transition and into a diplexer. For frequencies below 67 GHz, the sampled waves are sent directly to the reference and measurement receivers on ports one and two of the VNA. For frequencies above 67 GHz, the waves are down-converted by a mixer, utilizing a common LO from port 4. The VNA then measures the down-converted waves at the reference and measurement receivers on ports three and four.

Details of waveform measurement will be provided later in this section after the calibration procedure is discussed.

5.3 Calibration Procedure

This section outlines the system's large signal calibration procedure for performing multi-harmonic load-pull measurements. Due to the system's complexity and frequency range, particular attention is paid to the verification steps conducted after each calibration stage to ensure the accuracy and reliability of the measurements.

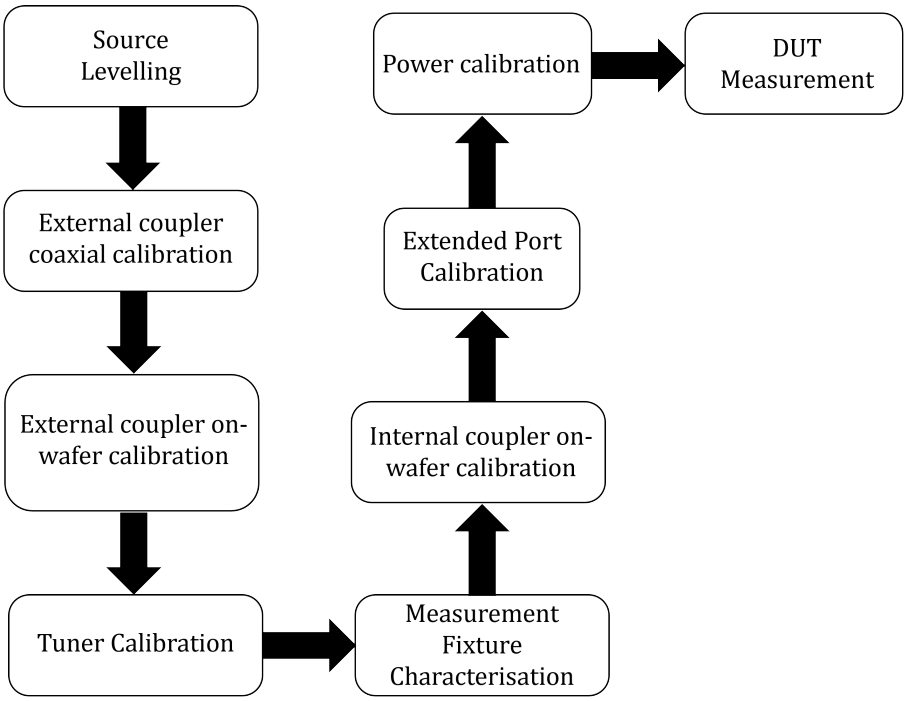

Figure 5.7: Calibration procedure flow diagram.

Figure 5.7 illustrates the basic calibration process for performing load-pull measurements. It follows a standard procedure for passive load-pull system calibration, as detailed in Section 3.2.1, with the addition of source levelling and measurement fixture characterisation.

5.3.1 Source Levelling

Source levelling is necessary for frequencies above 67 GHz due to the dual-band nature of the source, which consists of a straight-through path and an up-converter. The output power of the source varies significantly with frequency. Below 67 GHz, the output power decreases steadily as a function of frequency, reaching its lowest

point just before the up-converter kicks in. Once the up-converter kicks in, the output power peaks at approximately 10 dBm at the coaxial port of the source. Source levelling addresses these variations and ensures consistent power during calibration across the entire frequency range.

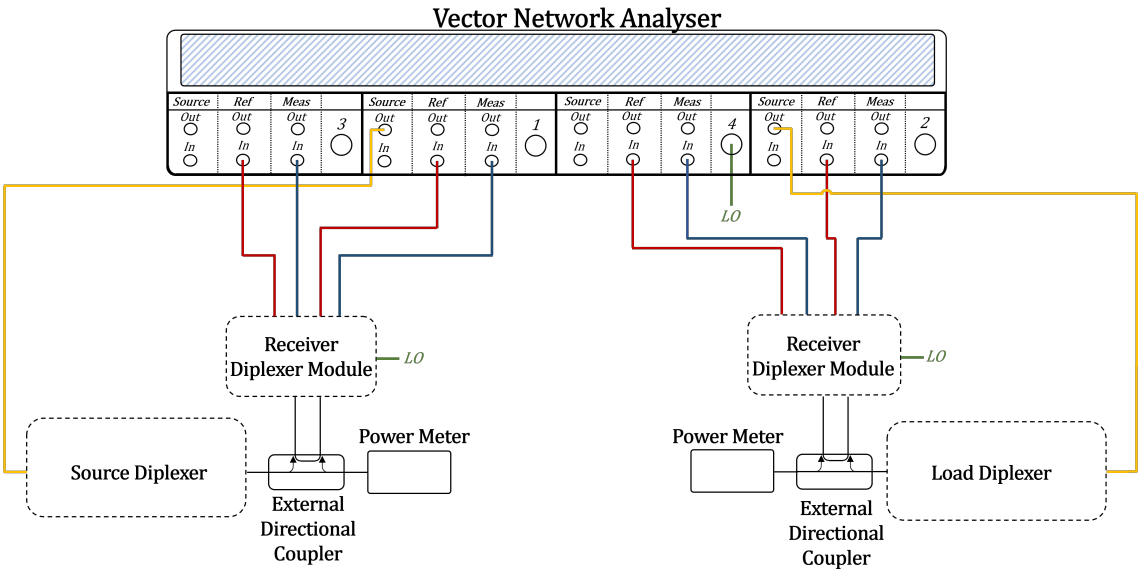

Figure 5.8: Source levelling block diagram. The levelling is performed using a 110 GHz power meter and an external 110 GHz directional coupler.

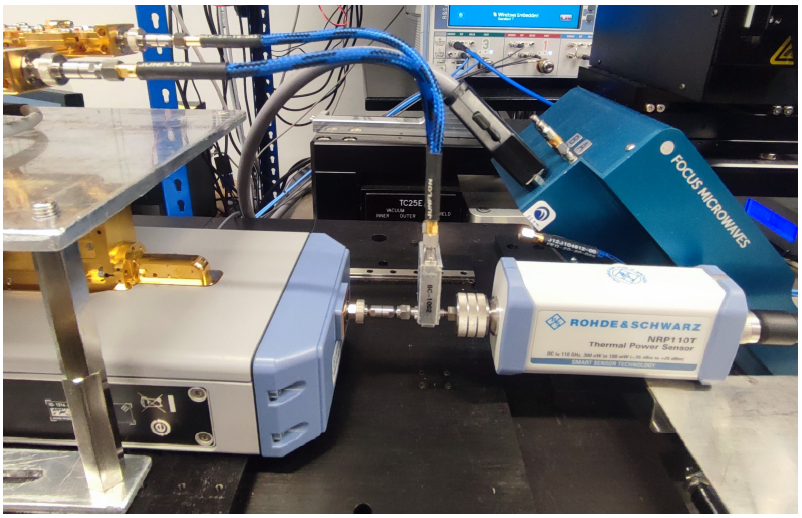

Figure 5.9: Setup showing the power meter connected at the source levelling reference plane.

The system is configured according to Figures 5.8 and 5.9. A power meter is positioned after the source diplexer and fixed to an external directional coupler in this configuration. The user selects a desired power level at the power meter

reference plane. The VNA sweeps the frequency, and the power is recorded at the power meter. An iterative algorithm adjusts the source power incrementally until the measured power matches the user-defined target. The source power settings are stored in the VNA as a frequency-dependent lookup table.

To verify the procedure, the VNA source power is set to the power used for levelling. The frequency is swept, and the measured power is compared to the target to evaluate the accuracy.

Although the difference between the targeted and measured power is not critical, it is important to ensure that calibration is performed with a levelled input power, particularly for harmonic measurements. In this system, for harmonic measurements where the fundamental frequency exceeds 22 GHz, the VNA generates the fundamental source power, while the third harmonic is produced as an up-converted signal by the source diplexer/amplifier. This leads to a significant variation in the power at the reference plane. A measurement performed without source levelling applied showed that, with the VNA source power set to its maximum of 10 dBm, the measured power at the source levelling reference pane ranged from -16 to 10 dBm across the 26-110 GHz frequency range. As the frequency increases from 26 GHz, the measured power decreases, reaching its minimum just before the multiplier kicks in. The levelling process enables the user to maintain a constant power level during the calibration procedure, particularly at frequencies near where the multipliers become active, where the power is lowest. This process ensures that the power can be set to its maximum, preventing further degradation of the dynamic range.

5.3.2 Tuner Characterisation and Calibration

The calibration process follows the standard passive load-pull procedure outlined in Section 3.2.1. The objective of the following three sections is to calibrate the passive tuner across all its impedance states.

External Coupler Coaxial Calibration

At this stage, the system is configured as shown in Figures 5.8 and 5.10, with the power meter disconnected. Using the unknown thru, open, short, and match (UOSM) method, a two-port coaxial calibration is performed at the external couplers. This approach moves the reference plane to the external couplers, establishing a baseline reference for characterizing the tuners.

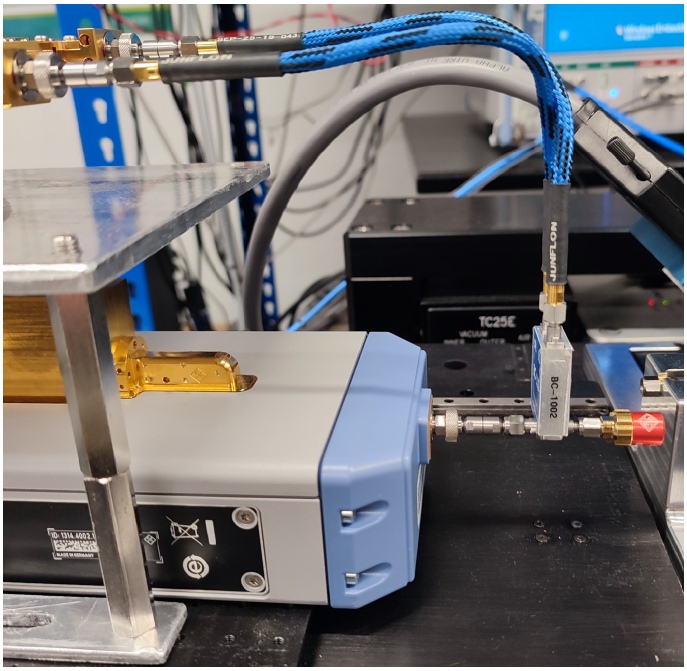

Figure 5.10: External coaxial calibration setup. Showing the short standard connected to the external directional coupler.

The R&S ZV-Z210 1 mm coaxial calibration kit is for this calibration. This kit has been characterised using a reference system, with the reflection coefficients of each standard provided in a lookup table.

Ideally, to verify a calibration, a test structure whose S-parameters are fully known should be used and compared, although for this case, we do not have any such test structures; due to no alternative, a sub-optimal means of verification was conducted by performing a measurement of the calibrated standards and comparing with the standard definitions. As shown in Figure 5.11, a UOSM calibration was performed, and each standard was subsequently measured. The error coefficients were re-computed when a standard was re-connected for evaluation to reduce the

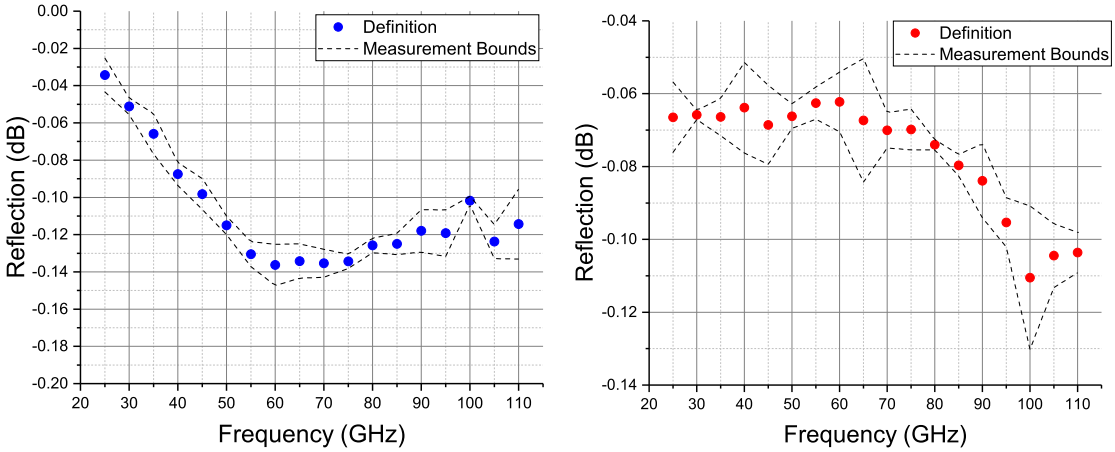

(a) Open

(b) Short

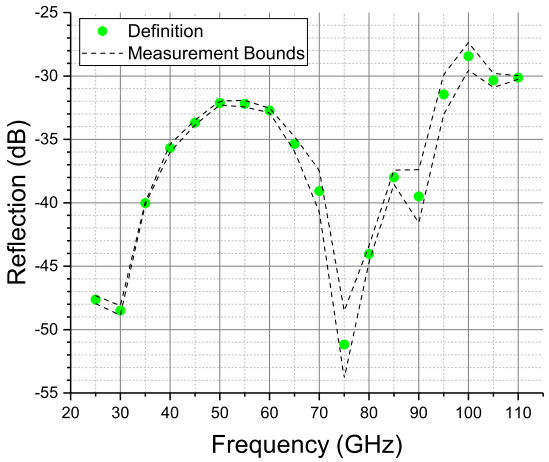

(c) Match

Figure 5.11: Reflection in decibels of the standard definition and the error bounds from performing UOSM calibration ten times, remeasuring each standard after calibration.

effect of connector repeatability. This process was repeated ten times, with the error bounds indicating the worst-case measurement. The average error vector between the short standard definition and the measured values across the ten calibrations was 0.02, 0.1 and 0.15% for 30, 60 and 90 GHz, respectively.

At these frequencies, the repeatability of the connection is crucial to obtain an accurate calibration. The same investigation was performed, but the standard was disconnected and re-connected this time before measurement. This showed a significant increase in the average error vector between the short standard definition and the measured values across ten calibrations; this increased to 0.3, 0.55 and 1.1% for 30, 60 and 90 GHz, respectively.

External coupler on-wafer calibration

Following the UOSM calibration, which brought the reference plane to the external directional couplers, the final stage of tuner characterisation is to calibrate to the end of the probe tips or the centre of a thru standard for TRL calibration. This allows for a complete characterisation of the source and load tuner.

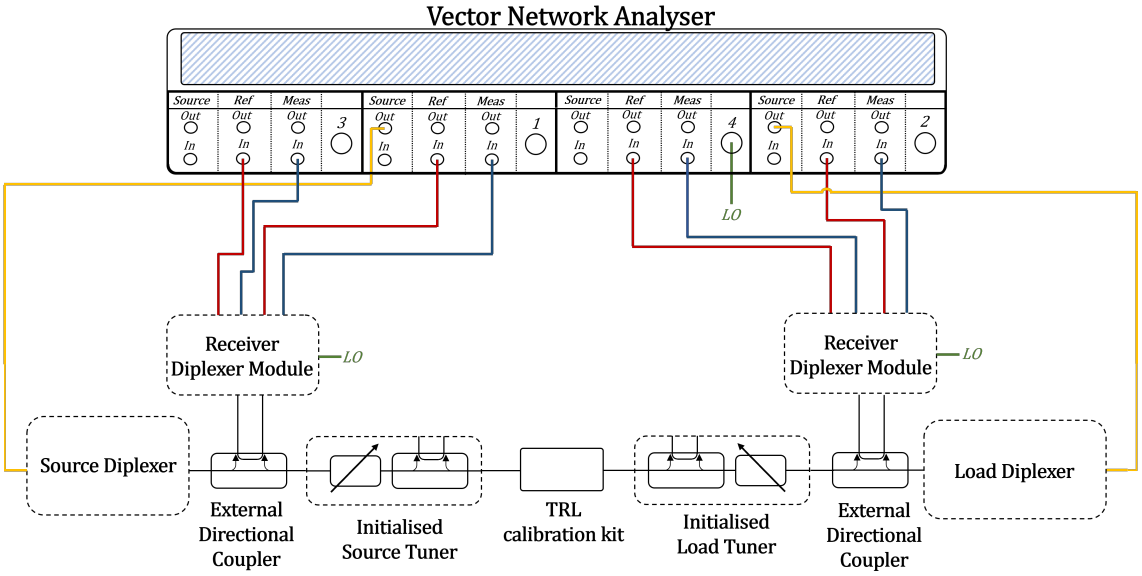

Figure 5.12: External coupler on-wafer calibration configuration diagram.

The system is configured as shown in Figure 5.12, with the external coupler connected to the tuners via a 1 mm coaxial cable, and a TRL calibration is performed

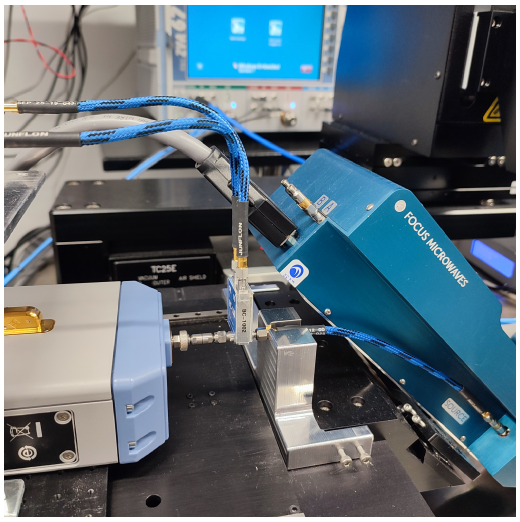

(a) Connection of external coupler to the source tuner.

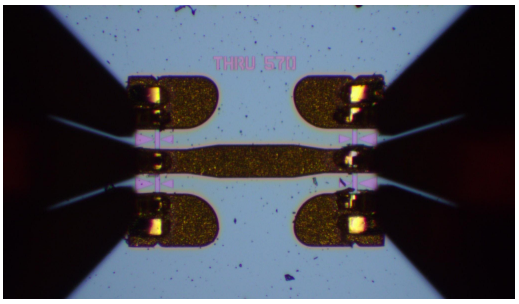

(b) Probing of an on-wafer thru standard

Figure 5.13: External coupler on-wafer calibration configuration images.

using on-wafer probes, as illustrated in Figure 5.3.2. The tuners are initialised, which positions the tuner slugs in a zeroed state defined by the software to ensure a consistent reference condition. This calibration establishes the reference plane for tuner characterisation, enabling the software to correlate the load reflection coefficient with a specific tuner slug position, as determined by the tuner calibration procedure, which is the following stage.

The TRL calibration will generate the S-parameter error boxes representing the source and load tuner. These error boxes can be used to perform the tuner calibration. To verify this calibration, each standard can be re-probed, if available; the optimal verification of any calibration is to probe a known standard that has not been used in calibration. Another method is the NIST calibration tool [13], which can be used to quantify measurement uncertainty. Both methods are susceptible to errors relating to standard definition, system characterisation and fabrication tolerances.

Tuner calibration

The tuner calibration is performed by selecting a density of reflection coefficient points, which determines the step size of the stepper motor, controlling the slug's

vertical and horizontal positions. The calibration procedure iterates through each combination of tuner slug positions in magnitude and phase for each frequency, performing an S-parameter measurement at every position to determine the actual reflection coefficient presented to the device. A two-port S-parameter matrix is generated for each tuner position and is used during harmonic measurements as part of moving the phase measurement reference plane from the oscilloscope to the probe tips; this process is discussed in detail in Section 5.3.6.

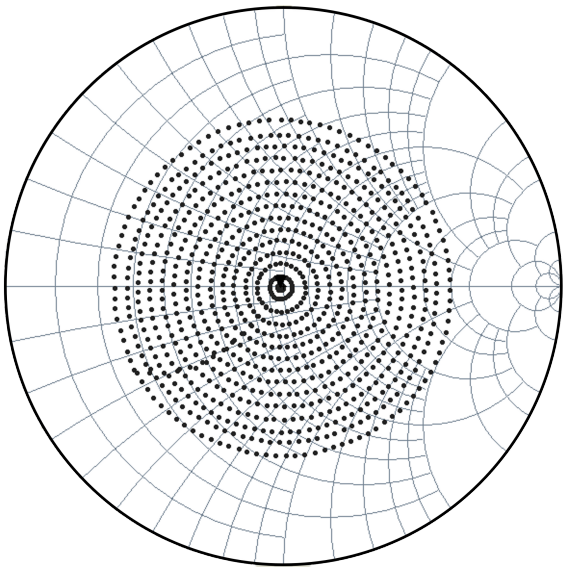

Figure 5.14: Calibrated reflection coefficient conditions for a single slug of the load tuner at 27.5 GHz.

Figure 5.14 shows the calibrated load reflection coefficients for 27.5 GHz. This process involves a trade-off between the number of calibrated impedance conditions and the calibration time. This system uses both the source and load tuners, each containing three slugs. For example, calibrating 300 slug positions for both tuners at a single frequency takes approximately 1.5 hours when using an IF bandwidth of 50 Hz.

5.3.3 Measurement fixture characterisation

To continue with the calibration procedure, the coaxial cables connecting the tuners to the external directional couplers are disconnected before the external directional couplers are removed from the setup; this configuration is shown in Figure 5.15 and

can be used to characterise the measurement fixtures.

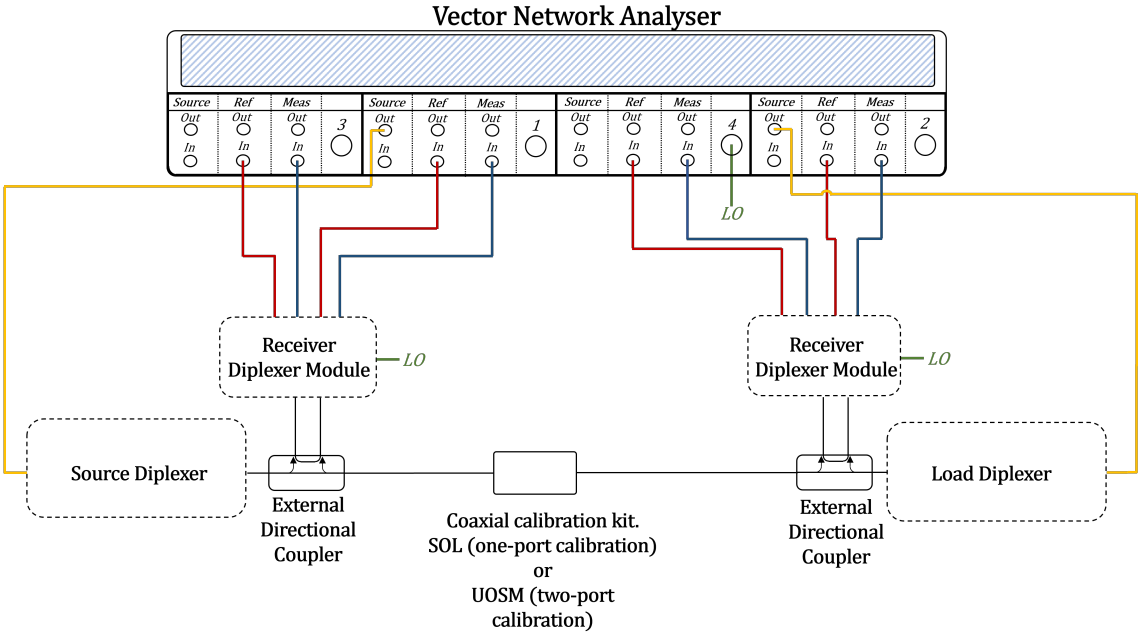

Figure 5.15: Measurement setup diagram for measurement fixture characterisation.

The VNA state is saved for recall, and the instrument is preset; a one-port (SOL) or two-port (UOSM) coaxial calibration can be performed to allow for the characterisation of coaxial measurement fixtures. Additional components, such as bias-tees, circulators, and amplifiers, are added to the source and load tuners for device measurements. These additional components present a different reflection coefficient to the tuners than the source module. This mismatch cascades with the reflection coefficient imposed by the tuner, resulting in a discrepancy between the imposed and measured load reflection coefficients. To address this, the reflection coefficient of the fixtures is characterised and compensated for.

An example of a set of source fixtures for the measurement of a Ka-band device is shown in Figure 5.16. When performing the tuner calibration, the tuner S-parameters are determined when driven by the source diplexer with a specific Γ_S, when measuring a device this source module is disconnected and an amplifier, followed by a circulator, and bias-tee are added which present a different Γ_S to the tuner. This results in a slight error between the actual imposed source reflection coefficient, measured by directional couplers inside the tuners and the reflection co-

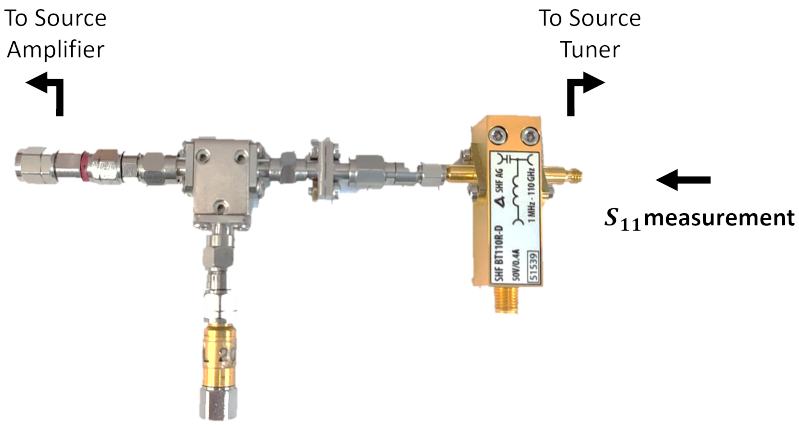

Figure 5.16: Additional source fixtures required for the measurement of device operating at Ka-band. It consists of a circulator and a bias-tee.

efficient using the tuner calibration data. This has the largest effect if the fixtures are reflective. To characterise this network, a one-port S-parameter measurement is performed by looking into the bias-tee. This S-parameter measurement is used to correct the source tuner calibration.

This stage is also essential for obtaining accurate waveform measurements. During waveform measurements, the phase meter determines the relationship between the harmonics; however, these measurements are taken at a point away from the measurement reference plane. The two-port S-parameters of the fixtures between the measurement reference plane and the phase meter are characterised to account for this. The configuration for waveform measurements is discussed in detail in Section 5.3.6.

5.3.4 Internal coupler on-wafer calibration

At this stage, the tuner has been characterised and calibrated at its impedance states. An internal coupler on-wafer calibration is performed to shift the measurement reference plane from the VNA receivers to the centre of an on-wafer thru standard as part of the TRL calibration process.

The setup, illustrated in Figure 5.17, involves removing the external directional couplers. The source and load diplexers are then connected to the tuners via a 1 mm coaxial cable, while the internal couplers of the tuners are connected to the receiver

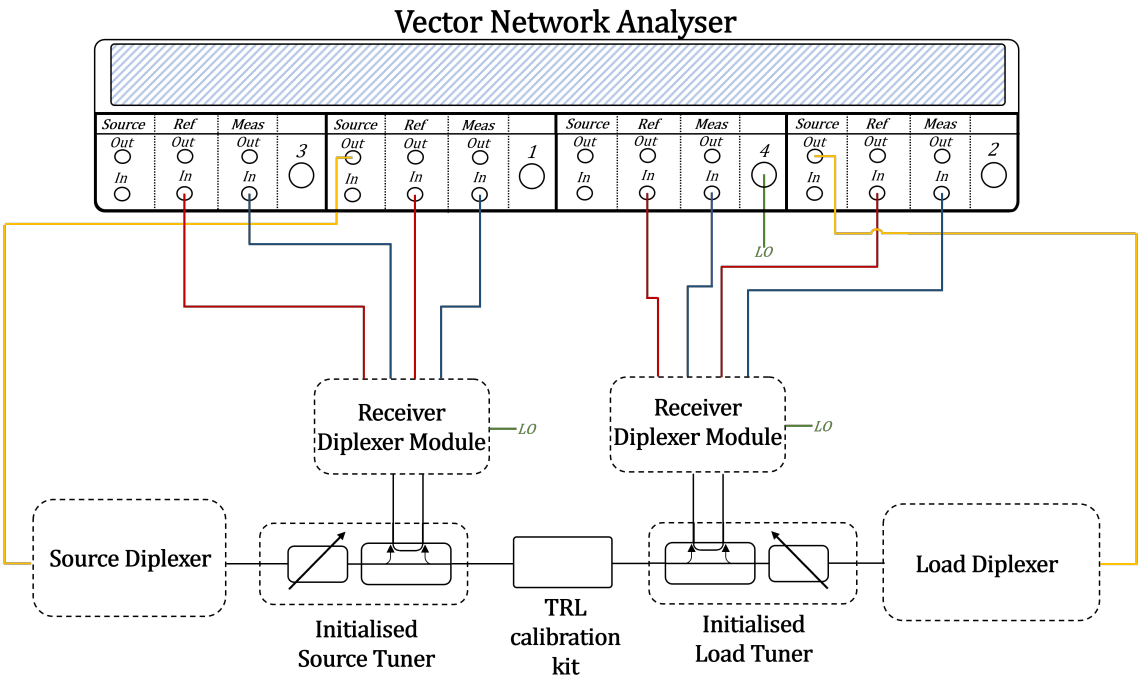

Figure 5.17: Internal coupler calibration setup diagram.

diplexer modules.

Standard TRL calibration verification procedures can be performed to verify this calibration stage, such as using the NIST calibration software [13] or a known standard.

5.3.5 Absolute Calibration

The absolute calibration consists of an extended and a power calibration. The goal of this stage is to perform an s-parameter calibration to a position as close to the center of the probes as possible but also be at a location where a power meter can be fixed. The power meter measures the power at that given reference plane. This power is compared with the power measured by the VNA. The ratio of these two is used to scale the calibration error terms, allowing for accurate power measurements at the reference plane without requiring a fixed power meter. The theory and maths behind the absolute calibration stage is described in the calibration literature review in Section 3.2.1. This system uses a phase meter rather than a harmonic phase reference, so it does not require a phase calibration.

Extended Calibration

The extended calibration follows the traditional calibration procedure as described in Section 3.2.1.

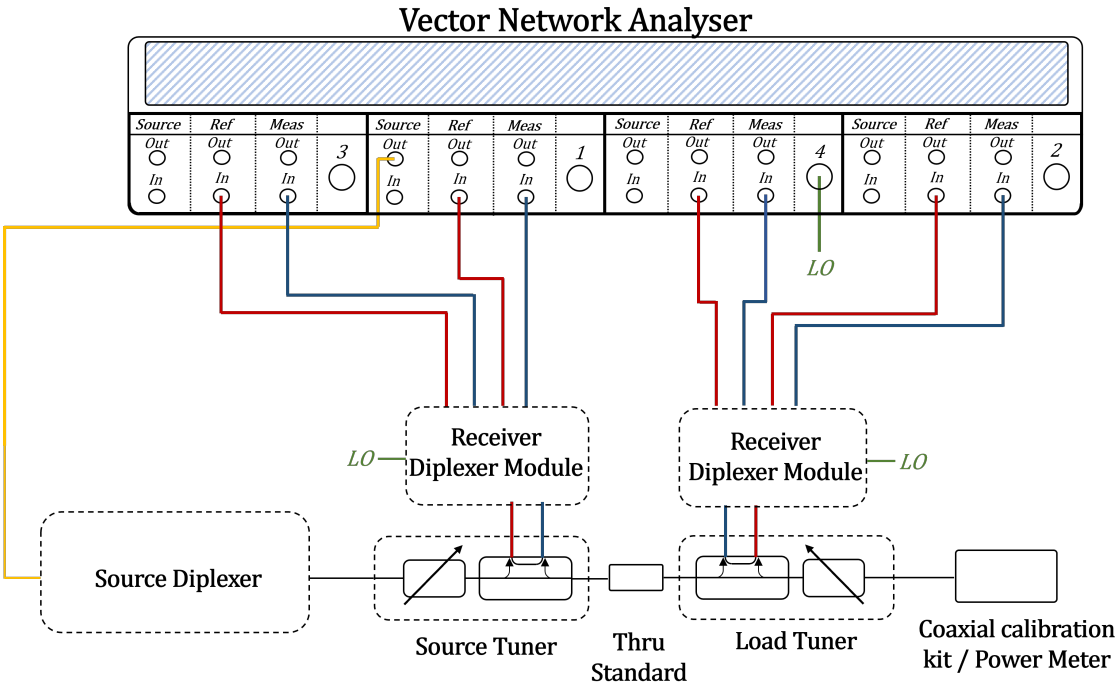

Figure 5.18: Extended and power calibration setup diagram.

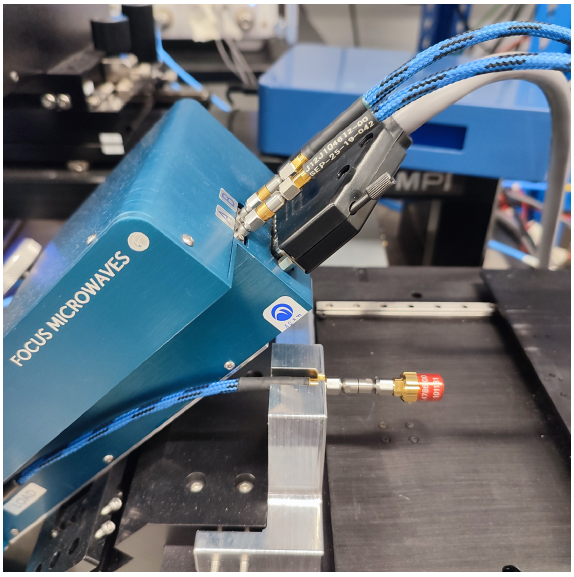

Figure 5.19: Connection of the R&S ZV-Z210 short standard to the extended port plane.

The system is configured as shown in Figure 5.18. A one-port coaxial calibration

standard is connected at the extended port plane, as shown in Figure 5.19. This is followed by the on-wafer probes landing on a thru standard on the target device substrate. The process establishes a common reference plane between the one-port calibration and the power meter measurement, enabling the calculation of the power scaling coefficient at the centre of the zero-length thru.

Power Calibration

Power calibration is performed by connecting a coaxial power meter at the extended port reference plane and probing the on-wafer thru standard.

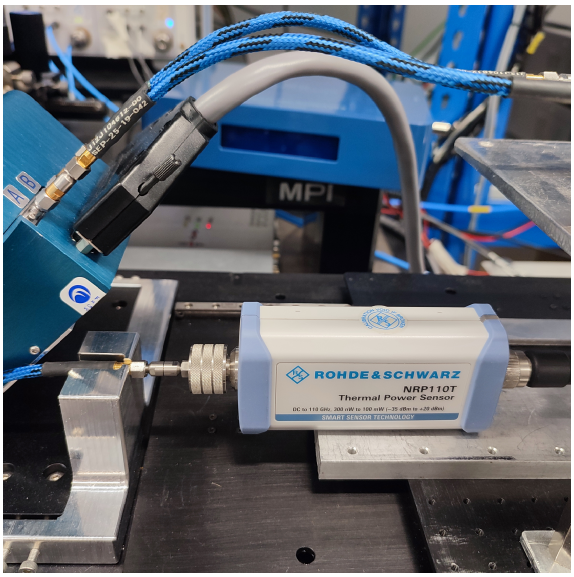

Figure 5.20: Connection of the R&S NRP110T power meter to the extended port plane for power calibration.

The reflection coefficient at the centre of the zero-length thru is determined using the internal coupler calibration coefficients, and the reflection coefficient at the extended port plane is also known. Therefore, the power meter measurement result can be normalised using these two reflection coefficients to obtain the power at the centre of the zero-length thru. A ratio of the measured power at the VNA to the measured power allows for calculating the absolute scaling term, e_{10}.

The accuracy of the scaling term is determined by the power meter. The RF power meter used in this work is the R&S 110 GHz thermal power meter. The accuracy of thermal RF power meters typically falls within the range of ± 0.5 dB.

For the power meter used in this work, the maximum uncertainty of a brand-new meter is ±0.3 dB [14].

The same configuration is used to perform a self-consistency check of this calibration stage. The tuners are set to the initialised position, the internal calibration coefficients are loaded onto the VNA, scaled by the power coefficient, and a measurement is performed. The S-parameters for the load tuner are used to move the reference plane of the power meter measurement to the centre of the zero-length through. This result is compared with the measurement from the calibrated VNA.

5.3.6 Configuration for waveform measurements

A phase meter was used for harmonic phase alignment due to the limited commercial availability of 100 GHz HPR modules when the system was first designed. The phase meter is a Keysight DCA-X N1000A oscilloscope with the N1046A 100 GHz sampling module.

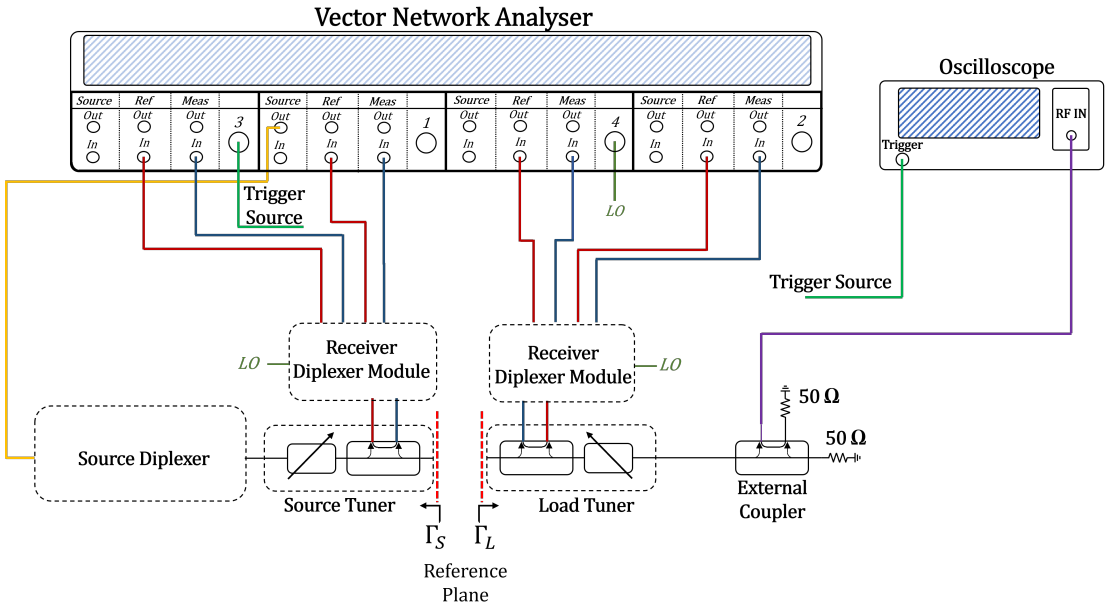

Figure 5.21: Configuration diagram for waveform measurements.

The diagram for waveform measurements is shown in Figure 5.21, and an image of the load-side fixtures are shown in Figure 5.22. A 110 GHz directional coupler is connected to a 1 mm coaxial cable from the load tuner, which samples the output

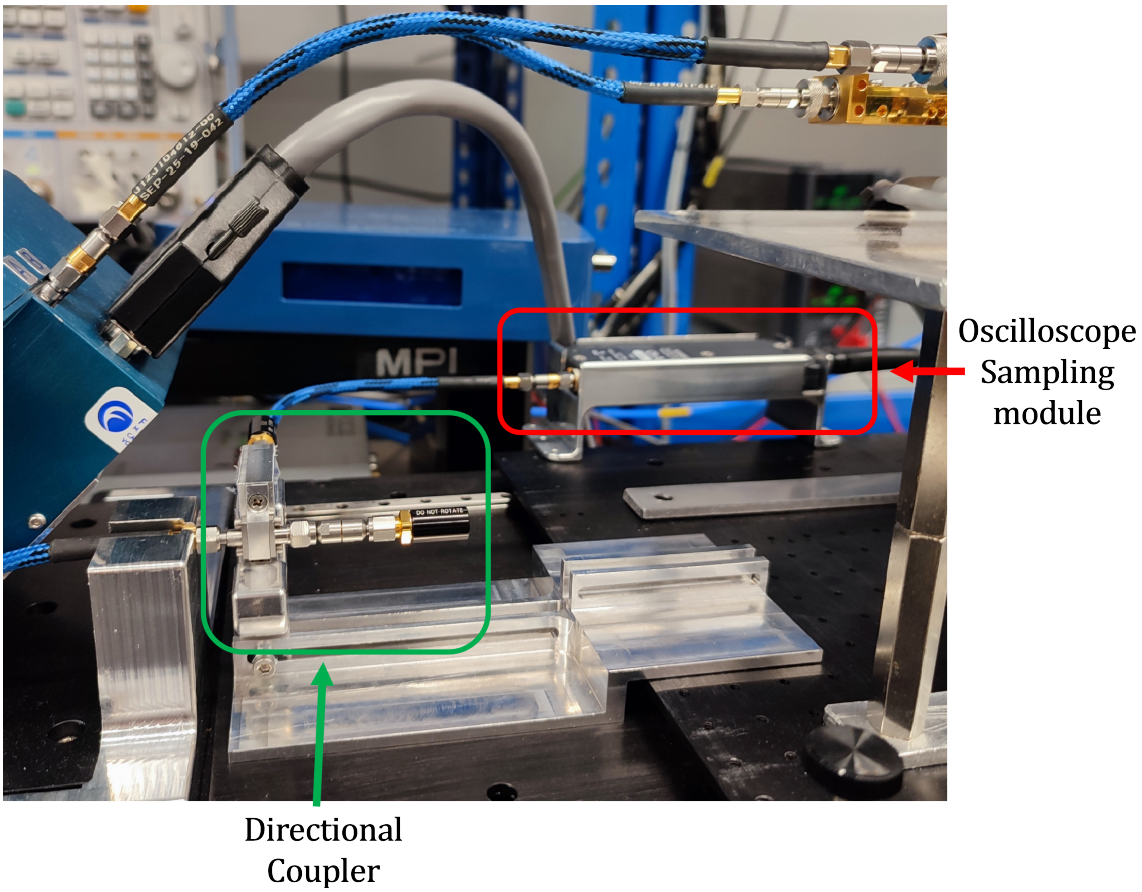

Figure 5.22: Load-side fixtures designed and manufactured for sampling and measuring waveforms.

power, and an 18 cm long 1 mm coaxial cable connects to the oscilloscope sampling module. This approach limits the power level measured at the sampling module, which has a maximum rated power of 16 dBm. The components are securely fixed in position, with a metal fixture to support the coaxial cable from the load tuner, along with custom-designed fixtures for the directional coupler and the oscilloscope module. A metal rail has been integrated into the system to allow for additional fixtures, such as a bias-tee, to ensure consistent alignment and stability of the networks. These fixtures prevent flexion of the coaxial cables or rotation of the components when tightening coaxial connectors, which is very sensitive due to the lower torque of 1 mm connectors (0.45 N·m) versus 3.5 mm connectors (0.9 N·m) [15].

Each component between the measurement reference plane and the oscilloscope sampling module has the possibility of introducing phase dispersion, which degrades the accuracy of the waveform measurement. Although limited phase dispersion is expected in the coaxial cables, the network consists of a directional coupler which does introduce a frequency dependence in phase. Hence the whole network after the 1 mm coaxial cable from the load tuner is characterised for its S-parameters across the desired frequency range. This can be characterised using the set-up shown in Section 5.3.3 or on a dedicated S-parameter measurement system. The full network parameters representing the path between the measurement reference plane and the oscilloscope sampling module are completed by performing a chain matrix calculation of the characterised fixtures and the tuner S-parameters at each position (calculated during tuner calibration in Section 5.3.2). During a measurement, the oscilloscope captures the phase relationship between the measured fundamental and harmonic frequencies. The measurement software applies the fixture de-embedding to determine the phase relationship at the DUT reference plane.

5.3.7 Final Verification

A final verification and self-consistency checks can be performed with the system setup in its internal coupler calibration configuration shown in Figure 5.17.

It is well-documented that a final vector calibration verification can be tailored for load-pull measurements [16]. The process involves performing a load-pull measurement across the Smith chart on the zero-length thru calibration structure and evaluating the power gain. In an ideal calibration, the power gain is 1 (0 dB). Since ratio terms are measured, the power scaling error term, e_{10}, is not required and is normalised to 1. Measurements were performed and are presented at 27.5 GHz and 82.5 GHz.

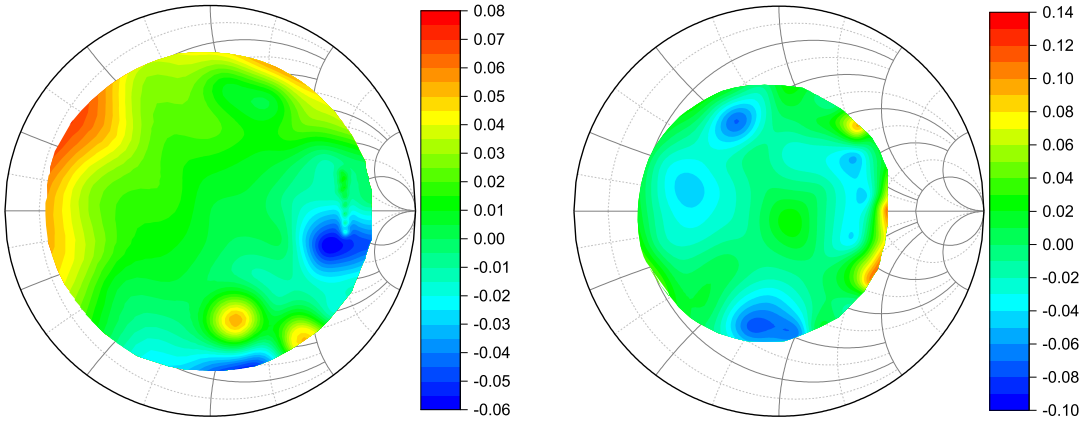

(a) 27.5 GHz (b) 82.5 GHz

Figure 5.23: Load-pull measurement of a zero-length thru showing the power gain in decibels.

Figure 5.23 (a) and (b) shows the verification load-pull measurements following the internal coupler calibration. The results indicate that the residual calibration error across the Smith chart is below 0.1 dB at 27.5 GHz and below 0.15 dB at 82.5 GHz.

A self-consistency check of the tuner calibration was performed. In Figures 5.24 (a), (b) and (c) show a sweep of the Smith chart is performed using the load-pull software, and the calibrated reflection coefficient from the internal vector and tuner calibration are compared. The results show a discrepancy between the two, worsening across frequency; a mean average error vector of 2.4, 5.2 and 8.5% was calculated for 27.5, 55 and 82.5 GHz, respectively.

The verification load-pull on the zero-length thru showed that the internal vector calibration was accurate across the Smith chart. The internal vector calibration

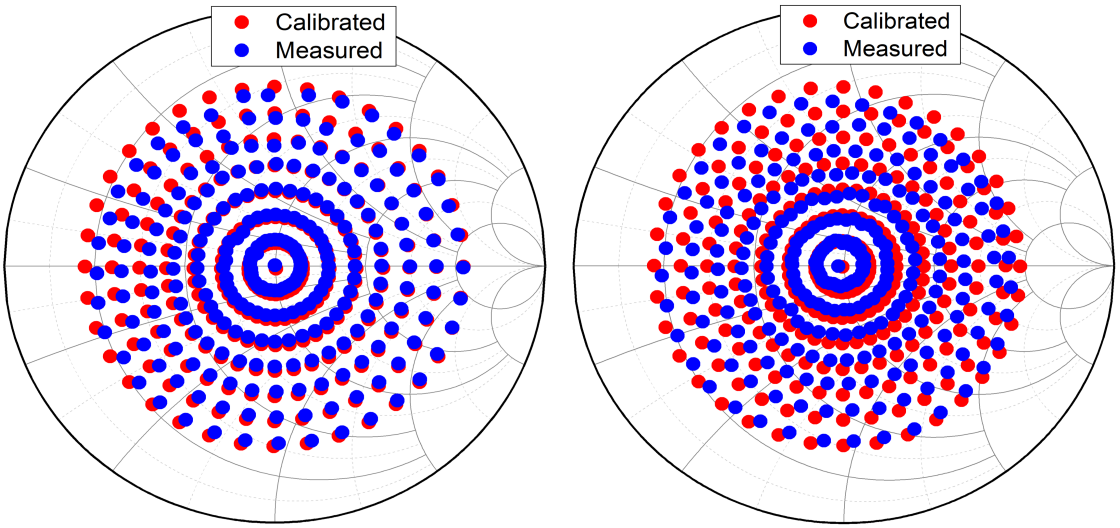

(a) 27.5 GHz

(b) 55 GHz

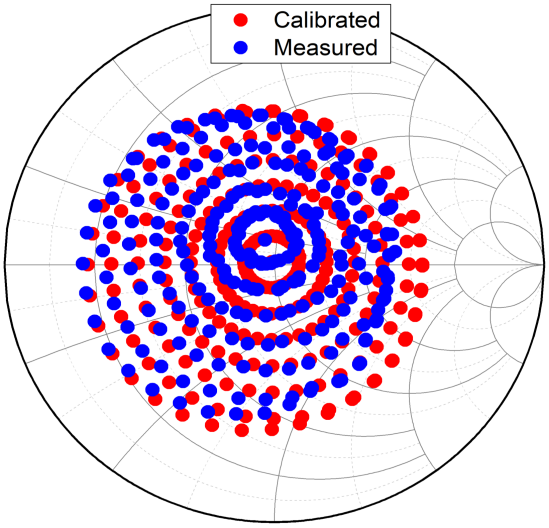

(c) 82.5 GHz

Figure 5.24: Load-pull measurement comparing reflection coefficient between the measured and tuner calibrated positions.

relies on a single calibration to move the reference plane from the VNA to the receivers and requires little system reconfiguration. In contrast, the tuner calibration stage involves multiple characterisation steps and reconfigurations, each incurring additional inaccuracies, such as the coaxial repeatability issues shown in Section 5.3.2.

5.4 Experimental Results

This section presents experimental results for a GaAs device, including characterisation at 27.5 GHz with waveform measurement and harmonic tuning. Measurements are also performed at a fundamental frequency of 82.5 GHz.

5.4.1 Ka-Band Measurements

The system is used to perform fundamental and harmonic load-pull characterisation of a Qorvo 90 nm gate-length GaAs device at 27.5 GHz. The load-pull is conducted at the fundamental frequency with all harmonics terminated to $50, \Omega$, followed by tuning up to the third harmonic to maximise output power and power-added efficiency.

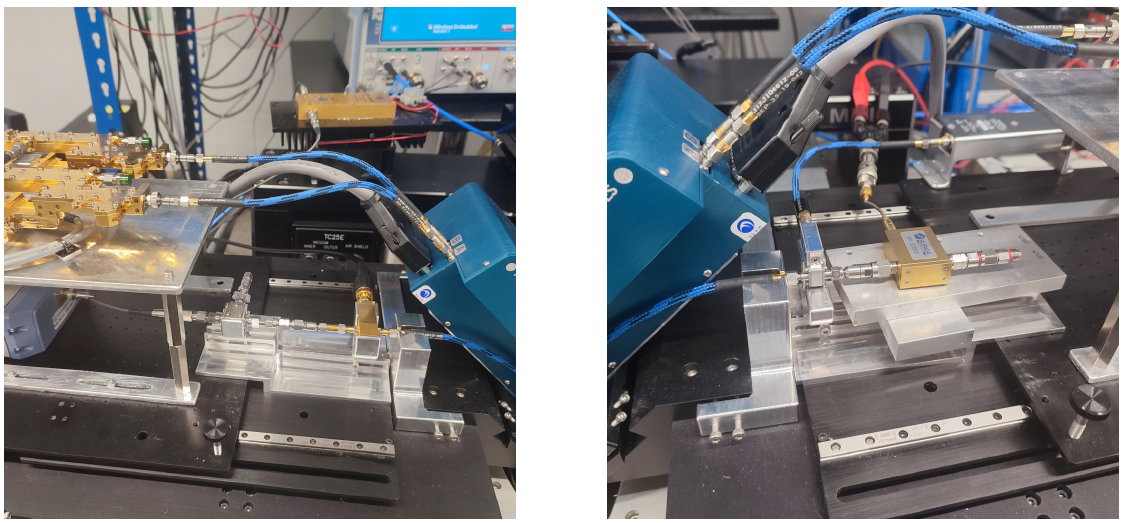

(a) Source set-up (b) Load set-up

Figure 5.25: Overview of the 27.5 GHz measurement setup.

The system is configured for device measurement by adding source and load fixtures, as shown in Figures 5.25a and 5.25b. On the source side, the source diplexer module is disconnected, and a bias-tee, circulator, and driver amplifier are connected to the source tuner. The driver is connected directly to the VNA source via a 1.85 mm coaxial cable, with a 3 dB attenuator placed at the input of the driver amplifier to improve input matching and attenuate feedback to the VNA source. The load diplexer module is disconnected from the tuner, and the waveform measurement fixtures and a bias tee are attached.

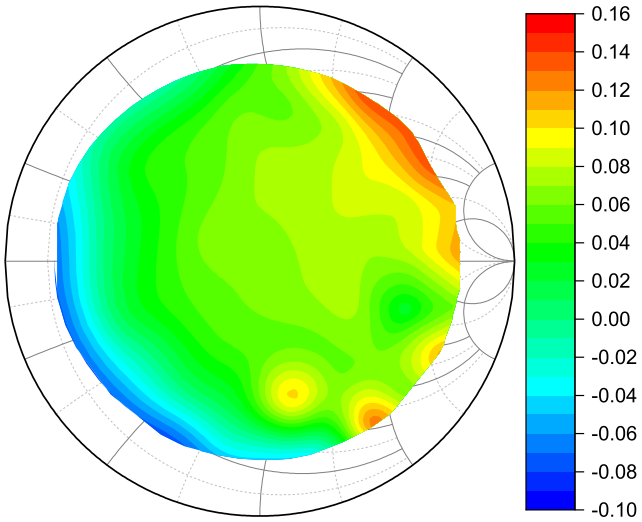

Figure 5.26: Power gain contours in decibels from a load-pull measurement of a zero-length thru standard at 27.5 GHz.

With the setup in its final measurement state, the calibration is verified like that described in Section 5.3.7 by performing a load-pull measurement on the zero-length thru to evaluate the residual power gain. The results are shown in Figure 5.26. This shows a maximum residual power gain of 0.15 dB, a marginal increase from the internal coupler TRL calibration load-pull verification.

The load-pull performance of the GaAs device in a backed-off condition is shown in Figures 5.27a and 5.27b, with output power and power gain displayed, respectively. The GaAs device is conditionally stable at this frequency, as shown in the power gain figure, which reaches 18.5 dB. Avoiding these load conditions to prevent oscillation and potential device damage is critical.

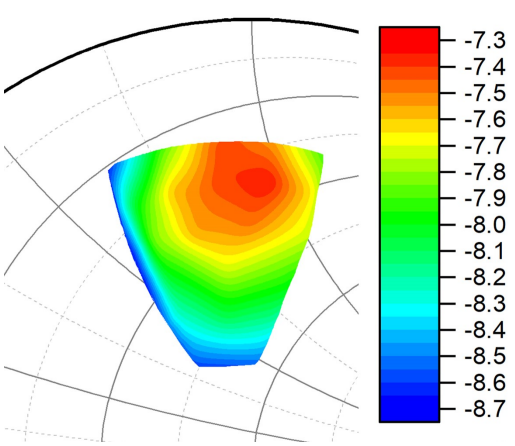

(a) Output power contours, optimum at $0.65\angle 87°$

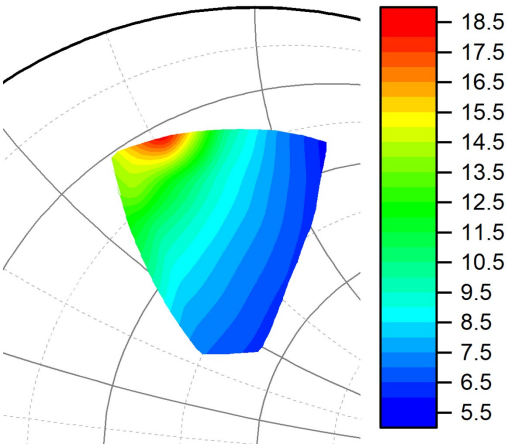

(b) Power gain contours, optimum at $0.75\angle 103°$

Figure 5.27: Load-pull measurements of a Qorvo 90 nm $6 \times 30\,\mu$m GaAs at 27.5 GHz in a backed-off condition with an available power of -10.5 dBm.

Following a load-pull measurement in a backed-off condition, an iterative process is performed to find the global optimum for output power at compression. A power sweep is performed at the impedance determined from the backed-off load-pull measurement, followed by a subsequent load-pull near compression to determine a new optimum impedance for output power. Once the global optimum is found, a power sweep is performed to find the available input power in which the device reaches compression. At 2 dB compression, 2nd and 3rd harmonic load-pull is performed to maximise PAE.

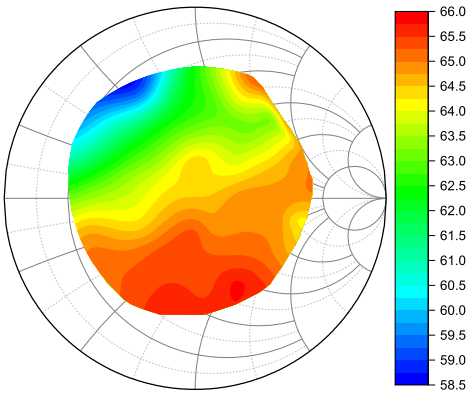

(a) Contours

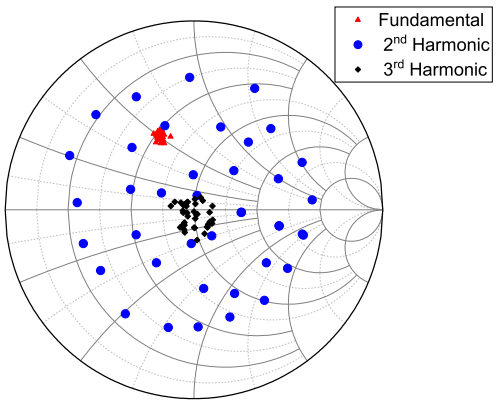

(b) Impedances

Figure 5.28: 2nd harmonic load-pull, PAE contours in percentage and tuned impedances, $P_{\mathrm{Av}} = 16.1$ dBm.

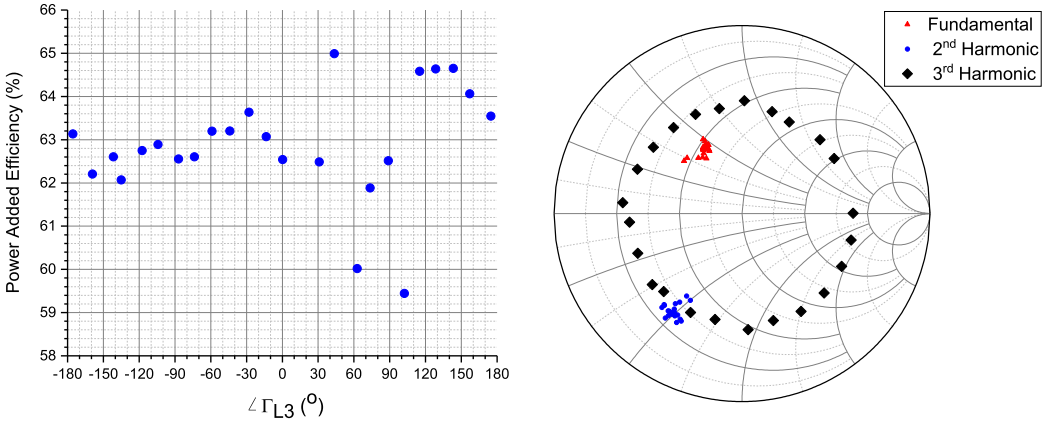

(a) Contours (b) PAE

Figure 5.29: 3rd harmonic load-pull, showing PAE as a function of phase at $|\Gamma_{\mathrm{L}}| = 0.6$ and tuned impedances, $P_{\mathrm{Av}} = 16.1\,\mathrm{dBm}$.

At 2 dB compression, the 2nd harmonic load impedance was swept across the Smith chart while keeping the fundamental impedance at the optimum for output power and the 3rd harmonic at $50, \Omega$. This is shown in Figures 5.28a and 5.28b, with a variation of 7.5% in PAE, with the optimum condition at 66%. The same procedure was followed for the 3rd, where the fundamental and 2nd were held at their respective optima, as shown in Figures 5.29a and 5.29b, $|\Gamma_{\mathrm{L}}| = 0.6$ was held whilst the phase was swept, this was due to device oscillations when the third harmonic was tuned to specific conditions. This sweep forms a compromise between device stability, measurement time and performance. The sweep resulted in a PAE variation of 6 %.

These graphs also highlight the difficulty of performing these measurements with a passive tuner using three tuning slugs to obtain specific harmonic impedances. The harmonic impedances are limited to 0.7 for 55 GHz and 0.6 for 82.5 GHz. Additionally, there is a skew in the other impedance terminations, meaning the harmonic load-pull was not performed in isolation, and the reported PAE is not self-consistent between the 2nd and 3rd harmonic sweeps.

Figure 5.30 shows a comparison between the power sweep of the GaAs device with and without harmonic tuning. The fundamental only measurement was tuned to a reflection coefficient of $\Gamma_{L1} = 0.37\angle 117\,°, |\Gamma_{L2}| = 0$ and $|\Gamma_{L3}| = 0$, whilst the harmonically tuned measurement was tuned to $\Gamma_{L1} = 0.37\angle 117\,°, \Gamma_{L2} = 0.64\angle -$

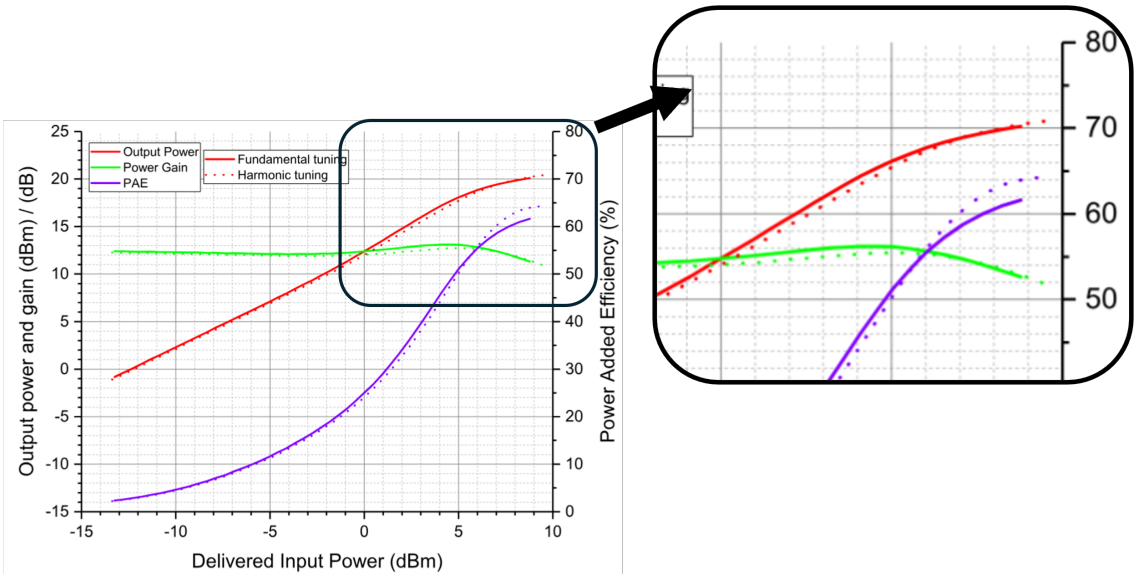

Figure 5.30: Power sweep comparing the gain, output power and PAE for the same device where the device was tuned at only fundamental frequency or the fundamental and harmonic frequencies. The load reflection coefficients were $\Gamma_{L1} = 0.37\angle 117\,^\circ, \Gamma_{L2} = 0.64\angle -120\,^\circ$ and $\Gamma_{L3} = 0.57\angle 129\,^\circ$. Inset showing the compression region where harmonic tuning is most impactful.

$120\,^\circ$ and $\Gamma_{L3} = 0.57\angle 129\,^\circ$. The inset shows the power levels where harmonic tuning has a non-negligible performance change. The results show a boost of 3% in PAE in the harmonically tuned measurement whilst gain appears to be flatter across input power, indicative of slightly improved linearity metrics. The harmonically tuned device achieves a maximum output power of 20.4 dBm, with a power gain of 10.9 dB and a PAE of 64.3% at 2 dB compression. This performance would improve further if the load-pull system was capable of tuning the second and third harmonic impedances to the edge of the Smith chart. This performance improvement is typical of harmonic tuning of a device pushed into compression, behaviour that is exploited in high efficiency power amplifier modes such as class F. Although this has never been practically demonstrated for devices over 20 GHz.

The measured waveforms at the input and output for the final 2 dB compressed are calculated from the measured a and b wave quantities for each frequency.

The gate and drain waveforms are shown in Figures 5.31a and 5.31b. These waveforms are measured at the calibration reference plane, which in this case is the gate and drain manifold of the device. Amplifier classes are determined at the

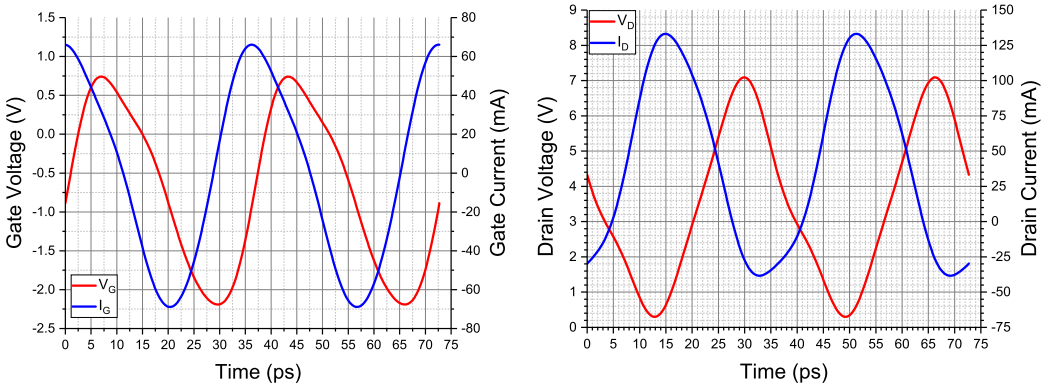

(a) Gate waveforms. (b) Drain waveforms.

Figure 5.31: Current and voltage waveforms for the 90 nm, 6x30 μm GaAs pHEMT at the a.) Gate b.) Drain manifold. Measured at 27.5 GHz up to the third harmonic, with an available input power, P_{Av} = 15.5 dBm, corresponding to 2 dB of compression.

current generator plane of the device, so to be able to determine the class of operation the device is operating in and to further enhance the performance, additional steps are required. Although not considered as part of this work, to view the waveforms at the current generator plane, the remaining parasitic elements relating to the device construction, must be de-embedded to move the reference plane from the measurement plane to the current generator plane.

To perform this de-embedding stage, an accurate device model, which consists of the bias-independent extrinsic parasitics and the bias-dependent intrinsic parasitics, is required. A review of the literature shows a limited number of techniques can accurately model devices up to 110 GHz using the small-signal model extraction approach. In GaAs it is more successful [17], but has proved difficult in GaN technology, with accurate modelling approaches reported to 67 GHz [18] [19].

5.4.2 W-Band Measurements

The same Qorvo GaAs pHEMT used in the previous section is measured but for RF performance in the W-band. Load-pull measurements are taken to evaluate the optimum output power and efficiency condition at a fundamental frequency of 82.5 GHz.

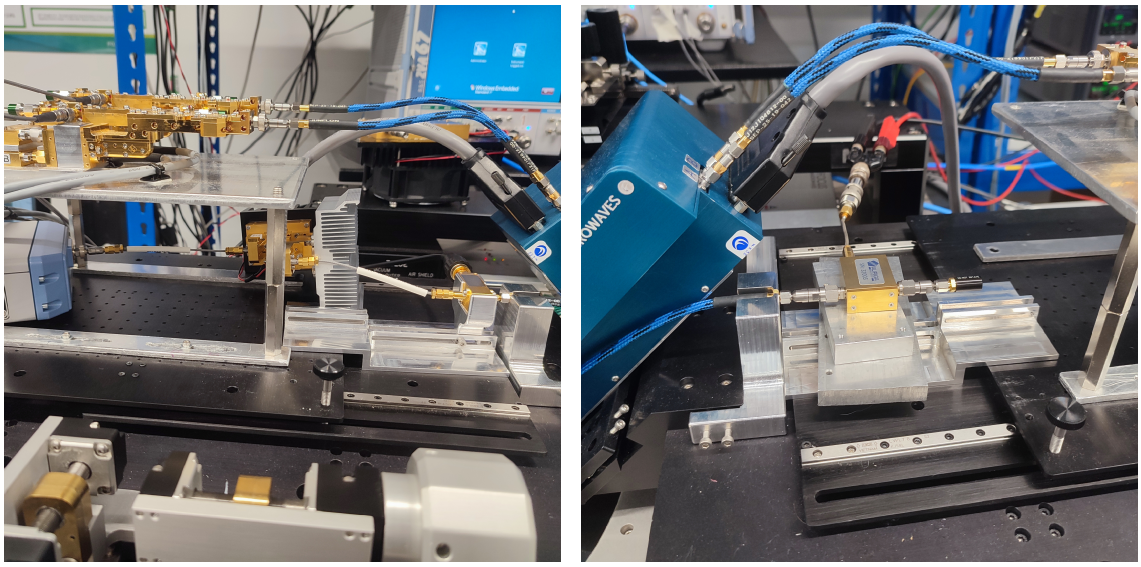

(a) Source set-up (b) Load set-up

Figure 5.32: Overview of the 82.5 GHz measurement setup.

The system is configured for device measurement by adding source and load fixtures, as shown in Figures 5.32a and 5.32b. On the source side, the source diplexer module is connected to two cascaded W-band driver amplifiers, which are joined by waveguide flanges. A 1 mm coaxial cable connects these to the bias-tee. On the load side, a bias-tee is connected, with its RF port terminated in 50 Ω.

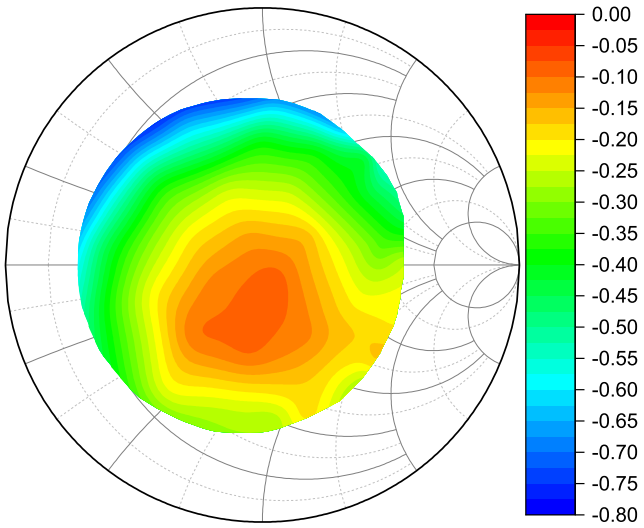

Figure 5.33: Power gain contours in decibels from a load-pull measurement of a zero-length thru standard at 82.5 GHz.

The calibration is verified by performing a load-pull measurement on the zero-

length thru, with the results shown in Figure 5.33. At this frequency, a significant error of 0.8 dB is observed, compared to the 0.14 dB error verified at the internal coupler TRL calibration stage. This discrepancy raises questions about how the system has changed between these two stages. I signpost the reasons for this discrepancy here but this is fully and comprehensively described in Chapter 6. The only thing that has changed between the initial load-pull measurement where the calibration was verified and this condition was the measurement set-up was changed. Firstly, the extended calibration and power calibration was performed, which involved the connection and disconnection of coaxial adapters along with positioning the power meter for measurement. Following this, the source diplexer modules were disconnected and pulled back away from the tuners to allow for space to connect measurement fixtures, such as the bias tee and driver amplifier. This leads to the hypothesis that mechanical changes to the system following calibration result in changes to the system which are not captured by the calibration error coefficients resulting in this error. It initially appears to be a very small change as the centre of the Smith chart still has a power gain of almost 0, and that this error has been magnified by tuning to higher reflection coefficients.

A load-pull was performed on the device in a backed-off condition at 82.5 GHz, with the output power and power gain contours shown in Figures 5.34a and 5.34b, respectively. At this frequency, the maximum achievable reflection coefficient is 0.7, making it impossible to achieve closed contours. Consequently, the optimum impedance remains unchanged when performing a load-pull at compression.

A power sweep of the device at the optimum impedance for output power achievable with the measurement system is shown in Figure 5.35. At the onset of compression, an output power of 19.2 dBm, a power gain of 3.2 dB, and a PAE of 34.5% was achieved.

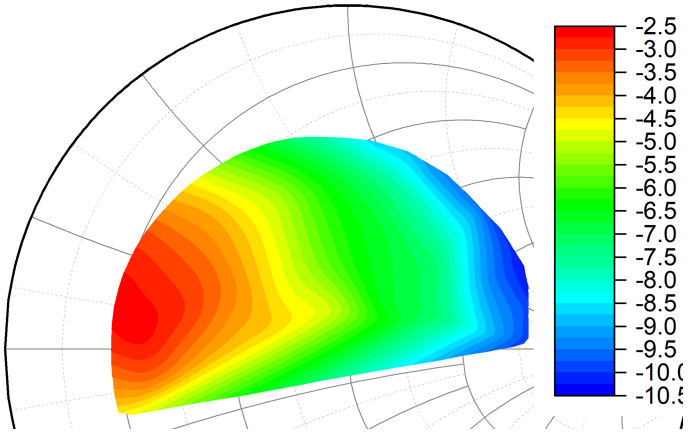

(a) Output power contours, optimum at $0.7\angle 172°$

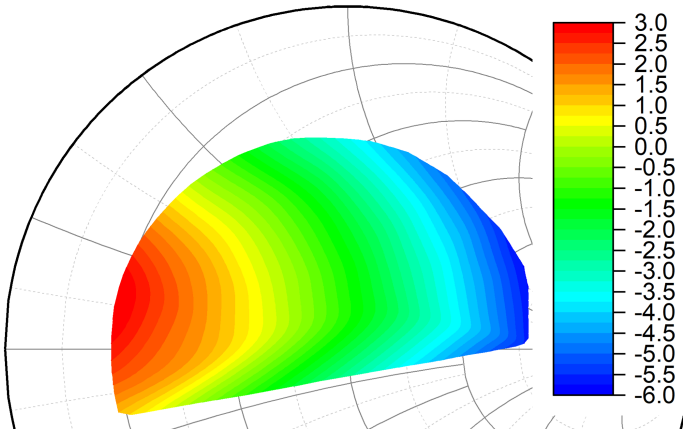

(b) Power gain contours, optimum at $0.7\angle 172°$

Figure 5.34: Load-pull measurements of a Qorvo 90 nm $6 \times 30\,\mu$m GaAs at 82.5 GHz in a backed off condition with an available power of -0.3 dBm.

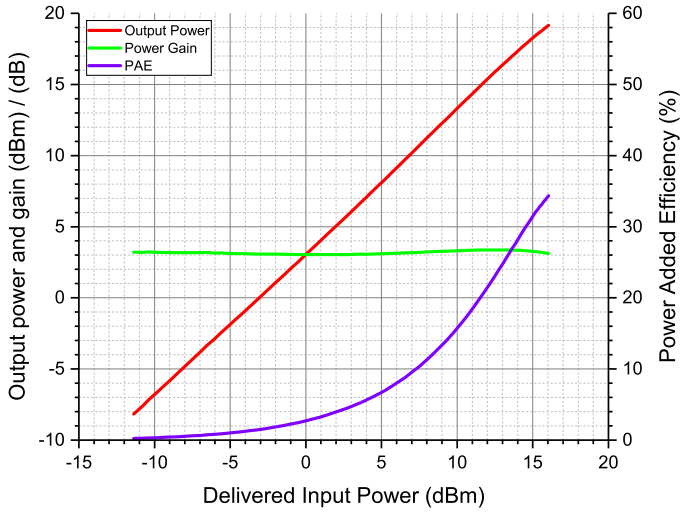

Figure 5.35: Power Sweep with $\Gamma_{L1} = 0.7\angle 172\,°$.

5.4.3 Discussion

A challenge emphasised by the 82.5 GHz measurements is the significant driver power requirement. In these measurements, the amplifier was driven to saturation yet struggled to compress the DUT; this highlights the limited commercial availability of suitable driver amplifiers.

When characterising devices near their $F_{\max}$, the device gain is very low, increasing the demand for driver power. The input mismatch loss was around 5 dB for the W-band measurements. While source tuning could theoretically reduce the mismatch loss, it introduces an additional mismatch between the driver amplifier and the source tuner, reducing the driver's maximum output power.

In addition to mismatch loss, there is a path loss of approximately 5 dB between the driver amplifier and the DUT, through the coaxial cable and tuner elements. These combined losses necessitate a driver amplifier capable of delivering output power approximately 10 dB greater than the DUT's maximum input power required for compression. Referring to the power amplifier survey in Figure 5.1, the power necessary to compress the DUT approaches the reported maximum for GaN PAs at W-band ($\approx$35 dBm).

To overcome the input mismatch loss and reduce the reliance on large driver amplifiers, unit cell transistors can be designed with matching networks to transform the impedance looking into the device to 50 Ω. This solution was not in the scope of this work and has several disadvantages. Firstly, adding a matching network to the input of a unit cell would inherently limit the bandwidth of the measurement to the region in which the cell is designed to be characterised. Secondly, to accurately capture the input reflection coefficient presented to the device an accurate characterisation of the network is required. Thirdly, its a solution that is unlikely to be adopted in industry due to the limited wafer space typically allocated to test cells and the significant cost of wafer space. A typical 0.15 μm gate length 6 inch GaN on SiC wafer costs approximately €50,000.

5.5 Conclusion

This chapter has demonstrated a state-of-the-art mm-wave single-sweep load-pull measurement system capable of multi-harmonic tuning and waveform measurement up to 100 GHz.

The chapter detailed the calibration and verification procedures to ensure reliable and accurate results. This included source levelling, which was used to maintain constant power during calibration by compensating for significant power variations caused by up-conversion. Subsequently, tuner characterisation and calibration were conducted to produce a look-up table of impedances for the load-pull software to control each tuner slug for multi-harmonic tuning. An absolute calibration was then performed to evaluate the absolute quantities at the measurement reference plane. Finally, a vector calibration was completed to shift the reference plane to the centre of a zero-length thru, allowing for direct measurements at the gate and drain manifold of the device.

Following calibration, a comprehensive load-pull characterisation was performed on a 90 nm GaAs device at 27.5 GHz, up to the third harmonic of 82.5 GHz. The results demonstrated improved PAE performance of at least 3% over fundamental-only tuning. Gate and drain waveforms at the extrinsic plane of the device were also presented. Additionally, fundamental measurements at W-band were conducted on the same device, achieving a demonstrated PAE of 34%.

This chapter underscored several limitations of the system, such as the restricted tuning range of the passive tuners, which reduced the effectiveness of harmonic tuning. It also highlighted the inability to achieve the fundamental optimum impedance at W-band. This is a significant takeaway, suggesting the need to explore upgrades to the measurement system, such as transitioning to a hybrid system to achieve higher reflection coefficients. However, further research is required to evaluate the feasibility and practicality of a hybrid or a dedicated active system.

Another important observation discussed in this chapter was the increased uncer-

tainty encountered when the load-pull system was configured to measure a DUT at E-band. During calibration, the maximum uncertainty in measuring a zero-length thru was 0.15 dB. However, this increased to 0.8 dB when the measurement was repeated after the system was configured for device measurements.

References

[1] H. Wang et al. *"Power Amplifiers Performance Study 2000 - Present"*. URL: https://ideas.ethz.ch/research/surveys/pa-survey.html.

[2] Anritsu. *VectorStar Broadband VNA ME7838/AX/EX/D/G*. URL: https://www.anritsu.com/en-gb/test-measurement/products/me7838.

[3] Keysight Technologies. *N5293AX03 110 GHz Frequency Extender*. URL: https://www.keysight.com/gb/en/product/N5293AX03/n5293ax03-110-ghz-frequency-extender.html.

[4] Virginia Diodes. *Vector Network Analyzer Extenders*. URL: www.vadiodes.com/en/products/vector-network-analyzer-extension-modules.

[5] Eravant. *Tx/Rx VNA Frequency Extenders*. URL: https://www.eravant.com/products/vector-network-analyzer-extenders/tx-rx-vna-frequency-extenders.

[6] F.M. Ghannouchi and R.G. Bosisio. "An Automated Millimeter-wave Active Load-Pull Measurement System Based on Six-Port Techniques". In: *IEEE Trans. on Instrum. and Meas.* 41.6 (1992), pp. 957–962. DOI: 10.1109/19.199442.

[7] N. C. Miller et al. "Improving the Precision of On-Wafer W-Band Scalar Load-Pull Measurements". In: *IEEE Journal of Microw.* 3.3 (2023), pp. 1005–1013.

[8] M. Guidry et al. "W-band Passive Load Pull System for On-Wafer Characterization of High Power Density N-polar GaN Devices Based on Output Match and Drive Power Requirements vs. Gate Width". In: *ARFTG Microw. Meas. Conf.* 2016, pp. 1–4.

[9] C. J. Clymore et al. "First Comparison of Active and Passive Load Pull at W-Band". In: *ARFTG Microw. Meas. Conf.* 2023, pp. 1–4. DOI: 10.1109/ARFTG57476.2023.10279609.

[10] V. Teppati et al. "A *W*-band On-Wafer Active Load–Pull System Based on Down-Conversion Techniques". In: *IEEE Trans. Microw. Theory Techn.* 62.1 (2014), pp. 148–153.

[11] C. De Martino et al. "Hardware and Software Solutions for Active Frequency Scalable (Sub)mm-Wave Load–Pull". In: *IEEE Trans. Microw. Theory Techn.* 68.9 (2020), pp. 3769–3775.

[12] A. Baddeley et al. "Millimeter-Wave On-Wafer Large Signal Characterization System for Harmonic Source/Load Pull and Waveform Measurements". In: *IEEE MTT-S Int. Microw. Symp. (IMS)*. 2023, pp. 1101–1104.

[13] D. Williams. *NIST Microw. Uncertainty Framework*. URL: https://www.nist.gov/servicesresources/software/%20wafer-calibration-software.

[14] Rohde & Schwarz. *RF & Microwave power meters*. URL: https://www.rohde-schwarz.com/fi/products/test-and-measurement/rf-and-Microw.-power-meters_63672.html.

[15] IEEE. "IEEE Standard for Precision Coaxial Connectors at RF, Microw., and Millimeter-Wave Frequencies–Part 1: General Requirements, Definitions, and Detailed Specifications". In: *IEEE Std 287.1-2021* (2022), pp. 1–136. DOI: 10.1109/IEEESTD.2022.9889249.

[16] V. Teppati et al. "Accuracy Improvement of Real-Time Load-Pull Measurements". In: *IEEE Trans. on Instrum. and Meas.* 56.2 (2007), pp. 610–613.

[17] B. Hughes and P.J. Tasker. "Bias Dependence of the MODFET Intrinsic Model Elements Values at Microwave Frequencies". In: *IEEE Trans. on Electron Devices* 36.10 (1989), pp. 2267–2273. DOI: 10.1109/16.40909.

[18] Jihoon Kim. "A New GaN HEMT Small-Signal Model Considering Source via Effects for 5G Millimeter-Wave Power Amplifier Design". In: *Applied Sciences* 11.19 (2021). ISSN: 2076-3417. URL: https://www.mdpi.com/2076-3417/11/19/9120.

[19] A. Jarndal and G. Kompa. "A New Small-Signal Modeling Approach Applied To GaN Devices". In: *IEEE Trans. Microw. Theory Techn.* 53.11 (2005), pp. 3440–3448.

Chapter 6

Error Correction Uncertainty Evaluation for Millimetre-Wave Load-Pull Systems

6.1 Introduction

As frequencies extend into the mm-wave bands, the design process increasingly depends on accurate measurements and precise device models. Higher frequencies also drive circuit miniaturisation, transitioning from designs using packaged ICs on PCBs to entire circuits integrated onto a single die in MMIC form.

Given the cost and complexity of MMIC production, generating accurate device models is essential to minimising the number of design/tape-out iterations required to produce a profitable product.

Accurate load-pull measurement data plays a critical role in the extraction and optimisation of device models. For large-signal behavioural models, such as the Cardiff model [1] and X-parameters [2], model extraction is directly based on load-pull measurement data.

Additionally, commercial compact models, such as the Angelov model [3] and EEHEMT1 [4], rely on load-pull data for validation and tuning of parameters.

This highlights the importance of obtaining accurate load-pull measurement results. The literature on measurement accuracy for power amplifier characterisation places a significant focus on S-parameter characterisation. This emphasis is justified, as large-signal calibration fundamentally relies on accurate S-parameter calibration.

For S-parameter calibration, the primary tool is the NIST Calibration Uncertainty tool [5], which calculates and propagates total measurement uncertainty. This tool uses known characteristics of the measurement setup or calibration kit, such as cable bend, the repeatability of coaxial connections, and fabrication process variations.

In this comprehensive paper [6], the authors use the NIST calibration uncertainty tool to propagate various errors through to the measured waves in a load-pull measurement. The authors consider factors such as coaxial cable bending, connector repeatability, calibration standard error, probe alignment, the HPR and random errors in their analysis. The authors present their findings as a sensitivity analysis of a measured device, detailing the load dependence of uncertainty.

However, the authors acknowledge that their proposed uncertainty model cannot be evaluated in real time. It requires a complete model of the measurement system and careful control of uncertainty modes, making it impractical for use in a real-world commercial load-pull measurement setup.

Another strategy employed in literature [7], [8], [9] and [10] focuses primarily on the evaluation of the uncertainty at the load-pull measurement stage without directly calculating uncertainty from calibration like in [6].

In [7], the authors investigate the effect of uncertainty due to the power scaling term. They demonstrate the increased uncertainty of output power, gain and efficiency when performing measurements at highly reflective load reflection coefficients.

In [8], the focus moves to the relative uncertainty on load-pull measurements. The authors perform a load-pull measurement and evaluate the uncertainty in the power gain when measuring a zero-length thru. The focus is placed on the correc-

tion of uncertainty, with the method demonstrated in simulation and then applied in measurement but without any direct plots of power gain uncertainty in a real measurement system.

This work was developed upon in [9] by showing measured uncertainty of power gain under load-pull conditions, with an uncertainty reaching 1 dB for an undefined frequency at the edge of the Smith chart. In [10], the work showed uncertainty for a frequency of 40 GHz with a measurement showing up to 1.8 dB. This paper also demonstrated that power gain is a better metric for viewing uncertainty than transducer gain.

These papers show that measurement uncertainty increases rapidly as the load impedance approaches the edge of the Smith chart. This is crucial for modern satellite communication applications, which increasingly use solid-state power amplifiers for Ka-band and W-band. With the increased use of III-V technology for high-frequency applications, there is a prevalence for the use of GaN devices, with unmatched power performance at Ka-band [11] and pushing towards to W-band and beyond [12], [13]. GaAs devices still dominate W-band and D-band solutions with the increased F_{t} and F_{max} and the lower regulated power requirements for these applications[14]. Both technologies have typical optimum reflection coefficients for a power match in the region of $|\Gamma_{\mathrm{L}}| = 0.8$ for these high-frequency applications.

This work fills the gaps in the literature by practically investigating the uncertainty present in real-world mm-wave load-pull systems. The methods proposed in this chapter attempt to determine route causes for the measurement error described in the literature by first determining best case uncertainty on different load-pull systems by eliminating perceived error sources (random error and systematic error). For the first time the effect of random error at the calibration stage is simulated and propagated through to load-pull measurement giving clear guidelines to load-pull measurement operators about the required VNA dynamic range. Secondly, systematic error sources are investigated, this being the first time that set-up related error specifically for load-pull measurements is investigated and can be actionably

quantified by the operator.

Section 6.2 details the measurement system and the calibration procedure, Section 6.3 introduces the metric used to quantify uncertainty in this work and establishes a baseline uncertainty level in two mm-wave load-pull systems. Section 6.4 presents a theoretical and experimental characterisation of uncertainty present in the load-pull systems. This topic was the point of discussion in a conference presentation [15], and the results were formalised and presented in the IEEE Microwave Theory and Techniques transactions paper from the author [16].

6.2 System Description

This section is based on measurements performed on two mm-wave load-pull systems in the laboratory at Cardiff University. They are used to investigate errors when calibrating and measuring mm-wave devices from Ka-band to W-band.

System one is a real-time, vector-receiver, active LP system with a maximum frequency of 67 GHz, shown in Figure 6.1. The system contains a 67 GHz Rohde & Schwarz (ZVA 67) VNA, using an external test set based on Marki 2-67 GHz (C-0265) directional couplers. The VNA receivers are connected to the directional couplers using 1.5 m semi-rigid 1.85 mm coaxial cables. For on-wafer measurements, any set of probes can be mounted, but the typical ground-signal-ground (GSG) probe pitch used on this system ranges between 100 and 150 μm with a maximum frequency of 67 GHz.

System two is a passive on-wafer LP system, capable of measurements up to 110 GHz, and is shown in Figure 6.3; this system was detailed in Section 6.2. This work is tailored for fundamental frequency measurements; therefore, the system is not set up to use the oscilloscope for phase coherence.

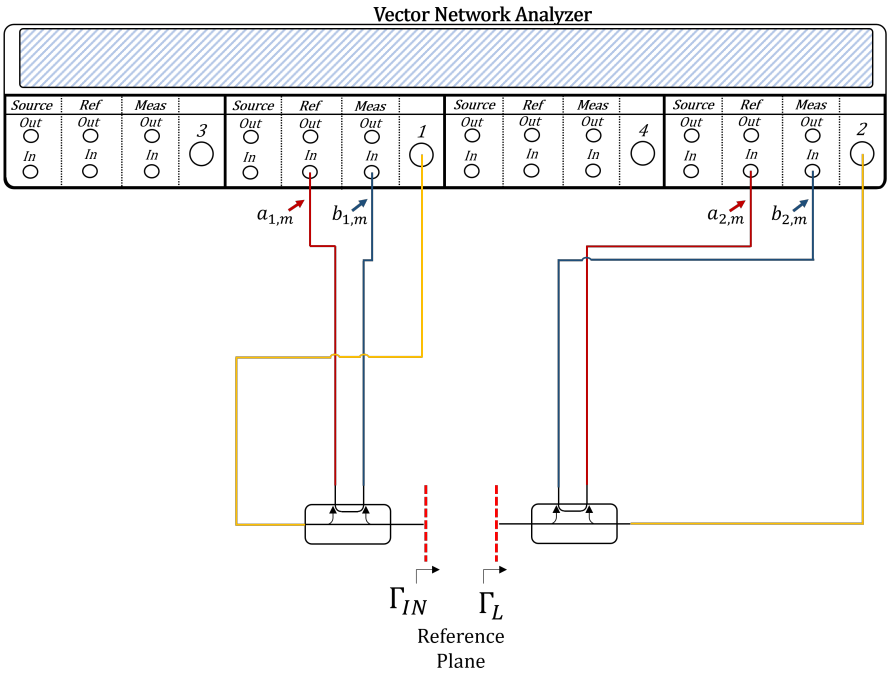

Figure 6.1: Active LP measurement system diagram [16].

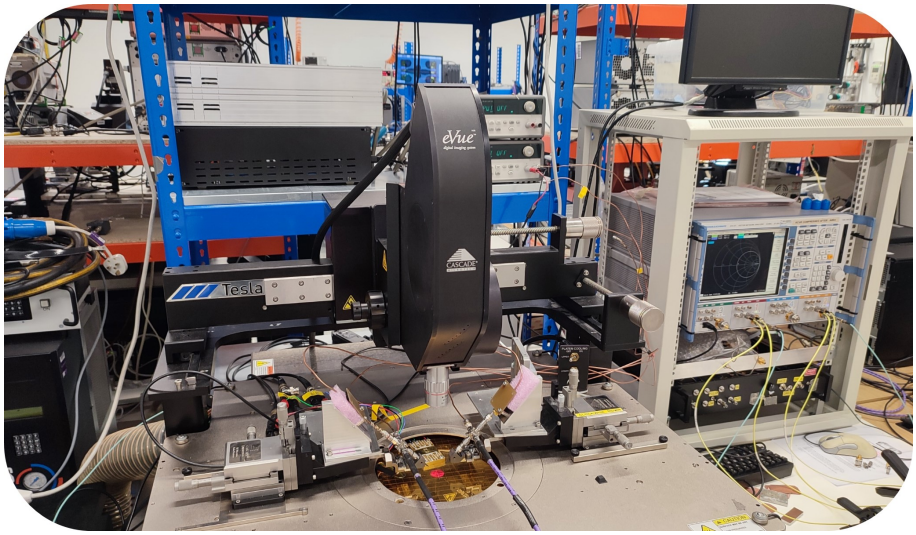

Figure 6.2: Active LP measurement system [16].

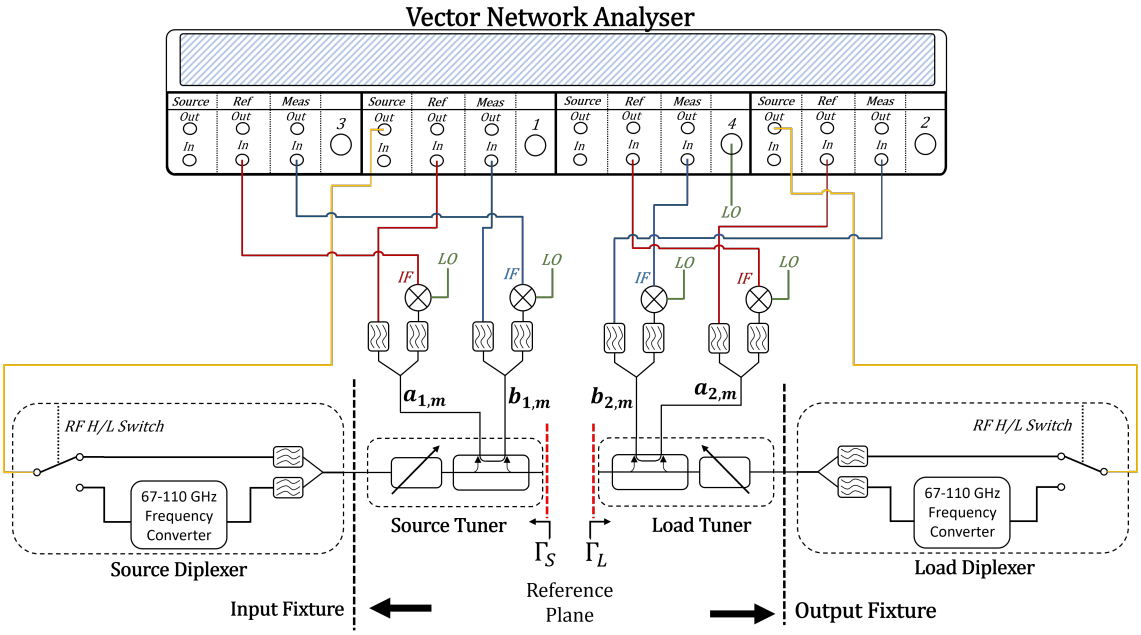

Figure 6.3: Passive LP measurement system diagram [16].

6.2.1 Calibration and Measurement procedure

The large signal calibration procedure is a standard procedure independent of the measurement system, except for tuner calibration for the passive load-pull systems. It is detailed in Section 2.3.2.

In this section, the TRL calibration algorithm[17] was used exclusively. This decision was influenced by the research on the accuracy of calibration algorithms for mm-wave on-wafer measurements. In [18], the authors compare standard calibration techniques, SOLT, LRRM, TRM, TRL, and additionally mTRL in [19]. The papers conclude that the error related to the definition of the standards prevent the SOLT from obtaining high accuracy measurements above 10 GHz. The TRM calibration shows a lower error than SOLT but still has the issue of accurately defining the match standard. The remaining three calibration techniques are far superior because there is no requirement to define the standards accurately. The authors in [18] compare up to 40 GHz and show a marginal improvement in the accuracy of TRL over LRRM. In [18] the authors conclude that there is negligible difference between LRRM and TRL up to 90 GHz, but beyond that frequency the TRL/mTRL

algorithm is significantly more accurate. The loss of accuracy of LRRM at higher frequencies is due to the extraction procedure of the load series inductance, assuming a constant response across frequency. In reality, as frequency increases, the equivalent model of the load becomes increasingly complex, which is not captured in the LRRM algorithm. The advantage of the mTRl algorithm over TRL is the extended frequency range. The line in both algorithms sets the calibration reference impedance; for the TRL, it is defined for frequencies covering the electrical length between 20° and 160°, and separate measurements can be performed covering different frequency bands. However, this typically results in discrepancies at band edges. In the mTRL algorithm, multiple line lengths can be combined, and the reference impedance term is averaged across the frequency band.

As the section covers large signal fundamental measurements, the wide bandwidth offered by the mTRL calibration is not required, so a TRL calibration is selected.

A calibration kit was designed for each material type to evaluate the calibration at the same reference plane in which a device is measured. This avoids the difficulties of de-embedding feed lines when measuring a device [20] [21].

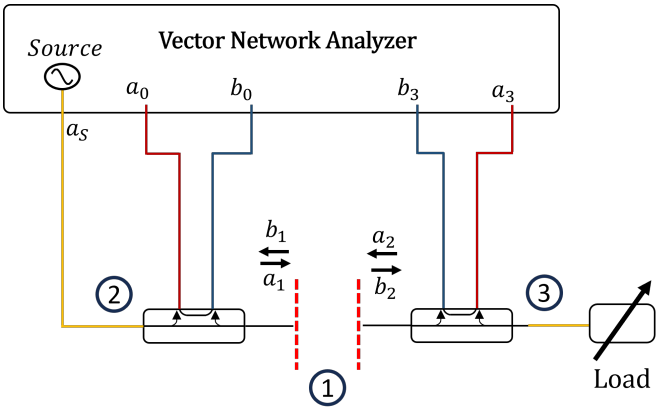

Figure 6.4: Generalised load-pull system diagram [16].

This list contains a summarised set of steps used in this section to perform large signal calibration, verification and measurement, with reference to the generalised system in Figure 6.4.

1. Configure the measurement system.

2. Perform on-wafer vector calibration at the DUT reference planes (position 1 in Figure 6.4).

3. Verification of vector calibration.

4. Perform absolute calibration at the extended output port (position 3 in Figure 6.4) Using a SOL coaxial calibration and power meter.

5. Add bias-tee, circulator and external amplifiers outside the reflectometers (position 2 and 3 in Figure 6.4)

6. Verification of large-signal calibration.

7. Perform LP measurement.

6.3 Uncertainty Evaluation

6.3.1 Background

As discussed, measurement uncertainty for load-pull has been well-documented, with a propagation of error study from modelled measurement and calibration kit characteristics to a set of measured waves detailing the sensitivity of error to load reflection coefficient in [6].

The uncertainty due to the inaccuracy of the power coefficient in absolute calibration and its subsequent impact on absolute measured quantities such as output power and efficiency was reported in [7].

This section focuses on errors throughout the large signal calibration, caused explicitly by configuring an mm-wave measurement system to measure a real device and its effect on the measured ratio quantities.

The method for evaluating calibration residual uncertainty, [8], [9], [10], [22] use the LP measurement of a zero-length thru, to evaluate a given metric, shown below:

The power gain is given by:

$$G_{\mathrm{P}} = \frac{P_{\mathrm{out}}}{P_{\mathrm{in}}} = \frac{|b_2|^2 - |a_2|^2}{|a_1|^2 - |b_1|^2} = \frac{|b_2|^2(1 - |\Gamma_{\mathrm{L}}|^2)}{|a_1|^2(1 - |\Gamma_{\mathrm{in}}|^2)} \tag{6.1}$$

where P_{in}, P_{out} are the delivered power to the input and output, respectively.

The transducer gain is given by:

$$G_{\mathrm{T}} = \frac{P_{\mathrm{out}}}{P_{\mathrm{Av}}} = \frac{|b_2|^2 - |a_2|^2}{|a_1|^2} = \frac{|b_2|^2(1 - |\Gamma_{\mathrm{L}}|^2)}{|a_1|^2} \tag{6.2}$$

Where P_{Av}, P_{out} are the available input power and the delivered output power, respectively.

This equation can be re-arranged for a zero-length thru to evaluate the residual calibration uncertainty, whereby a value $\neq 1$ is an error.

$$\Delta G_{\mathrm{T}} = \frac{(1 - \Gamma_{\mathrm{S}}^2)|a_1|^2}{|1 - \Gamma_{\mathrm{S}}\Gamma_{\mathrm{L}}|^2|b_2|^2} \tag{6.3}$$

Again, the gain ratio from an LP measurement of a zero-length thru should be 1 in an ideal calibration with no errors.

The gain ratio is given by:

$$G = \frac{|b_2|^2}{|a_1|^2} \tag{6.4}$$

The ratio of the reflection coefficient in magnitude and phase can also be used.

The reflection coefficient magnitude ratio is given by:

$$\Delta|\Gamma| = \frac{|\Gamma_{\mathrm{L}}|}{|\Gamma_{\mathrm{in}}|} \tag{6.5}$$

The reflection coefficient phase ratio is given by:

$$\Delta\angle\Gamma = \frac{\angle\Gamma_{\mathrm{L}}}{\angle\Gamma_{\mathrm{in}}} \tag{6.6}$$

All these methods will be used to evaluate the uncertainty in calibration. However, the power gain is preferred due to the evaluation across all four measured waves

and includes the terms Γ_{L}, Γ_{in}, a_1 and b_2.

In a real-world measurement system, it is not practical to directly calculate uncertainty for every applicable metric as was performed in [6] using the calibration uncertainty tool [5]. Instead, this section attempts to use a more practical method that can be used in any real-world measurement system to evaluate the level of uncertainty before measurement. Using these metrics, the authors will discuss the primary sources of practical measurement error. This will be set out in the following section, with a detailed flow identifying the source of the error.

6.3.2 Reference uncertainty

The first stage in the investigation is to understand the baseline uncertainty in both measurement systems shown in Figures 6.1 and 6.3, at key frequencies of interest. This provides a starting point to determine the best case uncertainty when the system is calibrated in an ideal scenario and compare this with the uncertainties reported in literature [9] and [10].

To determine the baseline uncertainty, the author attempts to minimise potential error sources, such as random error, relating to dynamic range constraints of the measurement system, such as minimising attenuation between the device plane and the VNA measurement receivers, setting the VNA source RF power close to its maximum and configuring the IF bandwidth to 1 Hz. Setting the IF bandwidth to 1 Hz is an ideal condition although lacks practicality, each measurement point taken at 1 Hz takes approximately 1.5 seconds. For an S-parameter measurement this is 3 seconds due to the forward and reverse measurement for each point, this is multiplied by three for the three different calibration standards and then again by the number of frequencies calibrated across. For load-pull measurements, only a forward measurement is taken but this is performed at every load point. For safety, the load-pull algorithm does not aggressively converge to automatically tune to the desired load point in a single measurement point but does this overall several measurements to prevent load conditions that lie outside of the Smith Chart which

can cause damage. A typical low density load-pull measurement across the smith chart for a single frequency consists of approximately 100-200 load-points, leading to an approximate time of 15 minutes. Systematic error sources are reduced, such as using probe alignment markers on the TRL calibration standards and an automatic chuck to achieve repeatable contact with the probes.

Precautions were taken to limit any error introduced by mechanical alterations to the system between calibration and measurement. The first was to ensure that the thru standard was the final standard to be measured and probed for the calibration to eliminate the need to re-probe between calibration and the verification load-pull measurement. The second precaution was to conduct the absolute calibration prior to vector calibration; although the vector or absolute calibration can be performed in any order, it is standard practice to conduct the vector calibration first. In this case, we assume that mechanical changes to the system can potentially introduce error; we prioritise the accuracy of the vector calibration over the absolute calibration.

A large-signal calibration was conducted ten times on both systems to establish a typical level of uncertainty under near ideal conditions.

Figures 6.5 and 6.6 illustrate the best-case residual uncertainties of the power gain, transducer gain, reflection coefficient magnitude and phase ratios for both the active and passive measurement systems. The power gain uncertainty is the most indicative of system error as it contains all four of the measured waves.

Firstly, a comparison was made of the uncertainty metrics for the active and passive systems at 27.5 GHz using the red traces in Figures 6.5 and 6.6.

These show that both systems exhibit similar baseline uncertainty levels across all four relative measures. For the uncertainty on the power gain, a typical maximum of $\pm\,0.1$ dB, although this is not a like-for-like comparison as the reflection coefficient on the active system was measured up to $\Gamma_L = 0.95$ compared to $\Gamma_L = 0.75$. At a common $\Gamma_L = 0.75$, the active system has a maximum uncertainty of ± 0.03 dB versus ± 0.1 dB for the passive system. A comparison of the residual transducer gain showed an almost identical maximum error of ± 0.04 dB for both systems.

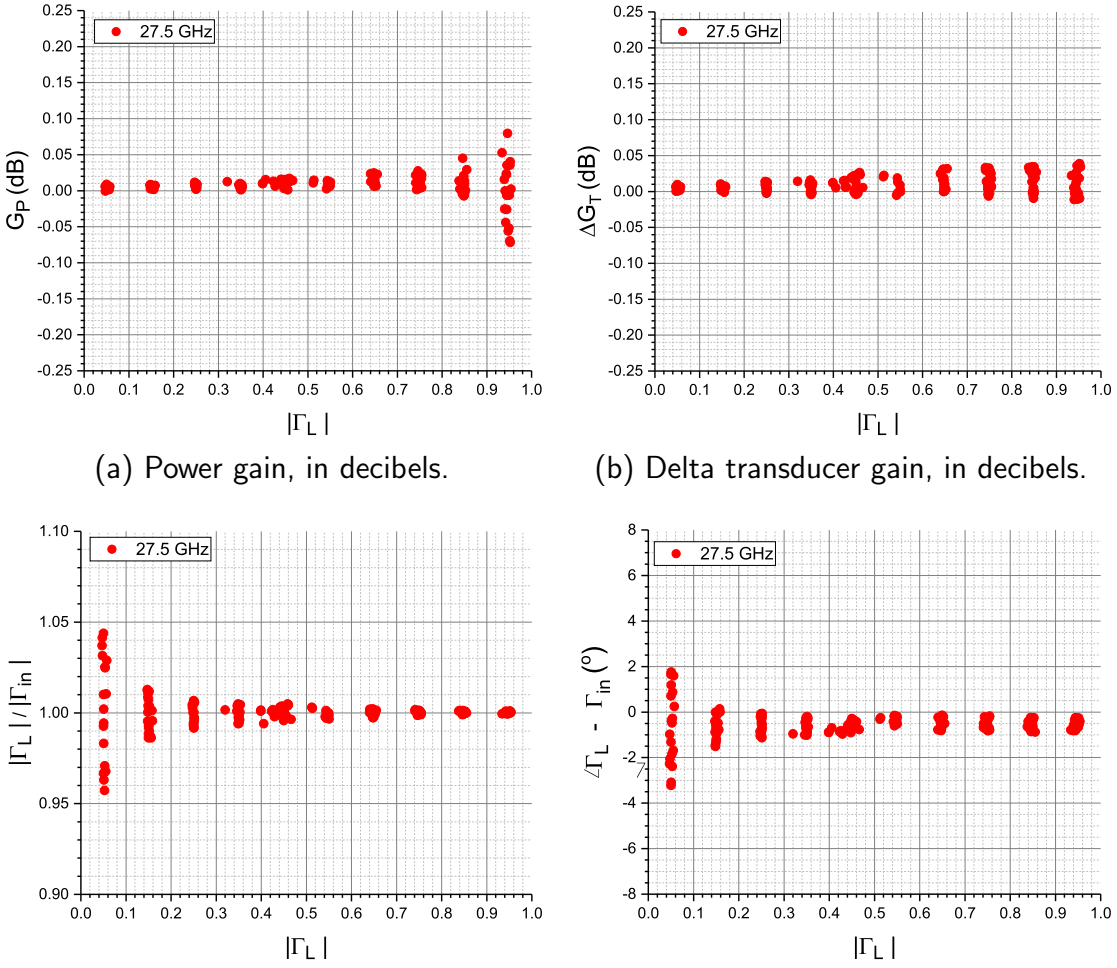

(a) Power gain, in decibels.

(b) Delta transducer gain, in decibels.

(c) Reflection coefficient magnitude ratio.

(d) Reflection coefficient phase ratio.

Figure 6.5: LP measurement showing typical best-case residual uncertainty versus the magnitude of Γ_L, as measured on a zero-length thru on the Active LP system at 27.5 GHz over an equally distributed set of load impedances across the Smith chart [16].

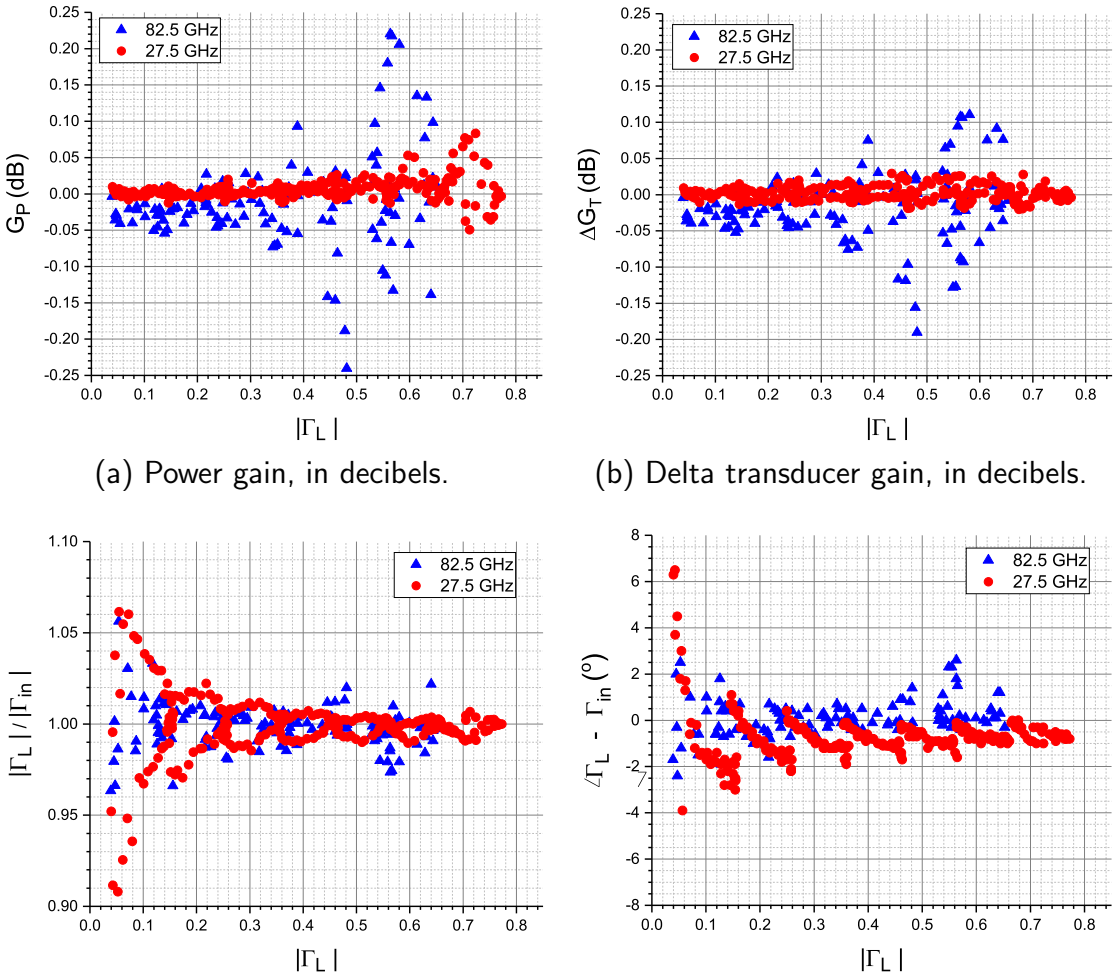

(a) Power gain, in decibels.

(b) Delta transducer gain, in decibels.

(c) Reflection coefficient magnitude ratio.

(d) Reflection coefficient phase ratio.

Figure 6.6: LP measurement showing typical best-case residual uncertainty versus the magnitude of Γ_L, as measured on a zero-length thru on the passive LP system at 27.5 and 82.5 GHz over an equally distributed set of load impedances across the Smith chart [16].

The reflection coefficient magnitude and phase ratios must be taken with care, they appear to magnify error a low reflection coefficient values. At low reflection coefficients, both values of the ratio are very small values, ideally the same, giving a ratio of 1. But at low values, marginal changes to the reflection coefficient caused by a limited system dynamic range can appear as large error but is in fact a very small error. This metric is important for load-pull characterisation of devices as it provides an indication of the accuracy of the load impedance the system is tuned too. From a designers perspective, it is crucial to know the impedance condition of the maximum output power or efficiency, error in this can be the difference between design success and underperformance.

For the active system, there was a maximum absolute magnitude uncertainty of ± 0.05 versus ± 0.1 for the passive system. The phase ratio also showed a similar trend as the magnitude ratio, with the greatest error near the centre of the Smith chart, with the active system showing an error of $\pm 4°$; this plot also showed a $1°$ mean error across the reflection coefficient sweep, compared to the passive system that showed a maximum uncertainty of $\pm 6.5°$ with a mean error of $1.5°$ across all conditions.

The final evaluation compares the levels of uncertainty across frequency range, using Figure 6.6, where the uncertainty metrics were compared for 27.5 GHz and 82.5 GHz. This comparison was only made on the passive system due to the limited frequency range of the active system. It is immediately apparent that the uncertainty metrics are significantly higher at 82.5 GHz. Even with a lower tuning range at 82.5 GHz, the maximum uncertainty is 0.25 dB versus 0.1 dB at 27.5 GHz. The residual transducer gain error is a maximum of $\pm\,0.2$ dB at 82.5 GHz versus ± 0.04 dB at 27.5 GHz. Although the uncertainty on the magnitude and phase ratios show a higher maximum uncertainty for 27.5 GHz, it is the author's opinion that this is related to dynamic range considerations more than raw calibration uncertainty. The magnitude and phase ratio have a maximum uncertainty of $\pm\,0.03$ and $\pm\,3\,°$, respectively at 82.5 GHz.

The uncertainties exhibited in Figures 6.5 and 6.6 show a good level of accuracy can be obtained for measurements under 67 GHz for both the passive and active measurement systems; however, there is a significant increase in uncertainty for frequencies above this.

At this stage, for both systems, the baseline uncertainties are categorised as measurement repeatability errors and are believed to be related to non-linear drift, especially for frequencies above 67 GHz where the extender kicks in. This additional uncertainty offers an opportunity to be investigated in future work, although potential reasons for this could relate to the lack of temperature regulation for these extender receiver modules or the receivers having a lower linearity compared to the base VNA. The motivation for this suggestion is following the two occasions of continuous measurement of a thru standard following calibration, where the load-pull system was tuned to a load reflection coefficient system of $0.7\angle 180\,^\circ$ at 82.5 GHz, and a wave measurement was taken once every 5 seconds for 14 hours and the power gain plotted. The noise-related random error was measured over a short time period and was calculated to be approximately 0.01 dB.

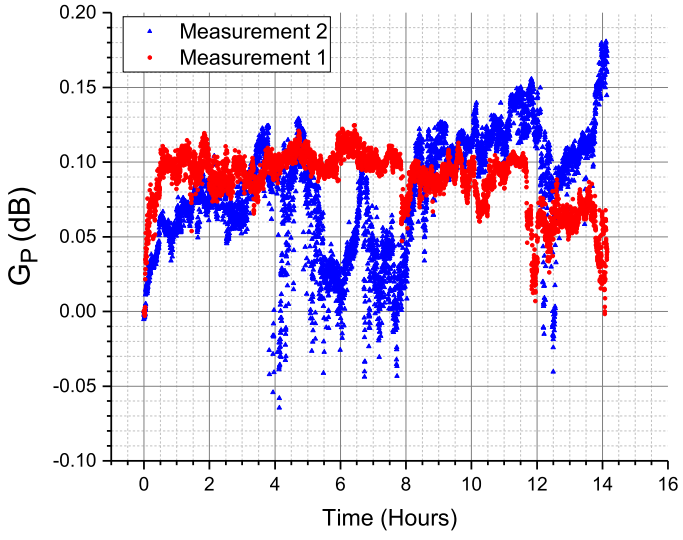

Figure 6.7: Power gain over time for the passive load-pull measurement system with $\Gamma_L = 0.7\angle 180\,^\circ$, performed twice at a frequency of 82.5 GHz.

There is a significant level of drift over time, with a maximum range of 0.2 dB. This drift was measured at the highest reflection coefficient obtainable at this fre-

quency on this system. The system drift becomes more significant when tuning to high reflection coefficients with negligible drift at 50Ω. A review of manufacturers data shows little published data of drift standards. This offers motivation for future investigations into understanding the reasons for this drift. Although measurement drift has been discussed in the literature, the research in [23] discusses and models the effect of nonlinearity in the VNA receiver chain and [24], which attempts to characterise and model the random changes in the VNA measurement behaviour by analysing the change in calibration coefficients related to the steady-state temperature and humidity drift and a change in noise and power levels. This chapter uses the uncertainties in this section as a baseline reference for further uncertainty and error analysis.

6.4 Calibration Error

With the baseline uncertainty evaluated in the previous section, any uncertainty above the baseline is considered a calibration error, and the route cause will be determined. From a rigorous evaluation of sources of errors that affect the overall measurement error, the two sources that will be considered in this section are related to the calibration dynamic range requirements for the measurement of high-power devices. The second is measurement setup-induced error following vector calibration.

The systems are configured separately to isolate the mechanisms for calibration error: for high-power measurements, increasing the attenuation levels between the DUT and receiver ports (Section 6.4.1) and configuring the system for measuring a device (Section 6.4.2).

6.4.1 Random Error

The ability to measure a DUT with greater output power comes with a trade-off with measurement accuracy due to the finite dynamic range of the VNA and the associated measurement hardware [25]. In modern VNAs, the maximum output

power available at the source port and dynamic range are frequency-dependent, but are typically around 10 dBm and 120 dB, respectively.

A VNA can accurately measure across only a finite dynamic range. When measuring high power levels, the VNA receivers begin to compress and eventually saturate, typically at -5 dBm; this introduces measurement error, as the calibration procedure assumes a linear power response on the measurement receivers. At lower power, the power reaches comparable levels to the receiver noise floor, reducing measurement accuracy.

This introduces a trade-off that the system operator must balance. Enough attenuation must be added to the receivers to prevent receiver compression but not too high to remain significantly above the noise floor to avoid a reduction in accuracy for all eventual measurement conditions in which the system will be used. The major limitation is that all calibration stages are typically performed using just the VNA source ports and are not typically performed using the same amplifier used to measure the large signal response of a device; these are added post-calibration. This limitation makes this trade-off critical for optimising load-pull measurement accuracy. In the Rohde & Schwarz ZVA 67 VNA specification document [26], the maximum source power available from the VNA is 10 dBm, and a maximum dynamic range of 120 dB with direct access to the measurement receivers. These figures are specified at the VNA ports and are degraded by measurement setup loss and attenuation.

This trade-off has been discussed briefly in [25], but to the author's knowledge, there have not been any detailed papers describing the optimisation of this trade-off for high power load-pull measurements.

This section investigates this trade-off through ideal simulations and practical measurements to demonstrate the trade-off's criticality and offer suggestions for the dynamic range required to measure with an x level of accuracy.

Simulations

The trade-off was evaluated in a simulation to eliminate all other forms of error and isolate the error to dynamic range. The simulation involved the vector calibration of a set of defined TRL calibration standards with an added Gaussian noise source to replicate dynamic range. These were propagated through to an ideal load-pull measurement of the calibrated thru standard. This simulation was implemented in MATLAB, and the procedure and simulation theory are detailed in this section.

Defining the S-parameter matrix for TRL standards. Below are the ideal S-parameter matrices for the thru, line, and reflect standards. In this analysis, a short is used as the reflect standard. For simplicity, the standards are defined as frequency-independent.

$$S_{Thru} = \begin{bmatrix} 0 & 1e^{j\phi} \\ 1e^{j\phi} & 0 \end{bmatrix} \tag{6.7}$$

$$S_{Line} = \begin{bmatrix} 0 & 1^{j(\phi+\theta)} \\ 1^{j(\phi+\theta)} & 0 \end{bmatrix} \tag{6.8}$$

$$S_{Short} = \begin{bmatrix} 1^{j\pi} & 0 \\ 0 & 1^{j\pi} \end{bmatrix} \tag{6.9}$$

Where ϕ is the electrical length of the thru standard and θ is the additional length of the line standard.

By multiplying these S-parameter definitions by $a_{1,f}^2$ and $a_{2,r}^2$, which are normalised to 1, the response, b, waves can be easily be determined to replicate a complete set of 24 S-parameter measurements.

$$\begin{bmatrix} b_1 \\ b_2 \end{bmatrix} = \begin{bmatrix} S_{Standard} \end{bmatrix} \begin{bmatrix} a_1 \\ a_2 \end{bmatrix} \tag{6.10}$$

Gaussian white noise is applied to the set of measured waves to replicate a given

dynamic range, using the MATLAB function, ***awgn*** and is performed N times, using uncorrelated noise realisations.

This dynamic range is swept across a practical range, creating a $24 \times D \times N$ matrix, where D represents the number of dynamic range conditions and N represents the number of uncorrelated noise realisations.

The S-parameter matrices can be reformed using the switch correction process described in Section 3.1.1 to assemble a set of noise-affected S-parameters for each standard in a matrix of size $2{\times}2{\times}3{\times}D{\times}N$.

A TRL calibration is performed $D{\times}N$ times, generating a set of error coefficients.

An ideal LP simulation is set up to evaluate the effect the dynamic range has on the residual calibration error for a load-pull measurement. A simulation of a load-pull measurement is performed on the raw ideal thru standard to ensure the same grid of load reflection coefficients is used. The measured waves from this load-pull are then corrected using the set of calibration coefficients for each dynamic range condition. The load reflection coefficient is swept in magnitude and phase covering the entire Smith chart, with $|\Gamma_{\mathrm{L}}|$ swept from 0 to 0.95 in steps of 0.05, and $\angle\Gamma_{\mathrm{L}}\,^{\circ}$ swept from $0\,^{\circ}$ to $350\,^{\circ}$ in steps of $10\,^{\circ}$.

Using the thru standard, the S-parameter equations can be re-arranged to calculate the value of the measured waves at each load condition.

b_2 is calculated using (6.11) - (6.14).

$$b_2 = S_{21}^{thru} a_1 + S_{22}^{thru} a_2 \tag{6.11}$$

$$b_2 = S_{21}^{thru} a_1 + S_{22}^{thru} b_2 \Gamma_{\mathrm{L}} \tag{6.12}$$

$$b_2(1 - S_{22}^{thru}\Gamma_{\mathrm{L}}) = S_{21}^{thru} a_1 \tag{6.13}$$

$$b_2 = \frac{S_{21}^{thru} a_1}{1 - S_{22}^{thru}\Gamma_{\mathrm{L}}}. \tag{6.14}$$

b_1 is calculated using (6.15) - (6.17)

$$b_1 = S_{11}^{thru} a_1 + S_{12}^{thru} a_2 \tag{6.15}$$

$$b_1 = S_{11}^{thru} a_1 + S_{12}^{thru} b_2 \Gamma_{\mathrm{L}}. \tag{6.16}$$

Substituting b_2 into the solution

$$b_1 = S_{11}^{thru} a_1 + S_{12}^{thru} \Gamma_{\mathrm{L}} (\frac{S_{21}^{thru} a_1}{1 - S_{22}^{thru} \Gamma_{\mathrm{L}}}). \tag{6.17}$$

a_2 is calculated using (6.18) and (6.19)

$$a_2 = \Gamma_L b_2 \tag{6.18}$$

$$a_2 = \Gamma_L (\frac{S_{21}^{thru} a_1}{1 - S_{22}^{thru} \Gamma_{\mathrm{L}}}) \tag{6.19}$$

The dynamic range was constrained to a maximum of 90 dB and a minimum of 50 dB to limit the analysis to a practical range [26] and was performed using $N = 10,000$ noise realisations.

A set of waves for each load condition was calculated and calibrated for each dynamic range condition using the large signal calibration equation in (3.63).

The standard deviation, σ, of the power gain from load-pull due to a given dynamic range during calibration was calculated for each magnitude of the load reflection coefficient to demonstrate the sensitivity.

The effect of dynamic range on LP measurements is shown in Figure 6.8. It is shown that the standard deviation of calibration error remains marginal, at less than 0.05 dB, for all displayed dynamic range conditions up to $|\Gamma_{\mathrm{L}}| = 0.4$. However, this error becomes significant when measuring highly reflective loads. When the dynamic range goes below 80 dB, the accuracy of the measurements begins to degrade significantly in highly reflective conditions. The probability distribution function of the power gain is plotted for each dynamic range condition at four highly reflective

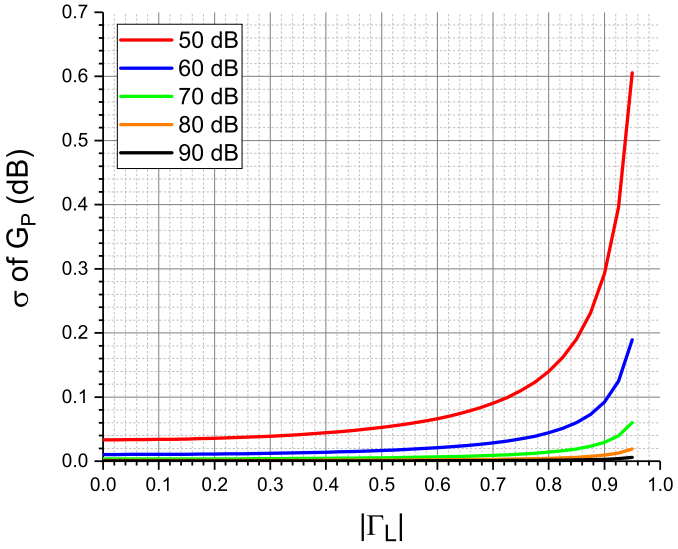

Figure 6.8: Simulated standard deviation of power gain for an LP measurement with 10,000 noise realisations, N for each reflection coefficient and dynamic range versus the magnitude of Γ_L [16].

conditions with $|\Gamma_L| = 0.8, 0.85, 0.9$ and 0.95.

Figure 6.9 shows the probability distribution functions of the dynamic range effect on four different highly reflective load conditions, from $|\Gamma_L| = 0.8$ to 0.95. For $|\Gamma_L| > 0.8$, when the dynamic range is reduced to 70 dB, the calibration error begins to exceed the baseline calibration error from Section 6.3.2. The error becomes significant if the dynamic range goes below this. Although this is unlikely in a practical measurement case, for the ZVA 67, the dynamic range would need to be degraded by 50 dB for significant error to occur. This is an important consideration for measuring harmonic quantities, where the optimal termination for a power amplifier is a reflection coefficient of 1.

The analysis was extended beyond the configuration of the measurement system to the standards themselves. The Gaussian noise was only applied to select standards in the calibration process, and the results were plotted to understand which standards are the most susceptible to result in a residual calibration error, as defined in this section. This was simulated for three conditions: the first, where the noise was applied equally to all standards; the second to only the thru standard; and the third to just the reflect and line standard.

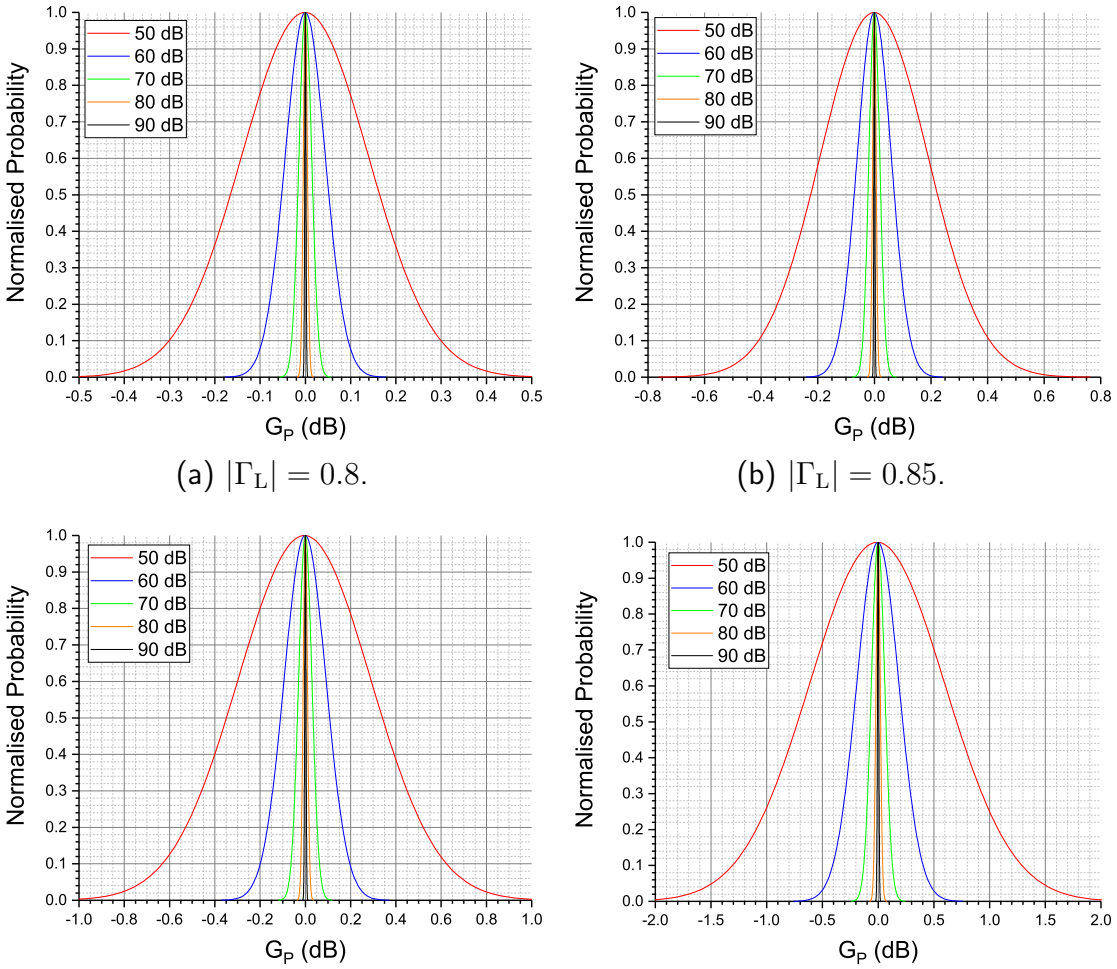

(a) $|\Gamma_L| = 0.8$. (b) $|\Gamma_L| = 0.85$.

(c) $|\Gamma_L| = 0.9$. (d) $|\Gamma_L| = 0.95$.

Figure 6.9: Simulated normalised probability distribution function of power gain for a given reflection coefficient with 10,000 noise realisations per dynamic range condition [16].

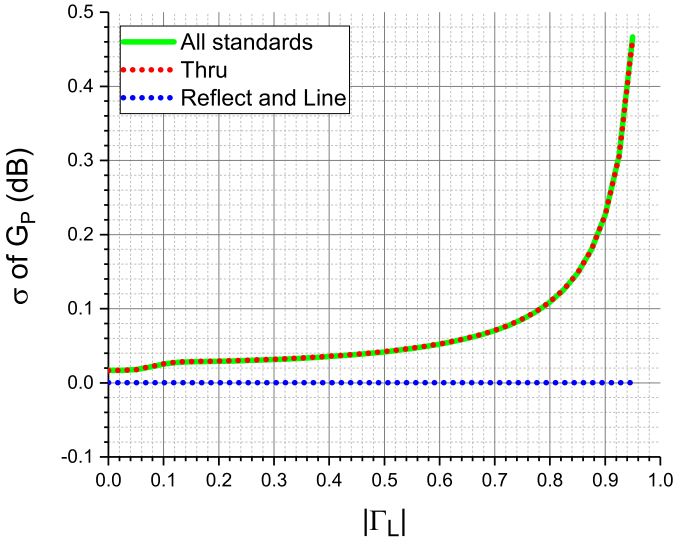

Figure 6.10: Simulated standard deviation of power gain for an LP measurement with 10,000 noise realisations for each reflection coefficient and dynamic range versus the magnitude of Γ_L.

In Figure 6.10, the results show that the dynamic range only impacts the measurement of the thru standard. No error was displayed when noise was applied to only the short and line standards. The author acknowledges that a reduced dynamic range on the line and short standards would result in calibration error and affect other parameters not considered in this section; for the case of the line, the calibration reference impedance would be affected.

Measurements

Section 6.4.1 established that a reduction in the system dynamic range during calibration impacts the accuracy of load-pull measurements; this error becomes significant in highly reflective terminations. This section investigates the impact of calibration dynamic range in an active load-pull measurement system at 30 GHz.

The system used for these measurements is the active load-pull system described in section 6.2 and shown in Figure 6.1 and 6.2. This system provides the best comparison to the simulation results due to no limitations in the tuning range.

The base VNA and the system were characterised to estimate the system dynamic range in each measurement condition to compare the measurement results directly to the simulations in Section 6.4.1.

For the Rohde & Schwarz ZVA67 VNA, the noise floor of the receivers could be directly measured. The noise floor of the VNA is improved with direct access to the receivers, which is the configuration used for LP measurements. The measured noise floor was approximately -117 dBm/Hz. Evaluating the receiver's linearity and compression level is a complicated and sensitive measurement; hence, the upper power limit was found using the equipment specification [26]. The receivers remain linear (<0.1 dB compression) up to -5 dBm and begin to further compress from -5 dBm to 0 dBm (<0.3 dB compression), no further information on compression is given for receiver power above 0 dBm. The maximum receiver power used for this work is -5 dBm.

These specifications give the maximum dynamic range of the instrument, which for an IF bandwidth of 1 Hz is 112 dB, which is a sufficient range to achieve accurate load-pull measurements, using Figure 6.8 as a reference. However, connecting hardware to perform LP measurements will result in a degraded dynamic range.

The hardware required for LP measurements consists of a set of coaxial cables, which connect to a pair of directional couplers. These couplers are fixed to a set of on-wafer probes that probe a DUT. Each element has an associated loss, degrading the system's dynamic range. At 30 GHz, the 1 m 1.85 mm coaxial cables each have approximately 5 dB of loss, and the directional coupler and probe to DUT transition around 10 dB. A total of 15 dB attenuation between the receivers and the DUT results in a degradation in the dynamic range only if the source power during calibration cannot also be raised by that amount. For this setup, the maximum available power at the DUT is approximately 0 dBm, leaving a maximum calibration dynamic range when the IF bandwidth is 1 Hz of 102 dB.

The first measurement condition was to fix the IF bandwidth at a standard setting for high-accuracy measurements of 100 Hz and perform a calibration with varying attenuation levels, allowing for a direct comparison with simulation. These settings result in a dynamic range for the initial condition of 82 dB, degraded by each attenuator added. The experiment was performed using the steps shown below.

1. Set up the measurement system for vector calibration with attenuation A on each receiver.

2. Set the IF bandwidth to 100 Hz.

3. Measure TRL calibration standard N times.

4. Calibrate the system using one set of calibration coefficients.

5. Perform the LP measurement with the IF bandwidth set to 1 Hz.

6. De-embed the calibration coefficients from the LP measurement to get uncorrected measured waves.

7. Apply calibration coefficients to the measured uncorrected waves N times.

8. Calculate power gain statistics.

9. Repeat steps 1) - 8), adding 10 dB of attenuation to the receivers each time.

The attenuation between the VNA receivers and the DUT was calculated using the calibration error box terms below to compare the dynamic range during measurement with the simulation.

$$\begin{bmatrix} b_{1,d} \\ a_{1,d} \\ b_{2,d} \\ a_{2,d} \end{bmatrix} = \frac{1}{e_{10}} \begin{bmatrix} \frac{1}{e_{01}} & -\frac{e_{00}}{e_{01}} & 0 & 0 \\ \frac{e_{11}}{e_{01}} & -\frac{\Delta E_A}{e_{01}} & 0 & 0 \\ 0 & 0 & \frac{1}{e_{32}} & -\frac{e_{33}}{e_{32}} \\ 0 & 0 & \frac{e_{22}}{e_{32}} & \frac{-\Delta E_B}{e_{32}} \end{bmatrix} \begin{bmatrix} b_{1,m} \\ a_{1,m} \\ b_{2,m} \\ a_{2,m} \end{bmatrix} \tag{6.20}$$

The large signal calibration equation in (6.20) shows the relationship between the measured and calibrated a and b waves. When scaled by the large signal coefficient, it tells the loss between the DUT and receivers, which can be converted into dB. For this method to remain accurate as the attenuation was increased, the coefficient was averaged across the number of calibrations N. This method was the most precise

way to determine the attenuation in each receiver path without reconfiguring the system to measure each quantity.

Using the methodology from steps 1) - 9), a set of calibrations at different attenuation conditions ranging from 15 dB to 45 dB was conducted, with $N = 1000$.

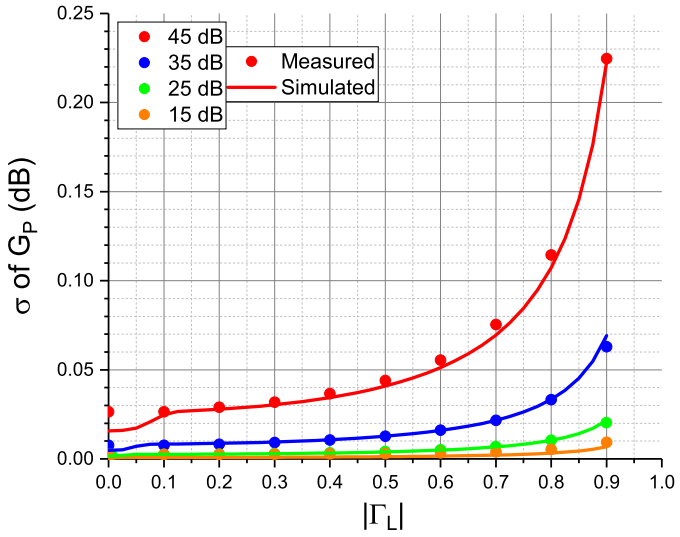

Figure 6.11: Measured (Scattered Points) and simulated (Solid Line) standard deviation of power gain from an LP measurement with 1000 calibrations for each attenuation condition versus the magnitude of Γ_L. The measurement was performed on the active LP system at 30 GHz [16].

Figure 6.11 shows a close agreement between the simulated and measured calibration error across various attenuation conditions. This indicates the characterisation of the system parameters was accurate, and the simulation can be used to predict the measured performance. The figure demonstrates the significant rise in the standard deviation of the calibration error when measuring highly reflective loads, especially when the attenuation between the DUT and receivers reaches 35 dB or higher. This attenuation is necessary for measuring devices with an output power of 1 W.

The measured results from these figures were taken, and the normalised probability distribution of the error at four reflection coefficients, which are reasonable load conditions when measuring mm-wave devices, are plotted in the figures below.

For a reflection coefficient of $|\Gamma_L| = 0.6$ - 0.9, in Figure 6.12. For 15 and 25 dB, the error reaches a maximum of 0.1 dB at 4σ; however, as attenuation rises, the maximum error also follows this, for 45 dB of attenuation, a maximum error of

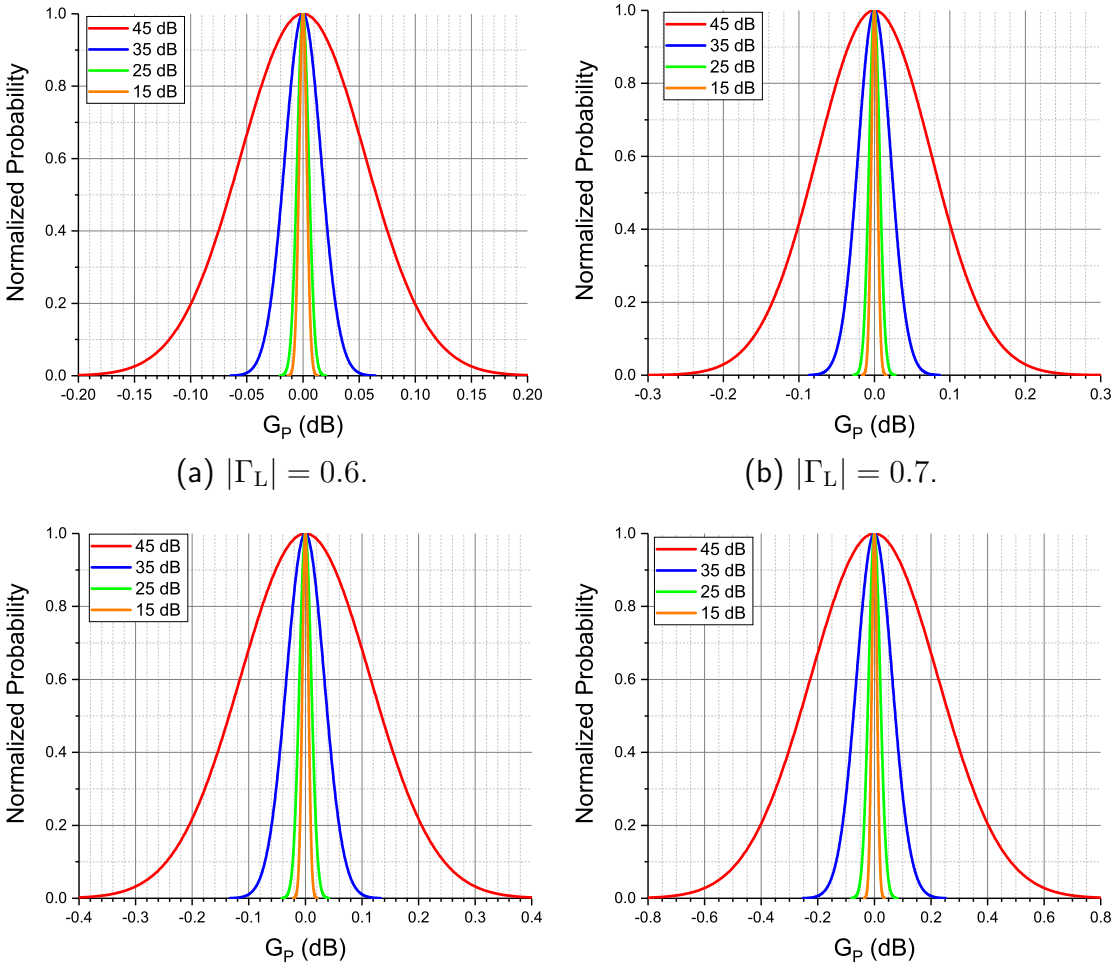

(a) $|\Gamma_L| = 0.6$. (b) $|\Gamma_L| = 0.7$.

(c) $|\Gamma_L| = 0.8$. (d) $|\Gamma_L| = 0.9$.

Figure 6.12: Measured normalised probability distribution function of power gain with 1000 calibrations for each attenuation condition. This was measured on the active LP system at 30 GHz with $|\Gamma_L|$ ranging from 0.6 to 0.9 [16].

0.8 dB at 4 σ is seen.

The IF bandwidth of the VNA must be reduced to below 100 Hz to reduce the calibration error seen in the PDF graphs. A methodology similar to the previous experiment is employed to demonstrate this case. In this case, the attenuation is fixed to 45 dB and the calibration IF bandwidth is swept from 1 Hz to 100 Hz to determine the IF bandwidth setting to reduce the error to an acceptable level ($\leq$ 0.1 dB).

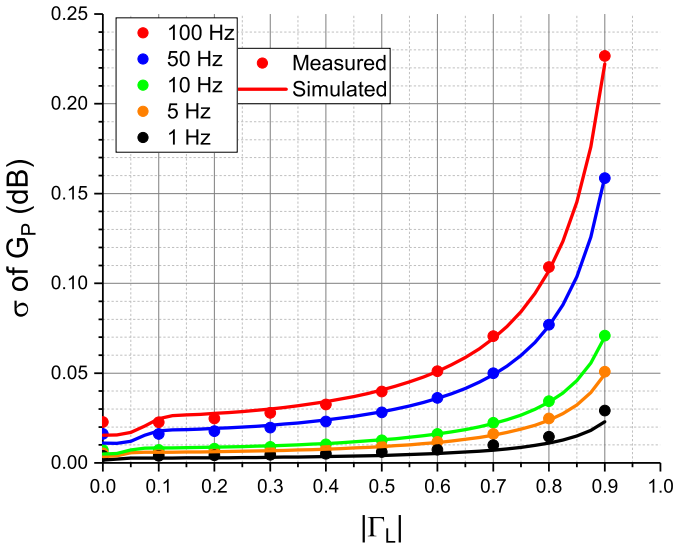

Figure 6.13: Measured (Scattered points) and simulated (Solid line) standard deviation of power gain versus the magnitude of Γ_L from an LP measurement, the attenuation is fixed at 45 dB, but the calibration IF bandwidth was swept from 1 Hz to 100 Hz. The system was calibrated 1000 times at each IF bandwidth. The measurement was performed on the active LP system at 30 GHz [16].

Similar to the investigation when changing attenuation, the plots in Figure 6.13 show the measured and simulated data to have a close match. It shows the worst case condition, where the IF bandwidth is set to 100 Hz and the standard deviation of error is 0.23 dB. By reducing the IF bandwidth from 100 Hz the error becomes 0.16, 0.07, 0.05 and 0.03 dB, for 100, 50, 10, 5 and 1 Hz, respectively. Similarly, the PDFs are plotted for four reflective load conditions for $|\Gamma_L|$ = 0.6 - 0.9.

The plot of PDF for varying reflection coefficients in Figure 6.14 shows the worst-case calibration error (4σ) is above 0.15 dB for an IF bandwidth of 100 Hz, for each displayed reflection coefficient. For this measurement setup, to achieve a calibration

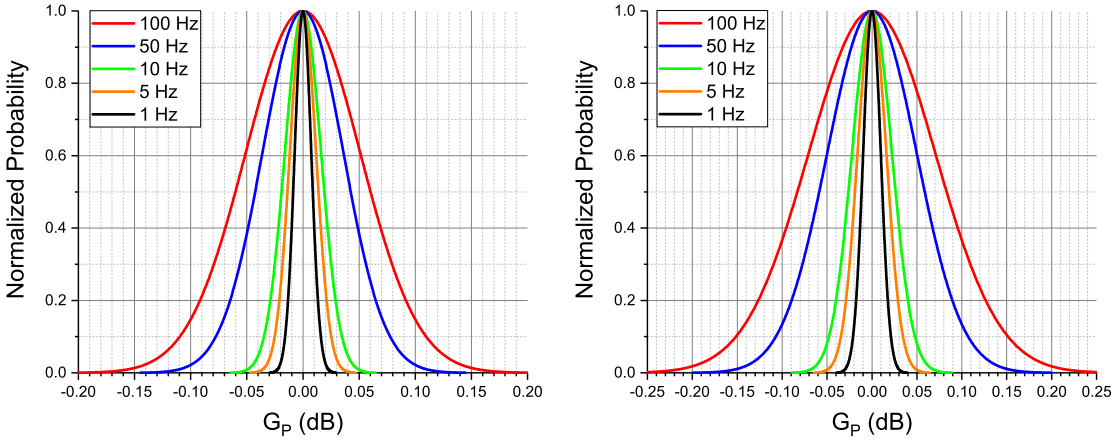

(a) $|\Gamma_L| = 0.6$. (b) $|\Gamma_L| = 0.7$.

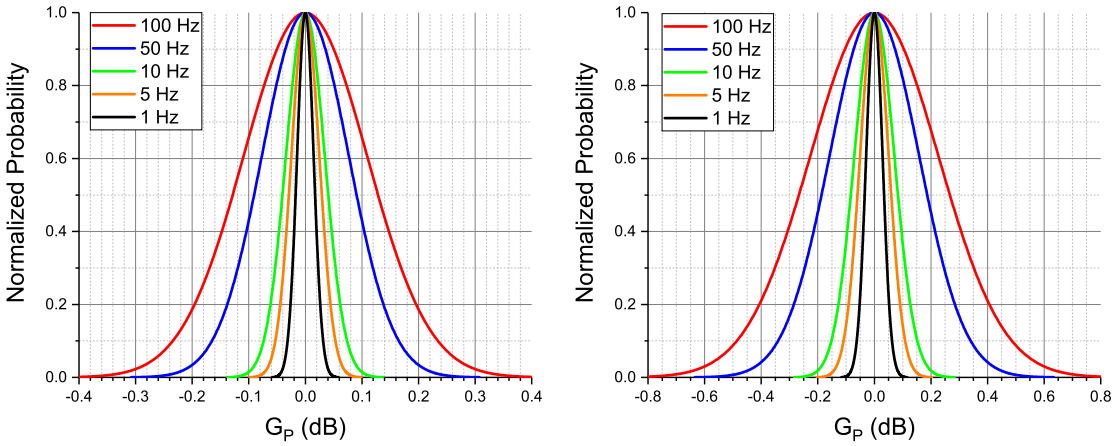

(c) $|\Gamma_L| = 0.8$. (d) $|\Gamma_L| = 0.9$.

Figure 6.14: Measured normalised probability distribution function at $|\Gamma_L| = 0.6$ - 0.9 of power gain for an LP measurement with 1000 calibrations for each IF bandwidth condition. Attenuation was set to 45 dB, and the results were from a measurement at 30 GHz [16].

error of less than 0.1 dB up to a reflection coefficient of 0.9, an IF bandwidth of 1 Hz must be used.

To the author's knowledge, these investigations are the first time calibration errors from dynamic range conditions for high-power LP measurements have been investigated and reported. The investigation shows the link and is confirmed in simulation and measurement; it shows that when the calibration dynamic range is reduced to $\leq$70 dB, the error is propagated to error on LP measurements; this error is sensitive to the measured reflection coefficient, with a rapid increase in error seen. To overcome the effect of reduced dynamic range when calibrating, the operator must reduce the IF bandwidth to sufficient levels to compensate for the degradation. This section guides LP operators on reducing calibration errors to acceptable levels.

6.4.2 Systematic Error

This section investigates the systematic error introduced to a measurement system when configuring the system for an LP measurement. The information learned from the previous sections informs us of the additional error introduced. The systems are configured so that the system has a dynamic range of greater than 80 dB for calibration and measurement, and systematic error is considered negligible if it falls below the baseline for the system determined in Section 6.3.

Following the steps in Section 3.2 to perform a large signal calibration and measurement, it is apparent that steps 4.) and 5.) require the system to be reconfigured to perform the calibration or measurement step. In theory, for 8-term calibration techniques, the load and source fixtures can be replaced and changed without affecting the calibration, allowing the operator to reconfigure the system to perform absolute calibration and to measure large signal devices.

The first reconfiguration stage is to perform the absolute calibration at an extended port plane; this involves a coaxial SOL calibration, followed by the connection of a power meter to provide a power reference to scale the calibrated waves from vector calibration. This must be performed at close proximity to the DUT reference

plane to ensure accuracy, as the power scaling term is determined only by a reflection coefficient normalisation from the extended port calibration procedure. This section argues that mechanical stability for this absolute calibration procedure is essential to obtain accurate measurements when measuring highly reflective conditions during load-pull. The absolute calibration reference planes are shown in Figure 6.15; for the passive system, this is performed at the end of a coaxial cable attaching to the load tuner; this is the closest proximity the extended calibration can be performed to the probe tips. In the active system, the extended port calibration can be performed directly on the load directional coupler port; this disadvantage of this is the extra rotational force placed upon this directional coupler when attaching the coaxial calibration kit and power meter.

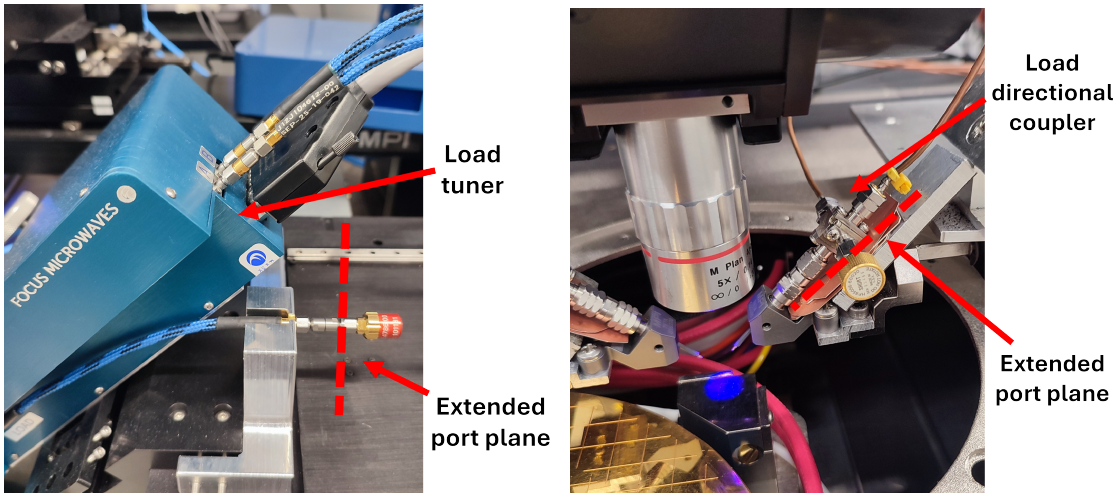

(a) Passive System (b) Active System

Figure 6.15: Extended port plane for the (a) passive and (b) active system. A semi-rigid coaxial cable connects the extended port plane to the load-side tuner in the passive load-pull system. For the active system, the calibration is performed at the load-side directional coupler coaxial port.

Step 5) also requires reconfiguration, which involves adding measurement fixtures into the system to perform load-pull measurements.

It is common practice to exclude the external amplifiers during the calibration stages; there are performance and safety reasons for this. Firstly, in [7], the authors discuss the uncertainty on the absolute scaling term and later discuss the error as a function of position on the Smith chart when performing load-pull. The experi-

ment involves measuring the insertion loss of the output reflectometer to evaluate uncertainty on the absolute scaling term. The work was performed at 18 GHz at two different power levels, using the VNA source or a preamplifier (TWTA). The experiment showed a significant increase in the uncertainty of the power when measuring highly reflective loads in the case of the power being calibrated using the preamplifier versus the VNA source. The conclusion was that the amplifier noise significantly affects the absolute scaling term due to the sensitivity of the measurement.

For safety reasons, using an amplifier during vector and absolute calibration is not common due to damage to structures and equipment. For calibration techniques that use a match standard, these have a much lower power handling capability compared to other standards. During the absolute calibration stage, the power from the source has to be precisely controlled so as not to damage the power meter, as there is little attenuation between the meter and the source. It is difficult to estimate the power at the power meter plane due to the lack of precise knowledge of the VNA source power, amplifier gain, and total path loss to the amplifier.

The system reconfiguration can cause small mechanical perturbations that change the network parameters of the elements within the calibration plane, which includes any element between the directional couplers and the path from directional couplers to the VNA receivers.

Figure 6.16 (a) shows the measurement configuration on the source side of the passive load-pull measurement system. The system is designed to be reconfigurable to perform the different stages of the calibration process. However, this brings the disadvantage of reduced stability of the system, the image shows that the downconversion modules sit on a frame above the source port of the tuner, which reduces the space to position the circulator, bias tee and amplifier. The bias-tee and circulator sit within custom-made mounts on a sliding rail system, but the amplifier sits away from the stage, connected by a 1.85 mm coaxial cable.

Figure 6.16 (b) shows a typical set-up for the active system, consisting of driver amplifiers, circulators and bias-tees connected to the source and load directional

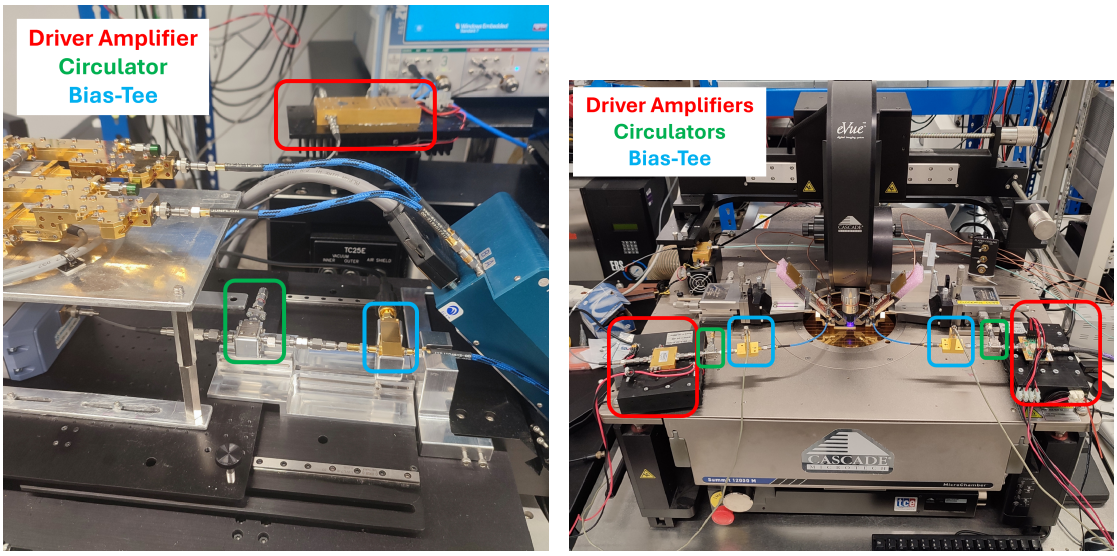

(a) Passive System (b) Active System

Figure 6.16: The (a) source side of the passive system and (b) the active system when they have been reconfigured to include measurement fixtures; these include a bias-tee and external amplifier.

couplers. In this system, the external fixtures are placed onto the probe station, which has a constant height, z, that does not change when manipulating the probe z-direction. This configuration was taken due to the limited space on the positioner to integrate all of the external fixtures.

These images highlight an important consideration for mechanical stability for on-wafer measurement systems. To ensure limited mechanical strain when the probes are raised, all fixtures should be mounted onto the same positioner as the probes. However, the disadvantage is that there is no mechanical isolation between calibration critical sections (any fixture captured by the vector calibration) and the external fixtures when connecting or disconnecting coaxial connectors, such as external amplifiers.

Measurements

In this section, the effects of the mechanical alteration of the system are explored practically, whilst following the steps in Section 3.2 to perform a large signal calibration. The attenuators from both the active and passive systems are removed to isolate the error to mechanical alterations, and the IF bandwidth is set at 1 Hz. The

methodology for this experiment is shown below:

1. Set up the measurement system for vector calibration with no attenuation on receivers.
2. Set the IF bandwidth to 1 Hz.
3. Measure TRL calibration standards.
4. Calibrate the system.
5. Perform LP measurement on thru standard.
6. Perform extended port calibration and power measurement.
7. Configure the measurement system for LP measurement by adding in a driver amplifier and bias-tee.
8. Perform LP measurement on the thru standard.
9. Repeat steps 1) - 8) N times.

The above steps are performed $N = 10$ times at 30 GHz for the active system and at 27.5 and 82.5 GHz for the passive system.

Figure 6.17 shows four examples of the load-pull measurement of a thru standard on the active system at 30 GHz after configuring the system for measurement. The figures show an increasing calibration error above the baseline error of ± 0.1 dB. The error increases rapidly moving to the edge of the Smith chart, with a power gain of approximately 0.8, 0.65, 0.55 and 0.5 dB for (a), (b), (c) and (d), respectively, at $|\Gamma_{\mathrm{L}}| = 0.9$.

Figure 6.18 shows four examples of the load-pull measurement of a thru standard on the passive system at 27.5 GHz after configuring the system for measurement. The figures show an increasing calibration error above the baseline error of ± 0.1 dB. The error increases rapidly, moving to the edge of the maximum tuneable range of the passive tuners, with a maximum power gain of approximately 0.35, 0.35, 0.2 and 0.3 dB for (a), (b), (c) and (d), respectively at $|\Gamma_{\mathrm{L}}| = 0.75$.

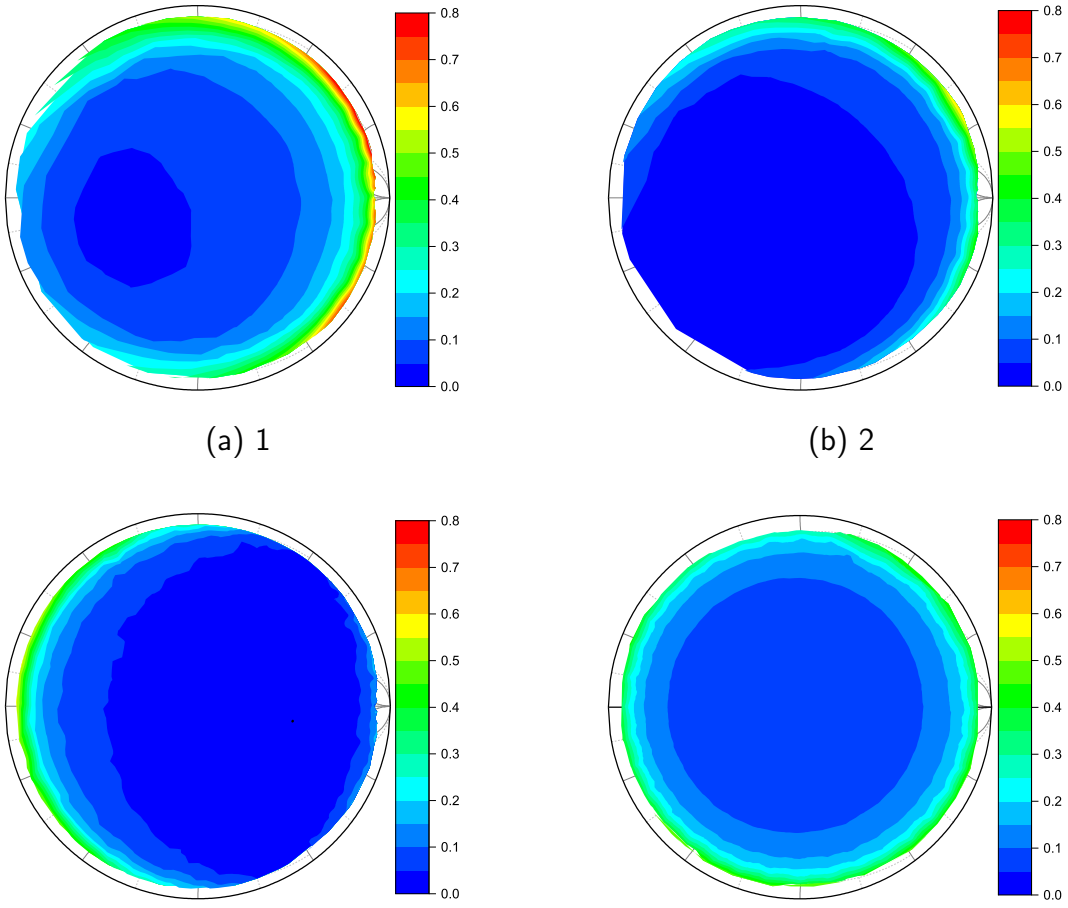

(a) 1 (b) 2

(c) 3 (d) 4

Figure 6.17: LP measurements of power gain in decibels for a zero-length thru on the active LP system at 30 GHz following a full large-signal calibration and the system configured for measurement.

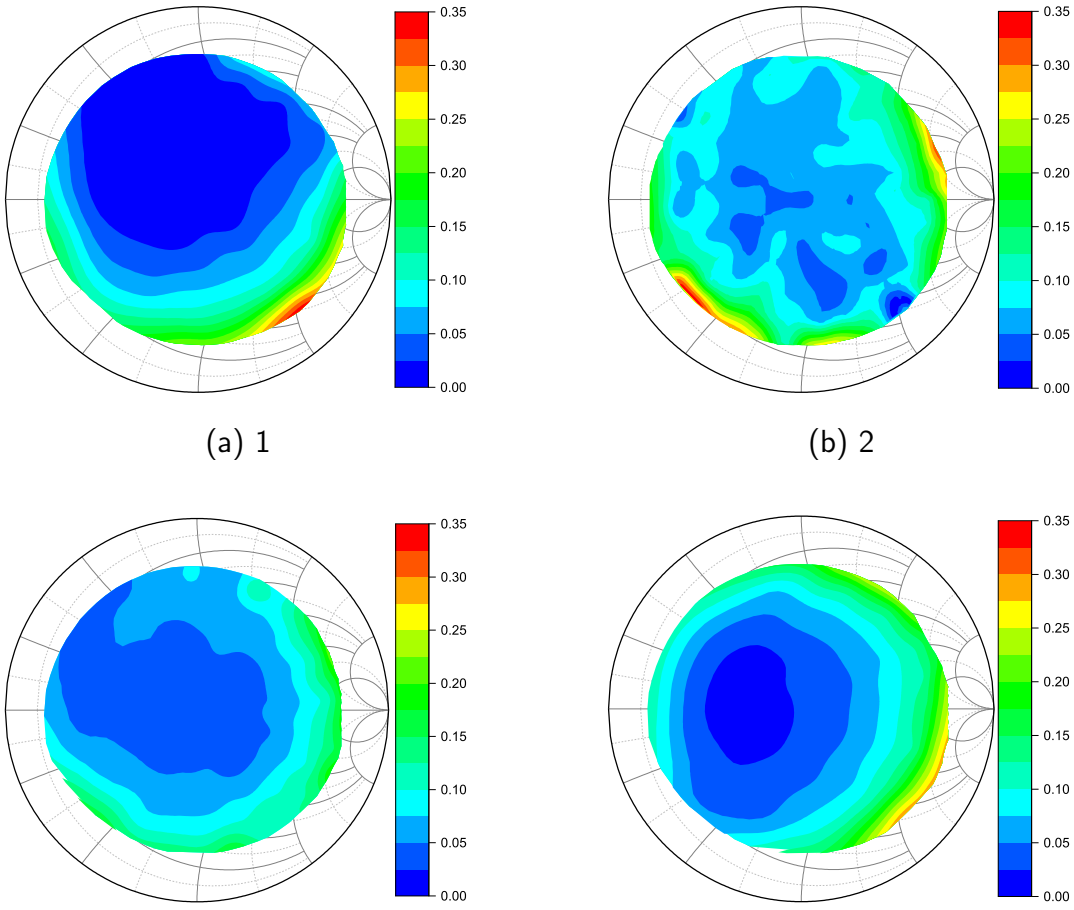

(a) 1 (b) 2

(c) 3 (d) 4

Figure 6.18: LP measurements of power gain in decibels for a zero-length thru on the passive LP system at 27.5 GHz following a full large-signal calibration and the system configured for measurement.

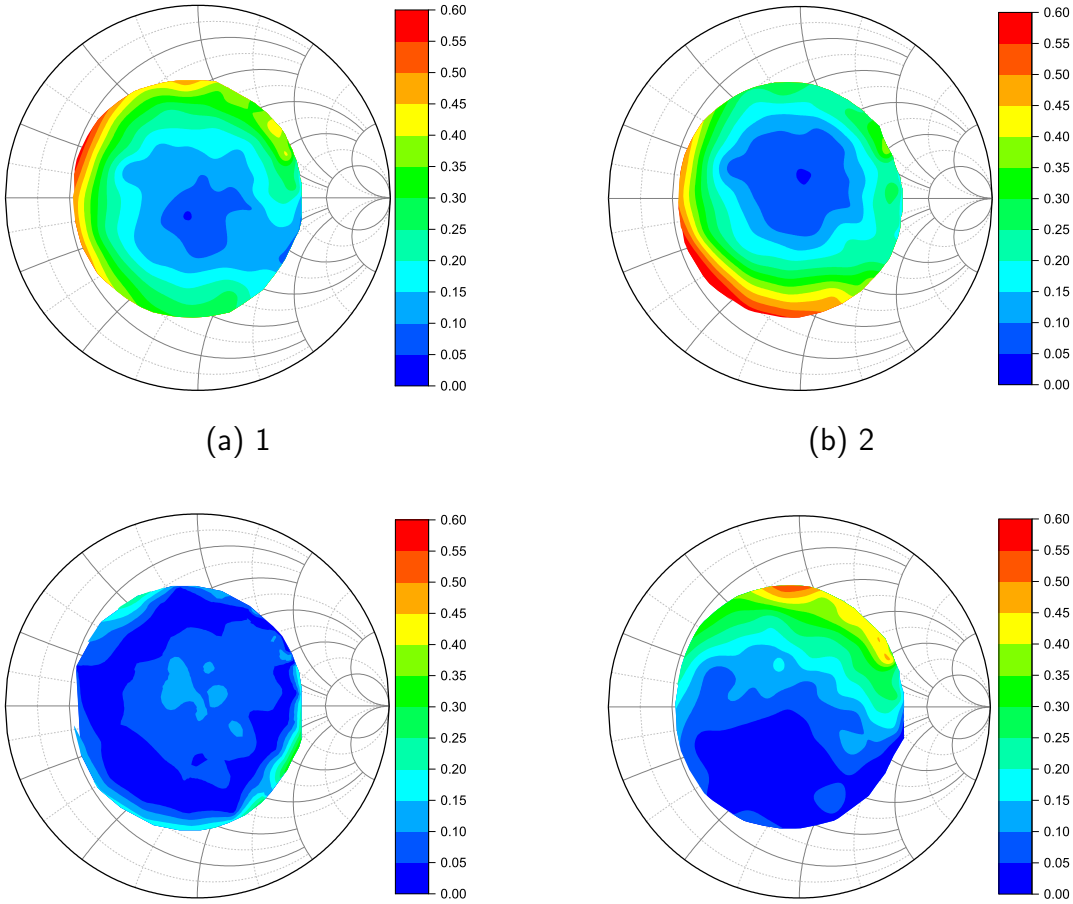

(a) 1 (b) 2

(c) 3 (d) 4

Figure 6.19: LP measurements of power gain in decibels for a zero-length thru on the passive LP system at 82.5 GHz following a full large-signal calibration and the system configured for measurement.

Figure 6.19 shows four examples of the load-pull measurement of a thru standard on the passive system at 82.5 GHz after configuring the system for measurement. The figures show an increasing calibration error above the baseline error of ±0.25 dB. The error increases rapidly, moving to the edge of the maximum tuneable range of the passive tuners, with a maximum power gain of approximately 0.6, 0.6, 0.35 and 0.6 dB for (a), (b), (c) and (d), respectively at $|\Gamma_L| = 0.65$.

In the following figures, a comparison between frequency and measurement system is presented, using the first graph (a) in each set of plots from Figure 6.17, 6.18 and 6.19.

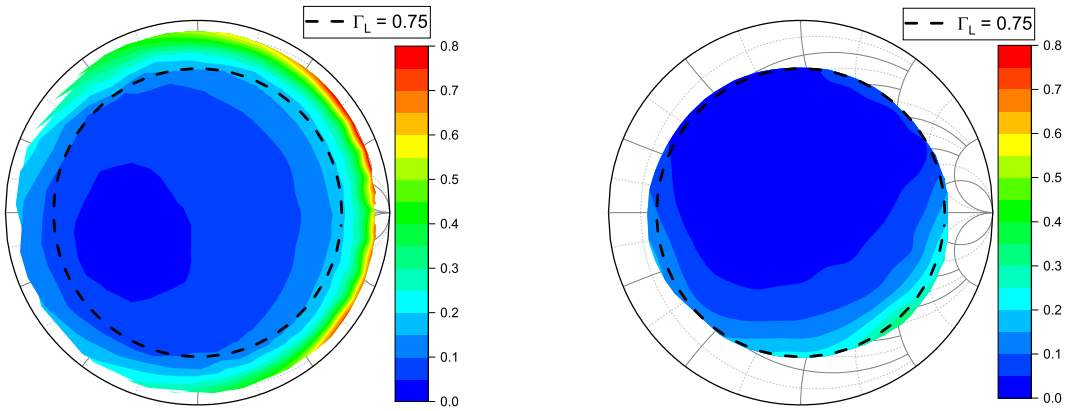

(a) Active System (b) Passive System

Figure 6.20: Measurement system comparison, showing LP measurements of power gain in decibels. The systematic error of the (a) active at 30 GHz and (b) passive system at 27.5 GHz [16].

In Figure 6.20, the systematic error from configuring the system for measurement is compared across both measurement systems at similar frequencies. The same scale was used for both figures, and a dashed line at $|\Gamma_L| = 0.75$ was used to compare the maximum error at a common reflection coefficient. The maximum error is similar for the active and passive system at the common reflection coefficient of 0.25 and 0.35 dB, respectively. These figures show a slightly increased error for the active over the passive system with a difference of 0.1 dB. The reason for the discrepancy of this error is due for two reasons, the first is that the comparison figure is typical error from ten measurements on each system, a limited number of measurements

were taken due to the time taken to calibrate and perform measurements. On the passive system, a full calibration can take up to a full day, whereas on the active system a full calibration and measurement could take several hours. The second reason is that the active system is less mechanically stable than the passive system, looking at the active system in Figure 6.16 (b), the measurement fixtures are connected directly to the directional couplers, which are then mounted directly onto the probes, leaving little mechanical isolation between the measurement fixtures and the calibrated measured system.

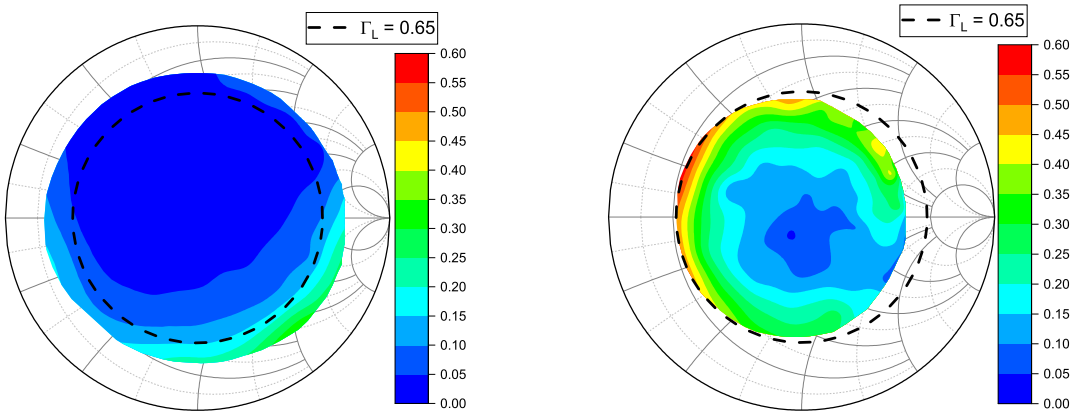

(a) 27.5 GHz (b) 82.5 GHz

Figure 6.21: Frequency comparison, showing LP measurements of power gain in decibels. The systematic error at (a) 27.5 GHz and (b) 82.5 GHz on the passive LP system.

In Figure 6.21, the systematic error from configuring the system for measurement is compared for the passive LP system across a wide frequency range. The same scale was used for both figures, and a dashed line at $|\Gamma_L| = 0.65$ was used to compare the maximum error at a common reflection coefficient. There is an increased maximum error for 82.5 GHz compared to 27.5 GHz at the common reflection coefficient. The maximum error is 0.2 and 0.6 dB at 27.5 and 82.5 GHz, respectively. These figures show a significant difference in the error for the E-band measurement up to 0.4 dB, highlighting the effect of reconfiguration and its frequency dependence. Across all measurements, there is a rapid increase towards the edge of the Smith chart; this significantly affects the accuracy of measurements at the E-band; this is of particular

concern for active implementations at this frequency, where a greater reflection coefficient can be reached.

Simulations

The important first stage in determining best case uncertainty in the load-pull calibration procedure and measurement set-up was to develop a simulation of the system. The simulation replicates the vector calibration, extended calibration, absolute calibration and device measurement. This was important to produce a baseline ideal system without any error sources, this allowed for the implementation of existing calibration algorithms and implementation of the power calibration. This proved very useful due to limited published material and equations for implementation of a full calibration procedure of a load-pull system, this information and knowledge exists and has been implemented in all real-world load-pull systems but rarely published works describe it.

The simulated system correctly showed that in an ideal case the power gain across the entire Smith chart should be zero. The simulation was also used to test possible conditions to see where error from reconfiguring the measurement system after calibration arises. This method does not provide any definitive proof about the source of the error it only offers a guide of the effect by adding small error in the system.

The simulation was created on Keysight ADS and consists of three schematics: the first is a simulation of the vector calibration stage using a TRL calibration kit; the second is the absolute calibration, and the third is a schematic that can perform a load-pull measurement, using the calibration coefficients determined in the calibration schematics.

Figure 6.22 shows the schematic for simulating the vector calibration stage of a large signal calibration. It consists of a switched source for forward and reverse measurements; the same control signal for the source switch, $SPDT\_Switch3$, is used to control $SDPT\_Switch1$ and $SPDT\_Switch2$; when performing forward or

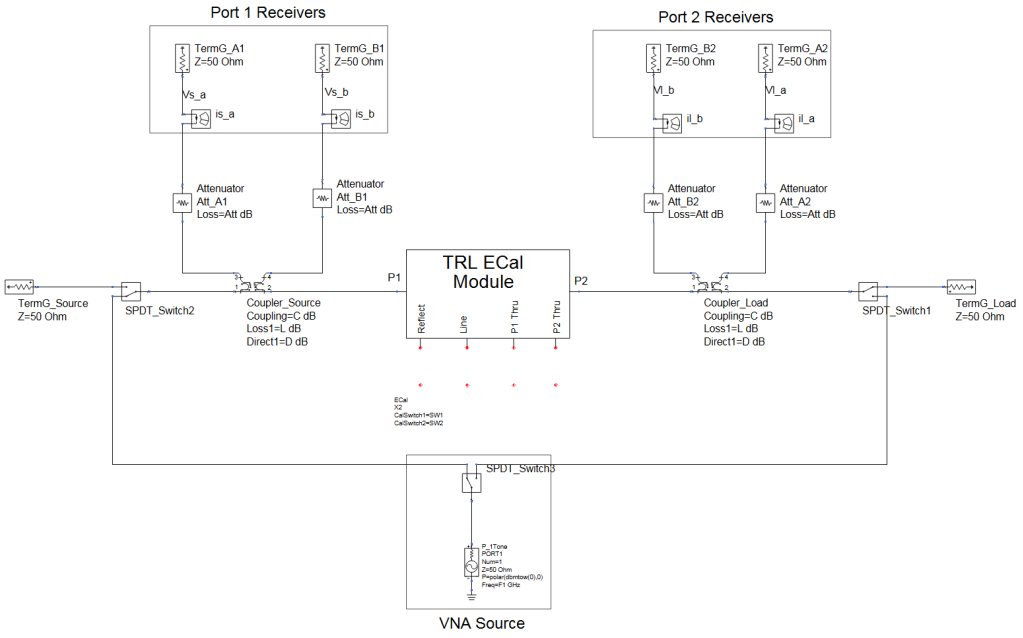

Figure 6.22: Schematic for simulating a vector calibration of a large signal measurement system.

reverse measurements, the system is always loaded with 50 Ω. A dual directional coupler is placed for sampling the waves, with controllable coupling C, loss L and directivity D. The receivers are represented by a 50 Ω load and a current and voltage probe for calculating the measured wave, with controllable attenuation Att to replicate receiver attenuation for high-power measurements. At the centre of the system is a TRL electronic calibration (e-cal) module, a set of ideal switches that toggle between the thru, reflect and line standards. The waves are saved for each measurement direction and standard, and the vector calibration coefficients are calculated.

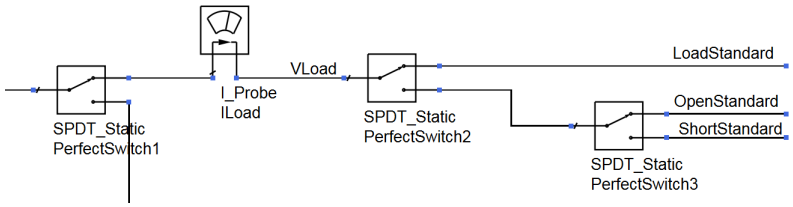

Figure 6.23: Schematic showing the extended calibration plane for simulating an absolute calibration.

The second schematic replicates the first, in this schematic however, the thru

standard is placed at the DUT reference plane and the circuit in Figure 6.23 is placed at the load-side to represent the extended calibration and absolute calibration stage. A set of switches transition between the SOL standards and the one-port calibration coefficients are calculated. When the load standard is measured, the voltage and current are saved and are used to represent the power measurement.

The absolute scaling term is calculated using the error coefficients for the vector calibration and (3.60). The calibrated input power can be compared with the power calculated using a set of voltage and current probes at the centre of the thru standard to verify the calibration.

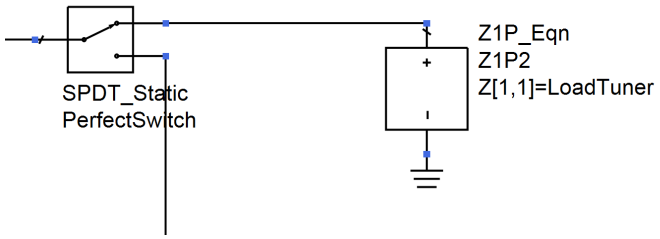

Figure 6.24: Schematic showing the variable load tuner for simulating a load-pull.

The third schematic is the load-pull simulation using the measurement system of the previous two schematics. In Figure 6.24 only the tuneable load component is shown, this impedance is swept across a defined grid. The measured waves are calibrated to view the waves at the DUT plane, and power and gain contours can be plotted.

Minor changes can be made to the simulated system to potentially replicate effects caused by reconfiguring the measurement system in an attempt to understand the cause of the systematic error. In these experiments, the parameters of the couplers were changed equally; these were the MVSWR, which is the VSWR of the mainline, the loss, the directivity and the coupling; for simplicity, these were changed identically on both couplers by 5%.

From Figure 6.25, the effect of changing the coupler parameters in isolation following the large-signal calibration. A load-pull measurement is performed, and the error parameters are plotted. The results show a large dispersion of all the parame-

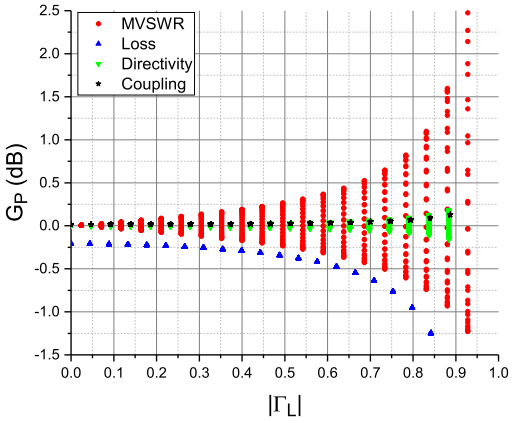

(a) Power gain, in decibels.

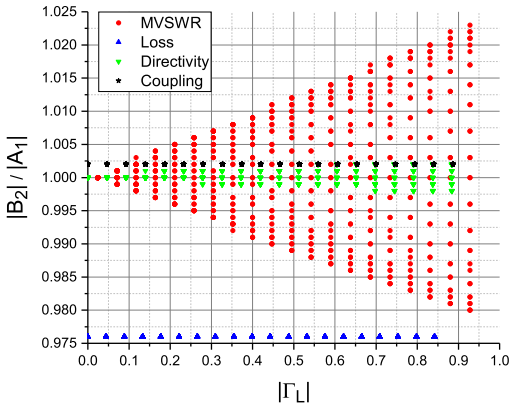

(b) Absolute wave ratio $|b_2|/—a_1|$

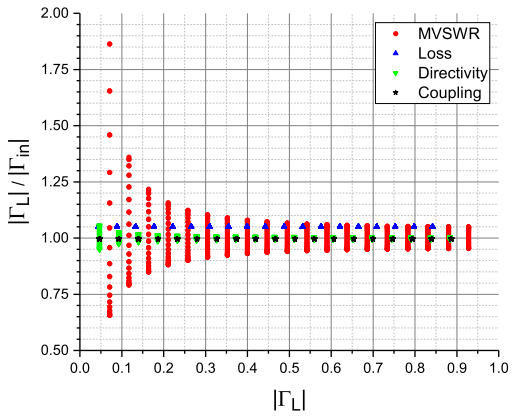

(c) Reflection coefficient magnitude ratio.

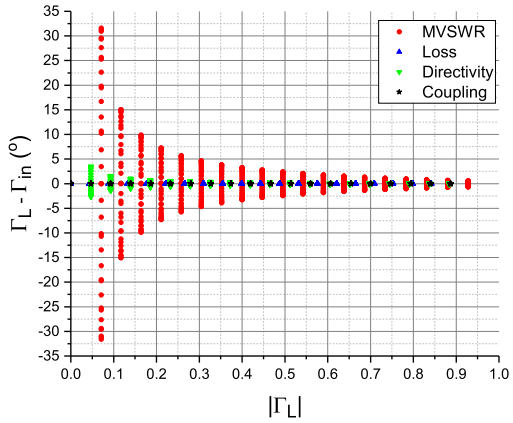

(d) Reflection coefficient phase ratio.

Figure 6.25: Calibration error metrics versus the magnitude of Γ_L when changing a parameter after the calibration stage, a load-pull was performed, and the parameters plotted. In each figure, the result of changing four parameters in isolation is the coupler matching $MVSWR$, loss, directivity, and coupling.

ters for a change in the coupler mainline VSWR. The change in the loss introduces a large change in G_P as the reflection coefficient moves towards the edge of the Smith chart.

The next set of experiments, parameters that could reasonably change when configuring the measurement system. In this, a small 1° phase change is applied to a_1, in the other two measurements, a small 5% loss is applied to either b_2 or a_2

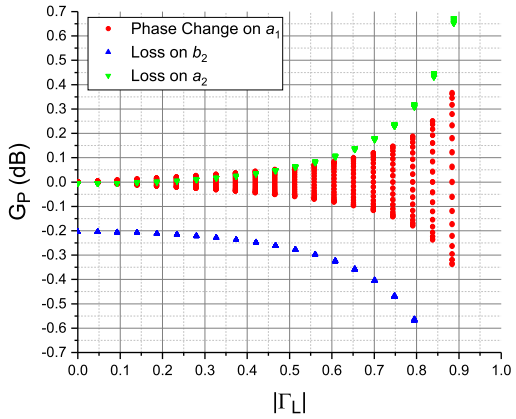

(a) Power gain, in decibels.

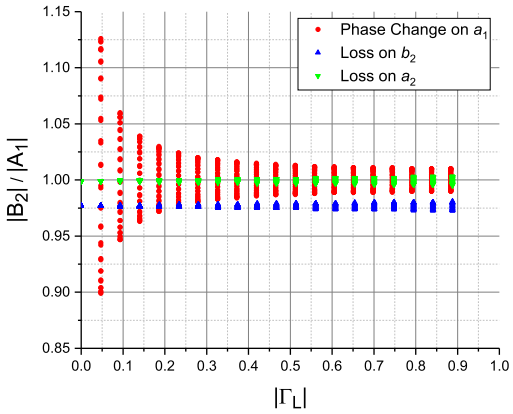

(b) Absolute wave ratio $|b_2|/|a_1|$

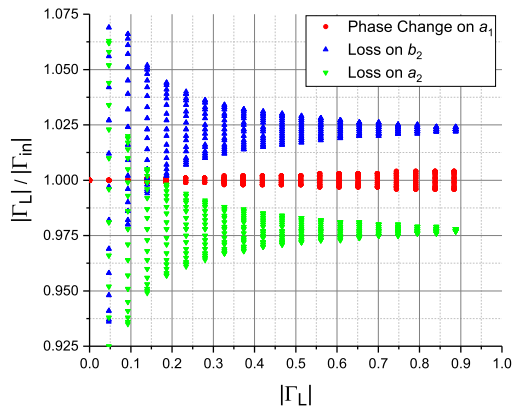

(c) Reflection coefficient magnitude ratio.

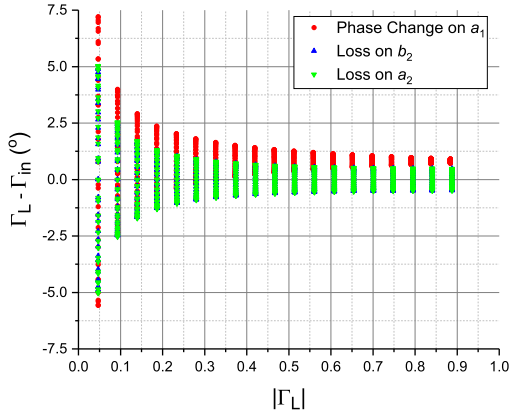

(d) Reflection coefficient phase ratio.

Figure 6.26: Calibration error metrics versus the magnitude of Γ_L when changing a parameter after the calibration stage, a load-pull was performed, and the parameters plotted. Each figure shows the result of changing the phase in the a_1 receiver path, the loss in the b_2 and a_2 receiver path.

Figure 6.26 (a) shows a significant deviation in G_P as a function of the reflection coefficient. There is no dispersion for the loss on b_2 and a_1, so it is independent of the phase of the reflection coefficient. For a phase change in the receiver path of a_1, the error depends on the reflection coefficient phase.

These results highlight the isolated effects on the error parameters when a single parameter is changed. While, in simulation, these effects can be directly determined using the calibration error box terms, the task becomes more complex in a real measurement system. This is because multiple terms may change when reconfiguring the system. No straightforward method exists to recompute the new error terms once the system has been reconfigured.

6.5 Conclusion

This chapter provides a comprehensive investigation of measurement uncertainty in real load-pull systems. Using an LP on a zero-length thru standard was the technique used to determine the calibration uncertainty. Firstly, the chapter determines a baseline level of uncertainty for a active and a passive load-pull system. This was obtained by limiting large error sources; the TRL calibration technique was used to maximise calibration accuracy at mm-wave frequencies, and other sources of uncertainty were reduced, such as lowering the calibration IF bandwidth on the VNA to maximise dynamic range and limiting error associated with mechanical alterations caused by altering the system following calibration. Calibration was performed 10 times, and the load-pull measurement on the thru standard determined the uncertainty. A maximum uncertainty of $< 0.15\,\mathrm{dB}$ was found for $|\Gamma_\mathrm{L}| = 0.95$ at 27.5 GHz on the active system, whilst on the passive system at 27.5 GHz, it was $< 0.1\,\mathrm{dB}$ at $|\Gamma_\mathrm{L}| = 0.75$ and $< 0.25\,\mathrm{dB}$ at $|\Gamma_\mathrm{L}| = 0.65$ for 82.5 GHz.

These uncertainties were described as being related to measurement repeatability and not discussed further. These uncertainties were used as a baseline for the best case as a platform for further investigations. When configuring the systems for real-world measurements, these uncertainties increased. The first mechanism described that caused an increased error was due to random errors related to the system's dynamic range. When an operator measures a high-power DUT, attenuators are added to prevent receiver saturation; due to a limited VNA source power, this leads to a degraded dynamic range during calibration. These considerations were inves-

tigated using a combination of simulation and measurements to determine what dynamic range was required during calibration to achieve accurate load-pull measurement results across the Smith chart. It was shown that there was a direct link between calibration dynamic range and accuracy when measuring highly reflective loads, with a rapid increase as the load reflection coefficient moves to the edge of the Smith chart. There was good agreement between the simulation and measurements, which concluded that a dynamic range of >70 dB is required to achieve high accuracy measurements (<0.1 dB).

The other mechanism discussed was calibration error introduced by reconfiguration of the measurement system. Following the vector calibration stage, the system must be altered to perform absolute calibration, which allows for the determination of the power scaling calibration error term and the addition of measurement fixtures such as circulators, bias-tees, and driver amplifiers. These alterations can cause mechanical perturbations, which slightly change the network parameters of the measurement; it was shown that these slight changes result in large calibration errors when measuring highly reflective loads. These errors are system-dependent and relate to how isolated any alterations are from the calibrated system, although this leads to a trade-off between mechanical stability and reconfigurability, which is required to perform these complex calibration and measurement procedures. For the systems described in this work, a similar maximum error was found when comparing at the same frequency and load reflection coefficient, 0.3 dB at $\Gamma_L = 0.75$ at Ka-band. Whilst on the passive system, at E-band, this maximum error increases to 0.7 dB.

References

[1] H. Qi, J. Benedikt, and P. J. Tasker. "Nonlinear Data Utilization: From Direct Data Lookup to Behavioral Modeling". In: *IEEE Trans. Microw. Theory Techn.* 57.6 (2009), pp. 1425–1432.

[2] D.E. Root et al. "X-parameters: The New Paradigm for Measurement, Modeling, and Design of Nonlinear RF and Microwave components". In: *Microw. Eng. Eur.* 12 (2008), p. 16.

[3] I. Angelov, H. Zirath, and N. Rosman. “A New Empirical Nonlinear Model for HEMT and MESFET Devices”. In: *IEEE Trans. Microw. Theory Techn.* 40.12 (1992), pp. 2258–2266.

[4] Keysight Technologies. *EE HEMT1*. URL: `qthelp://ads.2024update1/doc/ccnld/EE_HEMT1.html#EEHEMT1-reference2`.

[5] D. Williams. *NIST Microw. Uncertainty Framework*. URL: `https://www.nist.gov/servicesresources/software/%20wafer-calibration-software`.

[6] K. Łukasik et al. “Uncertainty in Large-Signal Measurements Under Variable Load Conditions”. In: *IEEE Trans. Microw. Theory Techn.* 68.8 (2020), pp. 3532–3546.

[7] A. Ferrero, V. Teppati, and A. Carullo. “Accuracy Evaluation of On-Wafer Load-Pull Measurements”. In: *IEEE Trans. Microw. Theory Techn.* 49.1 (2001), pp. 39–43.

[8] V. Teppati et al. “Accuracy Improvement of Real-Time Load-Pull Measurements”. In: *IEEE Trans. on Instrum. and Meas.* 56.2 (2007), pp. 610–613.

[9] S. Bonino, V. Teppati, and A. Ferrero. “Further Improvements in Real-Time Load-Pull Measurement Accuracy”. In: *IEEE Microw. and Wireless Compon. Lett.* 20.2 (2010), pp. 121–123.

[10] V. Teppati and C. R. Bolognesi. “Evaluation and Reduction of Calibration Residual Uncertainty in Load-Pull Measurements at Millimeter-Wave Frequencies”. In: *IEEE Trans. on Instrum. and Meas.* 61.3 (2012), pp. 817–822.

[11] H. Wang et al. *“Power Amplifiers Performance Study 2000 - Present”*. URL: `https://ideas.ethz.ch/research/surveys/pa-survey.html`.

[12] B. Cimbili et al. “High-Efficiency Watt-Level E-band GaN Power Amplifier with a Compact Low-loss Combiner”. In: *IEEE Top. Conf. on RF/Microw. Power Amplifiers for Radio and Wireless Appl. (PAWR)*. 2023, pp. 42–44.

[13] E. Ture et al. “High-Power (>2 W) E-Band PA MMIC Based on High Efficiency GaN-HEMTs with Optimized Buffer”. In: *IEEE MTT-S Int. Microw. Symp. (IMS)*. 2019, pp. 1407–1410.

[14] Fixed Radio Systems; Characteristics and requirements for point-to-point equipment and antennas. *ETSI EN 302 217-2 V3.3.0 , 2021*. Tech. rep. ETSI, 2021.

[15] A. Baddeley, R. Quaglia, and P. Tasker. “Evaluation and Improvement of mm-wave Load Pull Measurement accuracy”. In: *ARMMS RF & Microw. Society Conf.* Apr. 2024.

[16] A. Baddeley, R. Quaglia, and P. J. Tasker. “Calibration Error Reduction in Millimeter-Wave Load–Pull Systems Measuring Highly Reflective Loads”. In: *IEEE Trans. Microw. Theory Techn.* (2024), pp. 1–13. DOI: `10.1109/TMTT.2024.3495544`.

[17] G.F. Engen and C.A. Hoer. “Thru-Reflect-Line: An Improved Technique for Calibrating the Dual Six-Port Automatic Network Analyzer”. In: *IEEE Trans. Microw. Theory Techn.* 27.12 (1979), pp. 987–993.

[18] D. F. Williams, R. B. Marks, and A. Davidson. “Comparison of On-Wafer Calibrations”. In: *ARFTG Microw. Meas. Conf.* Vol. 20. 1991, pp. 68–81. DOI: `10.1109/ARFTG.1991.324040`.

[19] S. Shin et al. “Comparison of On-Wafer Calibrations for Measurements of Active and Passive Devices at Millimeter-wave Frequencies”. In: Nov. 2023.

[20] A. Rumiantsev et al. “Application of On-Wafer Calibration Technology for Advanced High-Speed BiCMOS Technology”. In: *IEEE Bipolar/BiCMOS Circuits and Technol. Meet. (BCTM)*. 2010, pp. 98–101.

[21] K. Yau et al. “Device and IC Characterization Above 100 GHz”. In: *IEEE Microw. Magazine* 13.1 (2012), pp. 30–54.

[22] A. Aldoumani et al. “Enhanced Vector Calibration of Load-Pull Measurement Systems”. In: *ARFTG Microw. Meas. Conf.* 2014, pp. 1–4.

[23] A. C. Stelson et al. “Quantifying Receiver Nonlinearities in VNA Measurements for the WR-15 Waveguide Band”. In: *IEEE Trans. Microw. Theory Techn.* 70.5 (2022), pp. 2743–2749.

[24] A. Lewandowski and D. Williams. “Characterization and Modeling of Random Vector Network Analyzer Measurement Errors”. In: *Int. Conf. on Microw.s, Radar and Wireless Commun. (MIKON)*. 2008, pp. 1–4.

[25] A. Ferrero. “High Power Load Pull Measurements: Today Technologies and Tomorrow Challenges”. In: *ARFTG Microw. Meas. Conf.* 2011, pp. 1–3.

[26] Rohde and Schwarz. *ZVA Vector Network Analyzer Specifications*. Oct. 2020. URL: `https://www.rohde-schwarz.com/brochure-datasheet/zva`.

Chapter 7

Error Correction Enhancement Technique for Accurate Millimetre-Wave Load-Pull Measurements

7.1 Introduction

It has been established in Chapter 6 that unavoidable errors can be introduced into a measurement system through two primary mechanisms. The first arises from the limited dynamic range during calibration, caused by the added attenuation required to perform load-pull measurements on high-output-power devices. The second involves changes to the system configuration to enable device measurement.

Both sources of error become increasingly significant at the edge of the Smith chart. This is relevant to mm-wave compound semiconductor devices that typically have an optimum reflection coefficient at highly reflective load impedances, where measurement errors are most pronounced. In turn, this error propagates to model accuracy, which is particularly problematic for PA designers because they rely heavily on accurate models to achieve first-pass success of tape-outs.

In the literature, several papers discuss the sources of calibration uncertainty and propose methods to correct it. In [1], the authors identify the strong load dependence of calibration uncertainty and attempt to mitigate it using power gain as the figure of merit (FoM). After calibration, they conduct a load-pull measurement on a thru standard and apply a weighted minimisation algorithm to adjust the error coefficients. This reduces the variation in power gain across the Smith chart. The algorithm was tested in simulation with the TRM, SOLT, and TRL calibration techniques and in measurement with SOLT and TRL. In both cases, the correction method effectively reduces residual uncertainty, achieving reductions of up to 0.4 dB in the SOLR case.

Building upon this work, [2] addresses the limitations of the original algorithm, particularly its reduced effectiveness at high reflection coefficients due to improper weighting, which led to convergence issues. To address this, the authors improve the minimisation function by incorporating the Nelder-Mead multidimensional non-linear algorithm, achieving convergence within 100-200 iterations. Using the same dataset as [1], the revised algorithm shows improved performance, reducing the maximum error from 1.3 dB to 0.7 dB, compared to the original algorithm's which increased the maximum error to 4.9 dB. Additionally, the authors optimise the selection of load impedance points, finding that focusing on conditions around the edge of the Smith chart provides the best trade-off between accuracy and convergence time, achieving convergence in 31 s. In [3], the algorithm is further adapted for non-realtime measurement systems.

While these algorithms effectively reduce calibration uncertainty across the Smith chart, they act directly on the calibration coefficients without imposing constraints, potentially causing the coefficients to deviate from physical reality. Since power gain on the thru standard is the primary target, multiple solutions may minimise power gain, but the impact on other metrics remains unclear.

An alternative method for improving TRL calibration accuracy in load-pull measurements was presented in [4]. Here, the authors use an active load-pull system

to calibrate the measurement system directly. Standard S-parameter measurements were performed on the reflect standard, while load-pull measurements were conducted on the thru and line standards. These measurements generate sets of measurement waves, a and b, from which equivalent S-parameters are calculated using a least-squares approach.

This approach provides additional data points for calculating the S-parameters of the thru and line standards, resulting in a more accurate estimation. The authors validate their method by performing a load-pull measurement across the Smith chart on a thru standard, comparing gain (b_2/a_1) with that obtained from a standard vector calibration. The enhanced calibration achieves a maximum gain variation of 0.006 dB, compared to 0.06 dB for the standard vector calibration.

While effective at improving the quality of the calibration data, this method focuses exclusively on vector calibration and lacks practical details of the setup, such as the measurement frequency or connector types (coaxial/on-wafer). Furthermore, the load-pull on the thru and line standards is conducted before the final system configuration, meaning the approach still suffers from the errors discussed in Chapter 6. Implementing this method in commercial load-pull setups is challenging, as most software does not allow load-pull operations with uncalibrated data. Using uncalibrated data could reduce effectiveness due to a lack of prior knowledge about effective Smith chart coverage.

This chapter proposes a large signal correction methodology [5] which is an expansion on the traditional large-signal calibration procedure. An additional step is added to allow for a "recalibration" of the system once it is configured in its final measurement state. The additional step uses the underlying algorithm from [4] but applies it in a different way. In [4], a large dataset of measured waves is collected across the Smith chart for the computation of updated thru and line s-parameter matrices. The load-pull on the standards was performed prior to setting up the system for measurement on an uncalibrated, unperturbed system and subsequently tested on an unperturbed system, prior to correction the error was only 0.06 dB. This

method expands on this by integrating it seamlessly into a standard large signal calibration measurement system and the algorithm is applied at a stage to yield the most effective error correction. This allows for the mitigation of random and mechanical error issues discussed in Chapter 6. The chapter details the theory and implementation of the authors second-step calibration technique and demonstrates its effectiveness in improving measurement accuracy for real mm-wave devices in both active and passive measurement systems.

7.2 Procedure

The second-step calibration method in a practical load-pull measurement process flow is outlined below:

1. Perform a large-signal calibration.
2. Configure the system into its final measurement state by adding circulators, bias-tee and amplifiers.
3. Perform an LP measurement on the thru standard.
4. Perform an LP measurement on the line/s standard.
5. De-embed the calibration from the LP measurements to obtain uncorrected measured waves.
6. Perform a least squares operation on the uncorrected measured waves to calculate two new "equivalent" S-parameter matrices for the thru and line standards.
7. Recompute the TRL calibration coefficients using the new S-parameter matrices for the thru and line along with the original reflect S-parameter matrix.

This chapter focuses on TRL/mTRL applications due to their superior accuracy at mm-wave frequencies [6], [7]. However, the author sees no inherent reason why the

proposed method cannot be applied to other calibration techniques that utilise at least one line or thru standard, though a reduction in performance can be expected.

A two-step calibration solution using the proposed method is presented. The process begins with a standard calibration (Step 1), followed by a second calibration (Steps 3–7) that incorporates the method proposed in [4]. This method consists of performing a load-pull on the thru calibration standard, collecting the measured waves and performing a least squares method to generate an equivalent s-parameter matrix, this is performed once the system is mechanically stable. It is crucial to emphasise the necessity of performing Step 1 for at least two reasons. Firstly, in on-wafer systems, absolute power calibration inherently requires mechanical adjustments to connect the coaxial calibration kit for extended calibration and the power meter for the power reference. Secondly, the vector calibration provides an initial estimate of the corrected Γ_{L} at the DUT, essential in mm-wave on-wafer systems due to the significant discrepancy between the reflection coefficient at the receiver and DUT planes. This initial estimate ensures that the load-pull measurements in Steps 3–4 achieve adequate Smith chart coverage.

Knowing the Smith chart coverage is critical for maximising the accuracy of the technique. As demonstrated in [4], the method's accuracy improves as the radius of the reflection coefficient increases.

7.3 Method

7.3.1 Theory

The method is based on the condition that the *physical* network parameters of the thru and line standards are independent of Γ_{L}, while the *measured* network parameters can depend on Γ_{L} [4]. A least-squares algorithm generates "equivalent" measured S-parameters for the thru and line standards, which minimises the deviation across the set of Γ_{L} conditions. Specifically, if n different Γ_{L} conditions are measured, the uncorrected waves b_0, b_3, a_0, and a_3 can be assembled into a matrix

equation representing the standard S-parameter relationship, as shown below.

$$\begin{bmatrix} b_{0,1} & \dots & b_{0,n} \\ b_{3,1} & \dots & b_{3,n} \end{bmatrix} = \begin{bmatrix} S_{Raw} \end{bmatrix} \begin{bmatrix} a_{0,1} & \dots & a_{0,n} \\ a_{3,1} & \dots & a_{3,n} \end{bmatrix} \tag{7.1}$$

where S_{Raw} is the equivalent S-parameter matrix of either the thru or line.

The Moore-Penrose pseudo-inverse is used as part of the least squares method to derive S_{Raw} due to a rectangular A matrix. In MATLAB, the *pinv* function can perform this operation efficiently.

$$S_{\text{Raw}} = A^{+}B \tag{7.2}$$

where

$$A^{+} = (A^{T}A)^{-1}A^{T}\,. \tag{7.3}$$

The methodology is designed for practical implementation because most commercial LP software provides the calibrated waves and the error box coefficients in a calibration and measurement file. This method uses uncorrected waves derived from the measured waves and the original calibration coefficients.

The large-signal calibration equation that converts raw to calibrated waves has been presented in previous chapters; however, it is repeated here for convenience:

$$\begin{bmatrix} b_{1,d} \\ a_{1,d} \\ b_{2,d} \\ a_{2,d} \end{bmatrix} = \frac{1}{e_{10}} \begin{bmatrix} \frac{1}{e_{01}} & -\frac{e_{00}}{e_{01}} & 0 & 0 \\ \frac{e_{11}}{e_{01}} & -\frac{\Delta E_A}{e_{01}} & 0 & 0 \\ 0 & 0 & \frac{1}{e_{32}} & -\frac{e_{33}}{e_{32}} \\ 0 & 0 & \frac{e_{22}}{e_{32}} & \frac{-\Delta E_B}{e_{32}} \end{bmatrix} \begin{bmatrix} b_{1,m} \\ a_{1,m} \\ b_{2,m} \\ a_{2,m} \end{bmatrix} \tag{7.4}$$

Only the relative terms are modified in this method, while the absolute scaling term, e_{10}, remains unchanged. The measured waves are obtained from the known calibrated waves and the original error coefficients by inverting the matrix error box in (7.4).

After converting to raw waves, a new S_{Raw} can be calculated for the thru and line standards. These new values are passed through the TRL calibration algorithm using the original reflect measurement. This generates a new error box, which can be applied to any new measurements while maintaining the original scaling factor, e_{10}.

As discussed in [4], the authors define a calibration quality factor used to assess the self-consistency of the standard measurements. This chapter adopts this quality factor to inform the selection of LP measurements required to generate a new error box. The quality factor of the measured standards is calculated using the following equation:

$$Q = det\left(\left[R_{\text{d}}\right]\left[R_{\text{t}}\right]^{-1}\right) \tag{7.5}$$

Ideally, the Q-factor is unitary. According to the notation in [8], $[R_{\text{d}}]$ is the wave cascading matrix for the raw uncorrected line and $[R_{\text{A}}]$ and $[R_{\text{B}}]$ are the error boxes:

$$\left[R_{\text{d}}\right] = \left[R_{\text{A}}\right]\left[R_{\text{l}}\right]\left[R_{\text{B}}\right] \tag{7.6}$$

with $[R_{\text{l}}]$ being the cascade matrix of an ideal line, while $[R_{\text{t}}]$ is the cascade matrix of the raw uncorrected thru:

$$\left[R_{\text{t}}\right] = \left[R_{\text{A}}\right]\left[R_{\text{B}}\right]. \tag{7.7}$$

7.3.2 Application

In this section, the correction method is applied to the measurement of a thru standard to demonstrate its impact. The methodology follows that outlined in Section 7.3.1. The active and passive LP systems were configured for measurements at 30 GHz and 82.5 GHz, respectively. The systems were set up with 35 dB and 25 dB of attenuation between the DUT and receivers, respectively, with a calibration IF bandwidth of 1 Hz. The calibration was performed with a source power of -10 dBm

at the DUT plane for the active system and 0 dBm for the passive system.

The calibration setup introduces errors due to dynamic range and system alterations. Based on the results from Chapter 6 and the measurement configuration (receiver attenuation) of these systems, dynamic range considerations have a more significant impact on the active than the passive system. This section will present the standard calibration and the second-step procedure results, comparing the outcomes for both systems.

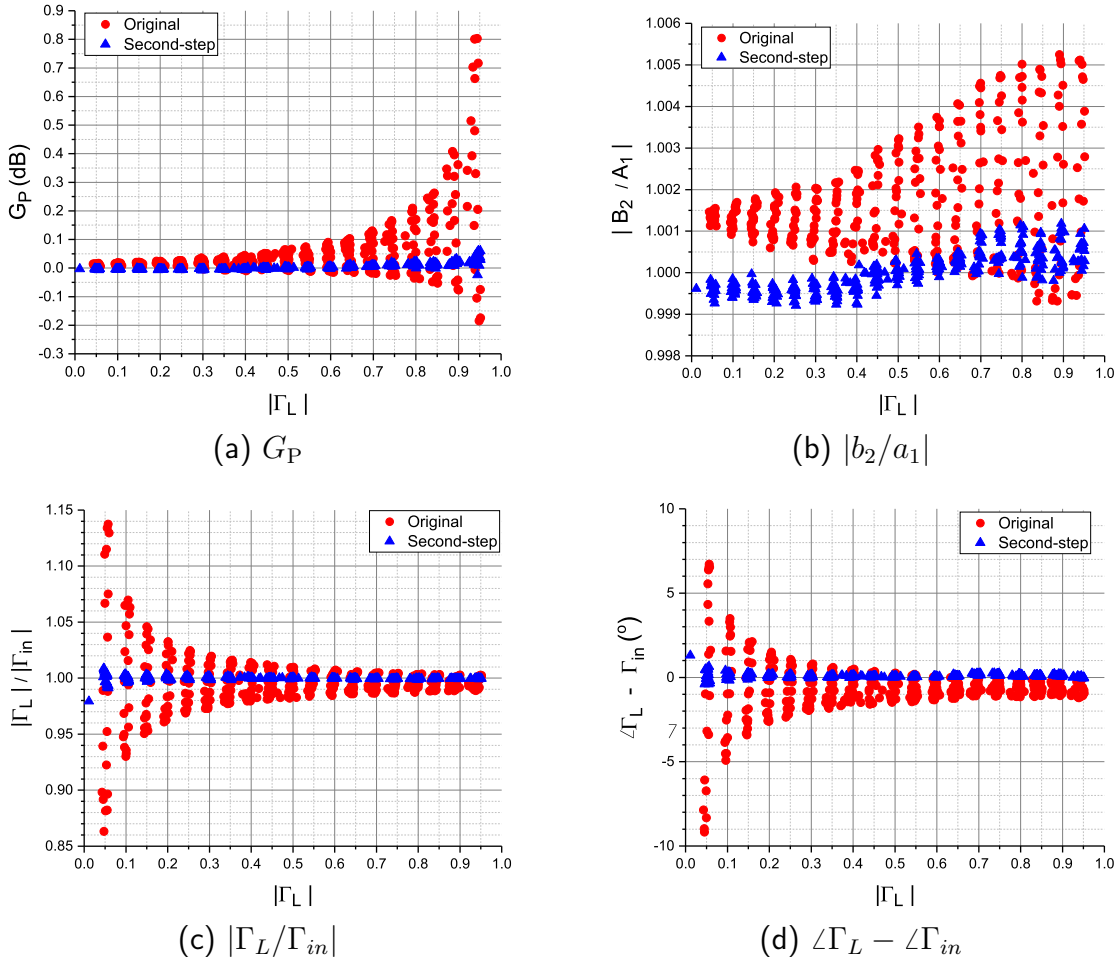

Figure 7.1: LP measurement showing calibration error for different performance metrics versus the magnitude of Γ_L for a zero-length thru on the active LP system at 30 GHz using the original and second-step calibration coefficients [5].

In Figure 7.1, a comparison is made of the measured characteristics of a zero-length thru using the original and second-step calibration coefficients with the active load-pull system at 30 GHz.

For each performance metric, load dependence is observed with the original cal-

ibration coefficients, particularly with dispersion at lower reflection coefficients for the Γ-related terms. However, G_{P} and b_2/a_1 show significant variation as the reflection coefficient moves toward the edge of the Smith chart.

When the second-step coefficients are applied, the error across all metrics is significantly reduced. Specifically, for G_{P}, the maximum error is reduced from 0.8 dB to 0.06 dB; for $|b_2|/|a_1|$, it is reduced from 1.005 to 1.0012, for $|\Gamma_L/\Gamma_{in}|$, it is reduced from 1.14 to 0.975 and $\angle\Gamma_L - \angle\Gamma_{in}$ from 9.5° to 1.5°. These results demonstrate the effectiveness of the second-step calibration procedure. The method was also tested on the passive load-pull system at E-band to further validate its applicability to different load-pull systems.

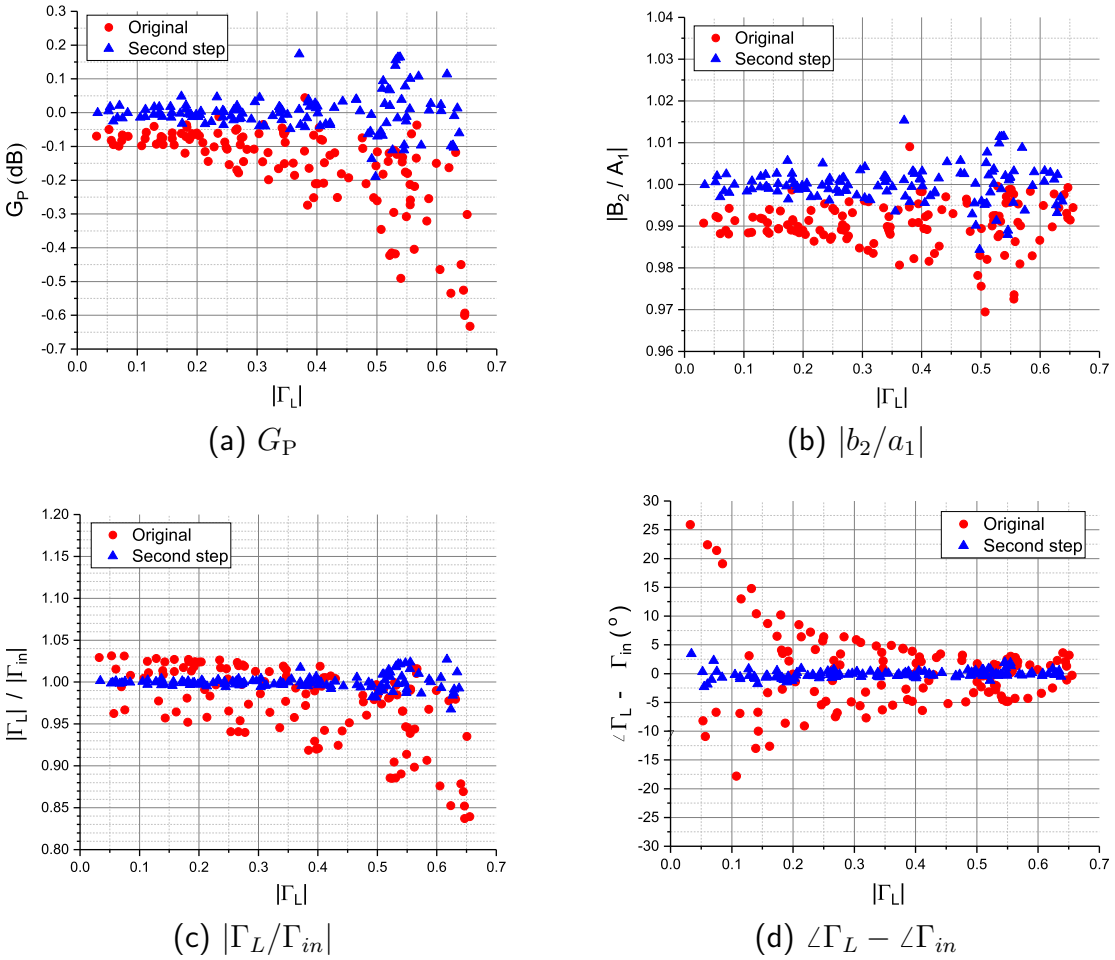

(a) G_{P} (b) $|b_2/a_1|$

(c) $|\Gamma_L/\Gamma_{in}|$ (d) $\angle\Gamma_L - \angle\Gamma_{in}$

Figure 7.2: LP measurement showing calibration error on performance metrics versus the magnitude of Γ_{L} for a zero-length thru on the passive LP system at 82.5 GHz using the original and second-step calibration coefficients [5].

In Figure 7.2, a comparison is made of the measured characteristics of a zero-

length thru using the original and second-step calibration coefficients with the passive load-pull system at 82.5 GHz.

When the second-step coefficients are applied, the error across all metrics is significantly reduced. Specifically, for G_{P}, the maximum error is reduced from 0.65 dB to 0.2 dB; for $|b_2|/|a_1|$, it is reduced from 0.97 to 0.985, for $|\Gamma_L/\Gamma_{in}|$, it is reduced from 0.84 to 0.97 and $\angle\Gamma_L - \angle\Gamma_{in}$ from 26° to 4°.

The second-step calibration procedure was applied to the calibration uncertainty arising from mechanical alterations discussed in Chapter 6 for each frequency and system to validate the method further.

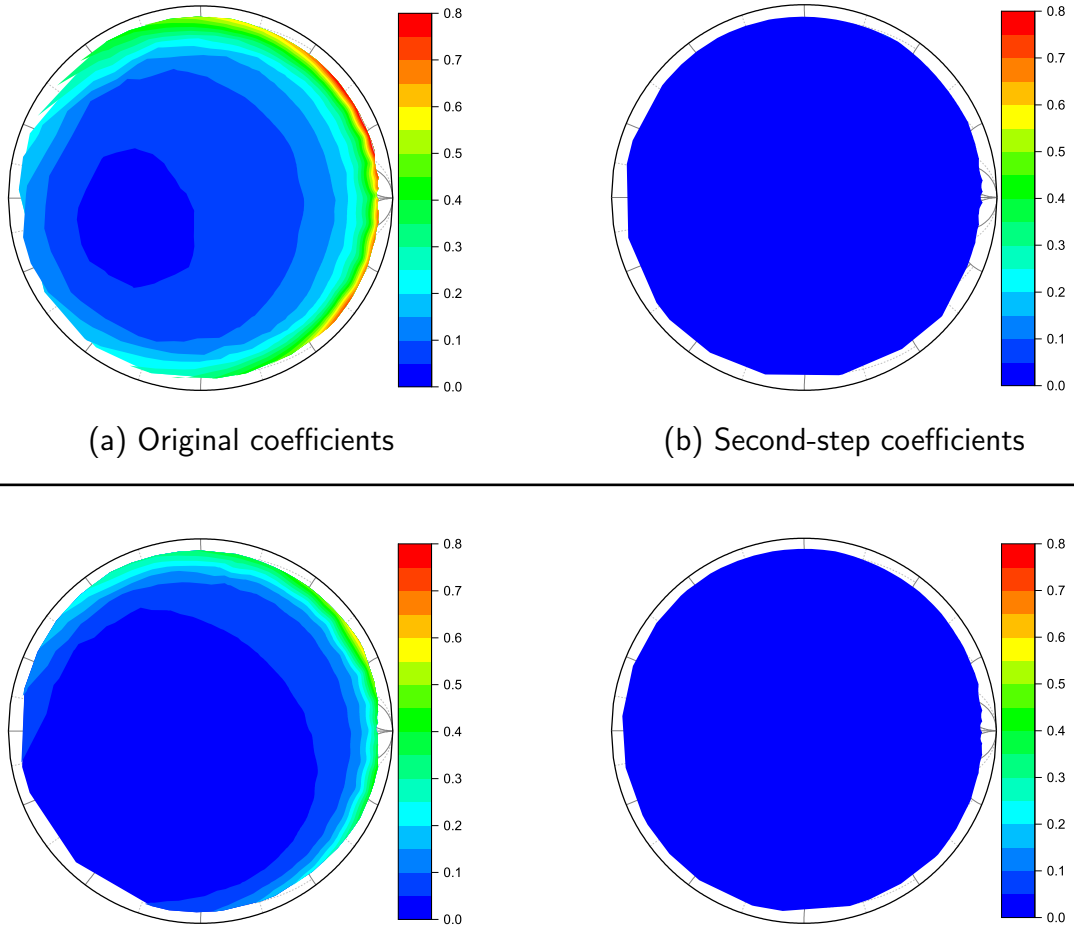

(a) Original coefficients (b) Second-step coefficients

(c) Original coefficients (d) Second-step coefficients

Figure 7.3: LP measurements of power gain in decibels for a zero-length thru on the active LP system at 30 GHz using the original (a) and (c) and second-step (b) and (d) calibration coefficients.

In Figure 7.3, (a) and (c) are the calibration uncertainties taken from Figures 6.17a

and 6.17b, respectively. The second-step technique was applied to both datasets to evaluate the improvement in error. In both cases, the calibration error was reduced from 0.8 and 0.65 dB to 0.05 dB.

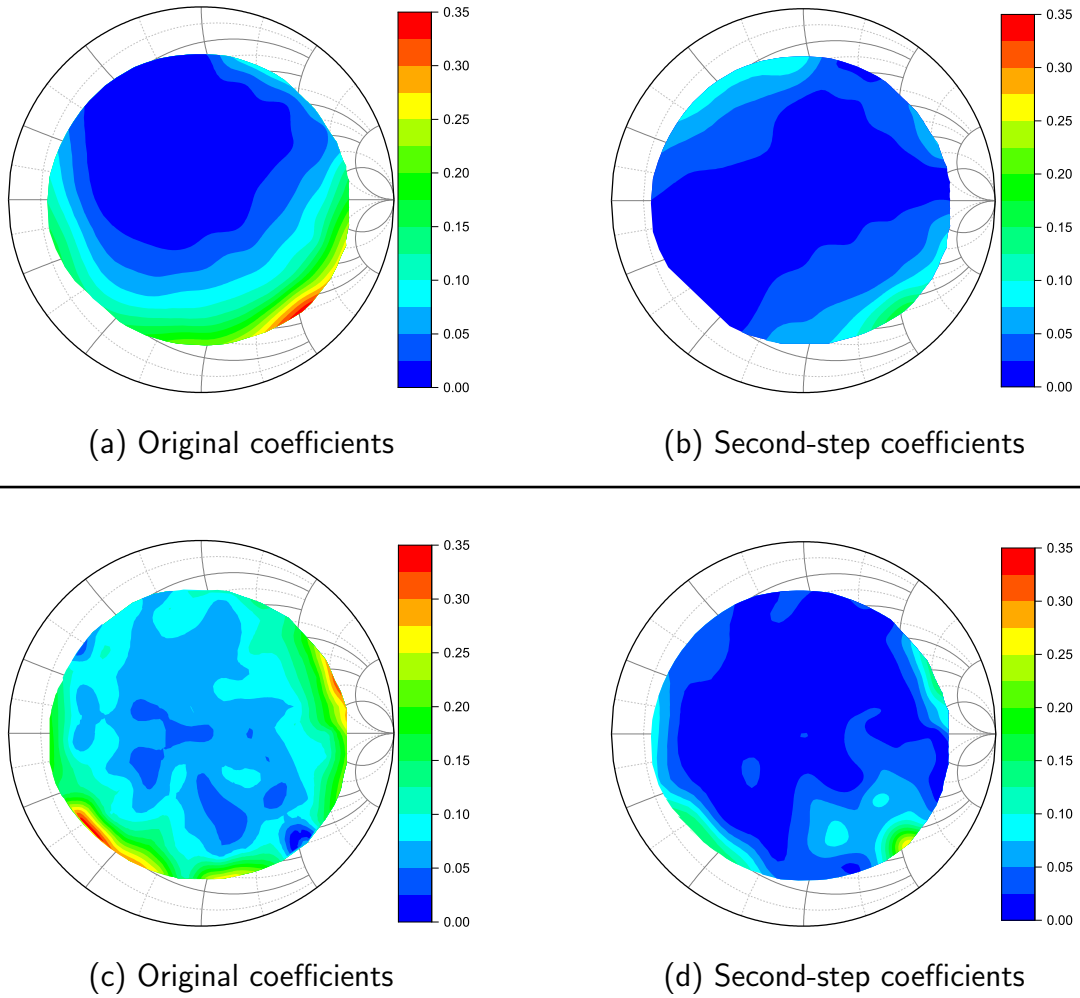

(a) Original coefficients (b) Second-step coefficients

(c) Original coefficients (d) Second-step coefficients

Figure 7.4: LP measurements of power gain in decibels for a zero-length thru on the passive LP system at 27.5 GHz using the original (a) and (c) and second-step (b) and (d) calibration coefficients.

In Figures 7.4, (a) and (c) are calibration uncertainty taken from Figures 6.17 (a) and (b), respectively. The second-step technique was applied to both datasets to evaluate the improvement in error. In both cases, the calibration error was reduced from 0.35 dB to 0.2 and 0.25 dB.

In Figure 7.5, (a) and (c) are calibration uncertainty taken from Figures 6.19a and 6.19b, respectively. The second-step technique was applied to both datasets to evaluate the improvement in error. In both cases, the calibration error was reduced

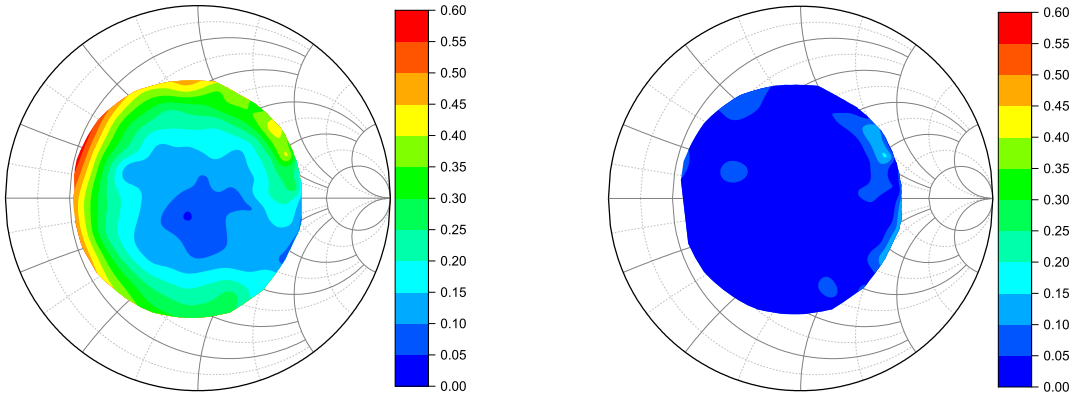

(a) Original coefficients

(b) Second-step coefficients

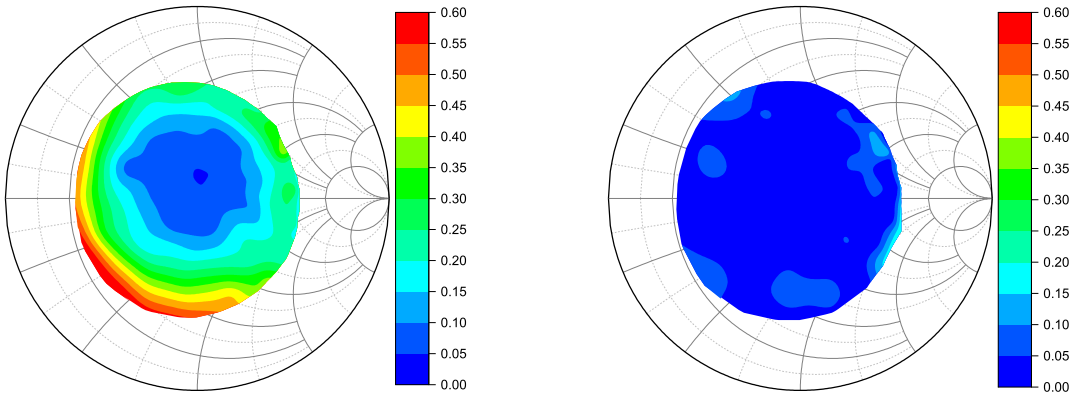

(c) Original coefficients

(d) Second-step coefficients

Figure 7.5: LP measurements of power gain in decibels for a zero-length thru on the passive LP system at 82.5 GHz using the original (a) and (c) and second-step (b) and (d) calibration coefficients.

from 0.6 dB to 0.2 dB and 0.15 dB.

The quality factor from (7.5) is applied to the measurement example shown in Figure 7.5 (a) and (b) at 82.5 GHz using the passive system. The results are summarised in Table 7.2, which demonstrates that the self-consistency of the method improves when LP measurements are performed on both the thru and line standards. Excluding the line standard has no significant effect on G_{P} as evidenced by the dynamic range simulations in Chapter 6, where G_{P} is only influenced by noise added to the thru standard. The error on the line standard would instead manifest in the calibration's reference impedance.

Table 7.1: Calibration Quality Factor.

Standards	Quality Factor
Ideal	1 + j0
Thru	1.042 - j0.0004
Thru + Line	0.998 + j0.008

Table 7.2: Second-Step Calibration Technique Summary.

Parameter	Vs Standard Method	Comment
Calibration Time	Small Increase	Additional Load-Pull
Accuracy	Large Increase	No added error from set-up
Complexity	Small Increase	A simple least squares operation
Applicability	Same	Can be applied on all systems.

7.4 Device Measurement

This section applies the second-step calibration methodology to the measurement of mm-wave devices using both passive and active systems. The DUT was initially measured using the original calibration coefficients, and in post-processing, the second-step calibration coefficients are applied. The device's large-signal metrics are then compared for each calibration method.

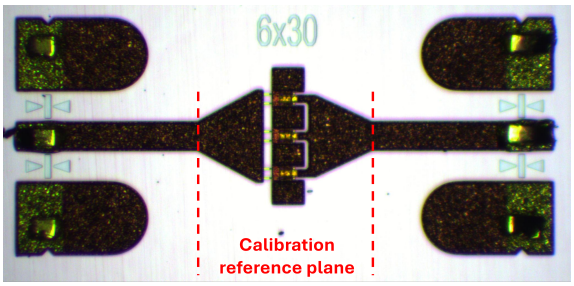

Figure 7.6: Qorvo GaN HEMT with a gate length of 0.15 µm and periphery of 6×30 µm.

The calibration was performed using a TRL calibration kit on the same wafer as the DUT, with the reference plane set at the centre of the thru standard to avoid de-embedding the feed lines when evaluating device performance at the gate/drain manifold [9], [10]. The calibration reference planes are indicated on the images of each device.

7.4.1 Ka-band GaN HEMT

The active system was used to demonstrate the calibration technique applied to the load-pull characterisation of a Qorvo GaN HEMT with a gate length of 0.15 µm and a periphery of 6×30 µm at 30 GHz. The measurement system was configured with 35 dB of attenuation between the receivers and the measurement reference plane, and the calibration power was -10 dBm at the DUT.

After configuring the system for device measurement, an LP measurement was performed on the thru standard to determine the calibration error. The second-step calibration procedure was applied in post-processing, and the results were compared. The results presented here are the same as those shown in Figure 7.1(a).

Figure 7.7 shows the calibration error using the original and second-step calibration coefficients. A reduction in calibration error is observed at $\Gamma_L = 0.95$ with the error decreased from 0.9 to 0.06 dB.

A standard LP characterisation of the GaN HEMT was performed using the original calibration coefficients. This involved a load-pull around the optimum impedance for power and a subsequent power sweep at the optimum impedance for a power

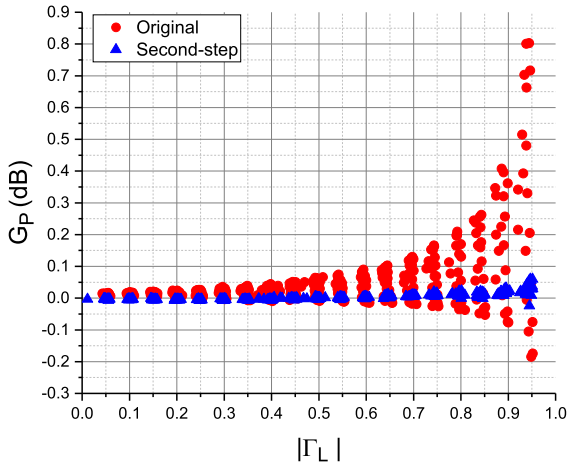

Figure 7.7: LP measurement of power gain in decibels versus the magnitude of Γ_L for a zero-length thru on the active LP system at 30 GHz [5].

and PAE match.

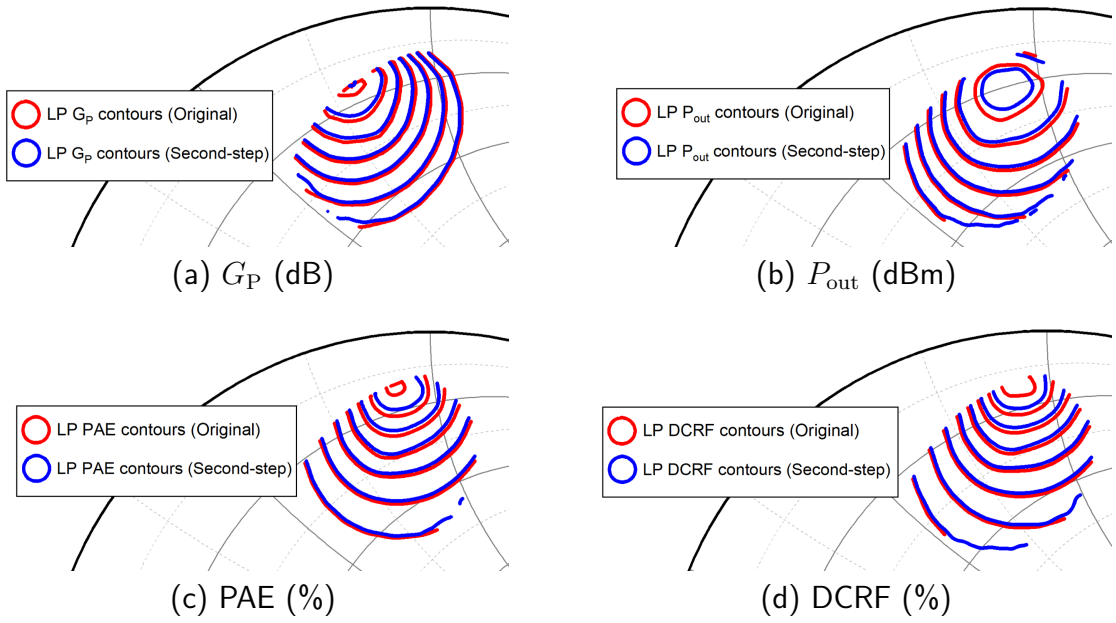

Figure 7.8: LP contours of the Qorvo 6 × 30 µm GaN HEMT at 30 GHz with V_D = 24 V, I_{DQ} = 50 mA/mm and P_{Av} = 24.3 dBm were measured using the active LP system. Contours are plotted, showing the original and second-step coefficients. The gain and output power are plotted using 0.5 dB contours with a maximum of 11 dB and 28 dBm, respectively. The PAE and DCRF are plotted using 5% contours with a maximum of 50% and 55%, respectively [5].

Figure 7.8 shows the load-pull contours of device performance metrics, highlighting a contour size and position difference between the original and second-step calibration coefficients. The mean differences across all measured load conditions are 0.08 dB, 0.08 dB, 0.8% and 0.8% for G_P, P_{out}, PAE and DCRF, respectively.

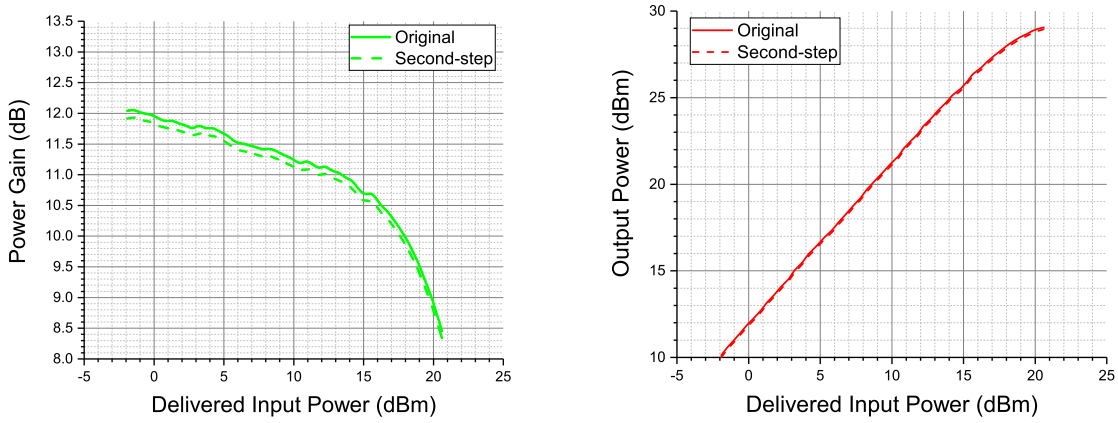

(a) G_{P} (dB) (b) P_{out} (dBm)

(c) PAE (%) (d) DCRF (%)

Figure 7.9: Power sweep of the Qorvo $6 \times 30\,\mu\mathrm{m}$ GaN HEMT at 30 GHz tuned for an optimum output power match with a $\Gamma_{\mathrm{L}} = 0.8\angle 93°$. The device operating conditions were $V_{\mathrm{D}} = 24\,\mathrm{V}$, $I_{\mathrm{DQ}} = 50\,\mathrm{mA/mm}$ using the active LP system. Showing a comparison of G_{P}, P_{out}, PAE and DCRF using the original and second-step calibration coefficients [5].

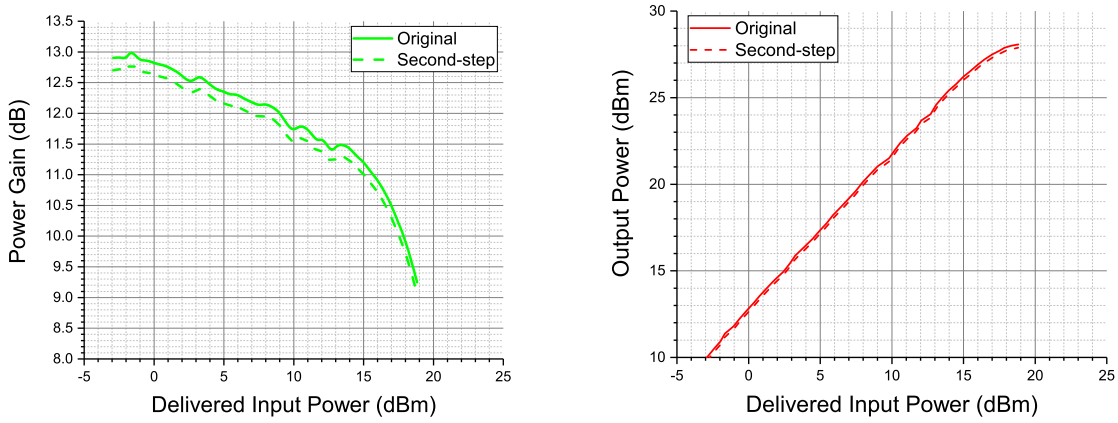

(a) G_{P} (dB) (b) P_{out} (dBm)

(c) PAE (%) (d) DCRF (%)

Figure 7.10: Power sweep of the Qorvo $6 \times 30\,\mu\mathrm{m}$ GaN HEMT at 30 GHz tuned for an optimum PAE match with a $\Gamma_{\mathrm{L}} = 0.9\angle 96°$. The device operating conditions were $V_{\mathrm{D}} = 24\,\mathrm{V}$, $I_{\mathrm{DQ}} = 50\,\mathrm{mA/mm}$ using the active LP system. Showing a comparison of G_{P}, P_{out}, PAE and DCRF using the original and second-step calibration coefficients [5].

The device was characterised across power levels to evaluate the difference between the original and second-step coefficients at the optimum impedance for output power and PAE.

The optimum for a power match occurred at $\Gamma_L = 0.8\angle 93°$, while the PAE match was closer to the edge of the Smith chart, at $\Gamma_L = 0.9\angle 96°$. The results show a minor difference in gain and output power, translating to a moderate difference in PAE and DCRF at compression. For Figure 7.9, the maximum differences are 0.12 dB, 0.12 dB, 1.4% and 1.5% for G_P, P_{out}, PAE and DCRF, respectively.

For Figure 7.10, the maximum differences are 0.2 dB, 0.2 dB, 2.5% and 2.5% for G_P, P_{out}, PAE and DCRF, respectively.

7.4.2 E-band GaAs pHEMT

The passive system was used to demonstrate the calibration technique applied to the load-pull characterisation of a Qorvo GaAs pHEMT with a gate length of 90 nm and a periphery of 6×30 µm at 82.5 GHz. The measurement system was configured with 25 dB of attenuation between the receivers and the measurement reference plane, and the calibration power was set to 0 dBm at the DUT.

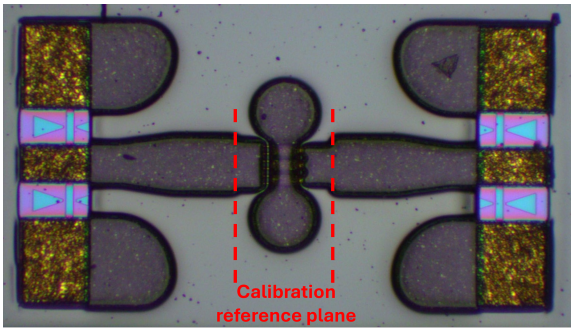

Figure 7.11: Qorvo GaAs pHEMT with a gate length of 90 nm and periphery of 6×30 µm.

After configuring the system for device measurement, an LP was performed on a zero-length thru to determine the calibration error. Figure 7.12 shows the error using the original and second-step coefficients error. The results presented here are the same as those shown in Figure 7.2(a).

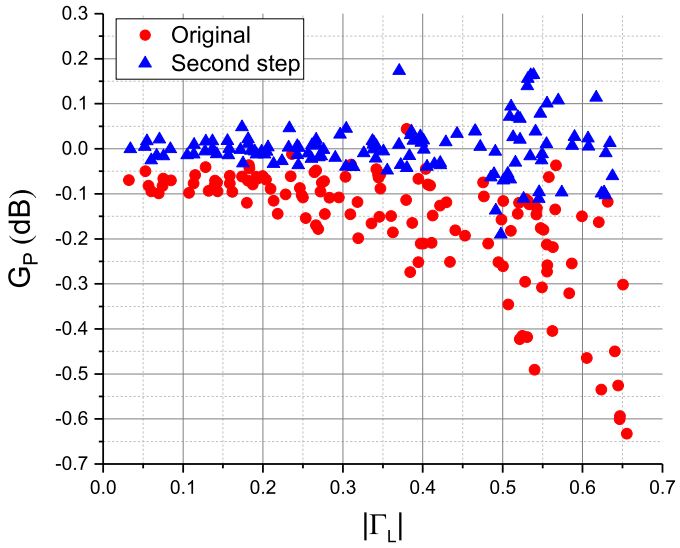

Figure 7.12: LP measurement of power gain in decibels versus the magnitude of Γ_L for a zero-length thru on the passive LP system at 82.5 GHz [5].

Figure 7.7 shows the calibration error using the original and second-step calibration coefficients. The second-step coefficients reduce the error to the baseline for this measurement system at this frequency. A reduction in error at $\Gamma_L = 0.65$ is observed with a decreased error from 0.65 to 0.1 dB.

A standard LP characterisation of the GaAs HEMT was performed using the original calibration coefficients. This involved a load-pull around the optimum impedance for output power, followed by a power sweep at the optimum impedance for a power match. Due to the limited tuning range of the passive tuners, closed contours were not achievable, and the power sweep was instead performed at the closest impedance to the optimum for output power.

In Figure 7.13, the load-pull contours of the device performance metrics are shown. All the contour plots exhibit differences in contour size and position, with each plot showing an additional contour for the second-step coefficients compared to the original. The mean differences across all measured load conditions were 0.35 dB, 0.32 dB, 7.1% and 3.6% for G_P, P_{out}, PAE and DCRF, respectively.

The device was characterised across a power sweep to evaluate the difference in performance metrics between the original and second-step coefficients at the optimum impedance for output power.

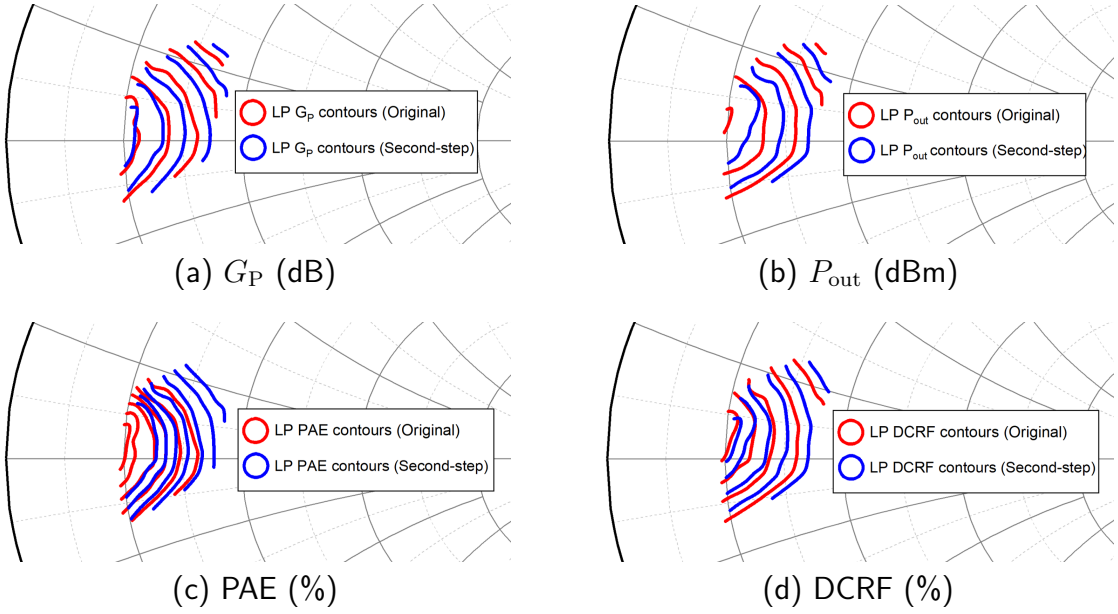

(a) G_{P} (dB) (b) P_{out} (dBm)

(c) PAE (%) (d) DCRF (%)

Figure 7.13: LP contours of the Qorvo 90 nm GaAs pHEMT at 82.5 GHz with $V_{\mathrm{D}} = 3.5\,\mathrm{V}$, $I_{\mathrm{DQ}} = 50\,\mathrm{mA/mm}$ and $P_{\mathrm{Av}} = 21.1\,\mathrm{dBm}$ were measured using the passive LP system. Contours were plotted, showing the original and second-step coefficients. The gain and output power are plotted using 0.5 dB contours with a maximum of 1.5 dB and 18 dBm, respectively. The PAE and DCRF are plotted using 2.5% and 5% contours with a maximum of 15% and 55%, respectively [5].

The optimum for a power match was at $\Gamma_{\mathrm{L}} = 0.7\angle 179°$. The results show a moderate gain and output power difference, which translates to a significant difference in PAE and DCRF at compression. For Figure 7.14, the maximum differences are 0.32 dB, 0.32 dB, 9.7% and 4.6% for G_{P}, P_{out}, PAE and DCRF, respectively.

A further verification step is performed for the measurement of the GaAs device. This chapter argues that the second-step calibration procedure should be used when an operator sees a calibration error following the verification load-pull measurement. In theory, this should only be required when the calibration cannot be performed with the system configured in its final measurement state. This case was demonstrated in the system characterisation section from Chapter 6, where a reasonable calibration error was achieved when the load-pull verification measurement immediately followed calibration. This knowledge can be used to verify the validity of the second-step calibration technique.

In the ideal case, the gain circles derived from S-parameter measurements at the same quiescent point should perfectly overlap the power gain contours from an LP

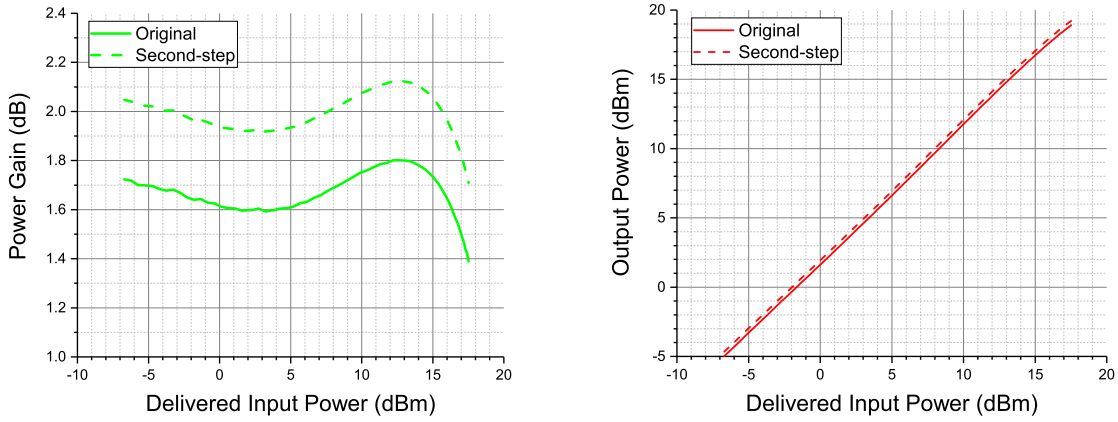

(a) G_{P} (dB) (b) P_{out} (dBm)

(c) PAE (%) (d) DCRF (%)

Figure 7.14: Power sweep of the Qorvo $6 \times 30\,\mu\mathrm{m}$ GaAs pHEMT at 30 GHz tuned for an optimum power match with a $\Gamma_{\mathrm{L}} = 0.7\angle 179°$. The device operating conditions were $V_{\mathrm{D}} = 3.5\,\mathrm{V}$, $I_{\mathrm{DQ}} = 50\,\mathrm{mA/mm}$ using the passive LP system. Showing a comparison of G_{P}, P_{out}, PAE and DCRF using the original and second-step calibration coefficients [5].

measurement when the device is operated in a linear backed-off condition.

These measurements are performed on the pHEMT device at 82.5 GHz as the device is unconditionally stable, power gain circles can be derived. The same device was used for the load-pull measurement and S-parameters to avoid device-to-device discrepancies. The S-parameters were measured on a dedicated S-parameter measurement system.

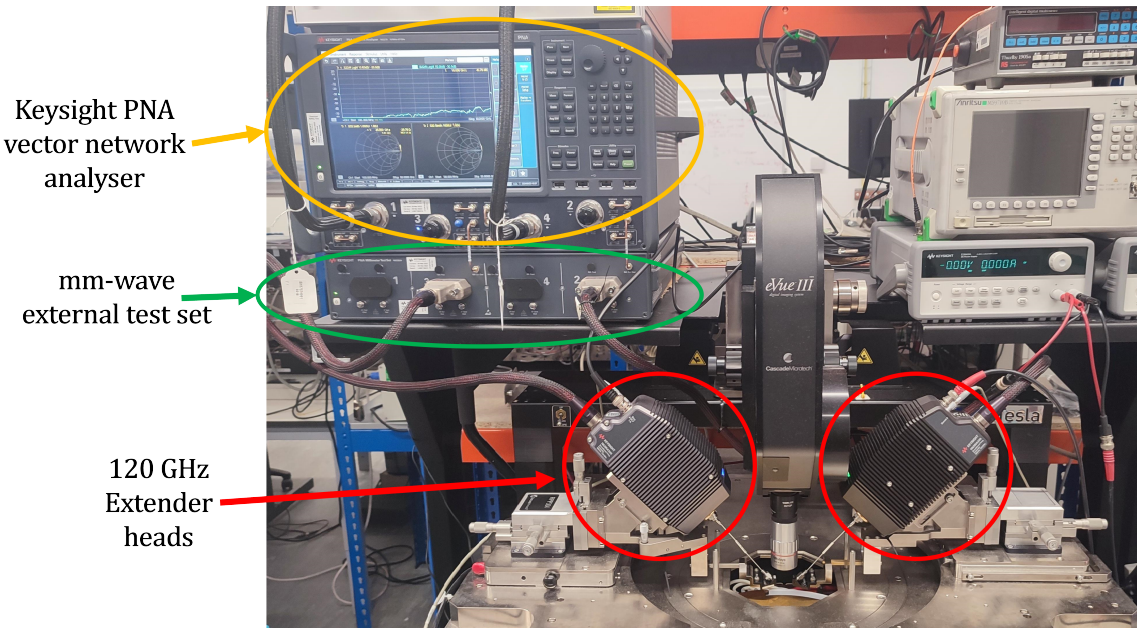

Figure 7.15: On-wafer S-parameter measurement system using the Keysight extender modules for frequencies up to 120 GHz.

The sample was loaded onto the vacuum chuck of the system in Figure 7.15, and an mTRL calibration [11] was performed due to its superior calibration accuracy at mm-wave [6], [7]. The line standards used in the calibration had a delay of 3, 7.6 and 21.9 ps, giving a valid calibration range of 3-120 GHz; the measurement system capability limits the upper frequency.

The S-parameter power gain circles are calculated using the following equations [12]:

The centre of the power gain circles is found using:

$$C_{\mathrm{P}} = \frac{g_p C_2^*}{1 + g_p(|S_{22}|^2 - |\Delta|^2)} \tag{7.8}$$

where

$$g_p = \frac{G_P}{|S_{21}^2|} \tag{7.9}$$

Where G_P is the desired gain circle expressed as a linear quantity.

Where

$$\Delta = S_{11}S_{22} - S_{21}S_{12} \tag{7.10}$$

and

$$C_2 = S_{22} - \Delta S_{11}^* \tag{7.11}$$

The radius of the circles are found using:

$$R_{\mathrm{P}} = \frac{\sqrt{1 - 2K|S_{12}S_{21}|g_p + |S_{12}S_{21}|^2 g_p^2}}{|1 + g_p(|S_{22}|^2 - |\Delta^2|)|} \tag{7.12}$$

Where K is Rollett's stability factor and is calculated:

$$K = \frac{1 - |S_{11}|^2 - |S_{22}|^2 + \Delta^2}{2|S_{21}S_{12}|} \tag{7.13}$$

Figure 7.16 shows the translation of S-parameter derived gain circles and the measured gain contours from LP in a backed-off condition (available input power of -2.5 dBm, the onset of compression is at approximately 16.5 dBm). Using the second-step calibration coefficients, the power gain from the load-pull better fits the S-parameter-derived power gain circles over the original calibration coefficients. The error at each measured reflection coefficient is calculated using the following equations.

The S-parameter power gain at each measured load-pull reflection coefficient is calculated using:

$$G_{\mathrm{P,S}} = \frac{|S_{21}|^2(1 - |\Gamma_{\mathrm{L}}|^2)}{(1 - |\rho_{\mathrm{in}}|^2)|1 - S_{22}\Gamma_{\mathrm{L}}|} \tag{7.14}$$

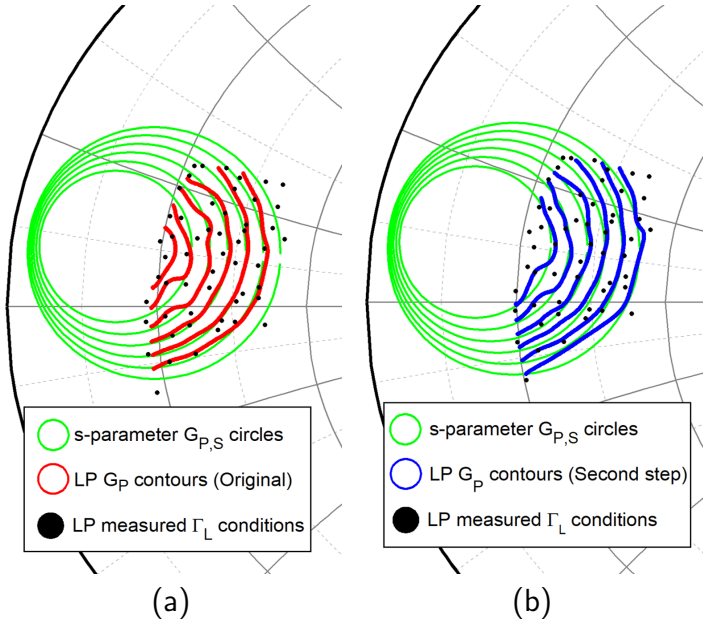

Figure 7.16: LP power gain contours and small-signal power gain circles of a GaAs pHEMT measured at 82.5 GHz in a backed-off state, P_{Av} = -2.5 dBm, for (a) original and (b) second-step calibration coefficients. The device was biased at $V_{\mathrm{D}} = 3.5\,\mathrm{V}$ and $I_{\mathrm{DQ}} = 50\,\mathrm{mA/mm}$. Maximum gain contour is 1.75 dB with 0.25 dB contours [5].

Where ρ_{in} is the S-parameter input reflection coefficient and is calculated:

$$\rho_{\mathrm{in}} = S_{11} + \frac{S_{12}S_{21}\Gamma_{\mathrm{L}}}{1 - S_{22}\Gamma_{\mathrm{L}}}\,. \tag{7.15}$$

Using these equations, the mean error between the S-parameter and LP power gain across all 54 measured load conditions is 0.25 dB for the original calibration coefficients and 0.09 dB for the second-step calibration coefficients.

These measurements demonstrate the effectiveness of the second-step calibration technique in improving the accuracy of device measurements. The characterisation of the GaAs device highlights a specific case where calibration accuracy is crucial. Despite the limited range of the passive tuners, the technology is operated closer to f_{max} where the gain is limited, especially in a compressed state. Minor calibration errors can lead to significant measurement inaccuracies, with differences in gain, output power, PAE and DCRF of up to 0.32 dB, 0.32 dB, 9.7% and 4.6%. These discrepancies substantially impact the performance metrics and could ultimately be the difference between the success or failure of a tapeout.

7.4.3 Error Correction Analysis

From a practical perspective, it is not immediately clear how the error in power gain propagates to the device's measurement after the operator performs the verification load-pull measurement on the thru standard.

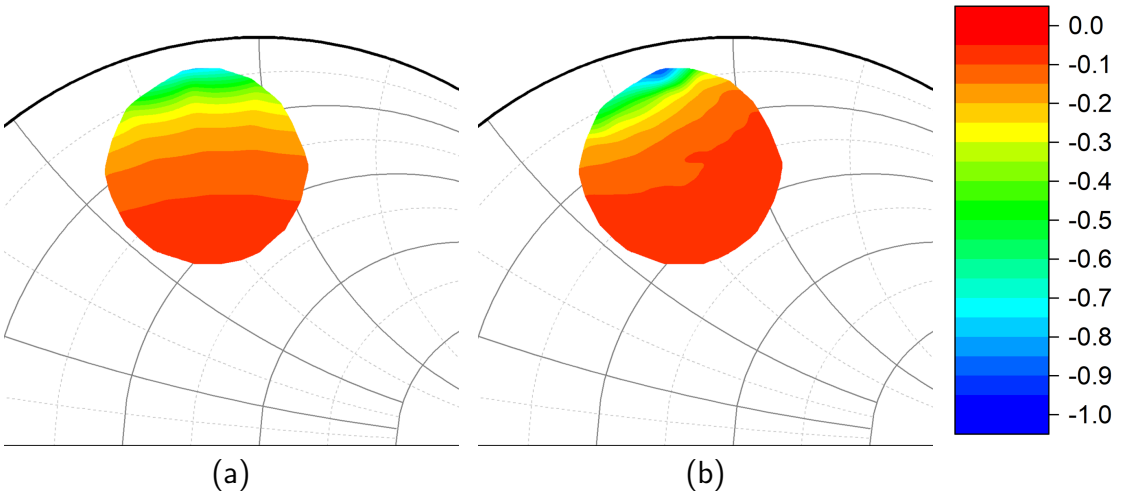

Figure 7.17: LP contours of power gain difference between original and second-step calibration coefficients. 0.1 dB step. (a) Thru standard and (b) GaN device at 30 GHz [5].

From Section 7.4.1, it's apparent that the observed calibration error X dB of the thru standard LP measurement does not directly translate to an X dB error when measuring the power gain of the DUT. This is demonstrated directly in Figure 7.17, which shows the difference in power gain between the original and second-step calibration coefficients. There is a change in contour shape and the magnitude of error appears to be higher for the GaN device at a high reflection coefficient. Using (7.16), the load-dependence of the error correction of the method described in this section can be analysed.

$$G_{\mathrm{P}} = \frac{P_{\mathrm{out}}}{P_{\mathrm{in}}} = \frac{|b_2|^2 - |a_2|^2}{|a_1|^2 - |b_1|^2} = \frac{|b_2|^2(1 - |\Gamma_{\mathrm{L}}|^2)}{|a_1|^2(1 - |\Gamma_{\mathrm{in}}|^2)} \tag{7.16}$$

where P_{in}, P_{out} are the delivered power to the input and output, respectively.

In this equation, the error in power gain is the sum of the error on the delivered input and output power. Therefore, this section investigates the load dependence of

error correction when the error is equally distributed between the input and output. Using this knowledge, different DUT types are used to demonstrate the overall power gain error depends up on the relationship between Γ_L and Γ_{in} of the measured DUT. The three device types investigated are zero-loss devices, such as a thru standard; lossy devices, such as an RF switch; and active DUT cases.

Simulation Setup

The simulations were conducted using the setup developed and described in Section 6.4.2. First, a vector and absolute calibration was performed, followed by a load-pull measurement on the thru standard, which showed no residual error. Next, a phase error was introduced into the measurement system, applied equally to both the input and output, by adding a 1.5° phase delay to the b_1 and b_2 receivers. The input side of the measurement system with the introduced error is shown in Figure 7.18.

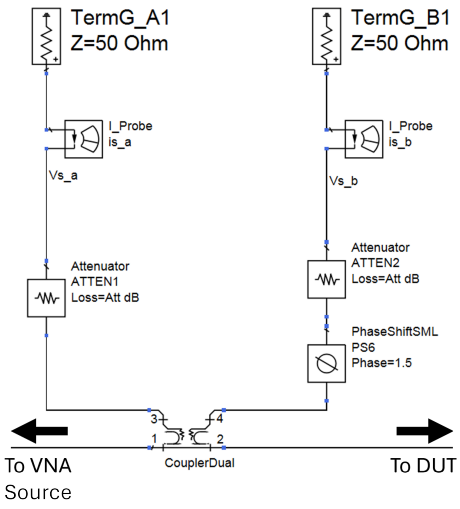

Figure 7.18: Receiver chain in load-pull simulation showing an additional 1.5° phase delay in the b_1 receiver.

The simulation was conducted with three different DUT types, which will be detailed in the following sections. A load-pull measurement was performed with and without the measurement system error for each case. The resulting power gain plots are then compared and analysed.

Zero loss DUT

In a zero loss DUT such as the thru standard, $\Gamma_{in} = \Gamma_L$ the error associated with both the input and output parameters becomes increasingly sensitive at the same rate as the load reflection coefficient moves towards the edge of the Smith chart, leading to a significant error.

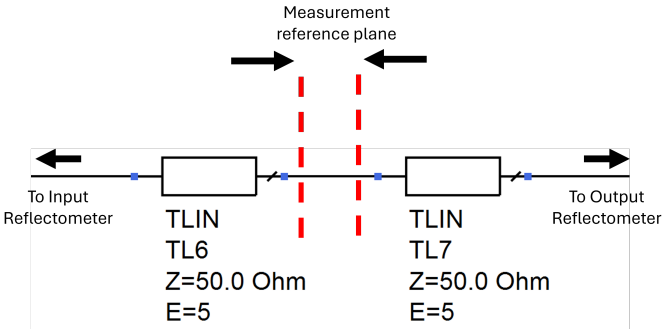

Figure 7.19: Schematic showing the thru standard definition and calibration reference plane.

In this simulation setup shown in Figure 7.19, the calibration was performed with the reference plane at the centre of the thru standard, defined as a 10° transmission line. The ideal and system with the error were simulated to show the error in the power gain.

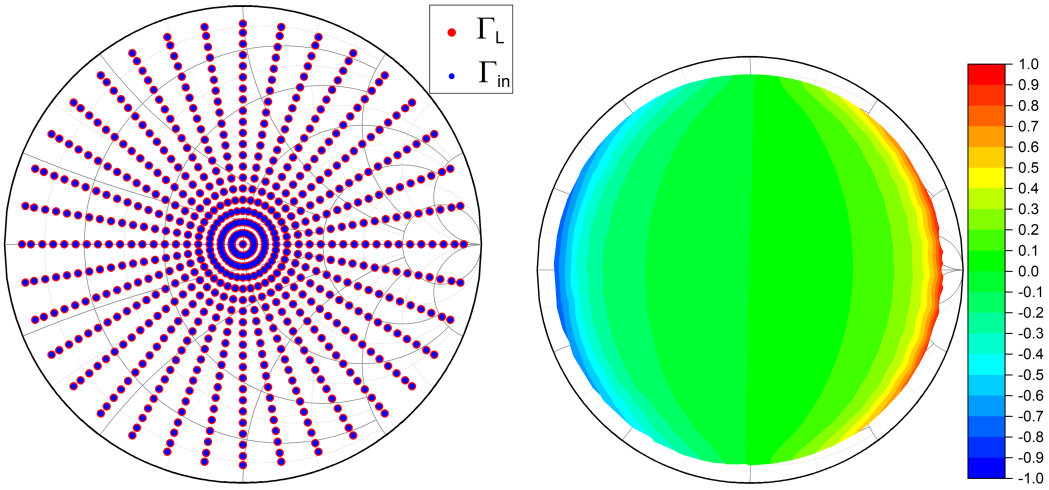

(a) Reflection Coefficient (b) Power Gain

Figure 7.20: LP simulation of the thru standard showing the (a) Ideal input and output reflection coefficients and (b) Power gain of the system with error.

Figure 7.20 shows the simulated reflection coefficient at the input and output. In

the ideal case, these parameters match. The phase error in the receivers results in a power gain error of up to ±1 dB at $\Gamma_L = 0.95$. This error forms the basis of the section; this same error is directly applied to the simulation of a switch and common source transistor to determine the error on power gain.

Lossy DUT

In a lossy DUT such as the switch, $\Gamma_{in} < \Gamma_L$ the error associated with the output parameter is significantly more sensitive than the input due to the reduced Smith chart coverage; this typically leads to a reduced error on power gain versus the thru standard load-pull measurement.

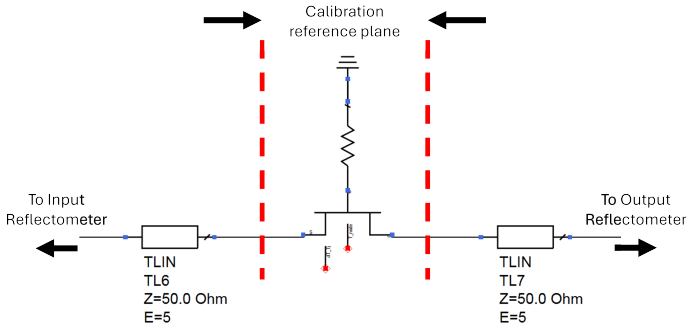

Figure 7.21: LP simulation set up for the Win Semiconductor NP12-01 4×50 µm switch model.

The simulation setup is shown in Figure 7.21, with a floating gate terminated with a resistor (to improve stability); in this state, the channel is conducting, and the switch is on. The device model used for the simulation was the Win semiconductor NP12-01 compact CPW model. The simulation was conducted at 80 GHz and the load impedance swept across the same points as the thru standard.

Figure 7.22 (a) shows the simulated reflection coefficient with reduced coverage and asymmetry of the input reflection coefficient. The on-resistance of the switch causes the asymmetry on the Smith chart. In (b), the power gain of the switch in the ideal and error conditions shows more error around the optimum insertion loss condition.

Figure 7.23 compares the power gain difference between the ideal system and the system with error for the thru and switch. (a) shows that near the optimum for

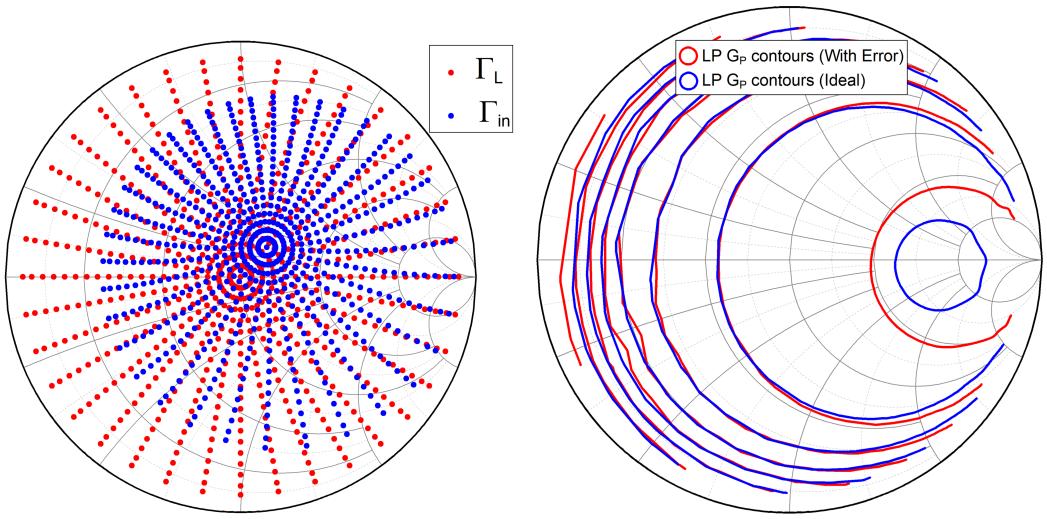

(a) Reflection Coefficient (b) Power Gain

Figure 7.22: LP simulation of the switch showing the (a) Ideal input and output reflection coefficients and (b) Power gain contours of the ideal measurement system and with error. The maximum contour is -0.5 dB with 1 dB contours.

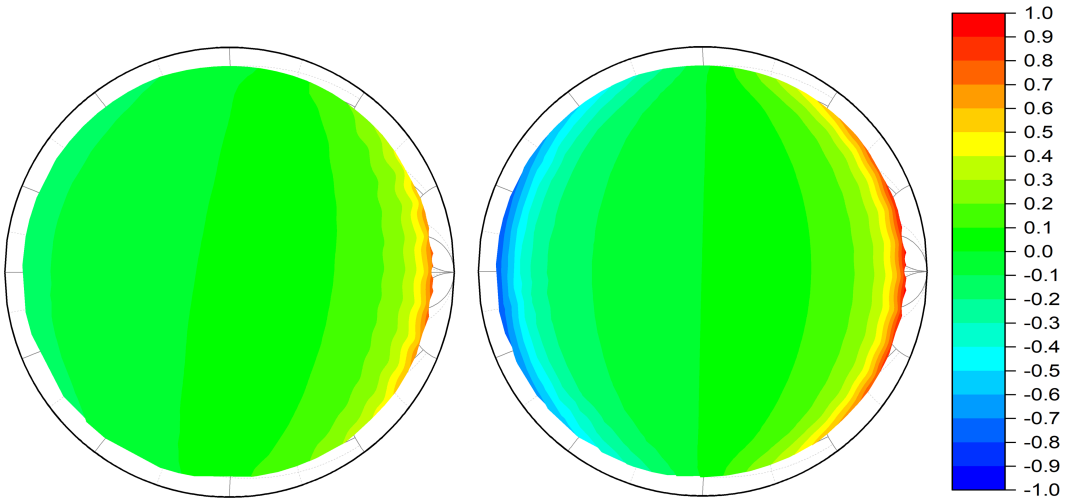

(a) Switch (b) Thru

Figure 7.23: LP contours of power gain difference between the ideal measurement system and with error. 0.1 dB step. (a) Switch and (b) Thru standard.

power gain, the contours are similar to (b) due to the switch's input and output reflection coefficients being similar to the thru standard. Moving towards the short side of the Smith chart, there is a negligible difference between the ideal and error conditions; this is partly due to the input reflection coefficient lying within an area with a low power gain error.

Active DUT

In an active DUT such as the common source transistor, feedback usually is low; this results in a weak correlation between Γ_{in} and Γ_L. The error associated with the output parameter becomes more sensitive moving towards the edge of the Smith chart, whilst the error related to the input is typically fixed due to the small radius of Γ_{in}; the error on power gain versus the thru standard load-pull measurement is heavily dependent of the location of Γ_{in}.

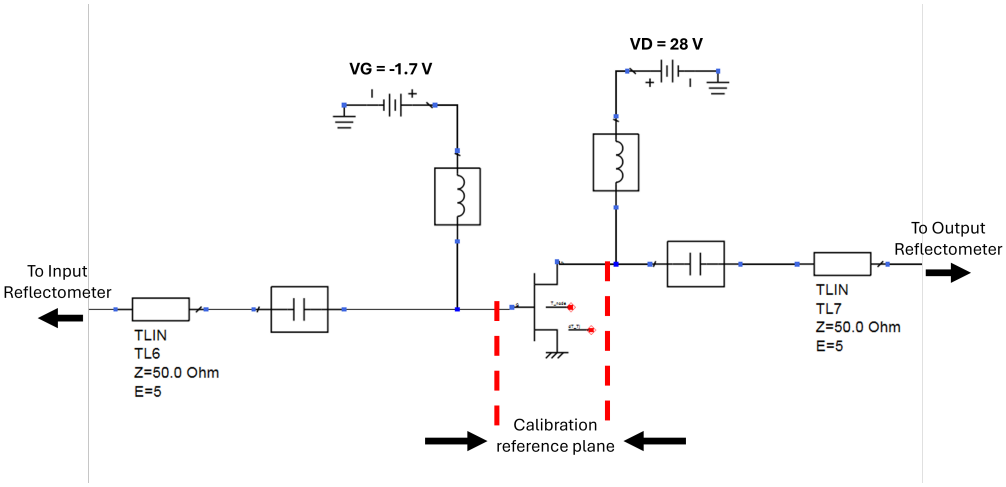

Figure 7.24: LP simulation set up for the Win Semiconductor NP12-01 $4 \times 50\,\mu m$ microstrip common source transistor model.

The simulation setup is shown in Figure 7.24. The device model used for the simulation was the Win semiconductor NP12-01 compact microstrip model. The simulation was conducted at 80 GHz and the load impedance swept across the same points as the thru standard. The device was biased in deep-class AB at 40 mA/mm with $V_G = -1.7V$ V and $V_D = 28$ V.

Figure 7.25 (a) shows the simulated reflection coefficient. The input reflection

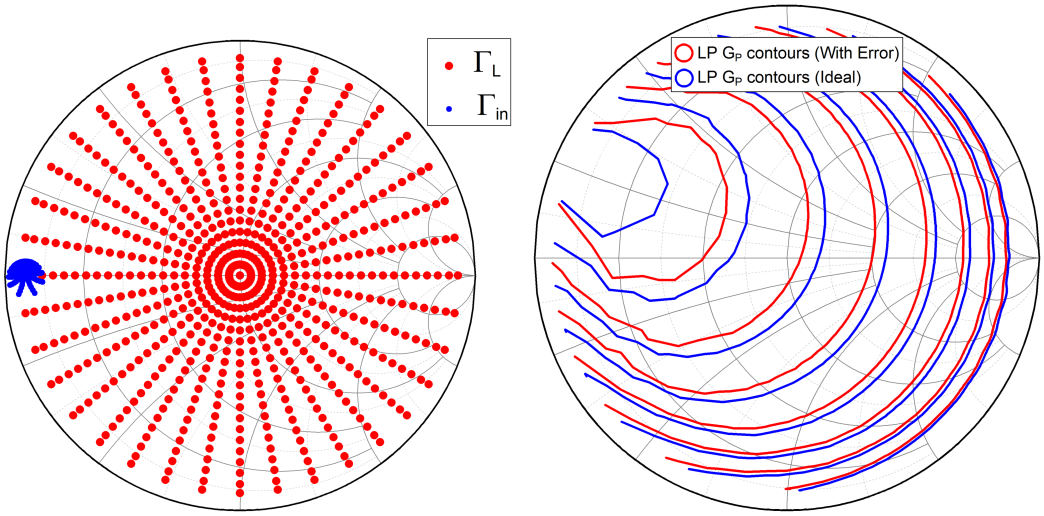

(a) Reflection Coefficient (b) Power Gain

Figure 7.25: LP simulation of the common source transistor showing the (a) Ideal input and output reflection coefficients and (b) Power gain contours of the ideal system and system with error. The maximum contour is 3 dB with 2 dB contours.

coefficient is loosely correlated with the load reflection coefficient; the impedance looking into the device always looks like a low impedance. In (b), the power gain of the device in the ideal system and the system with error show more errors around the optimum power gain condition.

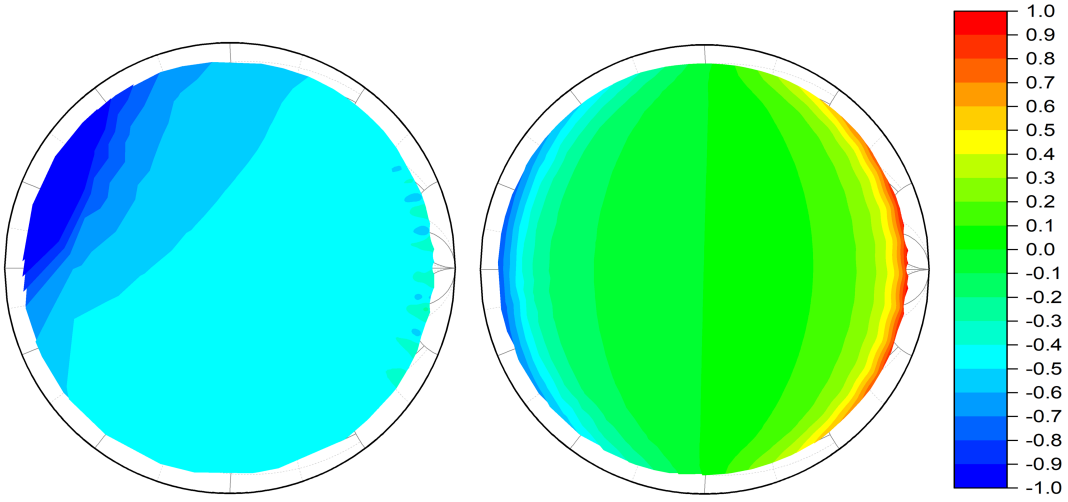

(a) Common source transistor (b) Thru

Figure 7.26: LP contours of power gain difference between the ideal measurement system and with error. 0.1 dB step. (a) Common source transistor and (b) Thru standard

Figure 7.26 compares the power gain difference between the ideal system and

the system with error for the thru and the common source transistor. (a) shows an entirely different error profile to the thru standard due to the input reflection coefficient always being near the short circuit, resulting in close to a fixed input-related error across all load reflection coefficient conditions.

7.5 Conclusion

This chapter builds upon the findings presented in Chapter 6, which identified key sources of error in mm-wave load-pull systems, particularly errors arising from system configuration. A literature review revealed that only one method had been published to address these errors, but it involved non-linear optimisation, which could result in non-physical calibration coefficients.

In contrast, this chapter introduces a practical method to "recalibrate" the measurement system using a second-step large-signal calibration procedure. This method requires load-pull measurements of the thru and line standards. A least squares approach is applied to the measured a and b waves to recalculate a new effective thru and line S-parameter matrix. These recalculated matrices are then fed back into the original TRL calibration algorithm, along with the original reflect measurement, to improve accuracy.

The chapter describes the authors second-step calibration method and its application to the practical measurement of mm-wave devices. The technique was applied to the load-pull characterisation and power sweeps of a Ka-band GaN HEMT. When the impedance was tuned to the optimum for PAE, the method improved the accuracy of power gain, output power, PAE, and DCRF by 0.2 dB, 0.2 dB, 2.5%, and 2.5%, respectively. Additionally, the load-pull characterisation of a GaAs pHEMT at 82.5 GHz demonstrated improvements of 0.32 dB, 0.32 dB, 9.7%, and 4.6% in the same parameters, respectively.

Simulation results showed how power gain errors measured on the thru standard propagate to errors in DUT measurements. For a switch DUT, the power gain error observed on the thru standard is typically greater than when measuring the switch

insertion loss, due to the reduced coverage of Γ_{in}. For common-source devices, the error is highly dependent on the location of Γ_{in}, which is usually concentrated in a small area on the Smith chart.

References

[1] V. Teppati et al. "Accuracy Improvement of Real-Time Load-Pull Measurements". In: *IEEE Trans. on Instrum. and Meas.* 56.2 (2007), pp. 610–613.

[2] S. Bonino, V. Teppati, and A. Ferrero. "Further Improvements in Real-Time Load-Pull Measurement Accuracy". In: *IEEE Microw. and Wireless Compon. Lett.* 20.2 (2010), pp. 121–123.

[3] V. Teppati and C. R. Bolognesi. "Evaluation and Reduction of Calibration Residual Uncertainty in Load-Pull Measurements at Millimeter-Wave Frequencies". In: *IEEE Trans. on Instrum. and Meas.* 61.3 (2012), pp. 817–822.

[4] A. Aldoumani et al. "Enhanced Vector Calibration of Load-Pull Measurement Systems". In: *ARFTG Microw. Meas. Conf.* 2014, pp. 1–4.

[5] A. Baddeley, R. Quaglia, and P. J. Tasker. "Calibration Error Reduction in Millimeter-Wave Load–Pull Systems Measuring Highly Reflective Loads". In: *IEEE Trans. Microw. Theory Techn.* (2024), pp. 1–13. DOI: 10.1109/TMTT.2024.3495544.

[6] S. Shin et al. "Comparison of On-Wafer Calibrations for Measurements of Active and Passive Devices at Millimeter-wave Frequencies". In: Nov. 2023.

[7] D. F. Williams, R. B. Marks, and A. Davidson. "Comparison of On-Wafer Calibrations". In: *ARFTG Microw. Meas. Conf.* Vol. 20. 1991, pp. 68–81. DOI: 10.1109/ARFTG.1991.324040.

[8] G.F. Engen and C.A. Hoer. "Thru-Reflect-Line: An Improved Technique for Calibrating the Dual Six-Port Automatic Network Analyzer". In: *IEEE Trans. Microw. Theory Techn.* 27.12 (1979), pp. 987–993.

[9] A. Rumiantsev et al. "Application of On-Wafer Calibration Technology for Advanced High-Speed BiCMOS Technology". In: *IEEE Bipolar/BiCMOS Circuits and Technol. Meet. (BCTM)*. 2010, pp. 98–101.

[10] K. Yau et al. "Device and IC Characterization Above 100 GHz". In: *IEEE Microw. Magazine* 13.1 (2012), pp. 30–54.

[11] R.B. Marks. "A Multiline Method of Network Analyzer Calibration". In: *IEEE Trans. Microw. Theory Techn.* 39.7 (1991), pp. 1205–1215.

[12] A. M. Ferendeci. *Power Gain Circles*. University of Cincinnati. URL: https://homepages.uc.edu/~ferendam/Courses/EE_611/Amplifier/PGain.html.

Chapter 8

Conclusion

Millimetre-wave systems have the potential to significantly enhance data rates, capacity, and latency for next-generation mobile and satellite networks. Additionally, they pave the way for advancements in other areas, such as automotive radar. However, the feasibility of these systems relies on MMIC designers achieving successful designs within a minimal number of tapeout cycles. This requires transistor models that accurately represent device operation at mm-wave frequencies, which, in turn, depend on reliable and accurate measurements.

This thesis addresses gaps in the literature related to mm-wave load-pull measurement systems, the accuracy of these measurements, and the correction of calibration errors. This chapter concludes each area and offers further research ideas to advance the field.

Chapter 5 introduces a first-of-its-kind single-sweep harmonic source/load-pull system with waveform measurement capability, capable of operating up to 100 GHz. This chapter details the calibration and measurement procedures, focusing on verification processes to ensure reliability and accuracy. Measurements of a GaAs pHEMT were conducted at both Ka-band and W-band frequencies.

The Ka-band measurements demonstrated the system's ability to perform harmonic load-pull, showcasing a potential improvement in performance metrics, including a 3% increase in PAE over fundamental tuning. Waveforms at the gate and drain manifolds were presented using data up to the third harmonic. While this data

is valuable, it does not provide direct insight into the device's operational mode due to the influence of input and output parasitics.

Measurements on the same device at W-band revealed limitations in the maximum reflection coefficients achievable with the passive tuner, which restricted the ability to reach the optimum impedance for power or efficiency. Despite this constraint, a PAE of 34.5% was achieved.

Errors identified during the device measurements highlighted the need to evaluate the measurement accuracy of load-pull systems, which became the primary focus of Chapter 6. This chapter provides a very useful and actionable method to verify load-pull measurement accuracy for mm-wave systems, along with critical calibration procedures to obtain accurate results.

The chapter establishes the best-case load-pull measurement uncertainty for both passive and active systems by minimising potential error sources, such as dynamic range limitations and mechanical alterations.

The analysis was performed by conducting a load-pull measurement on a thru standard in a fully calibrated system, which revealed the baseline calibration uncertainty worsens with increasing frequency. At Ka-band, the uncertainty was determined to be $\pm 0.15\,\mathrm{dB}$ for both passive and active systems, while at W-band, this increased to $\pm 0.25\,\mathrm{dB}$.

The analysis was extended to isolate mechanisms that caused a degradation in this error. The first case was the effect of measurement error caused by a degraded dynamic range during calibration due to the requirement to add attenuation to measurement receivers to prevent saturation and potential damage in high-power load-pull measurements. This analysis was confirmed using simulation and measurement and showed that to ensure a highly accurate load-pull measurement ($<0.1\,\mathrm{dB}$), the calibration dynamic range must be greater than $70\,\mathrm{dB}$. The second case examined unavoidable mechanical errors introduced during system configuration for device measurement. These included errors arising from absolute calibration and the inclusion of measurement components such as bias tees, circulators, and driver

amplifiers. It was observed that set-up errors increased with frequency, reaching up to 0.8 dB at a reflection coefficient of 0.7 at 82.5 GHz.

An extension of the large signal calibration procedure was presented in Chapter 7, which allows an operator to perform a simple operation, independent of the load-pull measurement system that involves taking a single measurement which is used to significantly improve the accuracy of the measurement independent of load condition.

The additional measurement is used to "recalibrate" the measurement system once it was configured for device measurement, where there is no longer a dynamic range limitation or any further significant mechanical changes are required. This technique was based on a load-pull measurement of a thru and line standard from a TRL calibration kit; using the measured waves, a least squares method, an equivalent S-parameter for the thru and line standards can be generated and used to update the calibration coefficients and therefore minimise errors to the systems baseline uncertainty. The method was applied to the active system, using an on-wafer GaN HEMT measured at 30 GHz and the passive system for a GaAs HEMT at 82.5 GHz, with a reduction in calibration error in all cases to the systems baseline uncertainty.

This thesis offers a comprehensive guide to load-pull measurement techniques, with detailed background on the hardware and calibration techniques underpinning every system. The work has application from research labs to industry, this thesis offers actionable suggestions to designers of future load-pull systems operating at mm-wave frequencies, to produce stable and robust mechanical systems that remain flexible to allow for complex calibration and measurement operations to be performed.

The second-step calibration algorithm presented can easily be integrated within a load-pull measurement system calibration procedure, the thesis contains all the necessary steps and equations to implement into software. This second-step calibration procedure is applicable in every load-pull measurement from high power, low frequency systems that suffer from significant error due to a reduced dynamic range

through to mm-wave frequency systems that suffer significantly more systematic error. This has the potential to significantly reduce load-pull measurement error for various applications, from designers looking for accurate performance estimations of unit cell transistors through to foundries developing device models, more accurate load-pull data allows for improved model accuracy.

8.1 Future Work

In Chapter 5, an underlying issue with the measurement system is the difficulty in performing load-pull measurements on GaN devices and for the GaAs device when measuring near the $F_{\max}$. These devices have an optimum fundamental impedance for output power near the edge of the Smith chart, which was beyond the range of the passive tuner. This issue is also a limitation when attempting to maximise performance by tuning harmonic frequencies. To further improve the functionality of the measurement system, hybrid tuning should be implemented; this will allow an extended tuning range. Several issues can be foreseen when moving to a hybrid system. The first issue concerns the availability of driver amplifiers on the market that could be used to extend the useable range of reflection coefficients. The additional power requirement for active tuning provides a difficult challenge as the load-pull amplifier will require an output power several times larger than the device under test. However, for harmonic tuning, this should be less of a challenge as when the device is pushed into compression, the harmonic output power is many orders of magnitude below the fundamental output power.

Another challenge foreseen is developing an active source that can be accurately controlled by the load-pull algorithm. As the source is unconverted for frequencies above 67 GHz, the phase and amplitude relationship between the VNA and the DUT varies non-linearly and would provide many convergence challenges for the load-pull algorithm. Developing an IQ modulator to allow for a linear change in amplitude and phase of a_2 after the up-converter would mitigate these issues.

Another avenue for future research stems from Chapter 5, where waveform mea-

surements at the extrinsic plane of the device were demonstrated. However, waveforms at the current generator plane are required to be more useful in understanding the device's mode of operation. At mm-wave frequencies (up to 120,GHz), the parasitics between the measurement plane and the current generator plane become significant. To better understand the device, it is therefore essential to de-embed these parasitics.

Established practices [1], [2], and [3] model a device using approximately 14 lumped elements, relying on direct extraction strategies to match measurement data. While these strategies work effectively up to 26.5 GHz, they struggle to achieve an accurate match at higher frequencies. Above 26.5 GHz, distributed effects become prominent, requiring an increase in the order of the extrinsic LC circuits. This approach has been proven successful for GaAs devices up to 120 GHz [4], where the authors developed test structures to extract different "shells" of the model individually.

For GaN devices, however, these architectures and extraction procedures tend to yield inaccurate models. This issue is addressed in [5], which develops an accurate GaN model extraction procedure up to 40 GHz by combining direct and optimisation-based extraction techniques. Despite these advancements, further research is required to develop accurate lumped-element models for GaN devices beyond 40 GHz. Such models would allow the use of results generated by the load-pull system to visualise the waveforms at the current generator plane.

These works pave the way for numerous investigations to advance this area. Waveform measurements at these frequencies remain relatively novel, with limited literature available. Key areas for further study include the model accuracy required to obtain reliable and actionable intrinsic waveforms and the impact of calibration strategies and algorithms on model extraction, particularly beyond 80 GHz.

References

[1] G. Dambrine et al. “A New Method for Determining the FET Small-Signal Equivalent Circuit”. In: *IEEE Trans. Microw. Theory Techn.* 36.7 (1988), pp. 1151–1159. DOI: 10.1109/22.3650.

[2] M. Berroth and R. Bosch. “High-Frequency Equivalent Circuit of GaAs FETs for Large-Signal Applications”. In: *IEEE Trans. Microw. Theory Techn.* 39.2 (1991), pp. 224–229. DOI: 10.1109/22.102964.

[3] B. Hughes and P.J. Tasker. “Bias Dependence of the MODFET Intrinsic Model Elements Values at Microwave Frequencies”. In: *IEEE Trans. on Electron Devices* 36.10 (1989), pp. 2267–2273. DOI: 10.1109/16.40909.

[4] P.J. Tasker and J. Braunstein. “New MODFET Small Signal Circuit Model Required for Millimeter-Wave MMIC design: Extraction and Validation to 120 GHz”. In: *IEEE MTT-S Int. Microw. Symp. (IMS)*. 1995, 611–614 vol.2. DOI: 10.1109/MWSYM.1995.405932.

[5] A. Jarndal and G. Kompa. “A New Small-Signal Modeling Approach Applied To GaN Devices”. In: *IEEE Trans. Microw. Theory Techn.* 53.11 (2005), pp. 3440–3448.